The Laser Mirror Alignment System for the LHCb RICH Detectors

Andrew Alan Macgregor

UNIVERSITY
of
GLASGOW

Department of Physics and Astronomy

April 2006

Thesis submitted for the degree of Doctor of Philosophy of the University of Glasgow

Acknowledgements

I would firstly like to sincerely thank my supervisor Dr. Paul Soler for his invaluable help, encouragement, teaching, guidance, friendship, support and excellent supervision throughout the years of my Ph.D. For the many hours he also spent explaining CP violation to me and patiently reading through and correcting this thesis. He truly is an excellent supervisor!

I would also like to thank Dr. Antonis Papanestis (RAL) for his help in setting up the full alignment simulation and obtaining the results, help with the Gaussian fit algorithm and for his general technical support. Dr. Sajan Easo (RAL/CERN), for his help in explaining the concept of GAUSS and for helping fight my corner so that I could start writing the mirror misalignment simulation tools. Dr. Nic Snailum (UEL) for his help and advice with image processing techniques. Dr. Gennady Kuznetsov (RAL), for his help with C++ programming. Prof. David Saxon (Glasgow), for his kind input. Dr. Chris Parkes (Glasgow), who also spent some time explaining CP violation. Not forgetting Dr. Andrew Pickford (Glasgow), for his help in introducing me to Linux when I first started, and for also explaining certain basic particle physics concepts to me so that I could understand my post-graduate particle physics lectures.

Words cannot express the deep gratitude I owe to my wife Phillipa, for her patience, encouragement, understanding and loving support these past years. She has been such a great help to me and has gone far beyond that extra mile. I would also like to give a special thanks to my parents for their love, support and encouragement and also lately for those special words "Is it finished yet?". Last but not least, I would like to thank my family and friends (not mentioned by name) for their friendship and support.

The financial support of the Particle Physics and Astronomy Research Council (PPARC) and CASE award partner, the CCLRC Rutherford Appleton Laboratory (RAL), is gratefully acknowledged.

Declaration

Except where explicit reference is made to the work of others, this dissertation is the result of my own work. None of this material has been submitted for any other degree at the University of Glasgow or any other institution.

Chapters 1-3 contain review material on the theory of CP violation and the description of the LHCb detector. The reviews are original but report the work of others. Chapter 4 contains wholly original work, except the description of the alignment software by A. Papanestis in section 4.1. The Gaussian fit algorithm in 4.4 was developed partly by the author but the main contributor was A. Papanestis. The image analysis software in 4.5 was developed by the author with input and advice from N. Snailum with respect to the Sobel Mask and Hough Accumulator. The development of the misalignment simulations in chapter 5 was performed in collaboration with A. Papanestis and S. Easo (RAL). The optimisation of the component location and final laser alignment performance also in chapter 5 is work performed by the author. The final conceptual design for the alignment system described in chapter 6 was performed by the author. Final engineering drawings were done by M. Woodward (CCLRC Engineering Dept.). The simulation and analysis framework for the full alignment simulation (chapter 7) was developed by A. Papanestis. Extraction of the final results using the framework was performed by the author in collaboration with A. Papanestis.

Andrew Macgregor

Contents

List of Figures

List of Tables

Chapter 1

Introduction

Particle physics is a study of the structure of matter. It could be argued that the first modern particle physicist was Lord Rutherford who undertook the famous "Gold Leaf" experiment to probe the structure of gold atoms in 1911 [64]. To his amazement he found that atoms have a dense positively charge nucleus. In 1912, German physicist Neils Bohr arrived in Manchester to work with Lord Rutherford. Four years later Bohr returned to the University of Copenhagen in 1916 and continued to investigate the structure of atoms and the radiation emanating from them. He received the 1922 Nobel Prize for his work [59].

Nearly one hundred years on and many discoveries later, the study of the structure of matter still continues and advances in technology have brought great improvements in the tools that can be used to aid this study. Today there are many particle factories, accelerators and detectors dedicated to the further study of the structure of matter.

The Large Hadron Collider (LHC) due to be commissioned in 2007 [31] at CERN, is the latest generation accelerator. It will be the first collider capable of generating 14 TeV (7 TeV + 7 TeV) pp hadron collisions. These high energy collisions can be used by the four experiments of the LHC, ATLAS, CMS, ALICE and LHCb to truly test the validity of the Standard Model of particle physics and to search for new physics. Figure 1.1 shows the positions of the super proton synchrotron (SPS) that injects protons into the LHC and the four LHC experiments located around the LHC ring.

Of the four experiments located around the LHC ring, two of them, ATLAS and CMS are general purpose experiments. Their primary purpose is to search for the Higgs and new physics such as Super Symmetric particles. The third experiment, ALICE is a dedicated heavy-ion detector which is designed to exploit the unique physics potential of nucleus-nucleus interactions at LHC energies. The aim of ALICE is to study the physics of strongly interacting matter at extreme energy densities, where the formation of a new phase of matter (quark-gluon plasma) is expected. Finally LHCb is the dedicated B physics experiment that will measure CP violation in B meson decays. The aim of LHCb will be to precisely constrain the Cabibbo-Kobayashi-Maskawa matrix (see chapter 2) measurements with unprecedented accuracy, as well as continue the search for new physics.

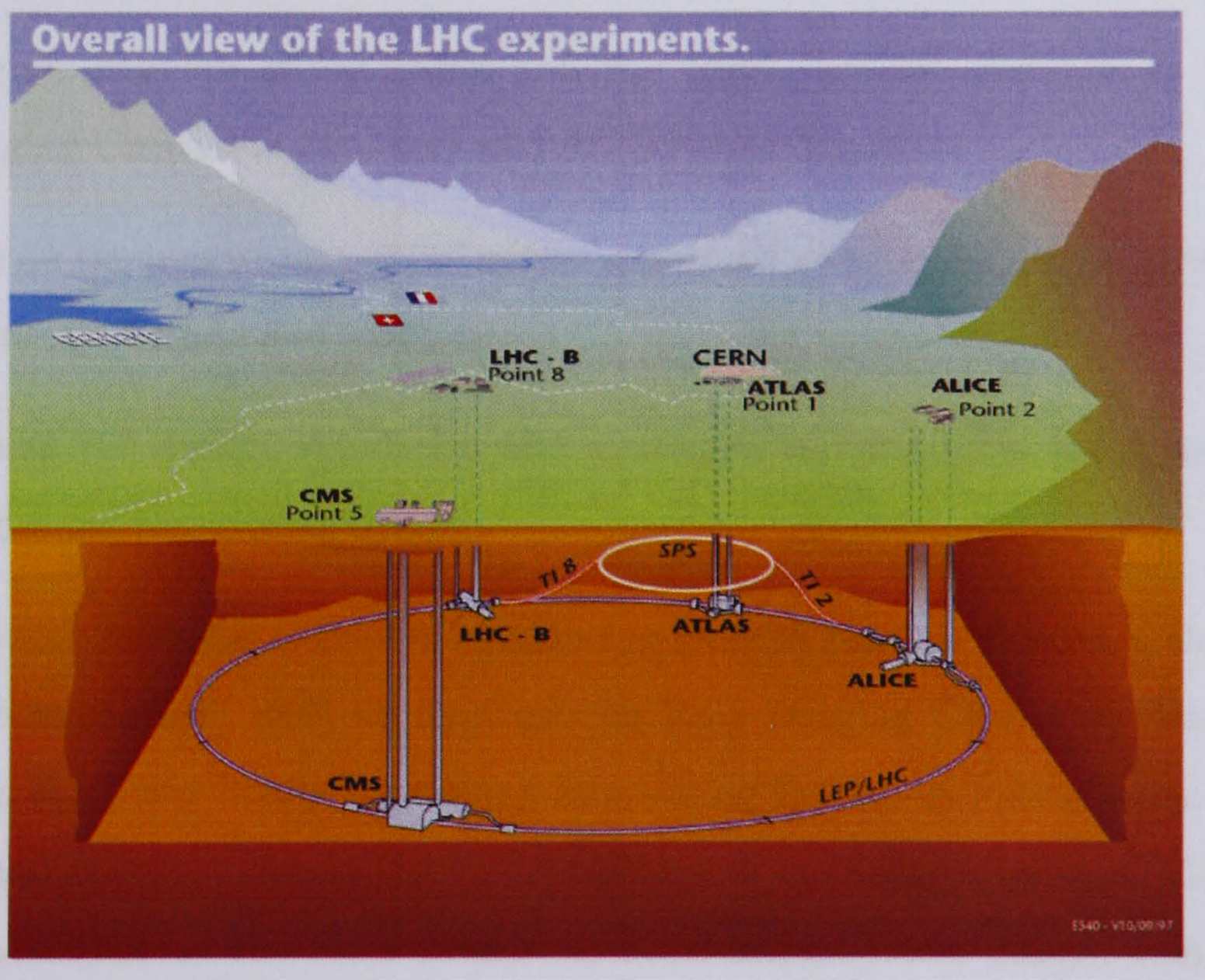

Figure 1.1: The LHC at CERN on the border of France and Switzerland.

The LHCb experiment contains a number of detectors, among these are two Ring Imaging Cherenkov (RICH) detectors. RICH detectors are very important in the particle identification process in that they are able to measure the speed of the charged particles that travel through them. This allows the mass of a charged particle to be calculated from its momentum and it can thus be identified. It is therefore important that the alignment of the optical components inside the RICH detectors are continually monitored, motivating the design of a system to precisely measure the positions of the RICH optics. This thesis describes the design, test and construction of the Laser Mirror Alignment Monitoring System for the RICH detectors of LHCb. The aims of this thesis are to:

1. describe the purpose of the LHCb experiment,

2. give an overview of the LHCb detector paying special attention to the Ring Imaging Cherenkov detectors and RICH2 in particular,

3. explain the importance of the mirror alignment monitoring system in the RICH detectors, its role and justification.

4. present the design, simulation and prototype test results of the Laser Mirror Alignment Monitoring System.

This thesis contains a chapter introducing modern particle physics, a chapter on the LHCb experiment with an emphasis on Ring Imaging Cherenkov detectors, a chapter on the Laser Mirror Alignment Monitoring System including image analysis software and results, a chapter on the simulation of the Laser Alignment Monitoring System, a chapter on the Final Alignment Monitoring System design, a chapter on the full alignment simulation results and a Conclusion.

Chapter 2

Theory of CP Violation

2.1 An Introduction to Modern Particle Physics

In the early 1920's a physicists view of the structure of matter would have been relatively simple. It was thought that there were only three different types of particle considered to be the fundamental constituents of matter. The first two, the proton, and electron were the building blocks of matter; and the photon was considered to be the building block of the electromagnetic system. But in the late 1920's this simple view was soon to change when in 1928 the British Scientist Paul Dirac postulated the existence of the positron [58] [57]. The first observation of this new particle came four years later in 1932 by Carl D. Anderson, who gave the positron its name (Interestingly, Anderson also unsuccessfully suggested, to rename the electron to "negatron") [15] [16]. Also, in 1932 the neutron was discovered by Chadwick [23].

Only a year after Dirac's postulation, a further complication arose in 1929 when the Austrian physicist Wolfgang Pauli proposed the existence of an additional neutral particle released in β decay. The theoretical existence of the neutrino and the mounting evidence that neutrons were not composed of a proton and an electron, led the Italian-born American physicist Enrico Fermi in 1933 to develop his theory of β decay [40]. Fermi suggested that in the decay process a proton, electron and neutrino come into existence at the moment of the decay as a result of interaction with a new type of force, known as the weak nuclear force.

In the early 1930's with the addition of the positron and the postulation of the neutrino to the list of particles, the view of the structure of matter, though slightly more complicated, was still rewardingly simple. However, problems with this new picture arose when physicists realised that they were unable to answer why it is that the many protons contained in a nucleus do not repel each other in the way that they should. It was recognised that an unusually strong force far stronger than anything encountered to that point, must be holding the nucleus together.

In 1935 the Japanese physicist, Hideki Yukawa put forward a suggestion to explain this strong force [72]. His thought was simple, Yukawa postulated that in the same way that two atoms can form a covalent bond together by sharing electrons, that two nucleons can be brought together by exchanging a new postulated particle. He established that the range of the force is inversely proportional to the mass of this particle and thus predicted that its mass would be about 200 times the size of an electron. Because the postulated particle would have a mass somewhere in between an electron and a proton, it was to be called a meson (from the Greek word meso, meaning "middle"). In 1936, Carl D. Anderson made yet another discovery, a new particle at 207 times the mass of an electron [17]. Although initially thought to be a meson, the new particle was later identified as a muon. The meson (now known as the π meson, or pion) was not found until 1947 by the British physicist Cecil Frank Powell [24].

On the 29th September 1954, signatories from 12 member states signed the establishment of the European Centre for Nuclear Research (CERN) [60]. The new particle accelerator brought about a new era in experimental particle physics and by the early 1960's many new particles had been discovered. Thus the early theories about the structure of matter had now been proved to be curiously inadequate. 1964 ushered in the discovery of Charge-Parity (CP) symmetry violation in the neutral Kaon system [49], and also the suggestion from two independent sources (physicists Murray Gell-Mann and George Zweig) that protons, neutrons and mesons are made up of quarks [46] [73]. During the period of 1967-8, Weinberg and Salam independently developed the electroweak theory to explain the decays of newly discovered particles by incorporating the weak force interaction with electromagnetism [69] [66].

Backed by new discoveries and the development of new theories, from around 1973, Yukawa's suggestion that the meson is the exchange particle between nucleons was largely superseded by the theory of quantum chromodynamics (QCD). QCD postulates that the strong nuclear force is transmitted by the exchange of gauge bosons (force carriers) called gluons between the quarks and antiquarks making up protons and neutrons.

These developments led to the establishment of an overall understanding regarding fundamental particles and how they interact. The theory, developed in the early to mid 1970's, became known as the Standard Model. It incorporated all that was known at the time and successfully predicted the outcome of many experiments. Over 30 years on, the Standard Model, though under threat, remains the foundation stone and doorway to understanding in our present world of modern particle physics.

2.2 The Standard Model

The Standard Model seeks to explain all the phenomena in particle physics in terms of the properties and interactions of a relatively small number of particles. These particles are of three distinct types; leptons, quarks and gauge bosons. Leptons and quarks are spin-$\frac{1}{2}$ fermions and can themselves be classified into three families, where each family has two generations, as shown in table 2.1.

	Generation	leptons	quarks	anti-leptons	anti-quarks
1st Family	1st generation	e^-	d	e^+	$\overline{d}$
	2nd generation	ν_e	u	$\overline{\nu}_e$	$\overline{u}$
2nd Family	3rd generation	μ^-	s	μ^+	$\overline{s}$
	4th generation	ν_μ	c	$\overline{\nu}_\mu$	$\overline{c}$
3rd Family	5th generation	τ^-	b	τ^+	$\overline{b}$
	6th generation	ν_τ	t	$\overline{\nu}_\tau$	$\overline{t}$

Table 2.1: Families and generations of fermions

Gauge bosons, described in table 2.2, are spin-1 bosons and act as "force carriers" for the four fundamental forces; electromagnetic, weak, strong and gravitational.

Interaction	Field Particle	Mass (MeV/c^2)	Range
Strong	gluon	0	Short ($\approx 1\ fm$)
Electromagnetic	γ	0	∞
Weak	W^+, W^-	80220	Short ($\approx 10^{-3} fm$)
	Z	91187	Short ($\approx 10^{-3} fm$)
Gravitational	graviton	0	∞

Table 2.2: Fundamental forces and their mediatory field particles

The theory of strong interactions is unusual in that quarks are not directly observable except in bound states. This is because in the theory of QCD, instead of only having a standard charge of + or -, quarks also have colour charge which comes in three types, red, green and blue. Anti quarks have the colour charges anti-red,

anti-green and anti-blue (sometimes referred to as cyan, magenta and yellow respectively). The theory states that only particles of neutral colour (i.e. white or colourless) can exist in an unbound state and therefore quarks must be bound. Within the Standard Model these bound states known as hadrons come in two types; the meson (a bound state of two quarks with opposing colour charge e.g. pions (π) and kaons(K)) and the baryon (a bound state of three quarks of different colour charge e.g. protons and neutrons). Strong interactions between quarks also give rise to the observable nuclear force between hadrons in atomic nuclei. Some of the mesons and their properties that are considered later on in this chapter are given in table 2.3.

Particle	Quark Composition	Mass (MeV/c^2)	Mean Life (s)
π^0	$\frac{1}{\sqrt{2}}(u\bar{u}+d\bar{d})$	134.9766	8.4(+/-0.6) x 10^{-17}
π^+,π^-	$u\bar{d}$, $d\bar{u}$	139.57018	2.6033(+/-0.0005) x 10^{-8}
K^0_s, $\overline{K}^0_s$	$d\bar{s}$, $s\bar{d}$	497.648	0.8953(+/-0.0006) x 10^{-10}
K^+, K^-	$u\bar{s}$, $s\bar{u}$	493.677	1.2384(+/-0.0024) x 10^{-8}
D^0, $\overline{D}^0$	$c\bar{u}$, $u\bar{c}$	1864.6	410.3(+/-1.5) x 10^{-15}
D^+, D^-	$c\bar{d}$, $d\bar{c}$	1869.4	1040(+/-7) x 10^{-15}
D^+_s, D^-_s	$c\bar{s}$, $s\bar{c}$	1968.3	490(+/-9) x 10^{-15}
B^0, $\overline{B}^0$	$d\bar{b}$, $b\bar{d}$	5279.4	1.536(+/-0.014) x 10^{-12}
B^0_s, $\overline{B}^0_s$	$s\bar{b}$, $b\bar{s}$	5369.6	1.461(+/-0.057) x 10^{-12}
B^+, B^-	$u\bar{b}$, $b\bar{u}$	5279.0	1.671(+/-0.018) x 10^{-12}
J/Ψ	$c\bar{c}$	3096.916	($\Gamma = h/\tau = 91.0$ keV)

Table 2.3: Meson properties [38]

Within a meson, although the colour charge of each quark is dynamic through gluon exchange, in relation to each other bound quarks will always have opposing colour charge.

The 16 elementary particles of the Standard Model have quantum state properties. These include, spin, the baryon number (Bn), lepton number (L), strangeness (S), charmness (C), bottomness (B) and charge. All 16 elementary particles and their

properties, including rest mass (m_0), are given in table 2.4.

Particle	spin ($\hbar$)	Bn	L	S	C	B	charge (e)	m_0 (MeV)
u	1/2	1/3	0	0	0	0	+2/3	2.75
d	1/2	1/3	0	0	0	0	−1/3	6
s	1/2	1/3	0	−1	0	0	−1/3	105
c	1/2	1/3	0	0	1	0	+2/3	1250
b	1/2	1/3	0	0	0	−1	−1/3	4750
t	1/2	1/3	0	0	0	0	+2/3	174300
e^-	1/2	0	1	0	0	0	−1	0.511
μ^-	1/2	0	1	0	0	0	−1	105.658
τ^-	1/2	0	1	0	0	0	−1	1776.99
ν_e	1/2	0	1	0	0	0	0	$< 3 \times 10^{-3}$
ν_μ	1/2	0	1	0	0	0	0	< 0.19
ν_τ	1/2	0	1	0	0	0	0	< 18.2
γ	1	0	0	0	0	0	0	0
gluon	1	0	0	0	0	0	0	0
W^+	1	0	0	0	0	0	+1	80420
Z	1	0	0	0	0	0	0	91187.6
graviton	2	0	0	0	0	0	0	0

Table 2.4: Quantum properties of elementary particles [38]

The differences between an elementary particle and its antiparticle are that the antiparticle has opposite charge and internal quantum numbers but its spin and mass are identical.

2.2.1 Model Difficulties

Today, the Standard Model is regarded as a well established theory. However, it is not accepted as being complete for two main reasons:

1. The model contains 27 free parameters (or 29 for Majorana neutrinos) not including electric charges [52]. These parameters must be determined experimentally and cannot be independently calculated.

2. The model fails to describe gravitational interactions.

Though the Standard Model has been largely successful in its predictions, the first experimental deviation from the original theory came in 1998 when Super-Kamiokande published results indicating neutrino oscillation [39]. This implies the existence of non-zero neutrino masses. Since then, the Standard Model has been revised to allow neutrinos to have mass, but this revision has come at the expense of an additional number of free parameters.

Though the balance of matter and anti-matter in the Standard Model is nominally symmetric, a small allowance is made within the model for imbalance through the process of Charge-Parity (CP) violation as defined by the CKM matrix (see sections 2.3 and 2.4). However, the Standard Model has no mechanism that allows for CP violation in the quark sector to exceed that which is described by the CKM matrix.

2.3 CP violation in the Standard Model

2.3.1 Introduction

CP violation has been observed in weak interactions and is the phenomenon where the charge conjugate state under a parity transformation behaves differently from the original state. This was first observed for the neutral kaon system through indirect CP violation in 1964 by James Cronin and Val Fitch of Brookhaven National Laboratory. They showed, for example, that a K_s with a CP eigenstate of +1 can decay to $\pi^+\pi^-\pi^0$ with an eigenstate of -1 about 0.2% of the time [14] [49].

Indirect CP violation is where the violation is not in the observed decay, but through the mixing of the states of the particle that has decayed. To explain further, neutral kaons have the property whereby they can oscillate between a particle-antiparticle state. The superposition (or mixing) of quantum mechanical states, proposed by Erwin Schrodinger in 1935, implies that the state of any object is not known until a measurement of that state is performed. Effectively, the state is in a superposition of all available states until the measurement itself causes the object to be limited to a single possibility. A neutral kaon can be in the particle (K^o) and antiparticle ($\overline{K^o}$) state simultaneously until it decays (or interacts) at which point a particle detector can measure one state or the other. In a perfect CP invariant world, the kaon would not have a preference of state, and therefore statistically kaons would be distributed evenly between particle and antiparticle final states. What Cronin and Fitch had discovered was a small hole in the picture of a CP invariant world, and this hole was waiting to be explored. Since that time physicists have long predicted that CP violation would also occur in the B meson system. This phenomenon has only recently been confirmed in the decays of B_d mesons by the Babar and Belle experiments where they observed CP violations in the decay of $B_d \rightarrow J/\psi\ K_s$ in 2001 [7] [9].

Direct CP violation was first detected in 1999 by KTeV (Fermilab) [25] and NA48 (CERN) in neutral kaons [34]. Direct CP violation and indirect CP violation are both the result of quantum interference. However, the interference responsible for direct CP violation is not due to the mixing of the two possible states of a meson, but

between the possible paths by which it can decay. BaBar and Belle, the asymmetric B factories at SLAC and KEK respectively, recently showed evidence for direct CP violations in B meson decays. For example, starting with equal numbers of B and $\overline{\mathrm{B}}$ mesons, as they decay, it would be reasonable to expect equal numbers of $\mathrm{K}^+\pi^-$ and $\mathrm{K}^-\pi^+$ pairs. However, from equal numbers of B and $\overline{\mathrm{B}}$ mesons, collisions at BaBar produced 910 $\mathrm{K}^+\pi^-$ pairs but only 696 $\mathrm{K}^-\pi^+$ pairs [**?**]. In 2004 Babar published its results of direct CP violation in the decay $B^o \to K^+\pi^-$ measuring an asymmetry of -0.113±0.030(stat)±0.009(syst) at a level of 4.2σ [8]. Also in 2004, the Belle collaboration also published results on a similar analysis but with an asymmetry measurement of -0.088±0.035±0.013 at a level of 2.4σ [10].

2.3.2 Charge Conjugation (C)

Classically, the obvious application of the charge conjugation operator is the reversal of the electric charge. However this simplistic view of the charge conjugation operator is entirely insufficient. Since electric and magnetic fields have their origins in charges they are also subject to reversal. Furthermore, charge conjugation has some further implications at the quantum level. The operator also involves the reversal of all the internal quantum numbers such as lepton number, baryon number and strangeness. It does not however affect mass, energy, momentum or spin. Thus, under charge conjugation, a particle is replaced by its anti-particle such that its mass, energy, momentum, spin and position remain invariant.

2.3.3 Parity Conjugation (P)

The parity conjugation operator inverts all the spatial coordinates. The inversion is sometimes referred to as mirror symmetry, but to be precise, it is a mirror image that not only switches left and right but also up and down. This means that (+x,+y,+z) under parity inversion are replaced with (-x,-y,-z). Spin, being a purely quantum mechanical phenomenon, is not changed under parity inversion.

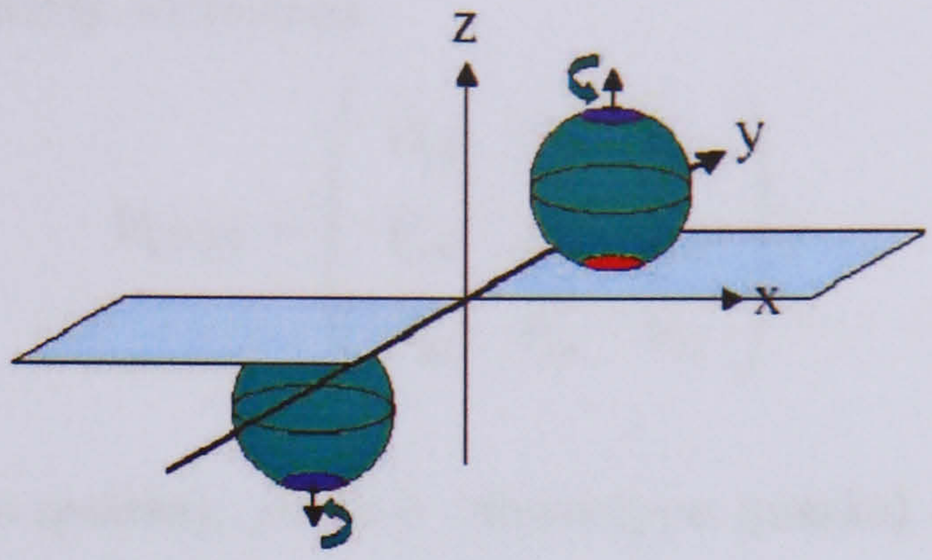

Figure 2.1: The inversion of spatial coordinates by parity conjugation.

2.4 The CKM Matrix

The beginnings of the CKM matrix started with the discovery of strange particles. They were called "strange" firstly because they lived far longer than the calculated expected weak decay rate, and secondly because two of the strange neutral mesons (now known as the neutral kaons K_L and K_S) had identical states but different half lifes. The reason was not known at the time. In the 1950's, Murray Gell-Mann suggested that these new particles had a conserved quantum number which he called "strangeness" [41]. In 1963, Nicola Cabibbo proposed a mechanism, using an additional new quark (aptly named the "strange" quark) that described quark mixing in the form of a 2x2 unitarity matrix in order to explain strange particle decays [13]. Ten years later, based upon Cabibbo's earlier work, the discovery of CP violation and the recent proposition of a fourth quark (called "charm"), Makoto Kobayashi and Toshihide Maskawa realised that if 6 generations of quarks are assumed in 3 families, an expressive 3x3 unitary matrix with complex phases can be produced where each element describes mixing between quarks [51]. The complex phases allow for small CP violations to occur in the mixing. The 3x3 Kobayashi-Maskawa (KM) unitarity matrix (it is now more commonly known as the Cabibbo-Kobayashi-Maskawa (CKM) matrix) was developed in 1973 and it measures the mixing probability of the different

quarks. It can be explicitly written as

$$V_{\mathrm{CKM}} = \begin{pmatrix} V_{ud} & V_{us} & V_{ub} \\ V_{cd} & V_{cs} & V_{cb} \\ V_{td} & V_{ts} & V_{tb} \end{pmatrix}, \tag{2.1}$$

where i=u,c,t (up-type quarks), j=d,s,b (down-type quarks) and V_{ij} is the mixing between i and j. However, using 3 angles (θ_{12}, θ_{13}, θ_{23}) and 1 complex phase (δ) the matrix can be conveniently written in the form

$$V_{\mathrm{CKM}} = \begin{pmatrix} c_{12}c_{13} & s_{12}c_{13} & s_{13}e^{-i\delta_{13}} \\ -s_{12}c_{23} - c_{12}s_{23}s_{13}e^{i\delta_{13}} & c_{12}c_{23} - s_{12}s_{23}s_{13}e^{i\delta_{13}} & s_{23}c_{13} \\ s_{12}s_{23} - c_{12}c_{23}s_{13}e^{i\delta_{13}} & -c_{12}s_{23} - s_{12}c_{23}s_{13}e^{i\delta_{13}} & c_{23}c_{13} \end{pmatrix} \tag{2.2}$$

Where $\mathrm{s}_{ij} = \sin\theta_{ij}$, $\mathrm{c}_{ij} = \cos\theta_{ij} = \sqrt{1 - s_{ij}^2}$ and ij are the generation labels. θ_{12} is the Cabibbo angle (θ_c)

2.4.1 Wolfenstein Parameterisation

Lincoln Wolfenstein's 1983 parameterisation of the CKM matrix [71] reflects the hierarchy of the strengths of quark transitions between the three families of quark by means of charged current interactions. The parameterisation is an expression of the CKM matrix in terms of Taylor expansions, and can be derived by introducing the following terms.

$$\lambda = s_{12}, \quad A = \frac{s_{23}}{s_{12}^2}, \quad \rho = \frac{s_{13}\cos\delta}{s_{12}s_{23}}, \quad \eta = \frac{s_{13}\sin\delta}{s_{12}s_{23}} \tag{2.3}$$

The matrix is expanded in terms of the sine of the Cabibbo angle, $\lambda = \sin\theta_{12} \sim 0.22$, and is often approximated to the third order, $\mathcal{O}(\lambda^3)$,

$$V_{\mathrm{CKM}} = \begin{pmatrix} 1 - \frac{1}{2}\lambda^2 & \lambda & A\lambda^3(\rho - i\eta) \\ -\lambda & 1 - \frac{1}{2}\lambda^2 & A\lambda^2 \\ A\lambda^3(1 - \rho - i\eta) & -A\lambda^2 & 1 \end{pmatrix} + \mathcal{O}\left(\lambda^4\right). \tag{2.4}$$

With each increase in order of the Wolfenstein parameterisation, the accuracy of the mixing increases. LHCb is expected to measure mixings up to $\mathcal{O}\left(\lambda^5\right)$,

$$V_{\mathrm{CKM}} = \begin{pmatrix} 1-\frac{1}{2}\lambda^2+\frac{1}{4}\lambda^4 & \lambda & A\lambda^3(\rho-i\eta) \\ -\lambda+\frac{1}{2}A^4\lambda^4-A^2\lambda^5(\rho+i\eta) & 1-\frac{1}{2}\lambda^2+\frac{1}{4}\lambda^4(1-2A^2) & A\lambda^2 \\ A\lambda^3(1-\tilde{\rho}-i\tilde{\eta}) & -A\lambda^2+A\lambda^4\left(\frac{1}{2}-\rho-i\eta\right) & 1-\frac{1}{2}A^2\lambda^4 \end{pmatrix}+\mathcal{O}\left(\lambda^6\right), \tag{2.5}$$

where $\tilde{\rho}=\rho(1-\lambda^2/2)$ and $\tilde{\eta}=\eta(1-\lambda^2/2)$.

2.4.2 The Unitarity Triangles

The CKM matrix has a property known as unitarity due to the physical properties it represents. Three unitarity conditions can be produced by taking each element in a column of the matrix, and multiplying it by the complex conjugate of its neighbour from another column. A further three unitarity conditions can be produced by repeating this method but with rows instead of columns. Thus the CKM matrix can be defined by the six unitarity conditions,

$$V_{ud}V_{ub}^* + V_{cd}V_{cb}^* + V_{td}V_{tb}^* = 0 \qquad (db) \qquad (2.6)$$

$$V_{us}V_{ub}^* + V_{cs}V_{cb}^* + V_{ts}V_{tb}^* = 0 \qquad (sb) \qquad (2.7)$$

$$V_{ud}V_{us}^* + V_{cd}V_{cs}^* + V_{td}V_{ts}^* = 0 \qquad (ds) \qquad (2.8)$$

and

$$V_{ud}V_{td}^* + V_{us}V_{ts}^* + V_{ub}V_{tb}^* = 0 \qquad (ut) \qquad (2.9)$$

$$V_{cd}V_{td}^* + V_{cs}V_{ts}^* + V_{cb}V_{tb}^* = 0 \qquad (ct) \qquad (2.10)$$

$$V_{ud}V_{cd}^* + V_{us}V_{cs}^* + V_{ub}V_{cb}^* = 0 \qquad (uc) \qquad (2.11)$$

Each term of a condition is complex and can be represented as a vector on a 2-dimensional complex plane. Since the sum of the conditions is zero, the three vectors form a closed triangle such that the sum of the angles are equal to π. For example, the unitarity condition (db), can be plotted as in figure 2.2. The angles α, β, and γ are defined as,

$$\alpha \equiv arg\left(-\frac{V_{td}V_{tb}^*}{V_{ud}V_{ub}^*}\right),\ \beta \equiv arg\left(-\frac{V_{cd}V_{cb}^*}{V_{td}V_{tb}^*}\right),\ \gamma \equiv arg\left(-\frac{V_{ud}V_{ub}^*}{V_{cd}V_{cb}^*}\right). \qquad (2.12)$$

In this arrangement, all the sides of the triangle have complex components, but

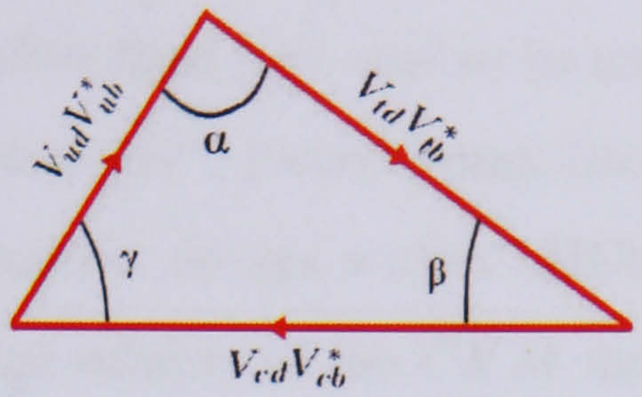

Figure 2.2: The unitarity triangle (db).

its representation can be simplified by making one of the terms real through normalisation (figure 2.3). Continuing to take the unitarity condition (db) as an example, it can be rearranged to give an equivalent equation by dividing both sides by the middle term. This gives,

$$\frac{V_{ud}V_{ub}^*}{V_{cd}V_{cb}^*} + 1 + \frac{V_{td}V_{tb}^*}{V_{cd}V_{cb}^*} = 0 \qquad (db) \qquad (2.13)$$

The corresponding representation of the (db) unitarity triangle will thus have one non-complex side, and it is in this way that the unitarity triangle is most commonly displayed.

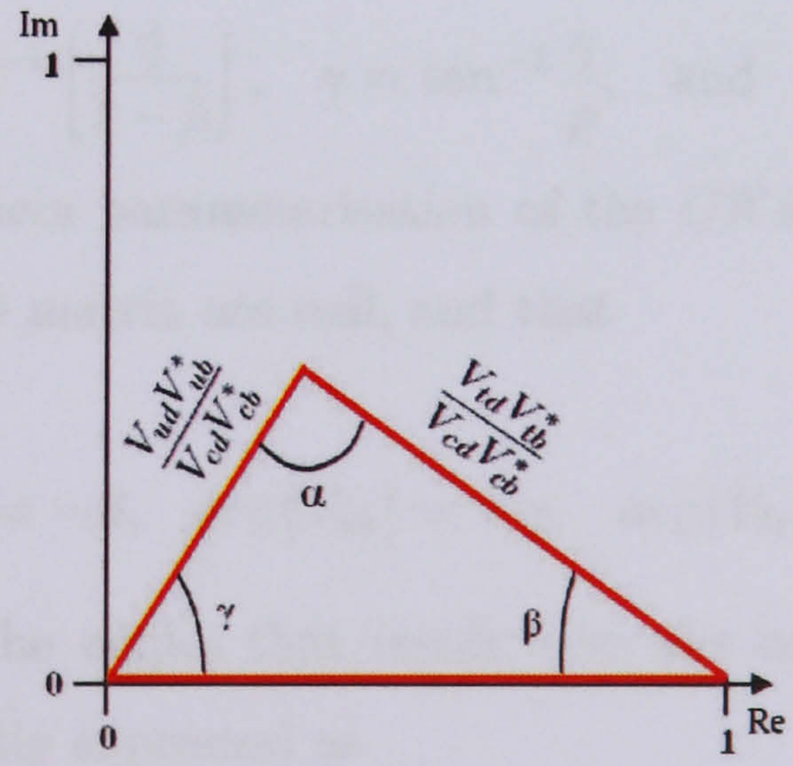

Figure 2.3: The unitarity triangle (db), represented such that the term $V_{cd}V_{cb}^*$ is real.

In this way, each of the six unitarity conditions can be represented by a unitarity triangle. However, four out of the six conditions (sb, ds, ct, uc) produce triangles that

have a very small angle associated with them. Of the remaining two conditions,(db) is experimentally more accessible than (ut), and so its corresponding triangle is often referred to as "The unitarity triangle". Nevertheless, both the (db) and (ut) triangles represent experimentally accessible decays within LHCb and therefore both will be used to experimentally test the validity of the CKM matrix.

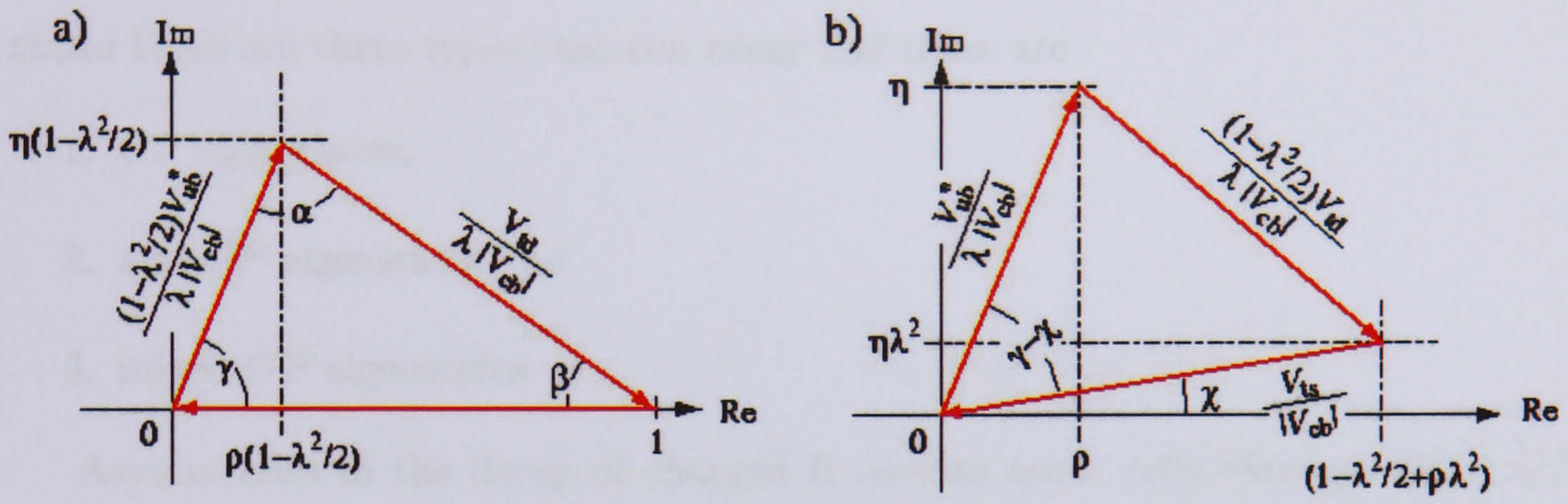

Figure 2.4: The unitarity triangle (db), represented such that the term $V_{cd}V_{cb}^*$ is real.

The relationship of the Wolfenstein parameterisation to the angles β, γ, and χ is given through

$$\beta = \tan^{-1}\left[\frac{\tilde{\eta}}{1-\tilde{\rho}}\right], \quad \gamma = \tan^{-1}\frac{\eta}{\rho}, \quad \text{and} \quad \chi = \eta\lambda^2. \tag{2.14}$$

The $\mathcal{O}\ (\lambda^5)$ Wolfenstein parameterisation of the CKM matrix implies that all but three elements of the matrix are real, and that

$$arg\{V_{td}\} = -\beta, \quad arg\{V_{ub}\} = -\gamma, \quad arg\{V_{ts}\} = \chi + \pi, \tag{2.15}$$

Thus, by including the angles that result from the complex phase, the CKM matrix can be conveniently expressed as

$$V_{\text{CKM}} = \begin{pmatrix} 1-\frac{1}{2}\lambda^2 & \lambda & -|V_{ub}|e^{-i\gamma} \\ -\lambda & 1-\frac{1}{2}\lambda^2 & A\lambda^2 \\ -|V_{td}|e^{-i\beta} & |V_{ts}|e^{-i\chi} & 1 \end{pmatrix} \tag{2.16}$$

2.5 The B Meson System

As with neutral Kaons, B mesons can violate CP conservation both directly and indirectly and there can also be interference between these two modes of CP violation. The final decay products are either in a flavour specific final state (charged B decays), or a flavour non-specific final state (neutral B decays). For flavour non-specific final states there are three types that can occur and these are

1. CP eigenstates,

2. non-CP eigenstates and

3. mixed CP eigenstates

Asymmetries in the decay of charged B mesons occur only through direct CP violation. Asymmetries in the decay of neutral particles can occur though direct CP violation, indirect CP violation and CP violation in the interference. These three forms of CP violation will now be considered.

2.5.1 Indirect CP Violation

Indirect CP violation is an asymmetry that occurs in the mixing of a particle B^o and its antiparticle $\overline{B^o}$, such that the mixing rate of $B^o \rightarrow \overline{B^o}$ is different to the rate of $\overline{B^o} \rightarrow B^o$. Thus, under indirect CP violation it is true that

$$\left|\frac{q}{p}\right| \neq 1 \tag{2.17}$$

with

$$\frac{q}{p} = \sqrt{\frac{M_{12}^* - \frac{i}{2}\Gamma_{12}^*}{M_{12} - \frac{i}{2}\Gamma_{12}}}, \tag{2.18}$$

where M_{12} and Γ_{12}, are both off-diagonal elements of the Hermitian 2×2 mass and decay matrices (the off-diagonal elements correspond to the mixing). Hence, a B^0 can convert to a $\overline{B^0}$ with probability:

$$P\left(B^0 \rightarrow \overline{B^0}\right)(t) = \left|\frac{q}{p} f_-(t)\right|^2$$

where

$$|f_{\pm}(t)|^2 = \frac{1}{4}\left[e^{-\Gamma_1 t} + e^{-\Gamma_2 t} \pm 2e^{-\overline{\Gamma} t}\cos(\Delta M t)\right] \tag{2.19}$$

and $M_1, M_2, \Gamma_1, \Gamma_2$ are the diagonal mass and decay matrix elements and $\overline{\Gamma} = (\Gamma_1 + \Gamma_2)/2$.

Indirect CP violation can be measured through the observation and tagging of jets and also through the observation of semi-leptonic B decays. Both B^o and $\overline{B^o}$ can oscillate between a particle-antiparticle state due to second order weak interactions (figure 2.5).

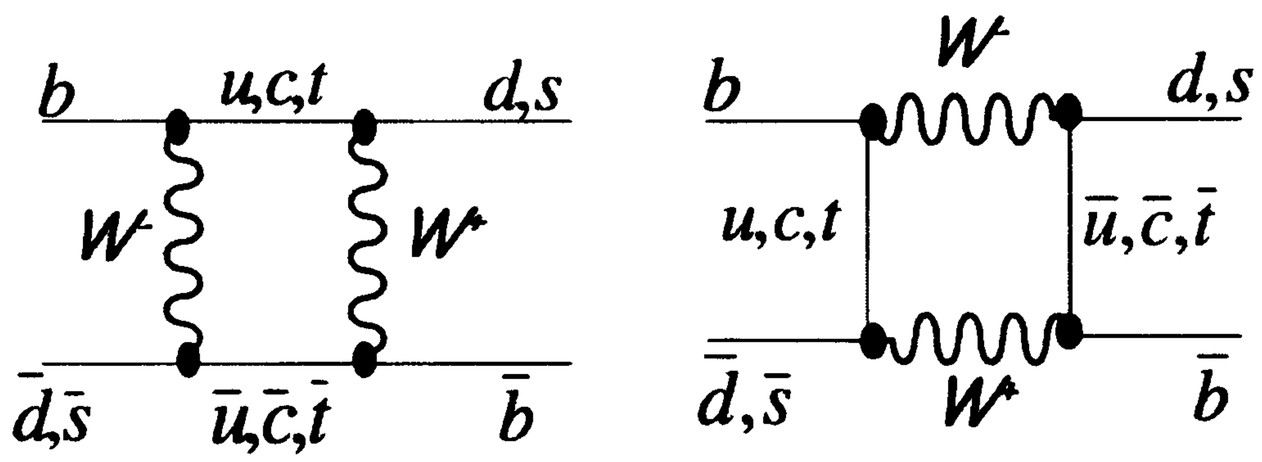

Figure 2.5: Box diagrams of B oscillations.

Assuming a pure state of B^o or $\overline{B^o}$ at time $t = 0$, the meson state will become a superposition of B^o, $\overline{B^o}$ at time $t > 0$ until the point of decay or detection. If CP symmetry is conserved, the final state of B mesons should be evenly distributed between particle-antiparticle states. Under indirect CP violation the distribution becomes asymmetric.

B mesons have a relatively long lifetime, and a considerable rest mass energy. These attributes play a positive role in the detection of semi-leptonic decays. In a semi-leptonic decay, the b quark will decay to either a c quark or u quark through the mediation of a W boson and the W boson can then produce a charged lepton and its corresponding neutrino. This process is described by the Feynman tree diagram of figure 2.6.

Due to the high rest mass of the b quark, the mediating W boson in the semi-leptonic decay will produce a high momentum lepton that can be tracked and identified. The point at which the B meson decays can be found by tracking the paths of

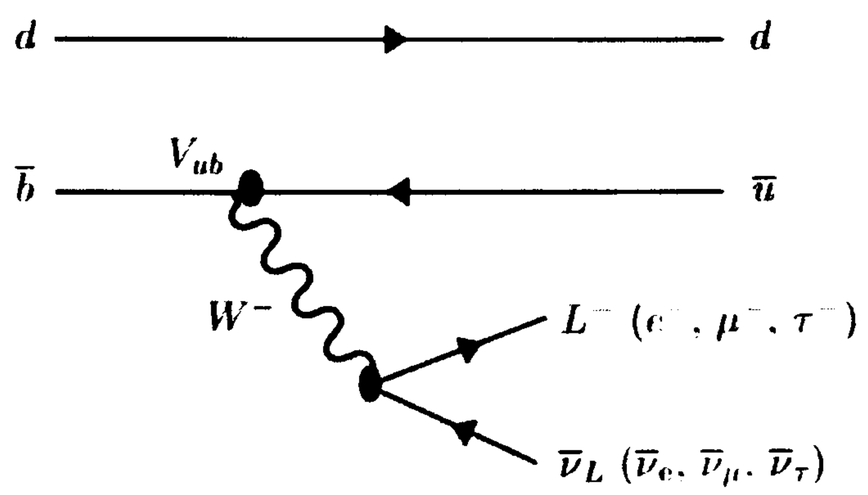

Figure 2.6: Feynman diagram of a semi-leptonic B decay.

the resulting meson and lepton. Thus, the final state of the B meson can be deduced through the identification of the lepton produced in the decay. This allows the identity of one of the B mesons to be tagged, and a search for the decay of the second B meson to be made to determine whether it has oscillated or not. Given high enough statistics, an accurate measurement of asymmetry can be made.

2.5.2 Direct CP Violation

With direct CP violation, the violation is in the decay, and the amplitude of the decay $\mathrm{B^o}\to f$ differs from the amplitude of $\overline{\mathrm{B^o}}\to f$, where f is a final state common to both decays. The two decay amplitudes A and $\overline{A}$ are written

$$A \equiv \langle f\,|H|\,\mathrm{B}\rangle, \qquad \overline{A} \equiv \langle \overline{f}\,|H|\,\overline{\mathrm{B}}\rangle; \tag{2.20}$$

where H is the Hamiltonian, and these differ such that

$$\left|\frac{\overline{A}}{A}\right| \neq 1 \tag{2.21}$$

In the measurement of direct CP violation, it is the final decay states that are important. For example, in a CP invariant world, starting with equal numbers of $\mathrm{B_s}$ and $\overline{\mathrm{B_s}}$ mesons, after they decay, there should be equal numbers of $\mathrm{K^+\pi^-}$ and $\mathrm{K^-\pi^+}$ pairs. However, direct CP violation allows an asymmetry in the decay path, such that an unequal number of $\mathrm{K^+\pi^-}$ and $\mathrm{K^-\pi^+}$ final states occur. Therefore, in the measurement of direct CP violating decays, the whole decay path needs to be tracked, and the product particles need to be identified.

2.5.3 CP Violation in the Interference

A final form of CP violation is through the interference of the mixing and the decay amplitudes and can be measured from the time dependent CP asymmetry [12],

$$\mathcal{A}(t) = \frac{\Gamma_f - \overline{\Gamma}_f}{\Gamma_f + \overline{\Gamma}_f} \tag{2.22}$$

$$= \frac{(1-|\lambda|^2)\cos(\Delta M t) - 2Im\{\lambda\}\sin(\Delta M t)}{(1+|\lambda|^2)\cosh(\Delta\Gamma t/2) + 2Re\{\lambda\}\sinh(\Delta\Gamma t/2)}, \tag{2.23}$$

where,

$$\lambda = \frac{q}{p}\frac{\overline{A}}{A}. \tag{2.24}$$

Separating the direct CP violating contribution from that which describes the CP violating contribution of the interference between mixing and decay amplitudes, the asymmetry can be written in the form

$$\mathcal{A}(t) = \mathcal{A}_{\rm CP}^{dir}\cos(\Delta M t) + \mathcal{A}_{\rm CP}^{mix}\sin(\Delta M t), \tag{2.25}$$

where

$$\mathcal{A}_{\rm CP}^{dir} = \frac{(1-|\lambda|^2)}{(1+|\lambda|^2)} \quad \text{and} \quad \mathcal{A}_{\rm CP}^{mix} = \frac{-2Im\{\lambda\}}{(1+|\lambda|^2)}. \tag{2.26}$$

For B_d^o decays where $\Delta\Gamma$ is small, $A_{\rm CP}^{dir}$ is negligible and so the CP asymmetry reduces to

$$\mathcal{A}(t) = -Im\{\lambda\}\sin(\Delta M t). \tag{2.27}$$

2.5.4 Survey of Experimental Results and the Physics Aims of LHCb

Compiled from the recent results of BaBar and Belle, the current status of the experimental constraint upon the unitarity triangle is given by the table shown in figure 2.7 and the plot in figure 2.8.

Observable	central $\pm$ CL $\equiv 1\sigma$	$\pm$ CL $\equiv 2\sigma$	$\pm$ CL $\equiv 3\sigma$
$\sin 2\alpha$	$-0.27^{+0.22}_{-0.16}$	$^{+0.49}_{-0.49}$	$^{+0.71}_{-0.62}$
$\sin 2\alpha$ (meas. not in fit)	$-0.11^{+0.43}_{-0.32}$	$^{+0.62}_{-0.67}$	$^{+0.76}_{-0.81}$
$\sin 2\beta$	$0.722^{+0.036}_{-0.036}$	$^{+0.072}_{-0.064}$	$^{+0.108}_{-0.091}$
$\sin 2\beta$ (meas. not in fit)	$0.682^{+0.125}_{0.028}$	$^{+0.182}_{-0.078}$	$^{+0.203}_{-0.128}$
α (deg)	$97.9^{+5.0}_{-6.4}$	$^{+16.8}_{-14.1}$	$^{+23.4}_{-20.9}$
α (deg) (meas. not in fit)	$93.1^{+9.6}_{-12.5}$	$^{+22.4}_{-18.5}$	$^{+29.8}_{-23.7}$
β (deg)	$23.1^{+1.5}_{-1.5}$	$^{+3.1}_{-2.6}$	$^{+4.9}_{-3.6}$
$\gamma \simeq \delta$ (deg)	$59.0^{+6.4}_{-4.9}$	$^{+14.2}_{-16.6}$	$^{+21.1}_{-23.1}$
$\gamma \simeq \delta$ (deg) (meas. not in fit)	$58.2^{+6.7}_{-5.4}$	$^{+15.6}_{-20.3}$	$^{+23.3}_{-24.6}$

Figure 2.7: The 2005 table of constraints on the unitarity triangle [36].

Though these measurements would suggest that the theory of CP violation through the CKM matrix is correct, low statistical accuracy means the margins of error surrounding each of the measurements are still too large for the theory to be properly validated. Thus, the main B physics aims for LHCb and the general purpose LHC experiments, ATLAS and CMS, will be to precisely constrain the CKM measurements with unprecedented accuracy, as well as continue the search for new physics.

2.5.5 Measurement of the angles of the unitarity triangle by LHCb

Some of the B decay modes that will be studied by LHCb are given in figure 2.9. By measuring the asymmetries in the decays of the B $\overline{\text{B}}$ pairs for each decay mode, with high enough statistics, the complex phase angles can be accurately calculated. This will require the experiment to have very good capabilities to distinguish between π and K mesons, since these particles are the product particles of many of the decays

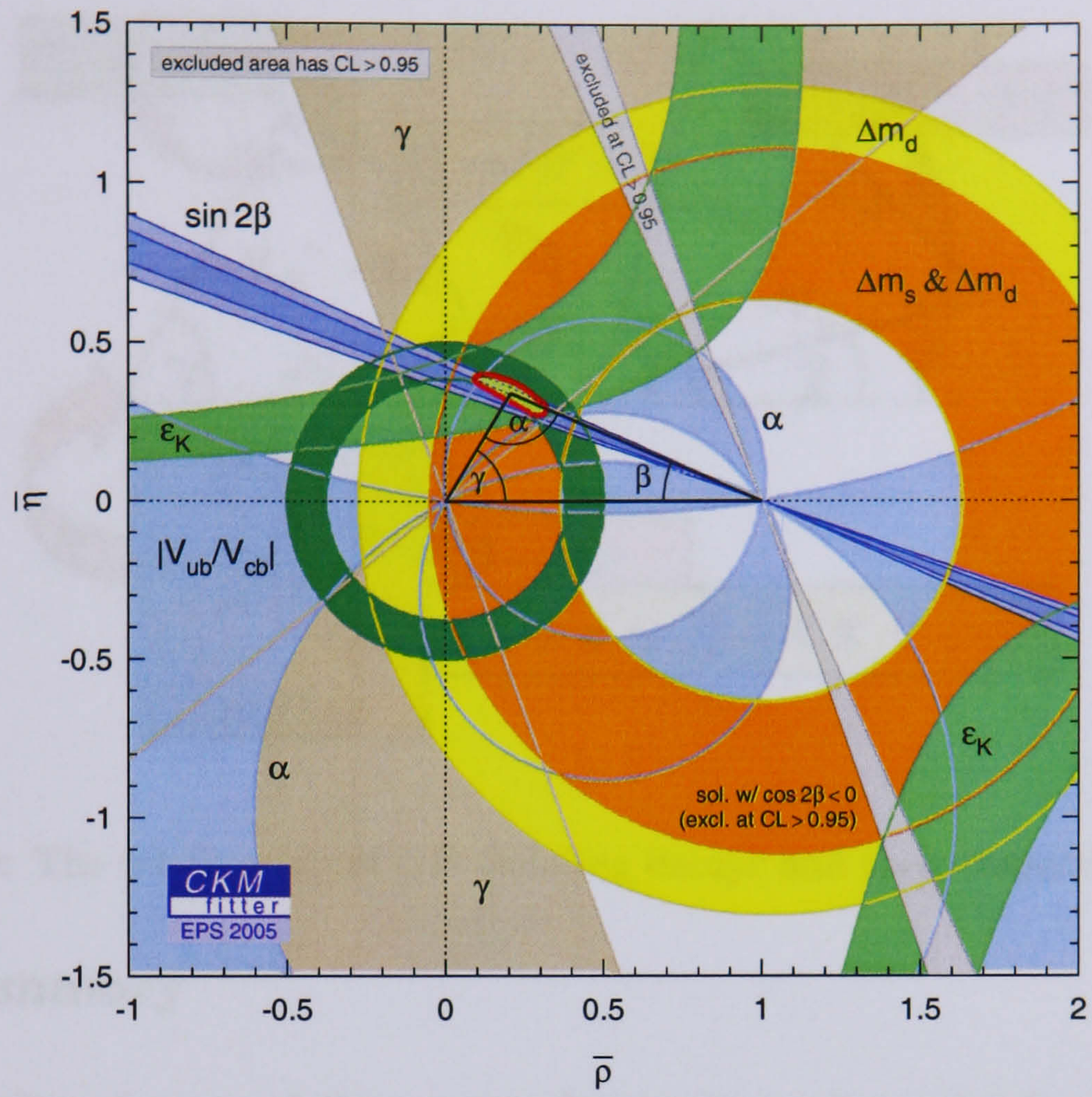

Figure 2.8: Constraining the CKM triangle [36].

and they both have relatively long lifetimes. Therefore, misidentification of these particles could lead to incorrect results for the unitarity angles. The following chapter will discuss the LHCb experiment and its particle identification system (the Ring Imaging Cherenkov or RICH detectors) that will allow these measurements to be performed.

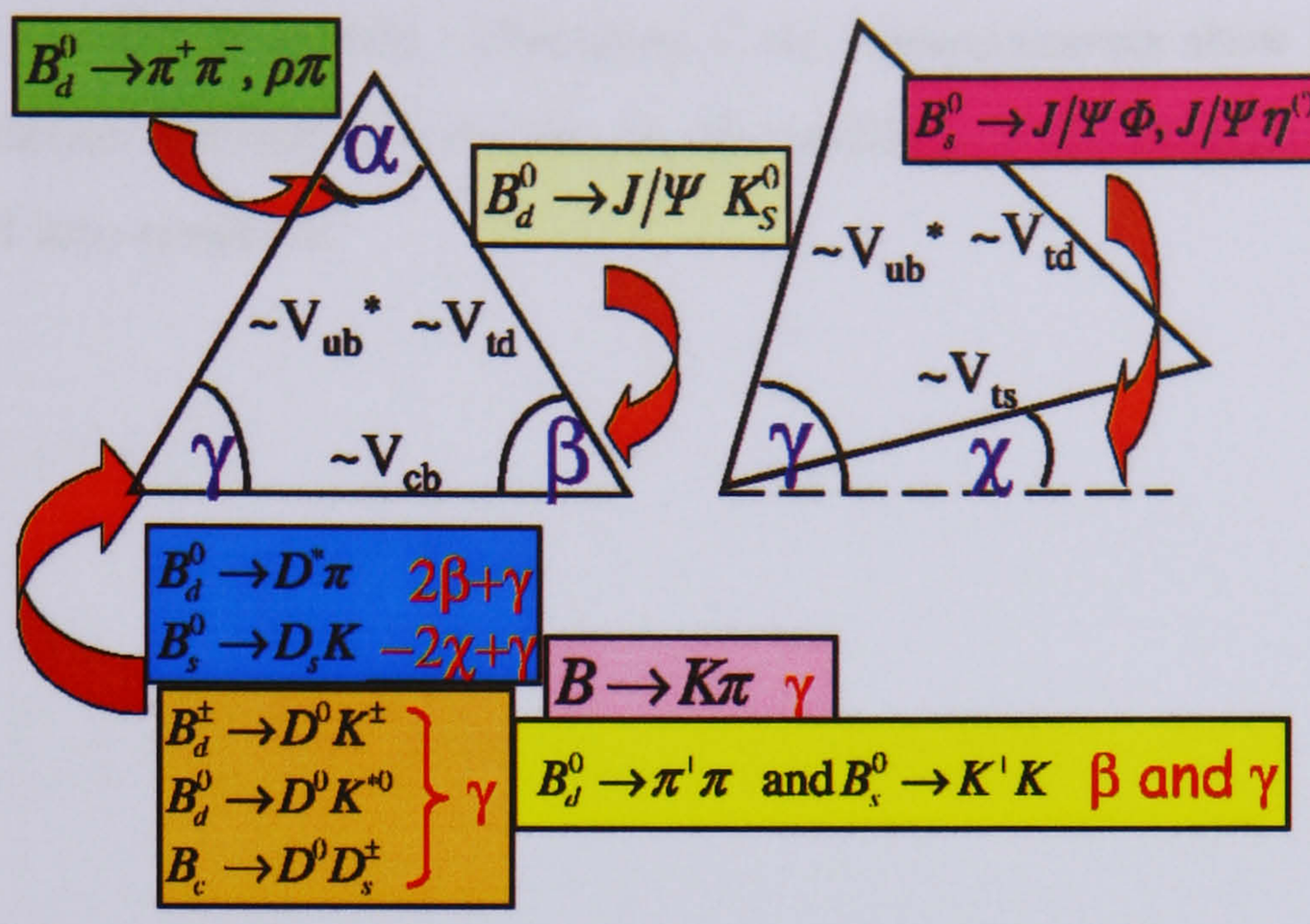

Figure 2.9: The relationship of CP violating decays and their respective angles.

2.6 Summary

The foundation of many of the present theories in modern particle physics is the Standard Model. The Standard Model seeks to explain all the phenomena in particle physics except gravity in terms of the properties and interactions of a relatively small number of particles. Each particle in the Standard Model, has an anti-particle. In its basic form the balance between matter and anti-matter in the Standard Model is nominally symmetric. However, a small allowance is made within the model for imbalance through the process of CP violation as defined by the CKM matrix. The CKM matrix describes the mixing probability between the different quarks in the Standard Model. With the CKM matrix, CP violation can occur through complex phases shown more conveniently as the three angles α, β and γ in the Wolfenstein parameterisation of the CKM matrix. This parameterisation can be represented by unitarity triangles, where the angles are representations of the complex phase element. These angles have been measured but are yet to be measured to a sufficient accuracy so that the CKM theory of CP violation can be properly tested. The LHCb experiment is designed to measure and constrain these angles with unprecedented accuracy and thereby test the validity of the theory. The Standard Model has no mechanism that allows for CP violation in the quark sector to exceed that which is

described by the CKM matrix. Therefore, if the measurements show beyond doubt that CP violation exceeds this maximum, the validity of the Standard Model itself will be called into question.

Chapter 3

The LHCb Experiment

3.1 Introduction to the LHCb Experiment

LHCb is a B physics experiment at the Large Hadron Collider (LHC) at CERN, that will test the consistency of the Unitarity Triangles by determining CP violations in a variety of decays of B_d and B_s mesons. Although the maximum luminosity of the LHC is $10^{34}cm^{-2}s^{-1}$, LHCb will operate at the lower luminosity of $2\times10^{32}cm^{-2}s^{-1}$ (where one inelastic interaction per bunch crossing dominates), lowering the radiation levels and simplifying the event reconstruction [12, p.404]. Taking advantage of this optimal luminosity and the high energy of the LHC, LHCb will be capable of gathering the high statistics unavailable to previous generations of detectors, necessary for a comprehensive study of CP violation [12, p.401].

3.2 Detector Overview

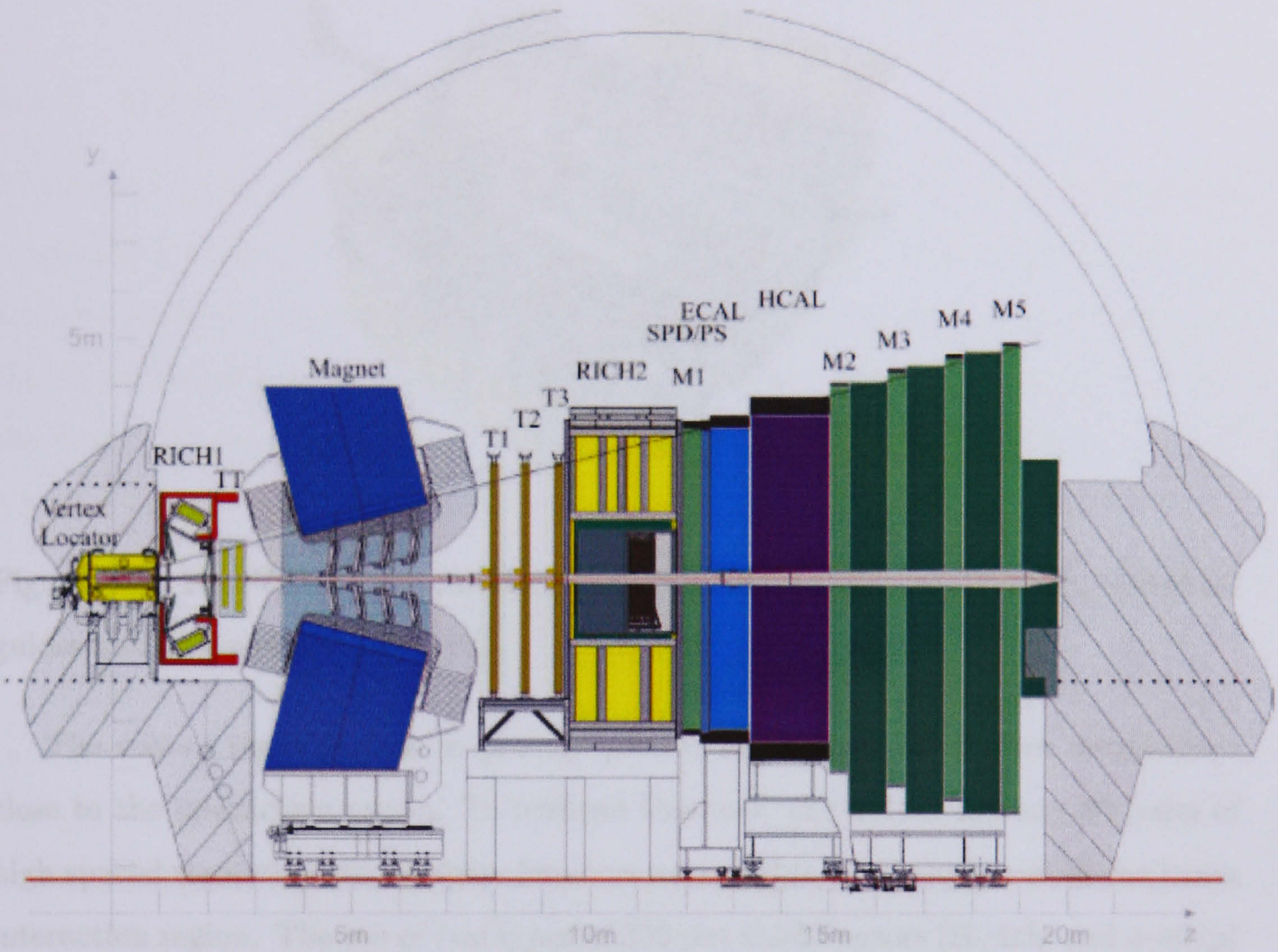

Figure 3.1: LHCb [32, p.3]

The LHCb detector is a single arm spectrometer using forward detector geometry. Following Figure 3.1, LHCb consists of a beam pipe, Vertex Locator (VELO), two Ring Imaging Cherenkov (RICH) detectors, a dipole magnet, tracking stations (TT, T1, T2 and T3) a calorimetry system (Electro-magnetic (ECAL) and Hadron (HCAL)) and a number of muon stations (M1-M5). The acceptance of the detector ranges from 10 mrad to 250 mrad in the vertical plane and 10 mrad to 300 mrad in the horizontal plane [27, p.2].

3.2.1 Vertex Locator (VELO)

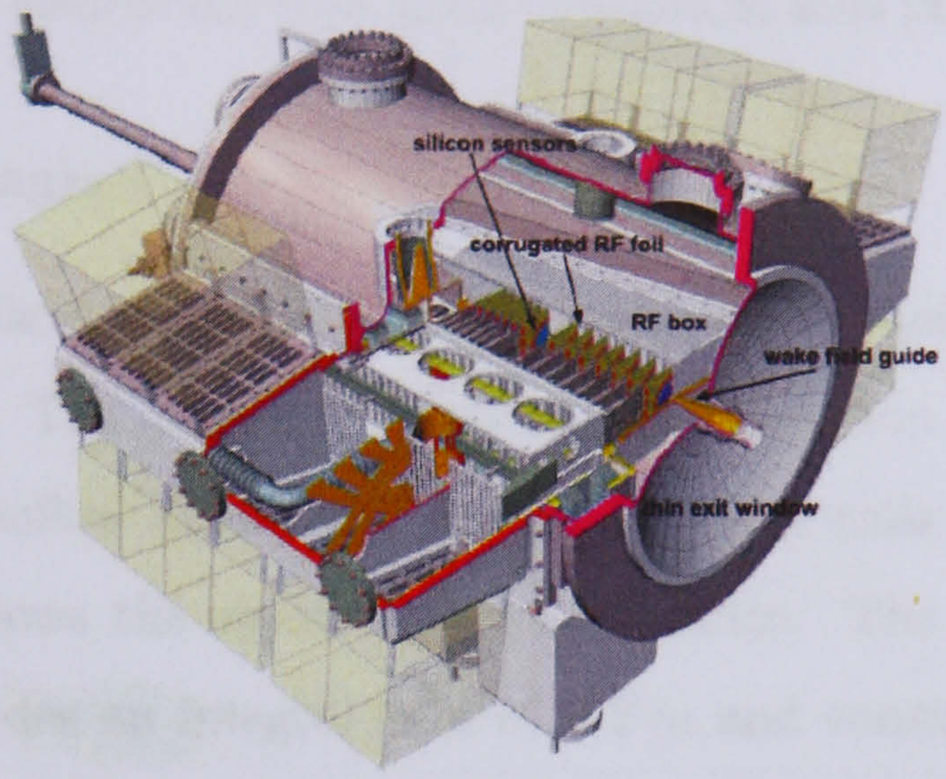

Figure 3.2: The VELO vacuum vessel with the silicon sensors, RF box, wakefield guides and exit window [31, p.12].

The role of the VELO is to provide precise measurements of track coordinates close to the interaction region. To perform this task, the VELO features 21 pairs of high spatial resolution silicon strip detectors arranged in two halves around the beam interaction region. The use of two types of 300 μm thick sensors (R-strip and ϕ-strip) in the geometry allows for a fast track finding algorithm. To avoid damage from the

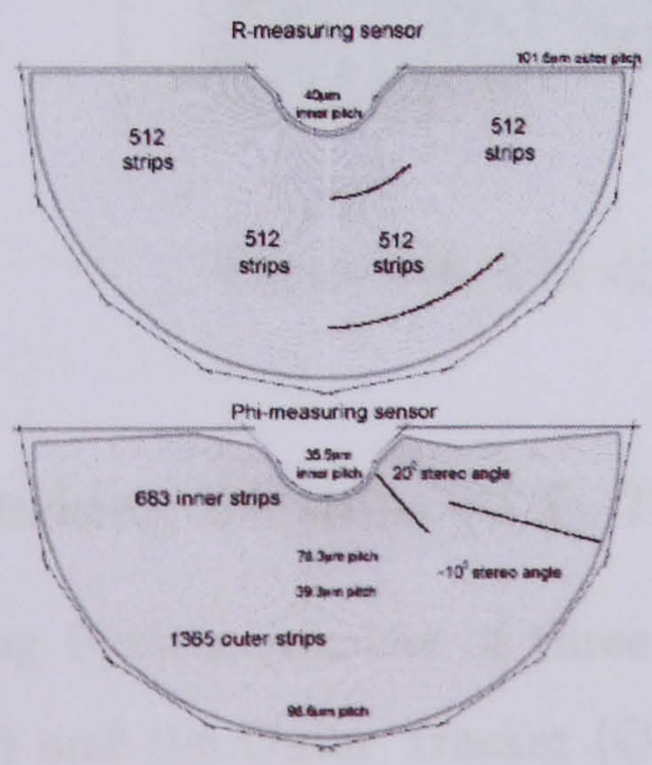

(a) R and ϕ strip sensors

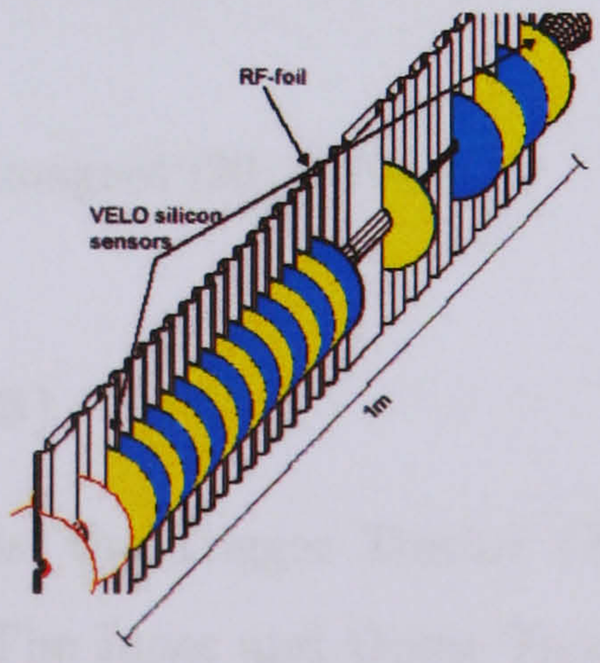

(b) Arrangement of silicon sensors

Figure 3.3: The silicon sensors of VELO [31, p.17] [31, p.11].

LHC during injection, the silicon sensors are in two halves and are retractable. The detector halves are located in a vacuum vessel and are separated from the beam vacuum by specially formed 0.3 mm thick aluminium foils [31, p.11-18].

3.2.2 Dipole Magnet

The static magnetic field of the LHCb spectrometer is provided by a large warm dipole magnet (Figure 3.4). The magnet consists of a 1600 ton iron yoke and two coils that are wound from a hollow aluminium conductor. The coils have been designed so that their shape follows the spectrometer acceptance. The magnet, positioned on the beam line, provides an integral field of 4 Tm and consumes about 4.2 MW of power [53].

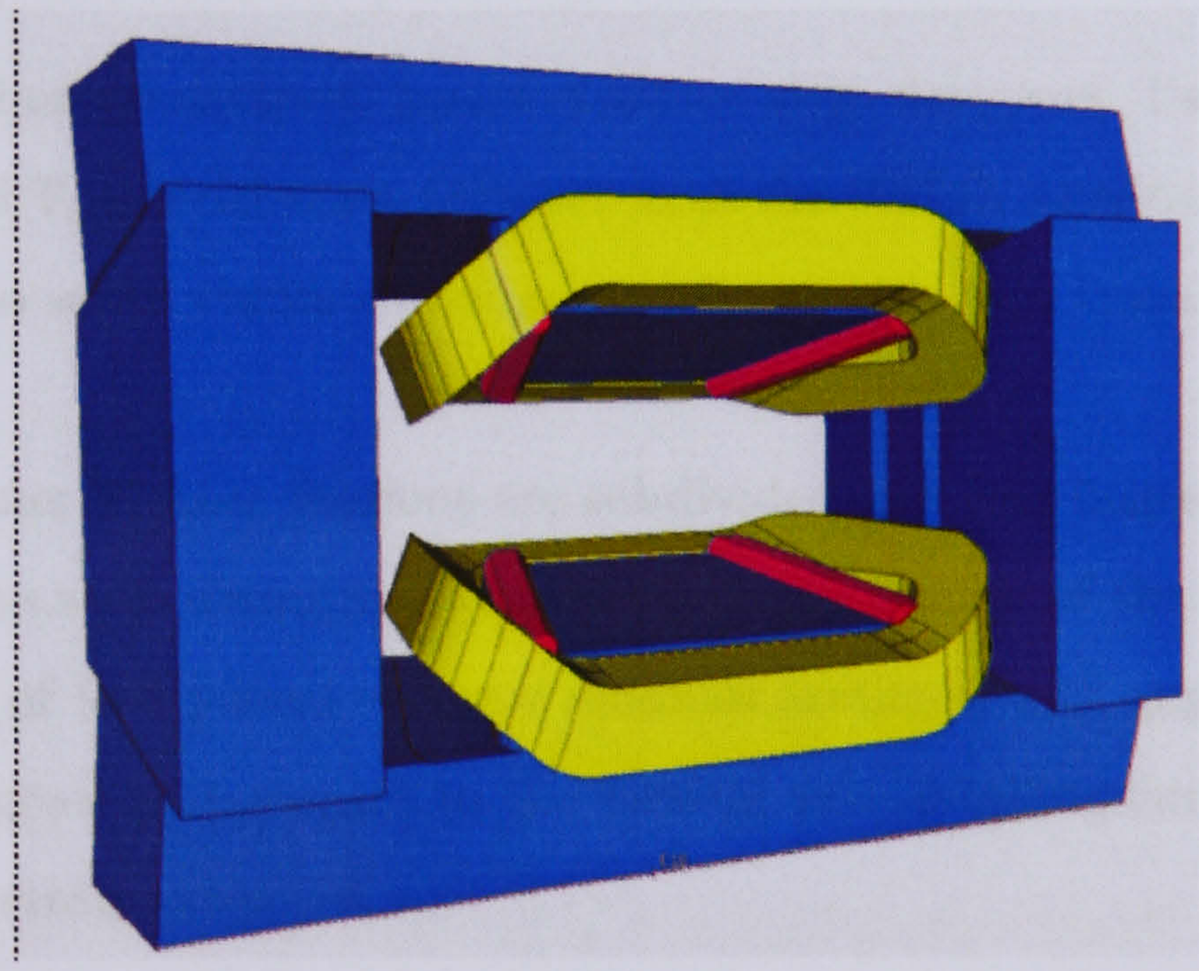

Figure 3.4: The dipole magnet [29, p.62].

3.2.3 Tracking Stations (TT, T1-T3)

The Tracking System consists of three parts, the Trigger Tracker (TT), the Inner Tracker (IT) and the Outer Tracker (OT). The Inner and Outer Trackers are made up of three tracking stations located downstream of the dipole magnet. The Inner Tracker is constructed of silicon detectors, where as the Outer Tracker uses straw tube technology. The Trigger Tracker has an active area of about 1.4 m × 1.2 m

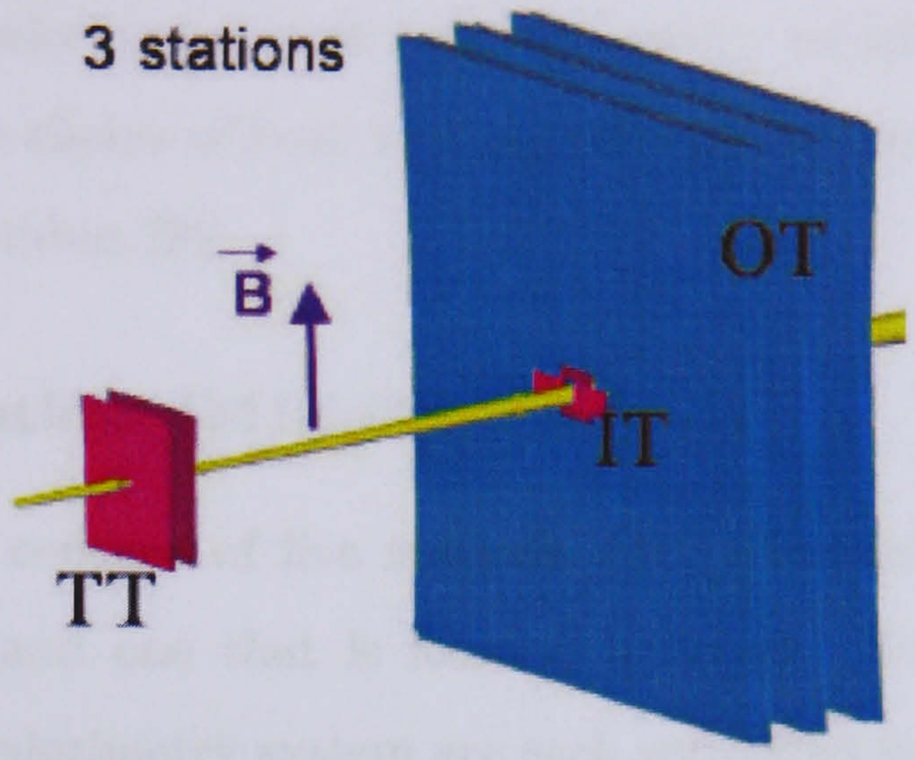

Figure 3.5: The tracking stations [70, p.2].

and consists of four symmetrical layers of silicon strip detectors. Using the magnetic field in front of TT, this detector, together with the VELO, provides the basis of the Level-1 trigger to select events containing particles with high transverse momentum (P_t).

The three Inner Tracker Stations are subdivided into four boxes each with either one or two silicon strip detectors per column. Each station of the Outer Tracker is constructed out of four planes of straw modules arranged with angular offsets of 0, +5, -5 and 0 degrees with respect to the vertical axis, totalling twelve planes. Each module has 128 straw tubes [70].

3.2.4 Pre-shower, Electromagnetic (ECAL) and Hadronic (HCAL) Calorimeters

The calorimeter system consists of a preshower detector, an electro-magnetic calorimeter and a hadron calorimeter. All three parts of the calorimeter system are divided into two halves that can be retracted laterally from the beam line.

The pre-shower detector is constructed out of two layers of scintillator that are separated by 1.5 cm of lead. Light from the scintillator is collected by wavelength shifting fibres that guide the light to multi-anode photomultipliers (MaPMT) that are located both on the top and bottom of the detector.

The electromagnetic calorimeter is divided into three regions with different cell sizes. The hadron calorimeter is an iron/scintillator calorimeter that has a tile geometry. The readout chains of both the electromagnetic and the hadron calorimeters use photomultiplier tubes [26].

3.2.5 Muon Stations (M1-M5)

The muon detector consists of five stations, four of which are located behind the calorimeter system and one that is located in front. The four stations that are located behind the calorimetry system are each separated by iron filters. The surface area of the stations increase as the distance from the interaction point increases such that the muon detector follows the 120 *mrad* horizontal acceptance of the LHCb spectrometer. Each of the stations are themselves divided into four regions, using a total of 20 different chamber types. With the exception of the central region of the first muon station, using triple GEM chambers [33], the five detector planes will use multi-wire proportional chambers. A GEM is a gas electron multiplier and consists of a thin, metal-clad polymer foil pierced with holes. Applying a potential between the two sides of the foil, causes an avalanche of electrons in the holes when a charged particle passes through. Triple GEM chambers are constructed of three consecutive planes to increase the gain of the detector [67]. Each muon station has four active gaps, where two are included in a logical OR, except the first station that has only two layers to minimize material in front of the calorimeter. Depending on the track density, the readout is performed using the signals of the wires, the pads or both. They are connected to form logical pads and a total of about 26,000 channels are used in the Level-0 trigger [28].

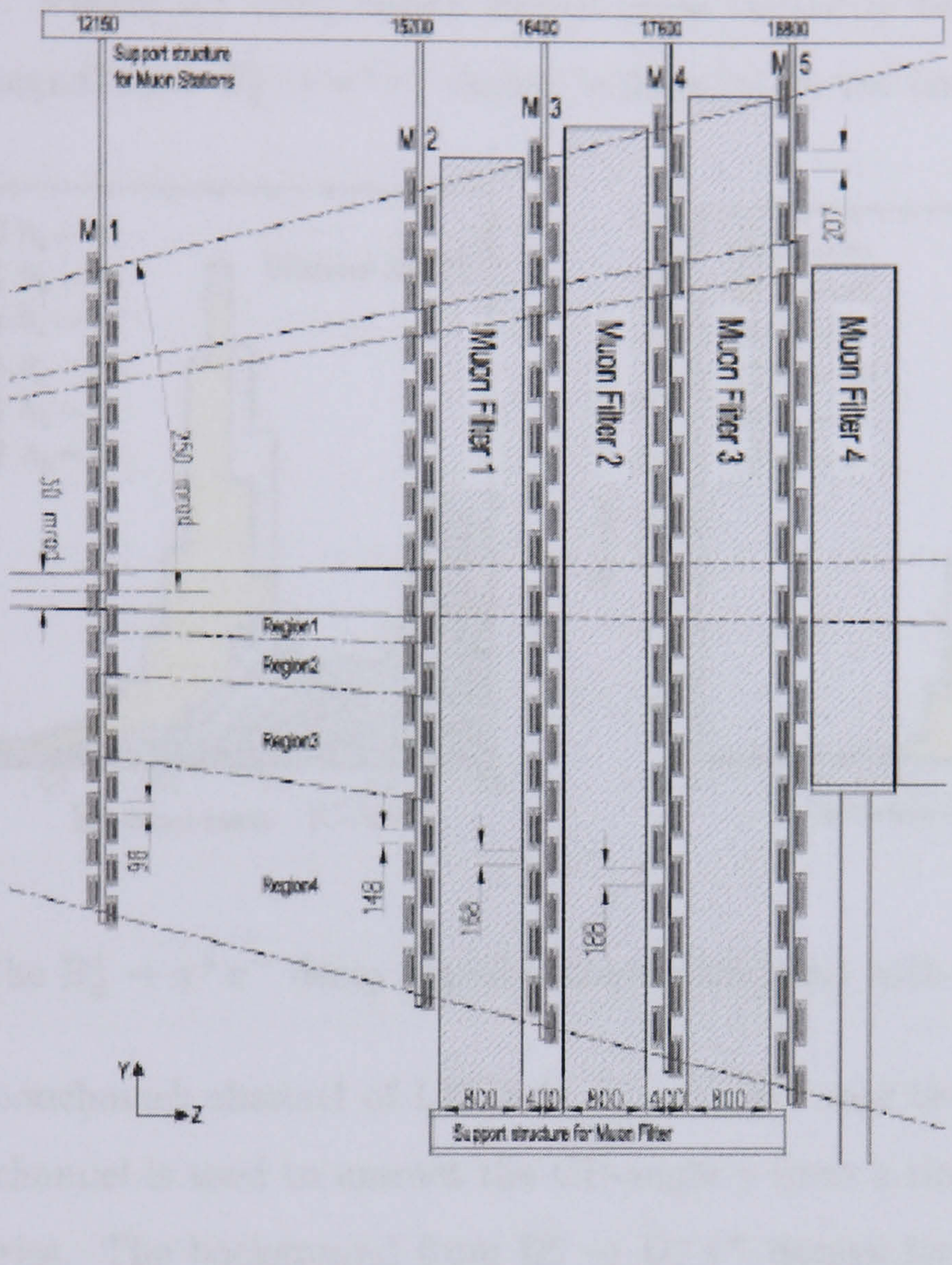

Figure 3.6: The arrangement of muon stations in LHCb [28, p.13].

3.3 Rich Imaging Cherenkov (RICH) Detectors

3.3.1 Physics Justification and Necessary Specifications

A fundamental requirement of the particle identification for the LHCb experiment is the ability to distinguish between pions and kaons in a variety of final states. Without this separation, the LHCb experiment will be unable to make measurements of asymmetries required to further constrain the angles of the CKM martix. In order for the LHCb experiment to achieve such a high level of particle identification, Ring Imaging CHerenkov (RICH) detectors are required. The importance of the RICH system in LHCb can be shown through the example of the measurement of the CP asymmetry of $B_d^o \to \pi^+\pi^-$ decays. This measurement requires the rejection of two-body backgrounds with the same topology such as $B_d^o \to K^+\pi^-$, $B_s^o \to K^-\pi^+$ and

$B_s^o \to K^+K^-$. Figure 3.7 (left) shows that if these two-body backgrounds are not rejected, the signal from $B_d^o \to \pi^+\pi^-$ decays is dwarfed by the backgrounds.

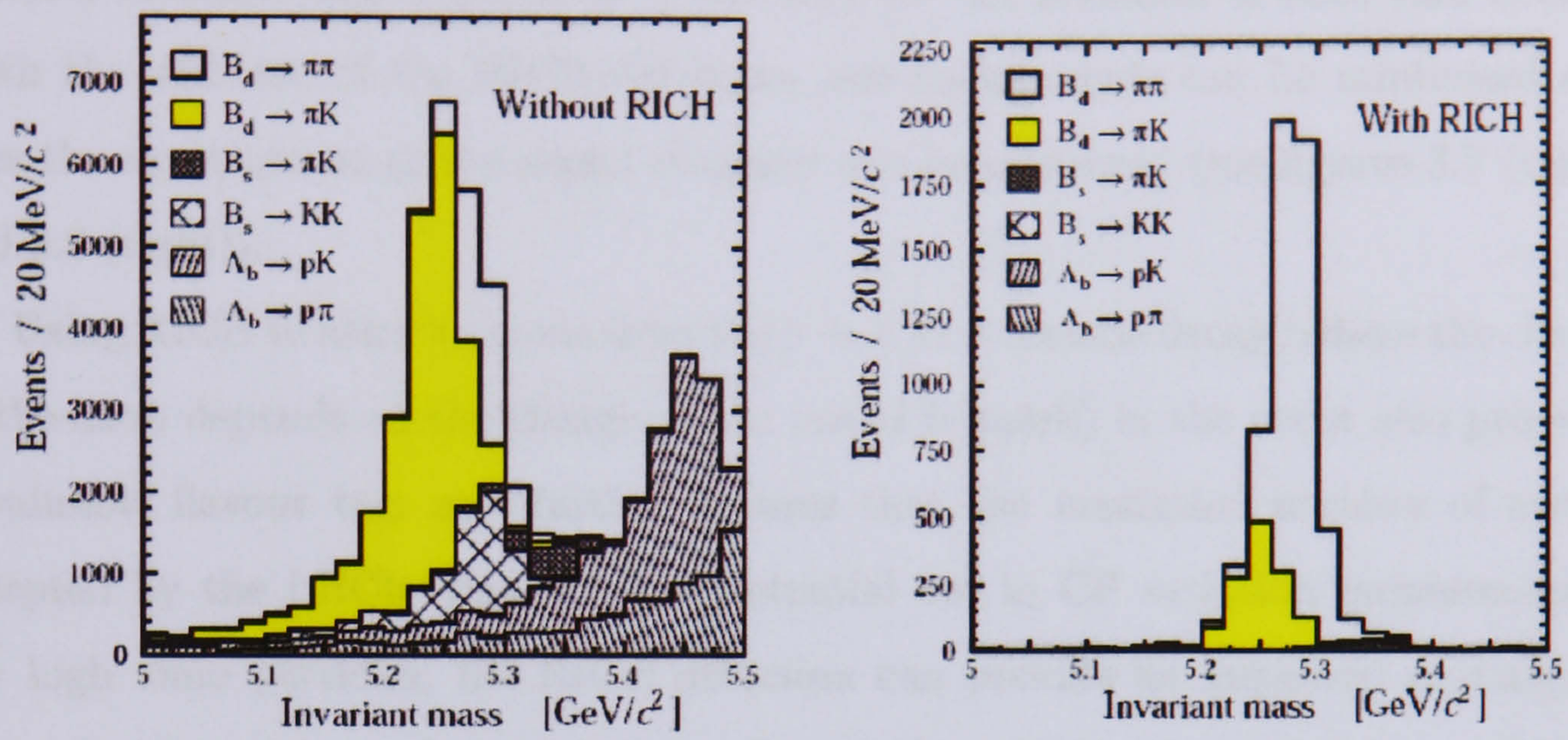

Figure 3.7: The $B_d^o \to \pi^+\pi^-$ decay signal without (left) and with (right) the RICH.

Another benchmark channel of LHCb is $B_s^o \to D_s^{\mp}K^{\pm}$ and the charge conjugate states. This channel is used to extract the CP-angle γ from a time-dependent fit to the asymmetries. The background from $B_s^o \to D_s^-\pi^+$ decays for this measurement is about 15 times greater and overwhelms the signal if particle identification from RICH detectors is not available (see figure 3.8 (left)).

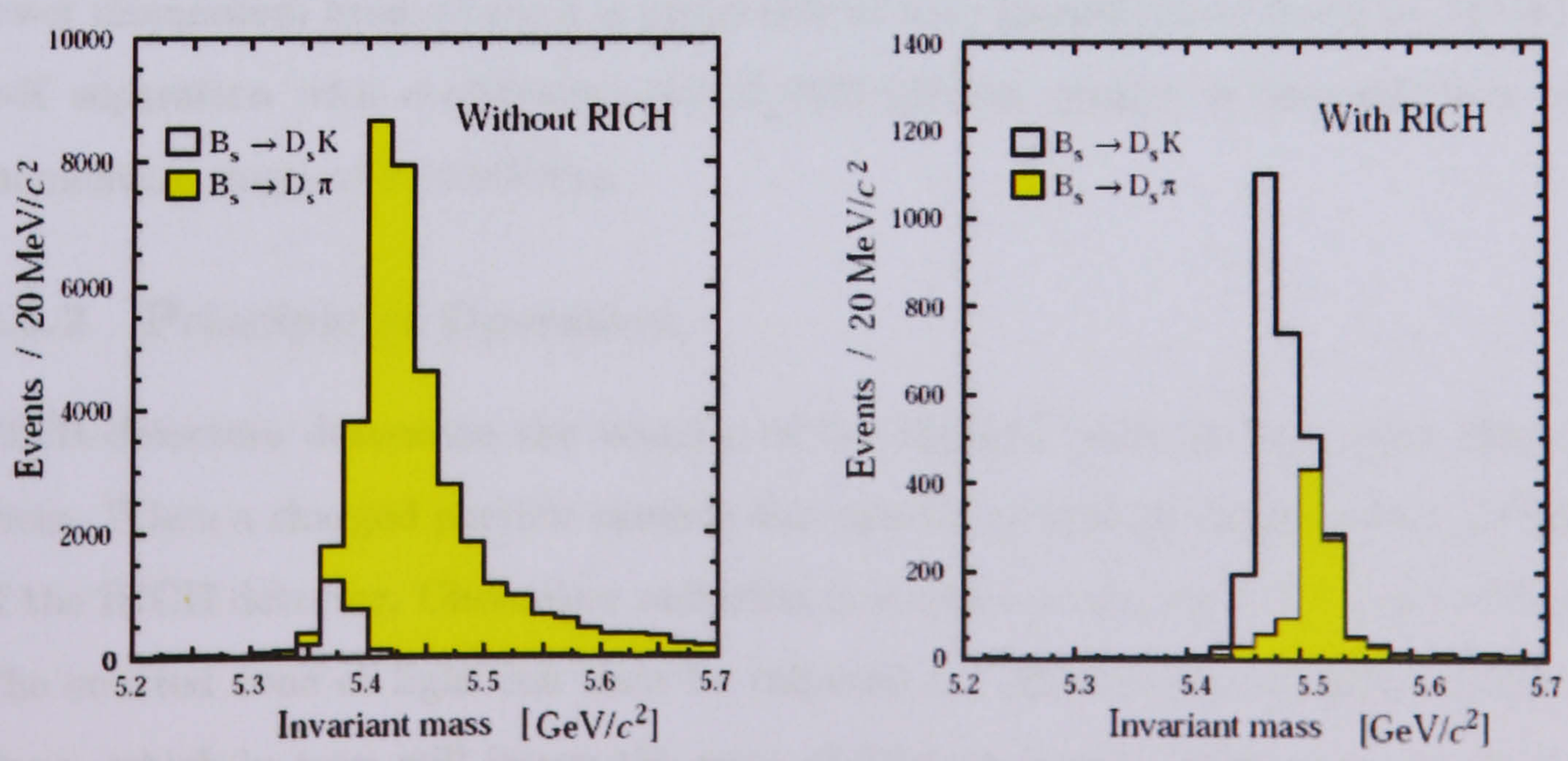

Figure 3.8: The $B_s^o \to D_s^{\mp}K^{\pm}$ decay signal without (left) and with (right) the RICH.

Another method that can be used to access the angle γ is through the use of channels such as $B^o \rightarrow D^oK^{*o} \rightarrow K^-\pi^+K^+\pi^-$ and $B^o \rightarrow \overline{D}^oK^{*o} \rightarrow \pi^-K^+K^+\pi^-$. Positive identification of particles is essential for the selection of such rare decays. With the addition of the RICH detectors, the backgrounds can be minimised and thus the asymmetries of the signal channels can be measured (see figures 3.7 (right) and 3.8 (right)).

Using RICH to identify kaons from the $b \rightarrow c \rightarrow s$ cascade decay (where the charge of the kaon depends on the charge of the initial b quark) in the event also provides a valuable flavour tag, and further ensures that the maximum number of events accepted by the LHCb trigger are of potential use in CP violation measurements. For high mass particles, the RICH detectors can provide an improved momentum determination and are also able to complement the calorimeters and muon system in the identification of electrons and muons.

The particle identification should cover the full angular acceptance of the LHCb spectrometer, from 10 *mrad* to 300 *mrad* and 10 *mrad* to 250 *mrad* in the horizontal and vertical projections respectively. The upper limit in momentum required for π-K separation is determined by tracks from two-body B-decay channels, 90% of which have a momentum of less than 150 GeV/c. The identification of tagged kaons and tracks from high multiplicity decays determines the requirement for the lower momentum limit where it is preferable to have identification down to 1 GeV/c. π-K separation with confidence level of 99% (3σ) or greater is desirable over the momentum range of 1-150GeV/c.

3.3.2 Principle of Operation

RICH detectors determine the velocity of the charged particles that pass through them. When a charged particle exceeds the velocity of light in the dielectric medium of the RICH detector, Cherenkov radiation is emitted in the form of a cone of light. The emitted cone of light can then be reflected off mirrors onto a photon detector plane, which in turn will image the cone of light as a ring. Each charged particle is responsible for producing photons that form a ring. As an example, figure 3.9 shows simulated rings created from particles traversing the LHCb RICH2 detector

(see section 3.4), where the dielectric medium is CF_4 gas.

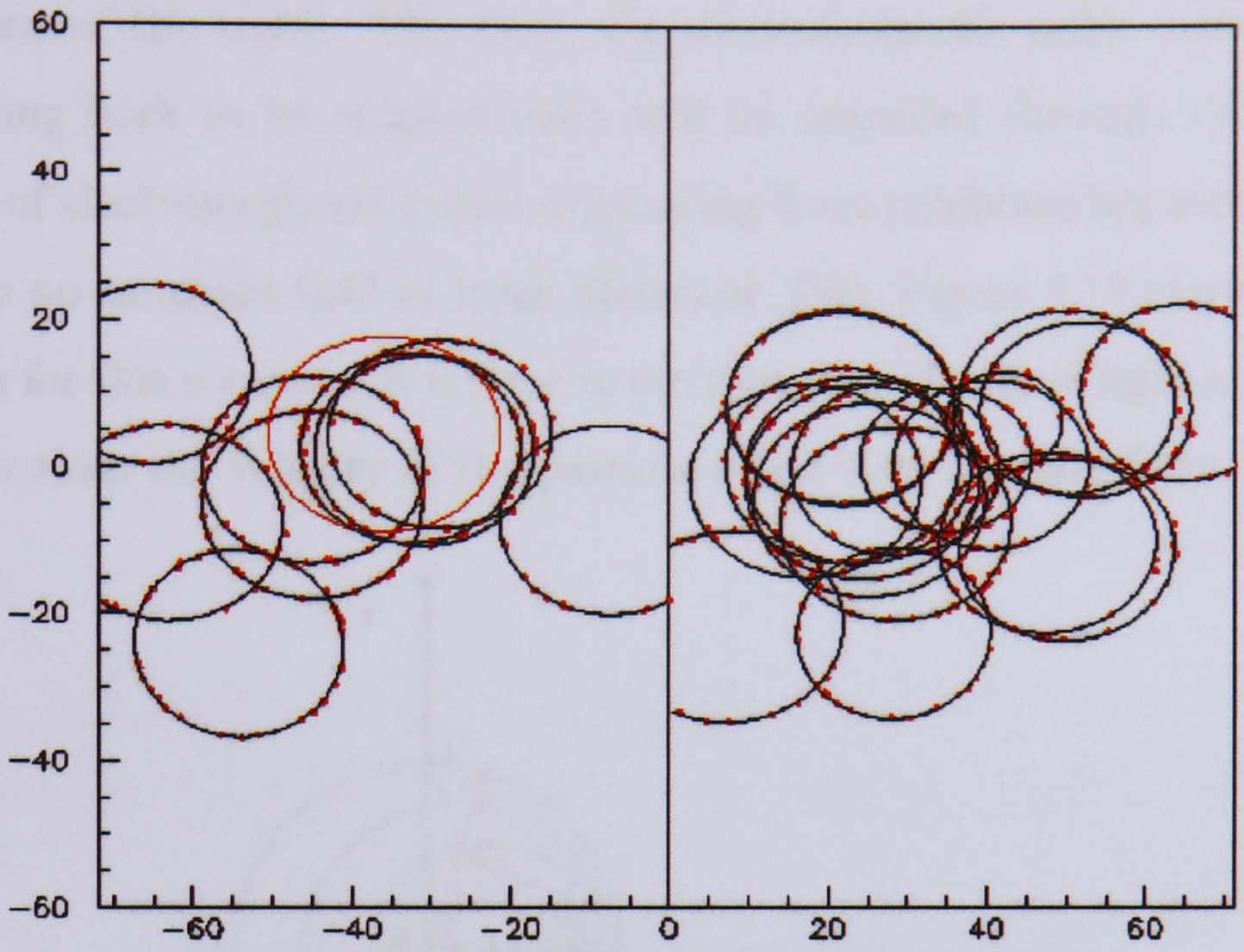

Figure 3.9: Cherenkov rings in the RICH2 detector of LHCb [27, p.13].

The size of each ring is dependent upon the velocity of the particle that caused it. The VELO and tracking stations, as well as the calorimeters, will determine the momentum and/or energy of the responsible particle. If the momentum or the energy is known for the particle and its velocity is determined by the RICH detector, then the particle mass can be calculated and thus the particle can be identified. The performance of the RICH detectors will be described in this chapter.

3.3.3 Cherenkov Radiation

The Cherenkov effect occurs when a charged particle exceeds the speed of light within a dielectric medium. Consider, for example, a proton travelling through a block of glass. As the proton passes through the dielectric glass medium, the electrons of the neighbouring atoms will become attracted to the passing proton and the nuclei repelled, thus these atoms will become polarised and elongated. As the proton moves out of the influential range of a polarised atom, the atom will quickly revert back to its normal state; this process will cause a very brief electromagnetic pulse to occur.

A slow moving proton travelling from A to B through glass, will cause the polar-

isation field of neighbouring atoms to have both azimuthal symmetry and symmetry along the axis of the track. Therefore, the electromagnetic pulse emitted from an atom reverting back to its original state will be cancelled through the destructive interference of electromagnetic pulses originating from neighbouring atoms; and thus there will be no resultant field at large distances [50]. Figure 3.10 shows a Huygens construction for this scenario. It is clear to see that the velocity of light in the medium c_m is greater than the velocity of the particle v and that no wave front is produced.

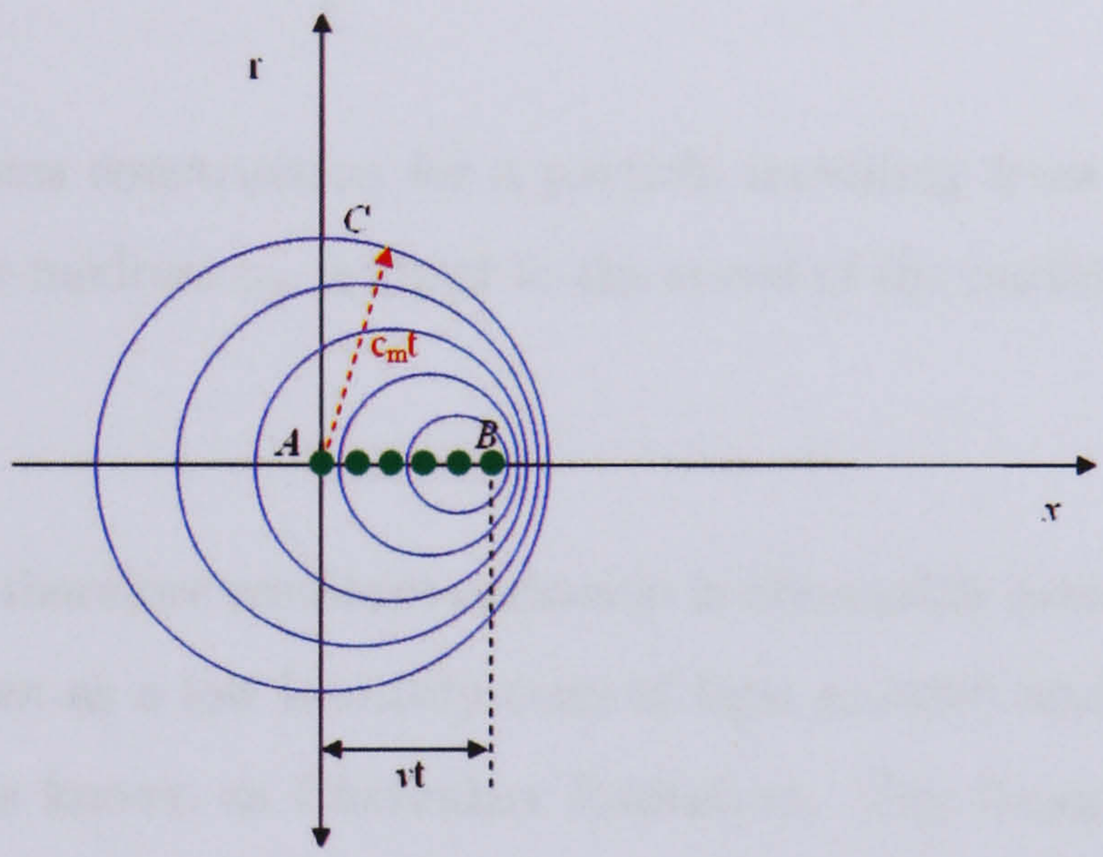

Figure 3.10: Huygens construction for a particle travelling from A to B, where the speed of light in the medium c_m is greater than the speed of the particle v in the medium.

In the case of a proton moving at a speed comparable to that of the speed of light, the polarisation field, though still azimuthally symmetric, is no longer symmetrical along the axis of the track. The resultant dipole field will be apparent even at large distances from the track of the proton. However, since the velocity of the proton is lower than the phase velocity of light in the medium, it is not possible for the radiation to be in phase along all portions of the track, therefore the radiated wavelets interfere destructively so that the resultant field intensity is still zero at a distant point (figure 3.11).

For a proton travelling higher than the phase velocity of light within the medium it is possible for the radiated wavelets from all portions of the track to now be in phase

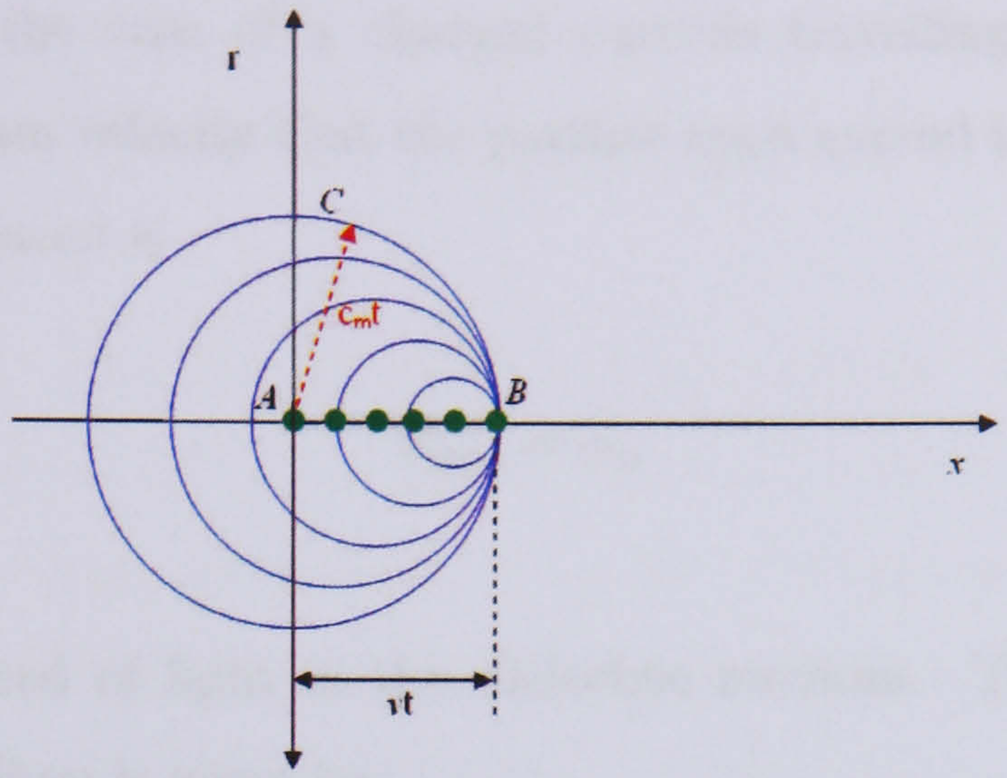

Figure 3.11: Huygens construction for a particle travelling from A to B, where the speed of light in the medium c_m is equal to the speed of the particle v in the medium.

constructively and therefore resultant radiation is observable even at a distant point. The radiation is seen as a low intensity cone of light emitted along the trajectory of the proton. This is known as Cherenkov Radiation. The Huygens construction of figure 3.12 shows that a wavefront is produced when the particle velocity exceeds the speed of light in the medium.

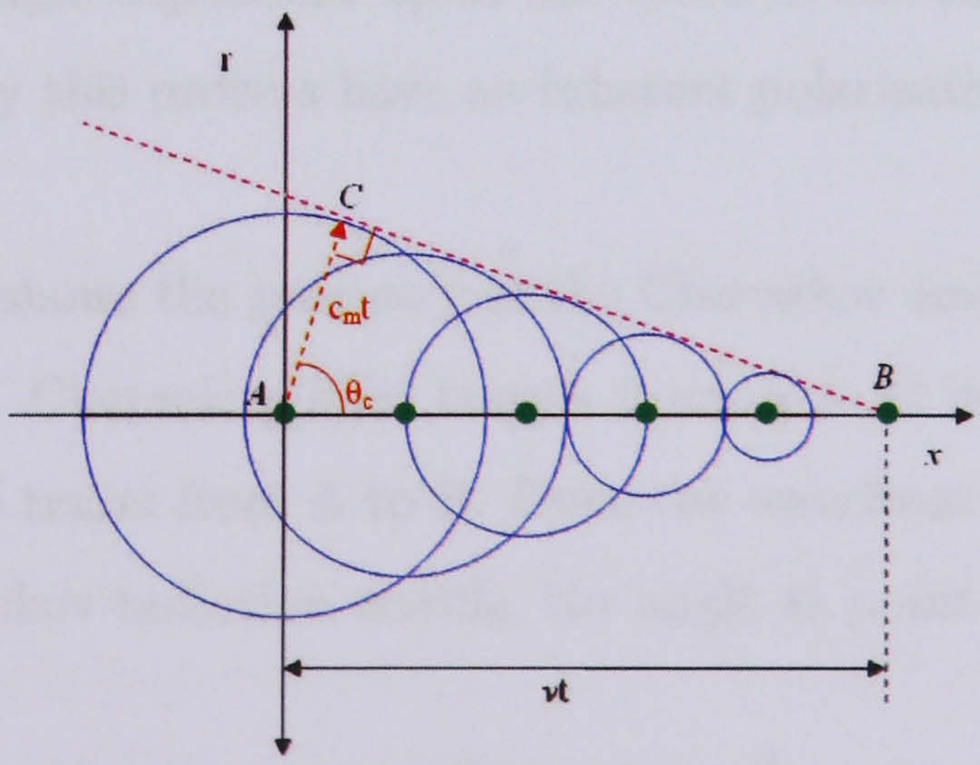

Figure 3.12: Huygens construction for a particle travelling from A to B, where the speed of light in the medium c_m is less than the speed of the particle v in the medium.

Generalising to the case of a charged particle travelling through a dielectric medium, the minimum velocity that the particle must exceed in order for Cherenkov radiation to be produced is

$$v_{min} = c_m \tag{3.1}$$

where c_m is the speed of light in the dielectric medium. The refractive index n of the dielectric medium is given by

$$n = \frac{c}{c_m} \tag{3.2}$$

where c is the speed of light in vacuum. Therefore, equation 3.2 can be substituted into equation 3.1 to give

$$v_{min} = \frac{c}{n}. \tag{3.3}$$

When a particle exceeds this minimum velocity, the Cherenkov cone produced opens up with an angle dependent upon the speed of the charged particle, and the photons produced by this process have an inherent polarisation perpendicular to the surface of the cone.

Figure 3.12 also shows the geometry of the Cherenkov emission angle θ_c following Huygens' Principle. Cherenkov light travels from A to C in the same time that it takes the particle to travel from A to B. Since the wavefront is perpendicular to the direction the Cherenkov radiation travels, the angle at point C is 90^o. Hence

$$\cos\theta_c = \frac{c_m}{v} = \frac{c}{vn} = \frac{1}{\beta n}, \tag{3.4}$$

where v is the velocity of the particle, β is the ratio of the velocity of the particle to the speed of light. The momentum p is related to β by

$$\beta = \frac{v}{c} = \frac{pc}{\sqrt{\mathrm{p^2c^2 + m^2c^4}}} \tag{3.5}$$

which can be used to determine the mass m of the particle.

In application to the LHCb RICH detectors, if c_m and n are known values, it is possible to use a measured value of θ_c to find the velocity v of the originating particle and hence calculate β. Given that the value for the momentum p of that particle is found by using tracking stations to measure the bend in the path of the particle as it travels through the dipole field of the magnet; it is also possible to calculate the mass m of the particle and thus identify it. This is the principle upon which Ring Imaging Cherenkov detectors are based. The wavelength distribution of Cherenkov radiation has a $1/\lambda^2$ dependence and therefore peaks towards the UV region of the electromagnetic spectrum. This places constraints on the materials used in the construction of RICH detectors.

Chromatic Aberration

Cherenkov radiation is not monochromatic and it follows from optical refraction that the velocity of light within a transparent medium is wavelength dependent, such that n is not constant over the wavelength range. For this reason, there will be some variation in the Cherenkov emission angle over the range of wavelengths produced when a charged particle travels at a constant velocity in excess of the speed of light through a dispersive dielectric medium. This phenomenon is known as chromatic aberration.

Figure 3.13 shows the variation in refractive index for the radiative media of the LHCb RICH detectors as a function of photon energy [27, p.6]. This covers the wavelength range of 124.3 nm (10 eV) to 1243 nm (1 eV).

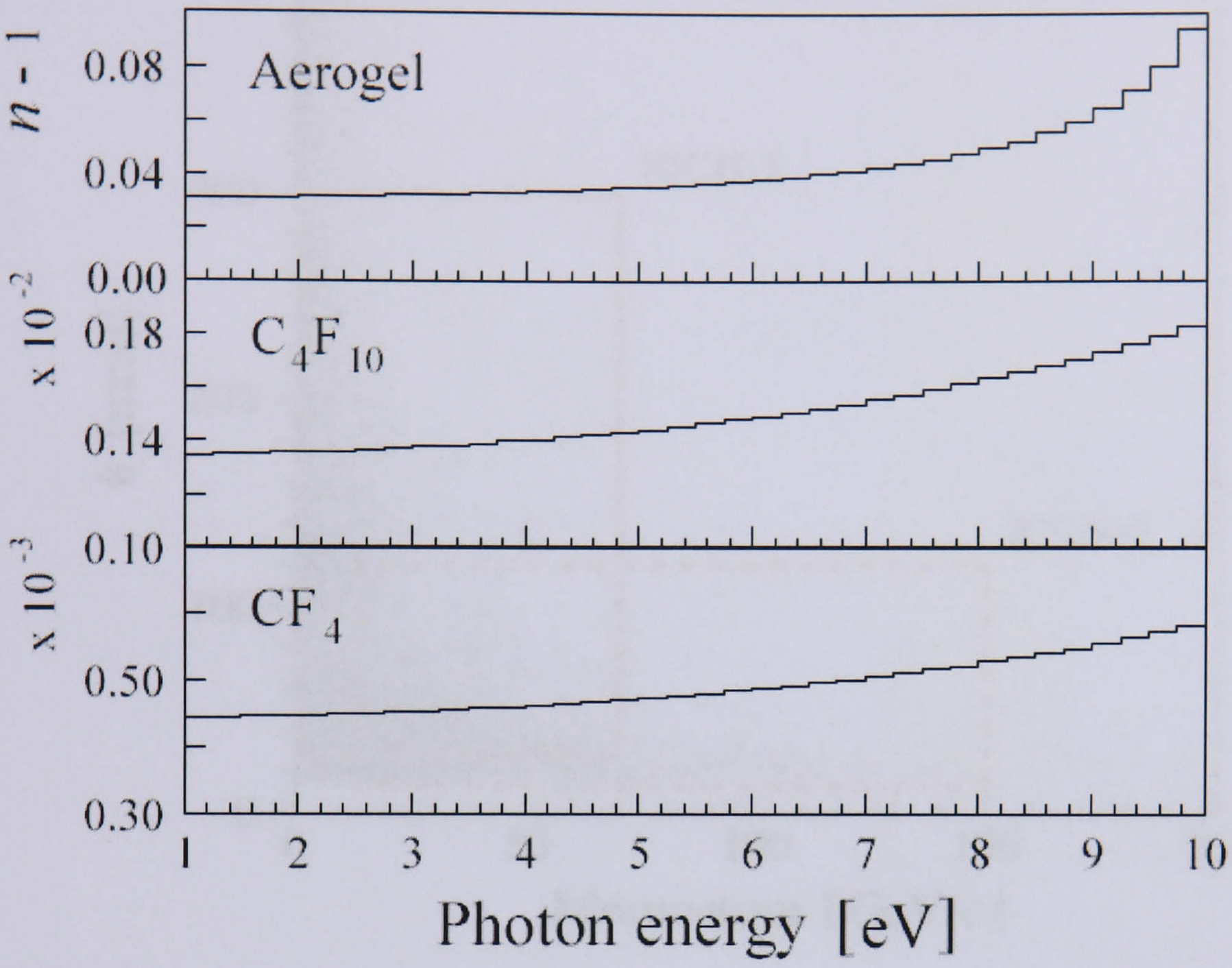

Figure 3.13: Spectrum of refractive indices for the three radiators used for the RICH detectors of the LHCb experiment [27, p.6].

3.4 LHCb RICH Detectors

The particle identification system of the experiment includes two RICH detectors, RICH1 and RICH2. RICH1 measures the velocities of the lower momentum particles, and RICH2 measures the velocities of the higher momentum particles. The basic requirement for this combined system is to provide particle identification over a wide momentum range from 1 to about 100 GeV/c [30, p.2]. Figure 3.14 shows the momentum range and acceptance covered by the two RICH Detectors, compared to the expected B decays in LHCb.

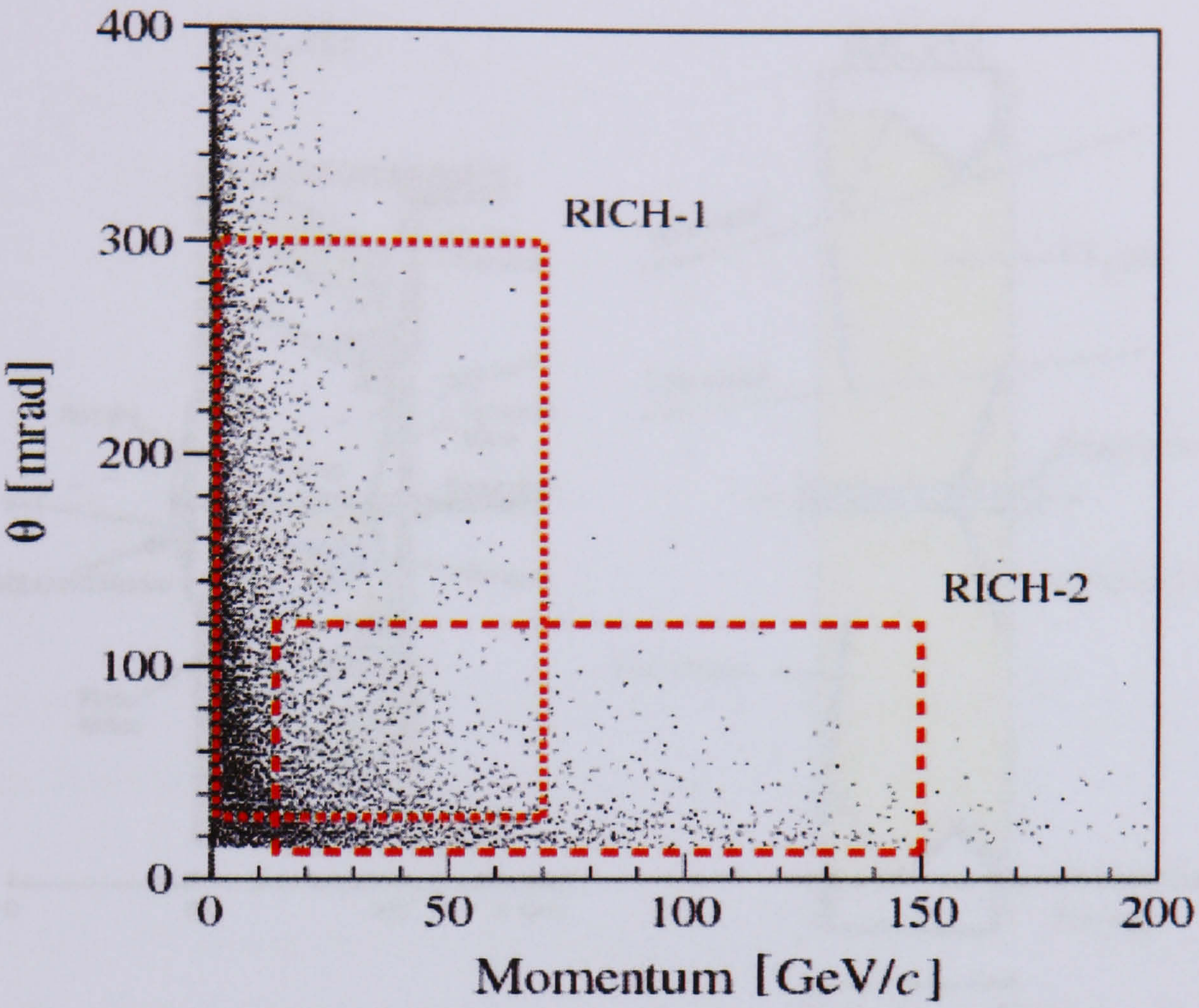

Figure 3.14: Momentum range and horizontal acceptance (θ) of RICH1 and RICH2 [27, p.2].

3.4.1 Overview of RICH1 and RICH2

RICH1 has two radiators (see Figure 3.15), the first is aerogel and the second is the gas medium C_4 F_{10}, with refractive indices of $n = 1.03$ and $n = 1.015$ respectively [32, p.3]. These dense radiators allow RICH1 to measure the velocities of the lower momentum particles in the 1-60 GeV/c range. RICH1 covers the full LHCb acceptance of 250 $mrad$ in the vertical plane and 300 $mrad$ in the horizontal plane.

RICH2 has a single radiator, the gas medium CF_4 with a refractive index of n=1.0005 [27, p.6]. This lower refractive index medium allows RICH2 to measure the velocities of the higher momentum particles. Since the high momentum particles traverse LHCb at a lower polar angle with respect to the beamline, RICH2 covers the reduced acceptance of 100 $mrad$ in the vertical plane and 120 $mrad$ in the horizontal plane.

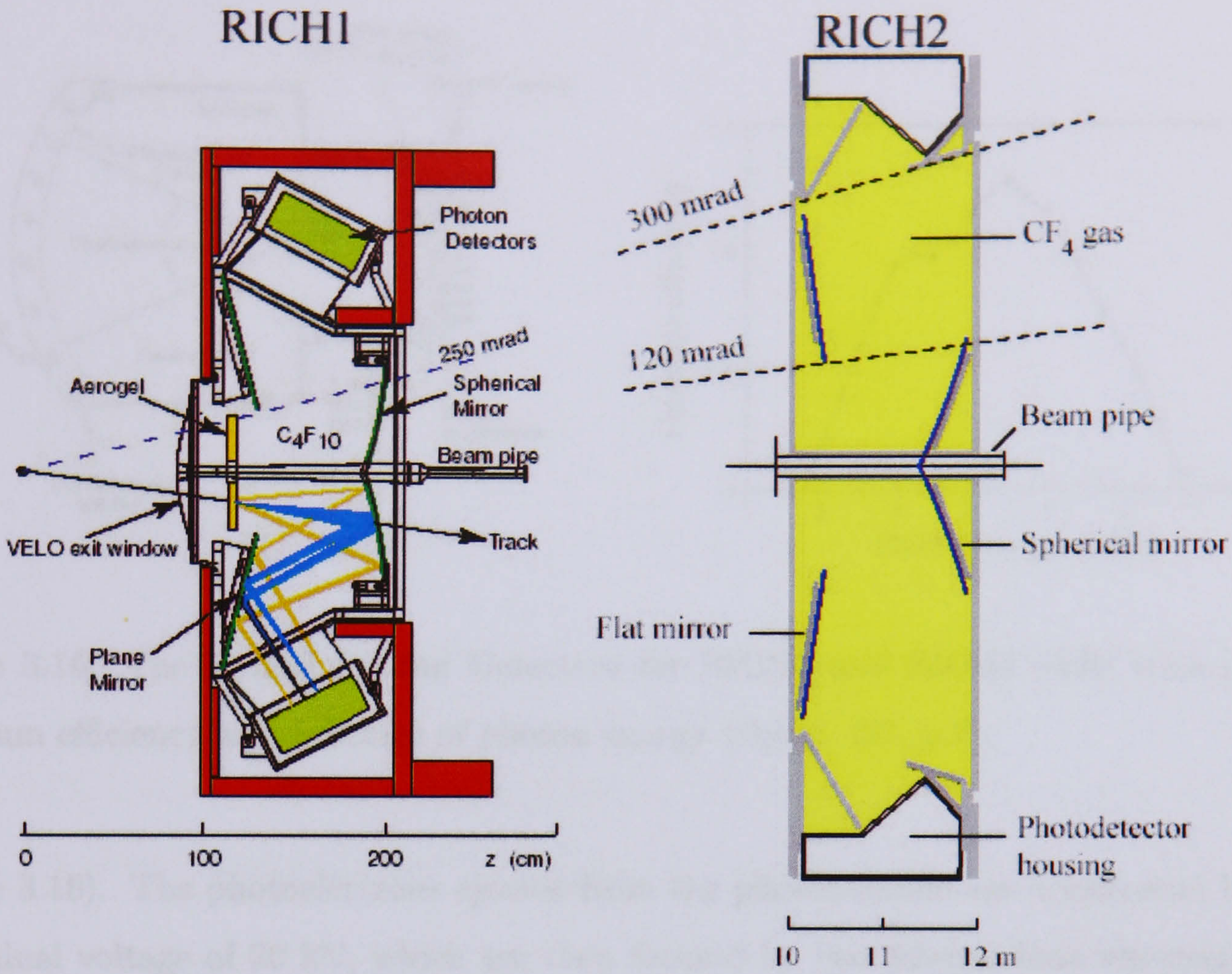

Figure 3.15: Design of RICH1 and RICH2 [32, p.3] [27, p.6].

The general layout of the two detectors are similar in format. They both use a combination of spherical and flat mirrors to reflect the Cherenkov radiation onto the photo-detector plane located outside of the detector acceptance. The main differing features being that RICH1 covers the full acceptance of 300 $mrad$, has an additional radiator and is mounted in a vertical position. Both detectors share the same photon detectors, the HPD (Hybrid Photon Detector).

Hybrid Photon Detectors

The HPD is a novel photon detection device comprising of a silicon pixel detector encapsulated inside a vacuum tube consisting of a photo-cathode, focusing electrodes and accelerating high voltage. The HPD designed for the LHCb experiment uses a 7 mm thick spherical quartz window with a multialkali photocathode deposit on its inner surface that achieves a quantum efficiency in excess of 25% at its peak (see

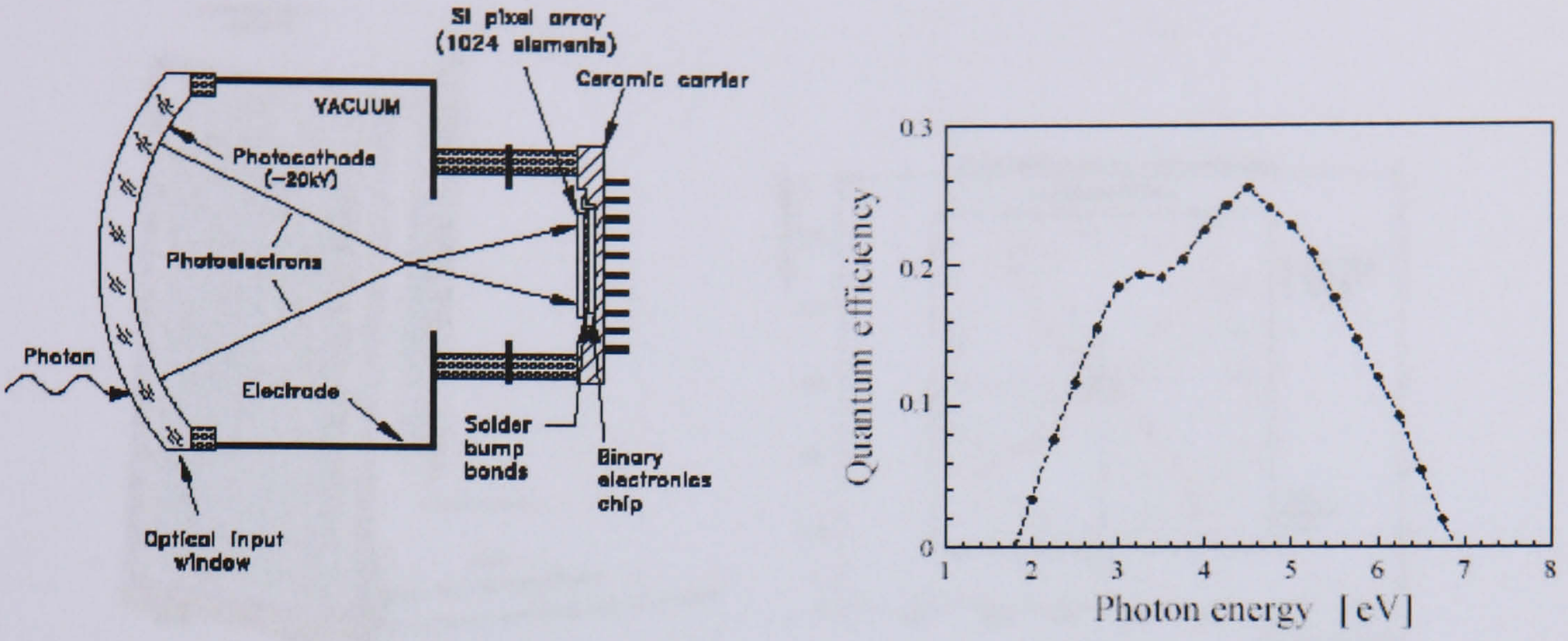

Figure 3.16: The Hybrid Photon Detectors for RICH1 and RICH2 (left) with its quantum efficiency as a function of photon energy (right) [27, p.7].

Figure 3.16). The photoelectrons ejected from the photocathode are accelerated by a nominal voltage of 20 kV, which are then focused by two intermediate electrodes onto an 8192 silicon pixel array anode, at ground potential. Each pixel has an area of 0.5 mm by 62.5 μm. The pixel readout chip designed for LHCb performs a logical OR of 8 consecutive pixels forming square super-pixels of 0.5 mm by 0.5 mm. The demagnification of the tube is a factor of five, giving the HPD an effective pixel size of 2.5 mm by 2.5 mm at the photo-cathode.

The HPD itself is cylindrical and has an overall diameter of 83 mm, of which, the active area is 75 mm. There are total of 486 HPDs used within the RICH detectors, of which 262 are used in RICH2 (131 per HPD panel). The close packed arrangement of HPDs in the photodetector plane gives an effective active area of 67% of the total area of the HPD plane (see Figure 3.17(a)).

Magnetic fields can distort the photoelectron images of the HPDs. Longitudinal fields of 10 G cause displacements in the electron trajectories (as seen in Figure 3.17(b)). To minimise the effect of the magnetic field produced by the dipole magnet on the photoelectrons, each tube is surrounded by a Mu-metal magnetic shield of 1 mm thickness, that extends 20 mm beyond the centre of the spherical quartz window of the HPD. With the Mu-metal shields, the HPDs can operate in

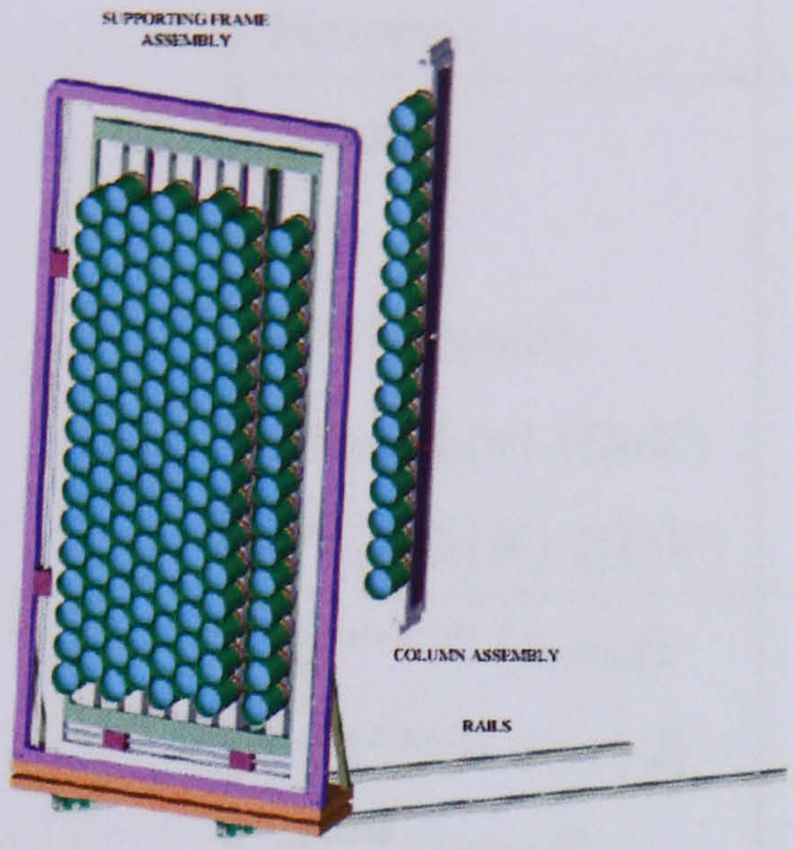

(a) The photodetector plane

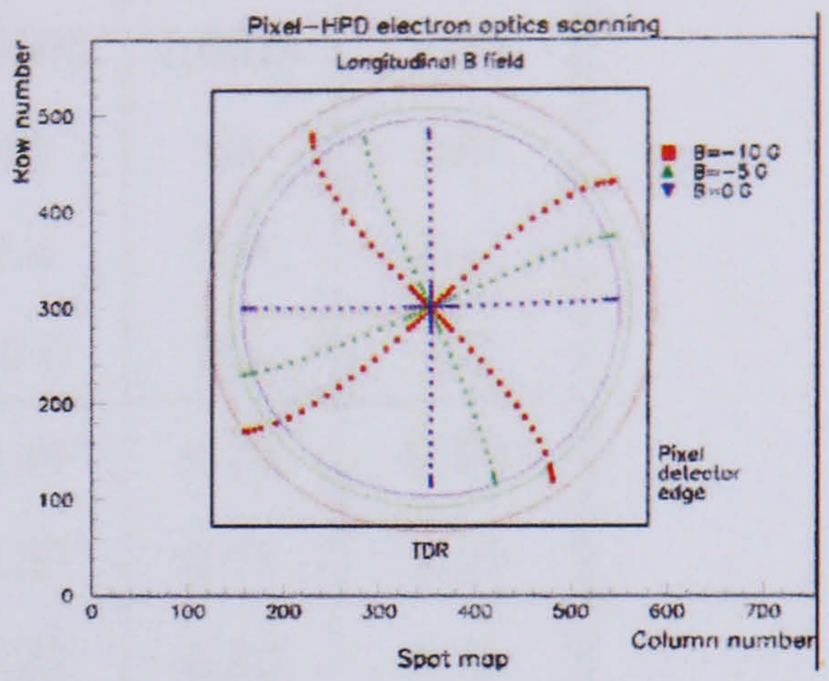

(b) Deviation of photoelectrons in a magentic field

Figure 3.17: Photodetector plane for RICH2 and distortions of photoelectron images due to the effect of magnetic fields [30, p.21].

fields of up to 25 G.

The expected number of photoelectrons detected from photons emitted along a saturated track (where the velocity of the particle is $\beta = 1$), with a finite length L in a Cherenkov medium is given by:

$$N_{pe} = \left(\frac{\alpha}{\hbar c}\right) L \epsilon_A \eta \int QRT sin^2\theta_c dE_\gamma, \tag{3.6}$$

where $\epsilon_A = 0.67$ is the coverage of the HPD plane active area, $\eta = 0.9$ is the HPD single photoelectron detection efficiency (following conversion by the photocathode), Q is the HPD quantum efficiency (shown in figure 3.16), $R = (0.9)^2$ is the mirror reflectivity and $T = 0.92$ is the transmission of a 5mm thick quartz plate which seals the Cherenkov gas volume separating the gas from the HPDs [27, p.8]. The expected number of detected photons for each Cherenkov media are given in table 3.1.

Material	CF_4	C_4F_10	Aerogel
L (cm)	167	85	5
n	1.0005	1.0014	1.03
θ_c^{max} $(mrad)$	32	53	242
Pthresh(π) (GeV)	4.4	2.6	0.6
Pthresh(K) (GeV)	15.6	9.3	2.0
$\sigma_\theta^{emission}$ $(mrad)$	0.36	0.74	0.60
$\sigma_\theta^{chromatic}$ $(mrad)$	0.50	0.81	1.61
σ_θ^{pixel} $(mrad)$	0.22	0.83	0.78
σ_θ^{track} $(mrad)$	0.24	0.42	0.26
σ_θ^{total} $(mrad)$	0.70	1.45	2.00
N_{pe}	23.2	30.3	6.8

Table 3.1: Radiator characteristics, resolution contributions per photoelectron (σ) and number of photoelectrons per ring (N_{pe}) [27, p.6] [31, p.71].

3.4.2 Particle Identification

Particle identification comes mainly from the RICH detectors in conjunction with the tracking stations and dipole magnet. Good particle identification is an essential requirement of LHCb. Without it, LHCb will not be able to determine exclusive decays of B particles, where the B decays hadronically to either pions or kaons. Figure 3.18 shows the simulation result for the separation of pions and kaons over the whole momentum range for the dielectric media used in LHCb.

Figure 3.19 shows the simulated π-K result of the media in both RICH1 and RICH2 as well as the separation with respect to particle momentum in the range up to 150 GeV/c. One can observe at least 3σ π-K mass separation in the momentum range 3 - 100 GeV/c (this implies a 0.1% misidentification in this momentum range). At low momentum the particle identification allows the experiment to perform tagging of B mesons by measuring the charge of a tagged kaon. At high momentum, the particle identification capabilities of the RICH can distinguish pions from kaons from

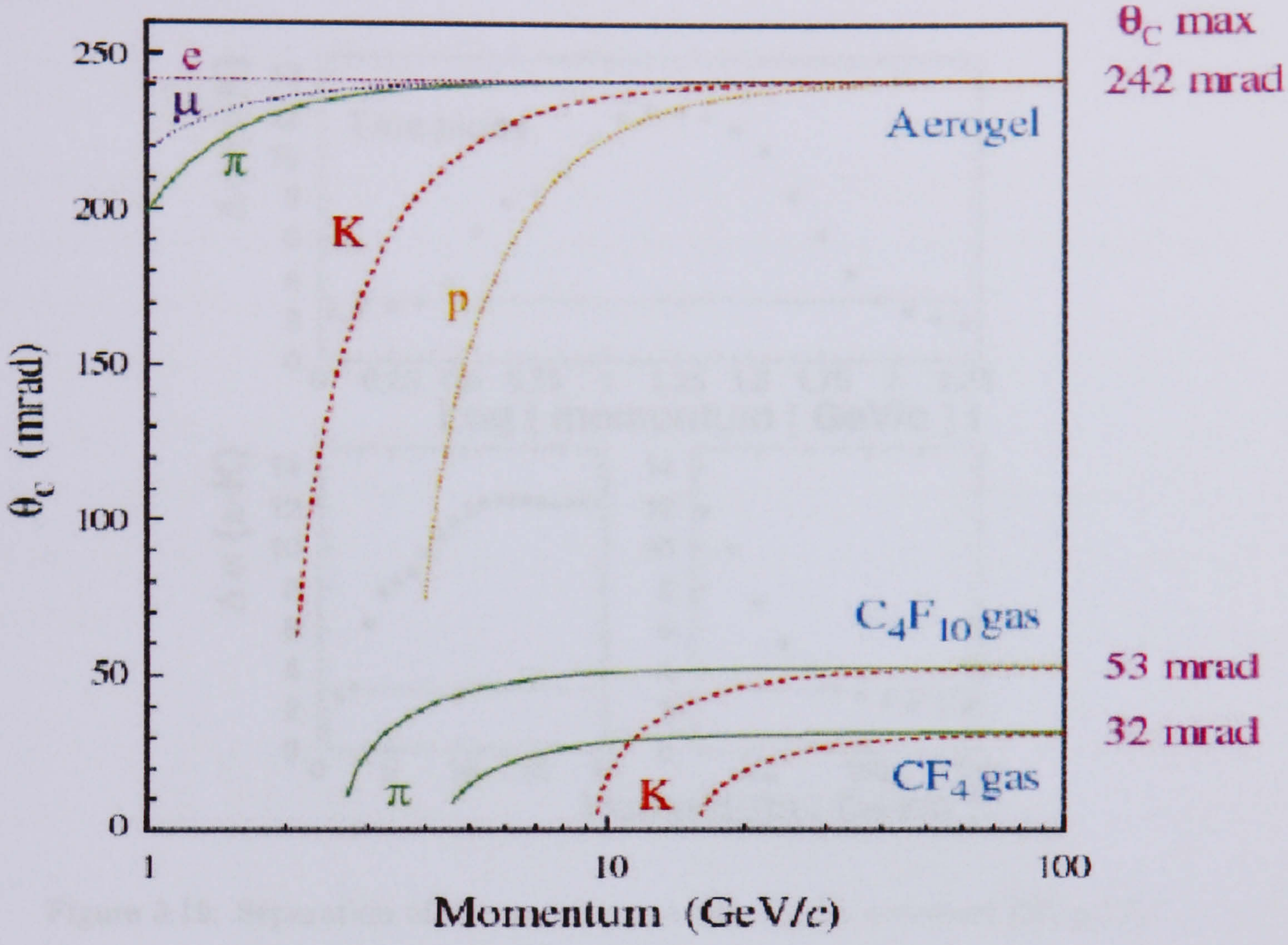

Figure 3.18: Separation of pions and kaons for the LHCb radiators [32, p.17].

the two hadron decay of B mesons.

Without the RICH detectors, for example, it would be impossible to see the $B_s \to D_s K$ decay signal (one of the CP violation channels of interest, to be used to measure the unitarity triangle angle γ) due to the high $D_s\pi$ background. However, with the use of RICH detectors a very well defined $D_s K$ decay signal can be seen (Figure 3.20).

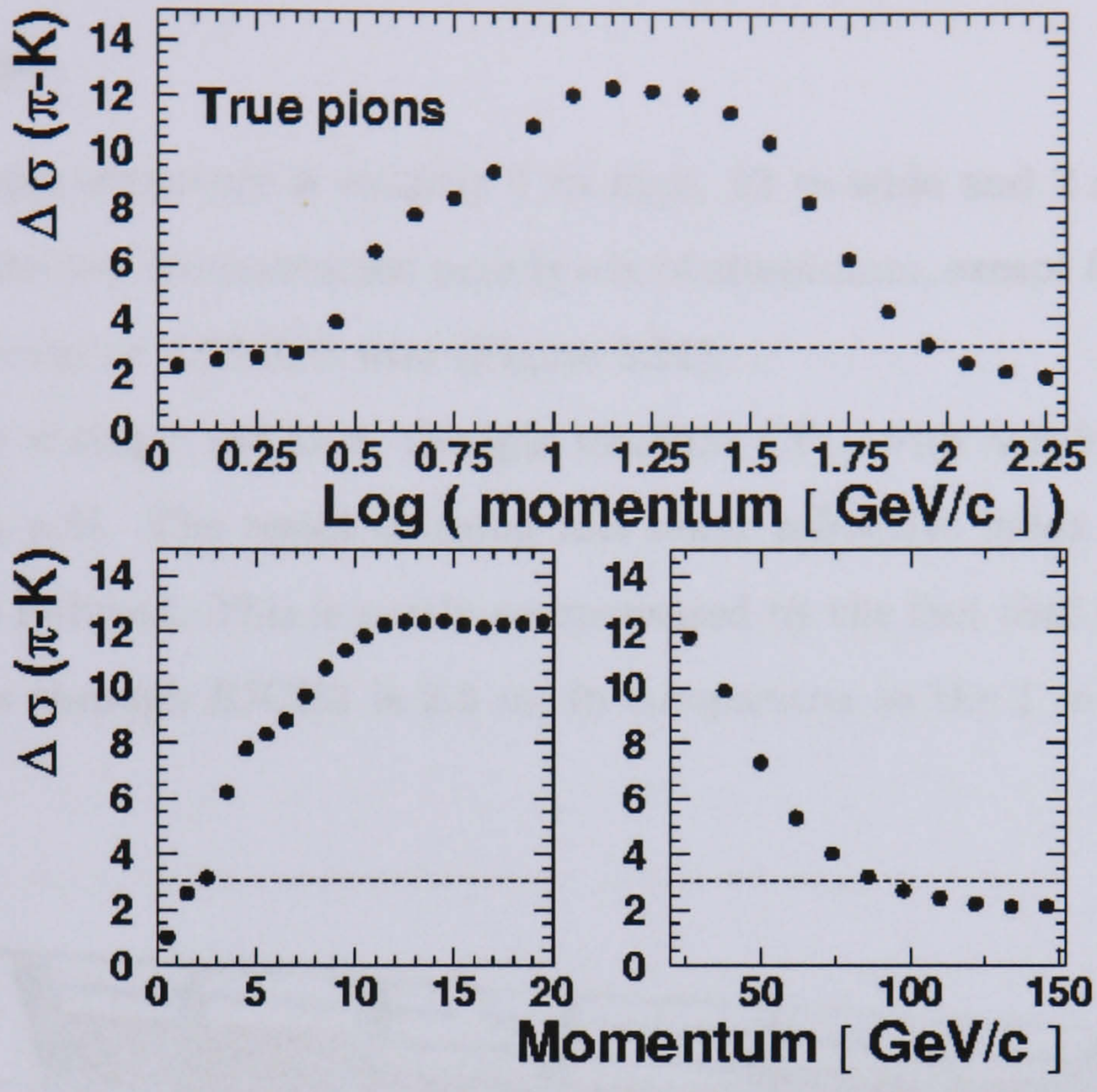

Figure 3.19: Separation of pions and kaons with RICH detectors [27, p.17].

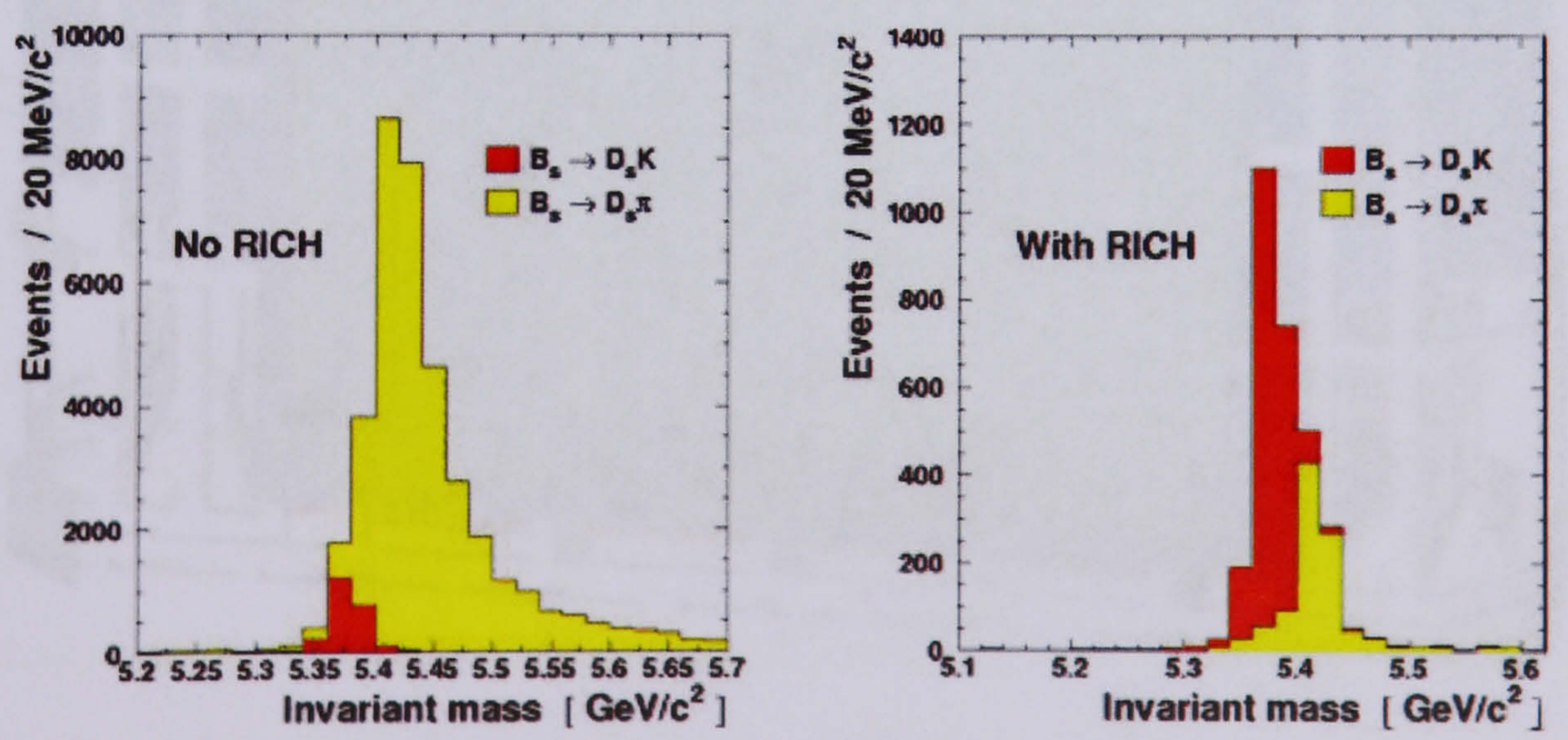

Figure 3.20: $B_s \rightarrow D_s K$ signal in LHCb, with and without RICH to identify kaons in the detector.

3.5 RICH2

3.5.1 Design

The RICH2 super-structure is roughly 7 m high, 12 m wide and 2 m deep, weighs around 30 tonnes and is constructed mainly out of aluminium, except for the magnetic shielding made out or ARMCO iron (Figure 3.21).

RICH2 has a single radiator, the gas medium CF_4, with a refractive index of n=1.0005 [27, p.6]. The result of using this lower refractive index gas is that the photon yield is reduced. This is partly compensated by the fact that the path length of the particles through RICH2 is 2.3 m, in comparison to the 1 m path length of RICH1.

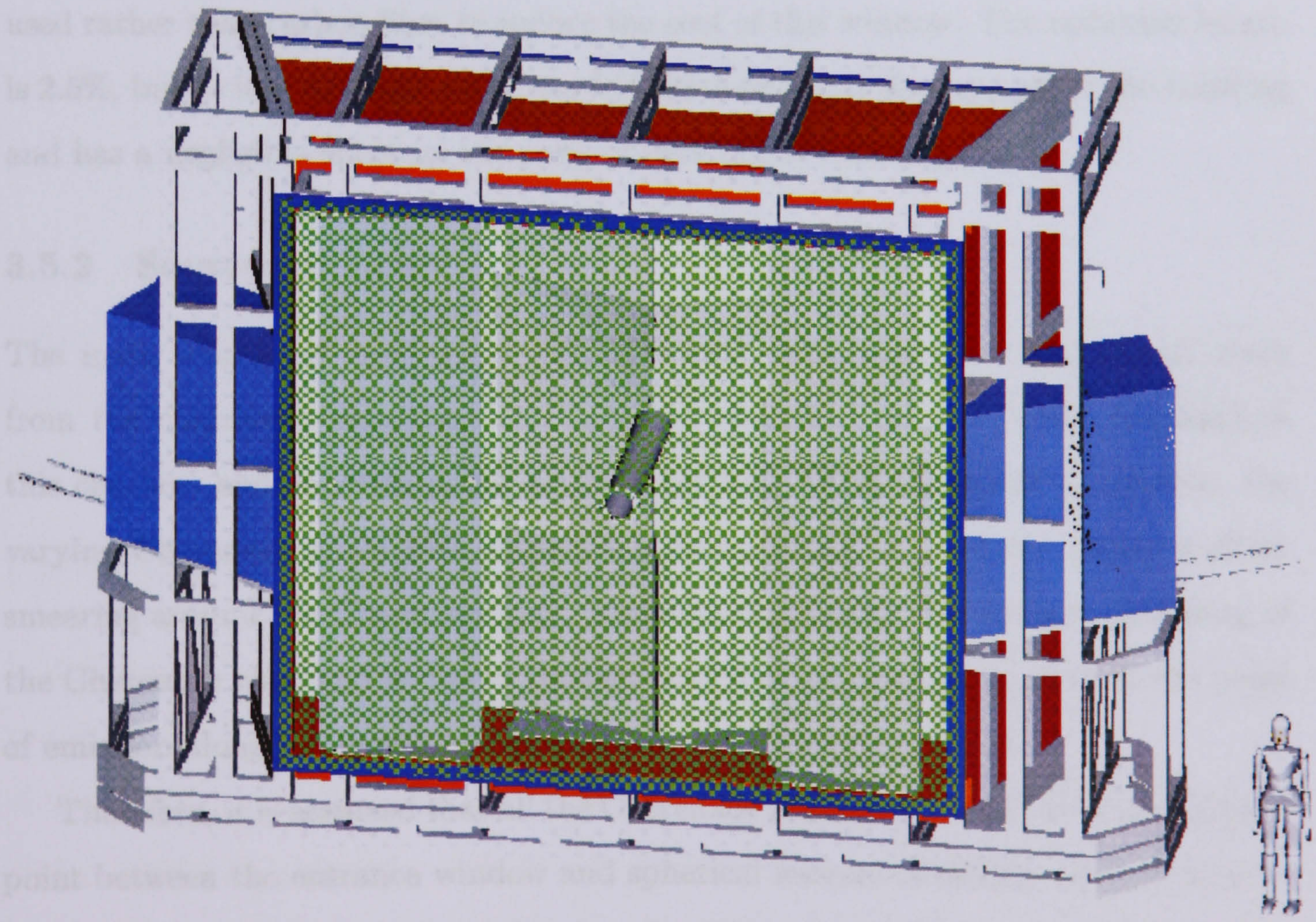

Figure 3.21: RICH2 [30, p.6].

The gas chamber comprises an aluminium skin, entrance and exit windows, which

themselves support a central tube that houses the beam pipe. There are two 6 *mm* thick quartz windows either side of the detector that separate the radiator gas volume from the photodetector assembly [27, p.6].

The entrance window must have as low a radiation length X_0 as possible so as to avoid secondary interactions that can produce unwanted Cherenkov rings. Background rings affect the pattern recognition capabilities of the RICH reconstruction software and can degrade the performance of the ring identification algorithm. Therefore the RICH 2 entrance window is constructed from a 28 *mm* thick polymethacrymide (PMI) foam layer sandwiched between two 1 *mm* thick carbon fibre reinforced epoxy skins. The radiation length for the entrance window is 1% X_0.

The exit window has been constructed from a 30 *mm* thick polymethacrymide foam layer sandwiched between two 1 *mm* thick aluminium skins. Aluminium was used rather than carbon fibre to reduce the cost of this window. The radiation length is 2.5%, but as it is downstream of the RICH2 detector, it does not affect the tracking and has a negligible effect on the performance of the calorimeter.

3.5.2 Sources of Error

The main sources of error within RICH2, aside from resolution limitations, come from the chromatic aberration of Cherenkov radiation (as previously discussed in this chapter) and emission-point error (Table 3.1). With chromatic aberration, the varying Cherenkov angle with respect to the wavelengths produced causes a slight smearing around the Cherenkov ring. Emission-point error also causes a smearing of the Cherenkov ring, and is due to the fact that it is not possible to identify the point of emission along the length of the detector of a Cherenkov photon.

Therefore, it is assumed that all the Cherenkov photons are emitted at the midway point between the entrance window and spherical mirrors of RICH2 (Figure 3.22).

As mentioned earlier in this chapter, the dielectric medium in RICH2 is the gas CF_4. The expected Cherenkov angle for photons produced by saturated tracks in RICH2 is 31 *mrad* [30, p.3]. The final resolution for the Cherenkov angle of photons in RICH2 is 0.7 *mrad* dominated by the emission-point error and chromatic aberration. In order not to degrade this resolution, the alignment error required needs to be

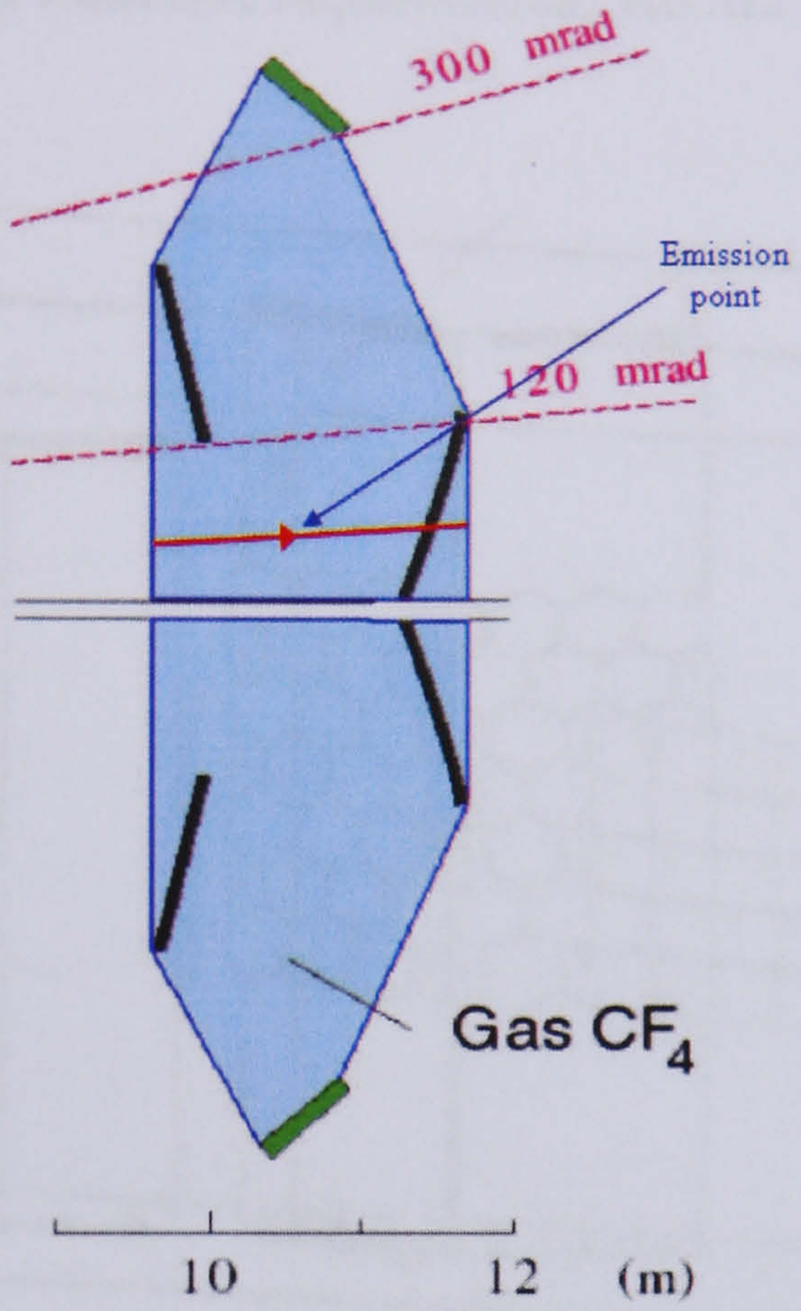

Figure 3.22: Emission point.

much smaller than this, and 0.1 mrad has been set as a goal so that the alignment resolution may remain negligible compared to the resolution from other sources (see table 3.1).

3.5.3 RICH2 Mirrors and Supports

Within the gas volume of RICH2 (Figure 3.23) there are four floor to ceiling sandwich panels for the flat and spherical mirrors. These panels are constructed from a 38 mm aluminium honeycomb core embedded between 1 mm thick aluminium skins. The four panels differ in size. The panels for the flat mirrors are 5250 mm high by 1480 mm wide, whereas the panels for the spherical mirrors are 6200 mm high by 1480 mm wide in order to cater for the difference in size of the gas chamber from the front to the back of the detector. These panels hold the supports for the mirror segments [30, p.12].

Due to the size of the mirrors, it has been necessary to segment them in order to

meet both the optical and radiation requirements. RICH2 has two spherical mirrors;

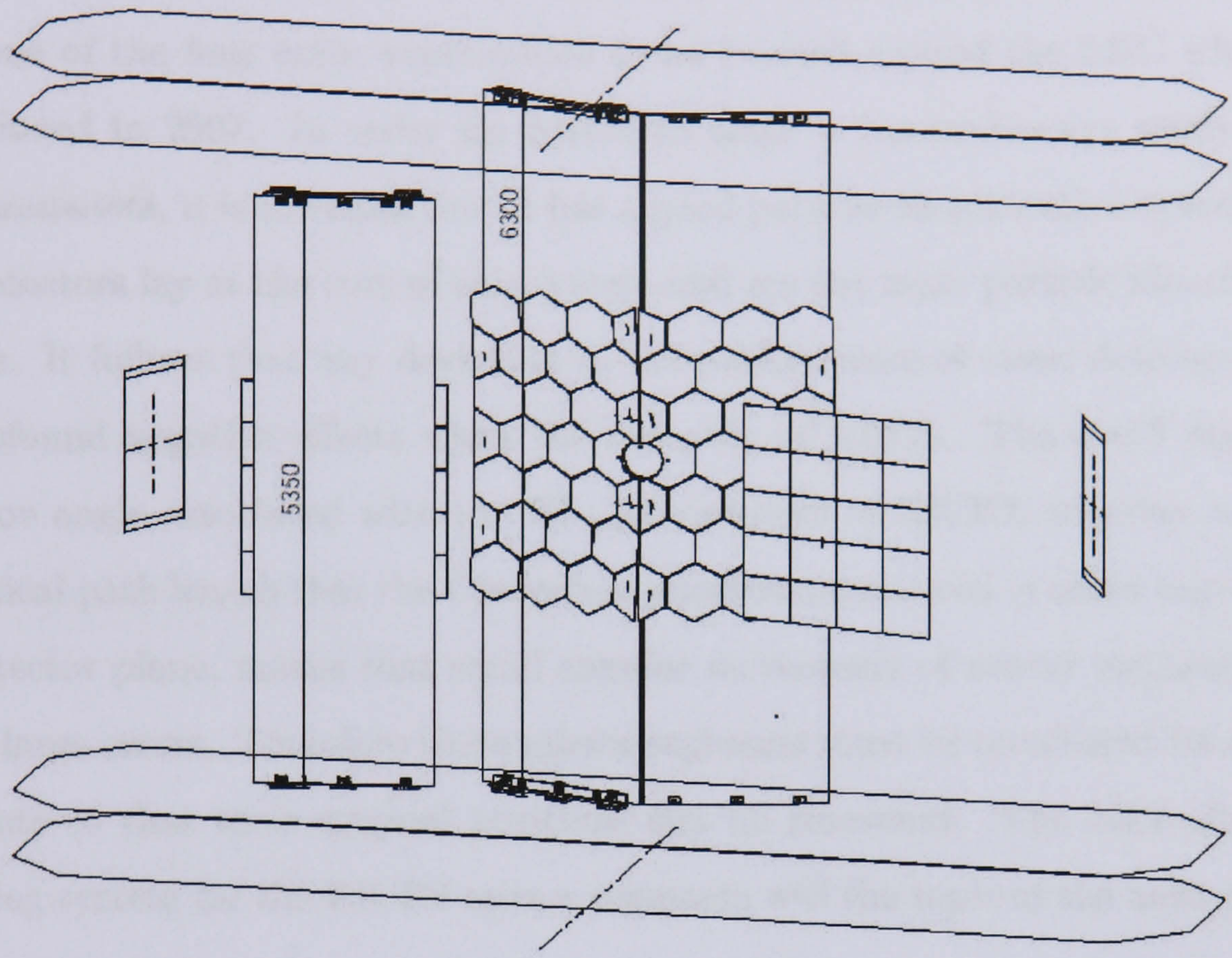

Figure 3.23: Mirrors of RICH2 [30, p.10].

each mirror has 20 hexagonal and 7 half-hexagonal segments, with an additional special hexagonal segment that surrounds the beam pipe. In addition to the spherical mirrors there are two flat mirrors with 20 square segments per mirror. Each segment has its own adjustable support held by the sandwich panels within the gas volume (these supports will be discussed in further detail in the next chapter).

The mirrors of RICH2 are made from a 6 mm thick Simax glass substrate. The optical surface has a roughness of 3 mm or better and is aluminium coated with SiO_2 as a protective layer and MgF_2 and HfO_2 as anti-reflective coatings. The reflective efficiency is measured to be around 87% between 250 nm to 500 nm and better than 70% between 210 nm to 250 nm over a wide range of incident angles.

3.6 Summary

The LHCb experiment is a dedicated second generation B physics experiment and will be one of the four main experiments to be located around the LHC when it is commissioned in 2007. In order for LHCb to make a comprehensive study of the CKM parameters, it is essential that it has a good particle identification system. The RICH detectors lay at the core of this system and are the main particle identification detectors. It follows that any deviation in the performance of these detectors could have profound negative effects upon the accuracy of LHCb. The small maximum Cherenkov angle associated with the CF_4 gas medium of RICH2, together with the large optical path length that the Cherenkov photons must travel in order to reach the photodetector plane, means that small angular movements of mirror segments could produce large errors. Therefore these mirror segments must be monitored for angular movements so that their original positions can be recovered. The laser alignment monitoring system for the RICH2 mirror segments will the topic of the next chapter.

Chapter 4

The Laser Mirror Alignment Monitoring System

4.1 Justification

A long-term behavioural analysis of mirror segment supports has shown that rotational movements as high as 0.15 *mrad* in the mirror segment positions could occur through changes in temperature and humidity over time [43]. In addition a finite element analysis of the sandwich panel characteristics can produce further movements as high as ± 0.15 *mrads* [42]. Hence a system that can monitor these movements must be utilised to ensure the optimum performance of the RICH.

Using saturated tracks (i.e. high momentum tracks where the maximum Cherenkov angle is achieved) and tracking data from the tracking stations, it is possible to determine relative movements in the positions of mirror segments, by comparing the expected final destination of Cherenkov photons with the measured destination [61].

The Cherenkov photons emitted along a particle track in the RICH radiator are distributed around a Cherenkov cone that is reflected off mirrors and then imaged onto a photo-detector plane as a ring. Therefore, the distance between the centre of the ring and its edge should represent the Cherenkov angle. If there are misalignments in the mirrors the reconstructed centre of the Cherenkov ring and the measured centre of the Cherenkov ring will differ.

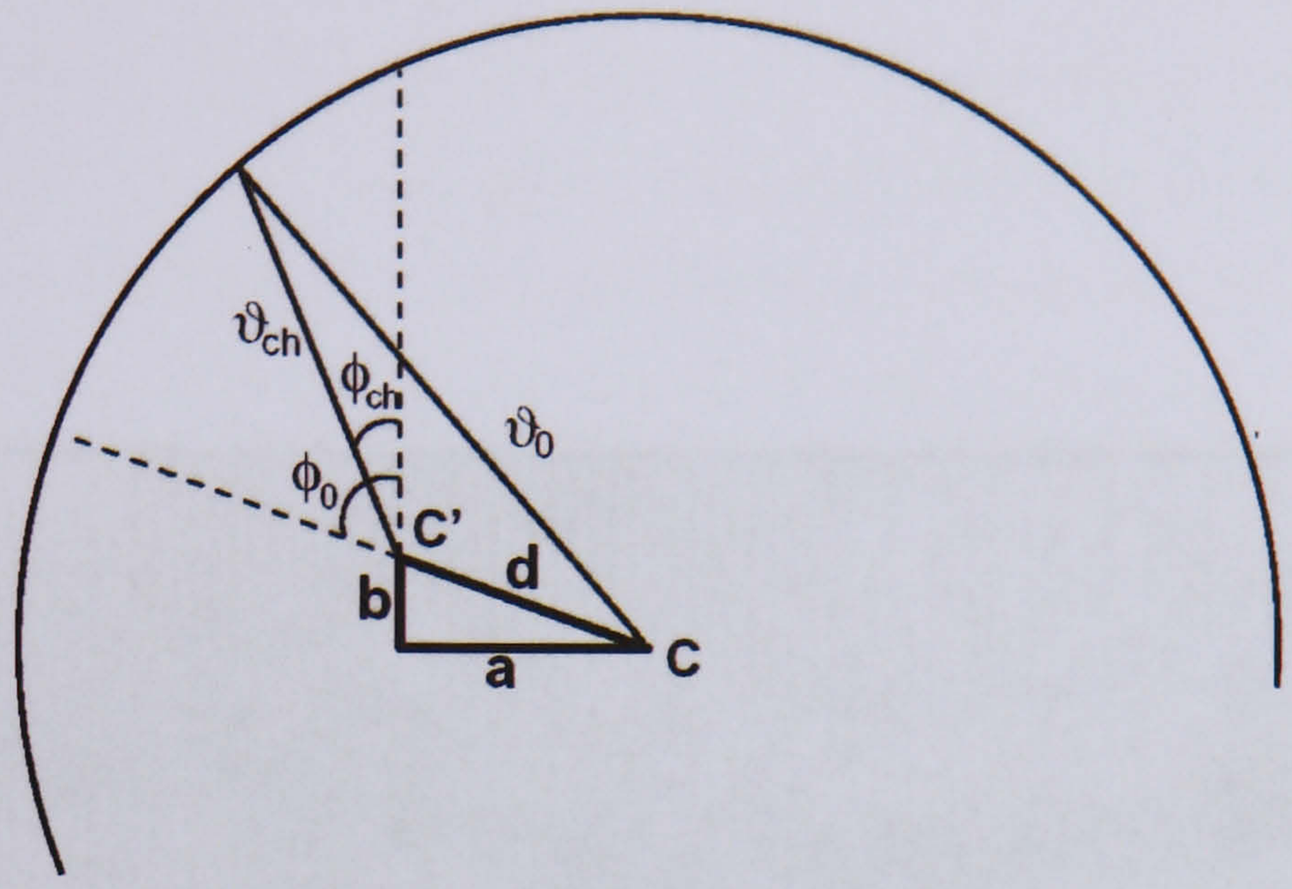

Figure 4.1: A Cherenkov ring misalignment leading to non-aligned centres [61].

Figure 4.1 shows how the measured and reconstructed centres of the Cherenkov ring become misaligned. Point C is the real centre of the ring, point C' is the reconstructed centre, θ_o is the real Cherenkov angle, θ_{ch} is the measured Cherenkov angle, and a, b and d are projections of the Cherenkov mirror tilts. They can be related by equation 4.1

$$\Delta\theta = \theta_{ch} - \theta_o = acos(\phi_{ch}) + bsin(\phi_{ch}). \tag{4.1}$$

where $\Delta\theta$ is the change in Cherenkov angle at the azimuthal angle ϕ_{ch}. As ϕ_{ch} increases from 0 to 2π rad (i.e. it follows the locus of all points along the ring), any misalignment present will change $\Delta\theta$. A misalignment plot can be made by plotting $\Delta\theta$ as a function of ϕ_{ch}, showing a sinusoidal (eq. 4.1), where a represents the change in x position of the centre and b represents the y position of the tilt (figure 4.2).

4.1.1 Justification of the laser based system

The software alignment method for recovering misaligned mirror segments performs well at recovering any misaligned segments. However, this algorithm relies on an iterative approach, so it needs initial conditions that are sufficiently accurate to determine the position of the mirror segments. It was found in ref. [61] that the initial conditions need to be known with an accuracy of 0.5 mrad in order to achieve a final

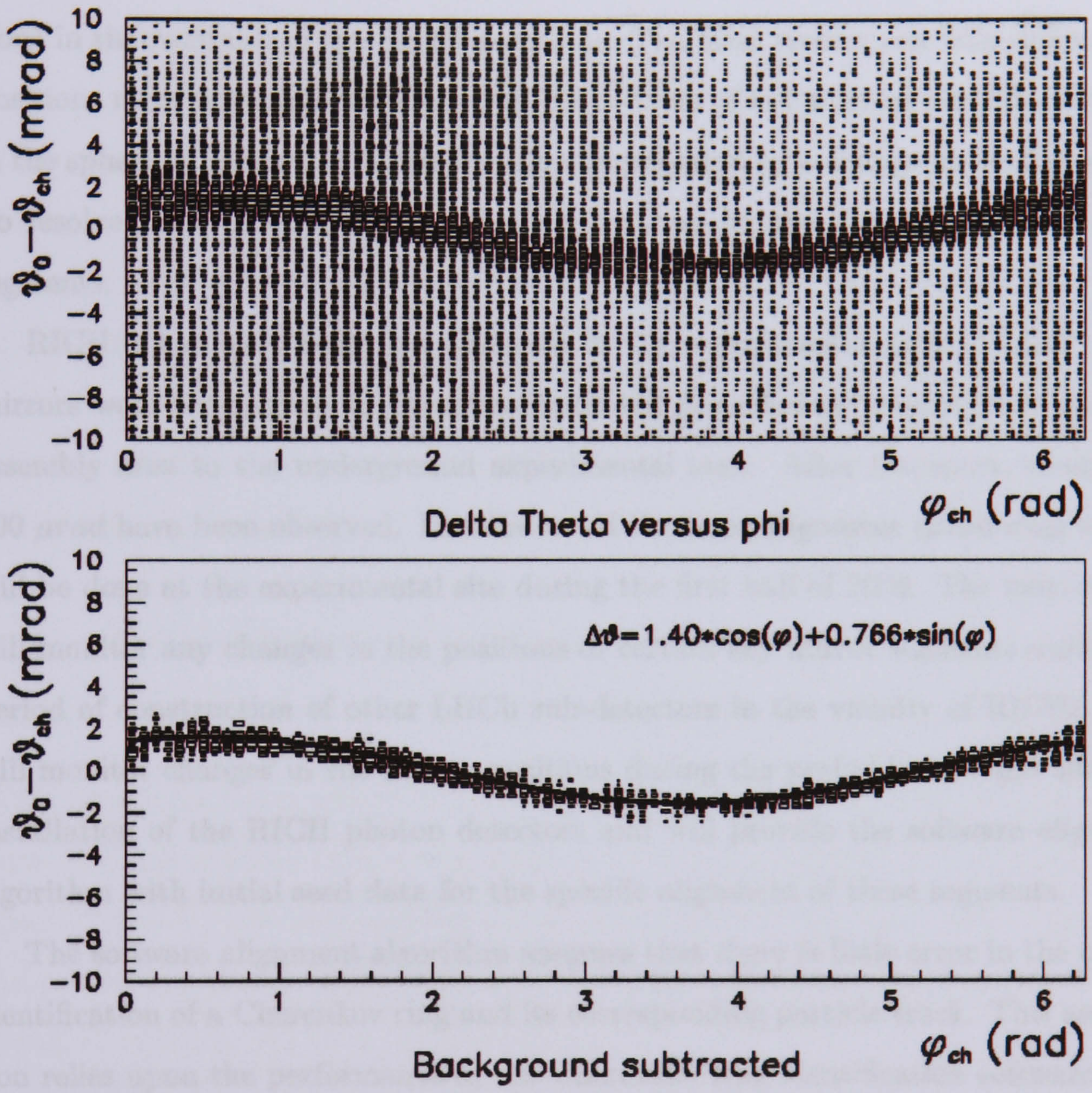

Figure 4.2: A 2D histogram of $\Delta\theta$ against ϕ_{ch} (top). The background was removed with a cut at 30% of the maximum on each column (bottom) [61].

misalignment resolution of 0.1 mrad. The laser based system is designed to supply alignment data about one or more key segments from each mirror to better than 0.5 *mrad* so it can feed the software system these initial conditions (named "seeds"). In addition, there is the issue of resolving ambiguous photons, where it is not known which mirror combination each photon has hit, thereby adding tails to the distributions in the residuals of the mirror positions. The laser system can help define these positions more accurately. Because RICH2 consists of two mirrors per side, a change in the spherical mirror can be incorrectly compensated by a change in the flat mirror. To resolve these ambiguities, the laser system can fix the positions of some of the segments.

RICH 2 has been built and installed in the experimental area of LHCb. The mirrors were pre-aligned to an accuracy of 150 μrad before transporting from the assembly area to the underground experimental area. After transport, changes of 100 μrad have been observed. Installation of the laser alignment monitoring system will be done at the experimental site during the first half of 2006. The laser system will monitor any changes in the positions of certain key mirror segments during the period of construction of other LHCb sub-detectors in the vicinity of RICH2. This will monitor changes in the mirror positions during the period before and after the installation of the RICH photon detectors and will provide the software alignment algorithm with initial seed data for the specific alignment of these segments.

The software alignment algorithm assumes that there is little error in the correct identification of a Cherenkov ring and its corresponding particle track. This assumption relies upon the performance of the Cherenkov ring identification software [61]. Although simulation results from Monte-Carlo data show that the Cherenkov ring identification software performs well, a degradation in both the performance of the ring identification software and the software mirror alignment algorithm could arise with real data if the seeds to the algorithms are not properly known. Under such circumstances, the laser based system would provide values for the mirror segment positions that feed into the initial conditions of the iterative alignment algorithm as a function of time, and flag any observed changes. The laser based alignment system will provide continued evaluation and monitoring of the performance of the final

software alignment algorithm.

4.2 The Laser Alignment Monitoring System Design

4.2.1 System Requirements

The aim of the laser mirror alignment monitoring system is to measure changes in the rotational positions of at least one of the mirror segments per mirror with a resolution of 0.1 *mrad* or better. This will supply a reference point or "*seed*" to the data based alignment monitoring system. All components of the laser alignment monitoring system must remain outside of the detector acceptance, so as not to unnecessarily interfere with particle trajectories and/or momenta.

The laser mirror alignment monitoring system must be able to achieve the required accuracy, be able to monitor mirror positions throughout data taking and be able to identify changes in position of the mirror segments as they arise.

4.2.2 Mirror Segment Movement

Theory

Consider a laser beam reflection on a uniform mirror surface. There are three rotations that the uniform mirror can make in its local coordinate system, only two of which (X and Y) will have an effect on the position of the reflected image. Figures 4.3 and 4.4 show a simple 2θ relationship between the incident and exit beams for local X and Y rotations of a given mirror segment.

A rotation about the local Z axis of the mirror (perpendicular to the mirror plane) will not affect the reflected beam since there is no angular change in the XY plane from which the beam is reflected.

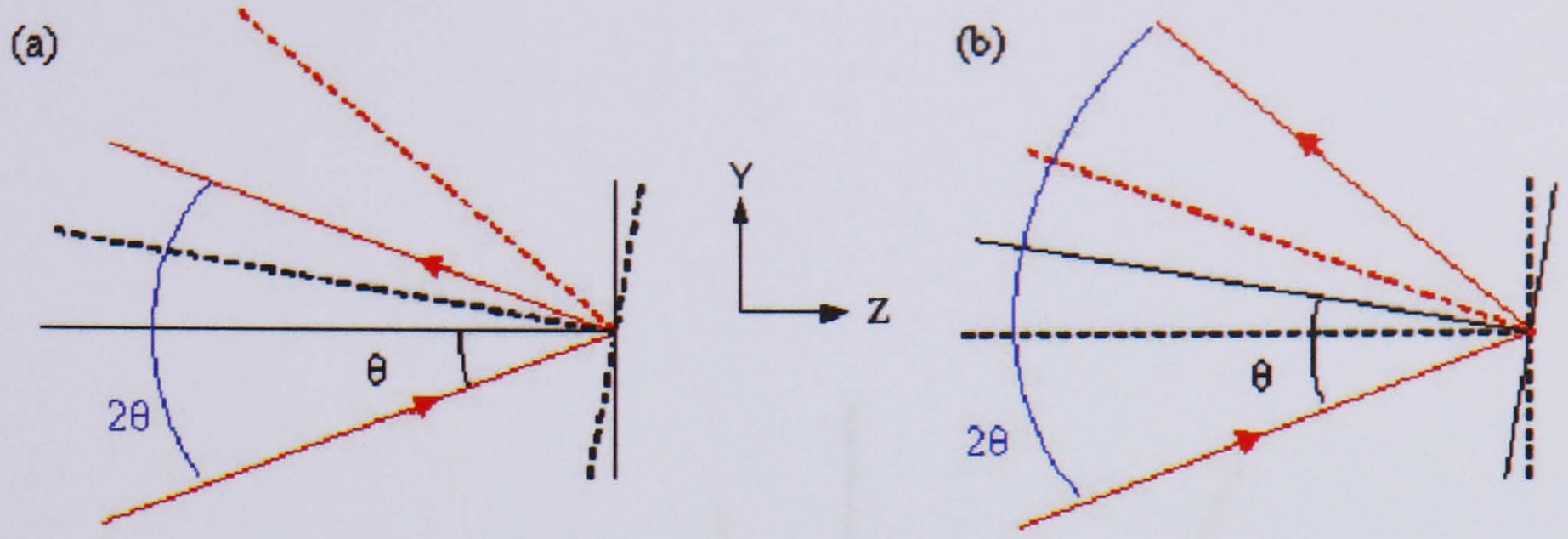

Figure 4.3: X Rotation.

4.2.3 RICH2 Mirror Support System

Every mirror segment in RICH2 has its own individual support and each support has the potential to move. Thus, over time and relative to each other, these mirror segments can move out of place. In order for the data based alignment system to run with optimal efficiency when recovering from these changes, it is important to choose key mirror segments that are well used in the reflection of Cherenkov photons. The possible key segments are located closest to the beam pipe on both spherical and flat mirrors (Figure 4.5).

The RICH2 Mirror Supports

The supports of the RICH2 mirrors are located on the sandwich panels. Each support has three parts; a polycarbonate ring; an adjustment stage and a cup. The polycarbonate rings are bonded onto the back at the centre of the segment (Figure 4.6(a)) creating a grip for holding the mirror in place.

The adjustment stage is screwed onto cups that extend the support away from the sandwich panel (cups of various lengths are required for the spherical mirrors in order to produce a concave surface - Figure 4.7). The mirror segments with the bonded rings are then screwed into place on the adjustment stage creating a complete unit (Figure 4.6(b)).

The adjustment stage of the mirror support has three adjustment bolts that can

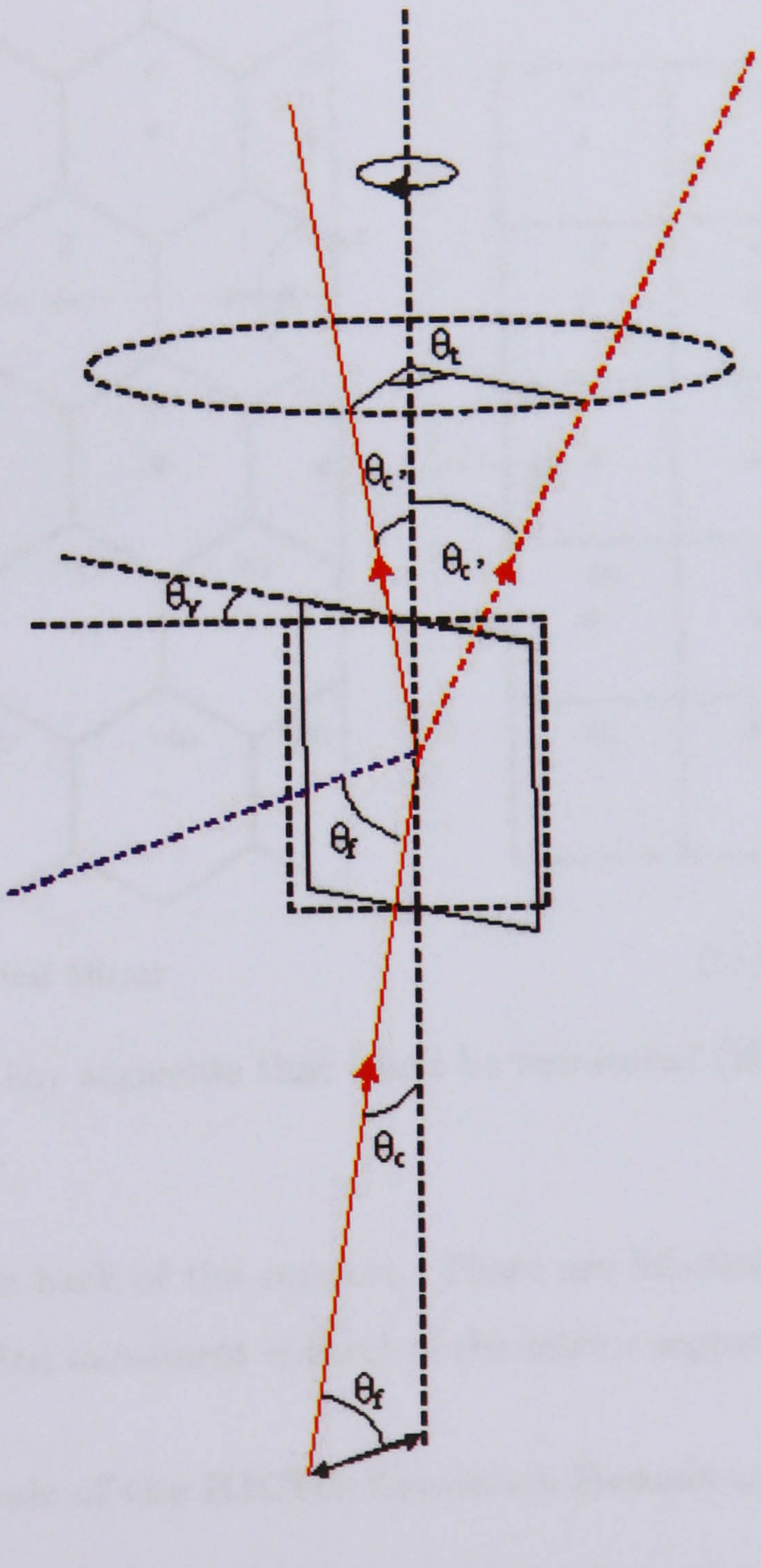

Figure 4.4: Y Rotation.

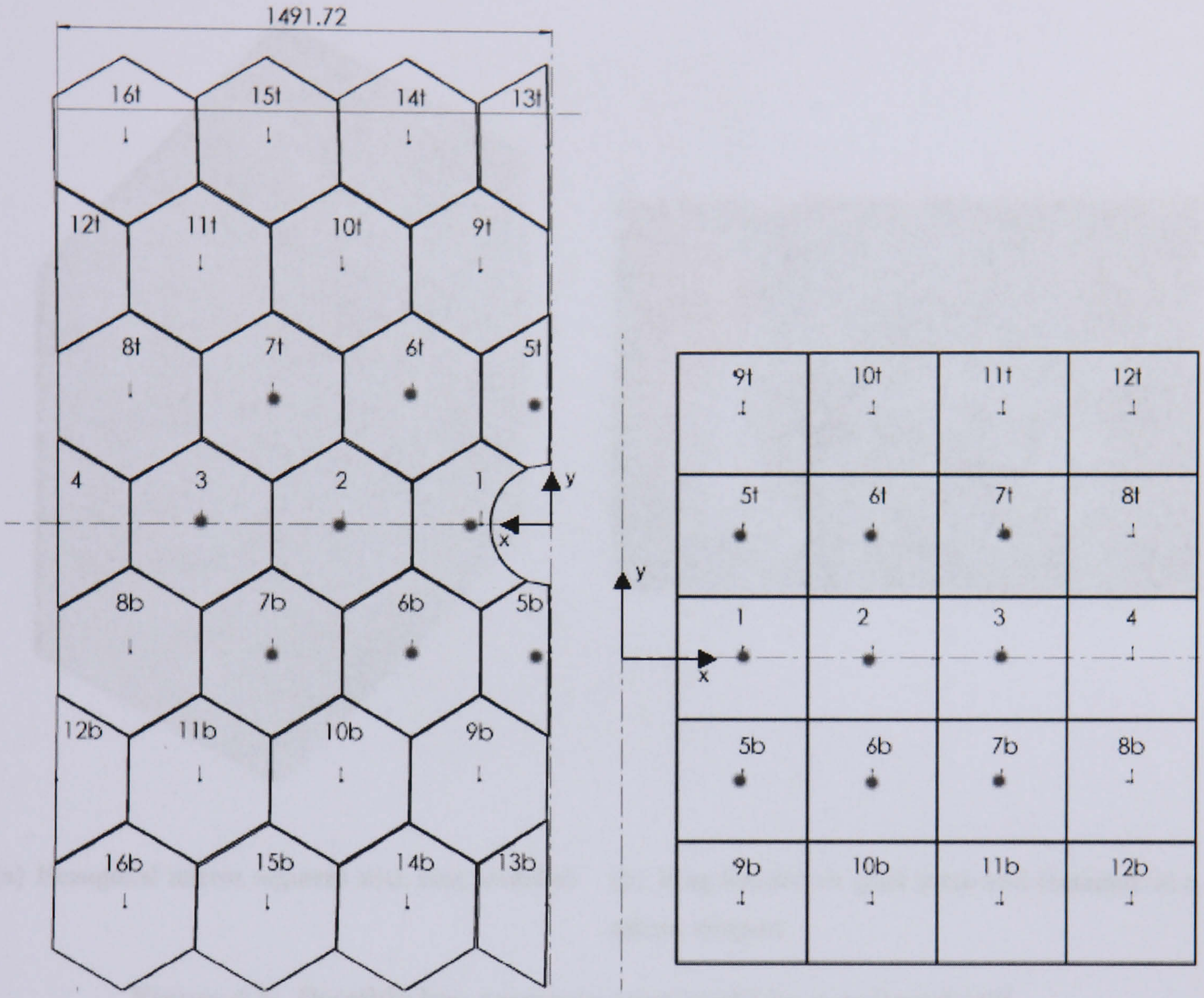

(a) Spherical Mirror

(b) Flat Mirror

Figure 4.5: Possible key segments that could be monitored (identified with a dot on the mirror segment).

be accessed from the back of the support. These are labelled in figure 4.8 as L, R and T and provide fine movement control of the mirror segment.

Mechanical Analysis of the RICH2 Sandwich Boards and Mirror Segments

The sandwich boards will flex slightly under the weight of the mirror segments and supports. This can be seen by the finite element analysis made by Christoph Frei (Figure 4.9) [30]. This analysis shows a maximum angular deflection (SMX) of $\pm 0.129\ mrad$.

In the process of bonding the polycarbonate rings onto the back of the spherical

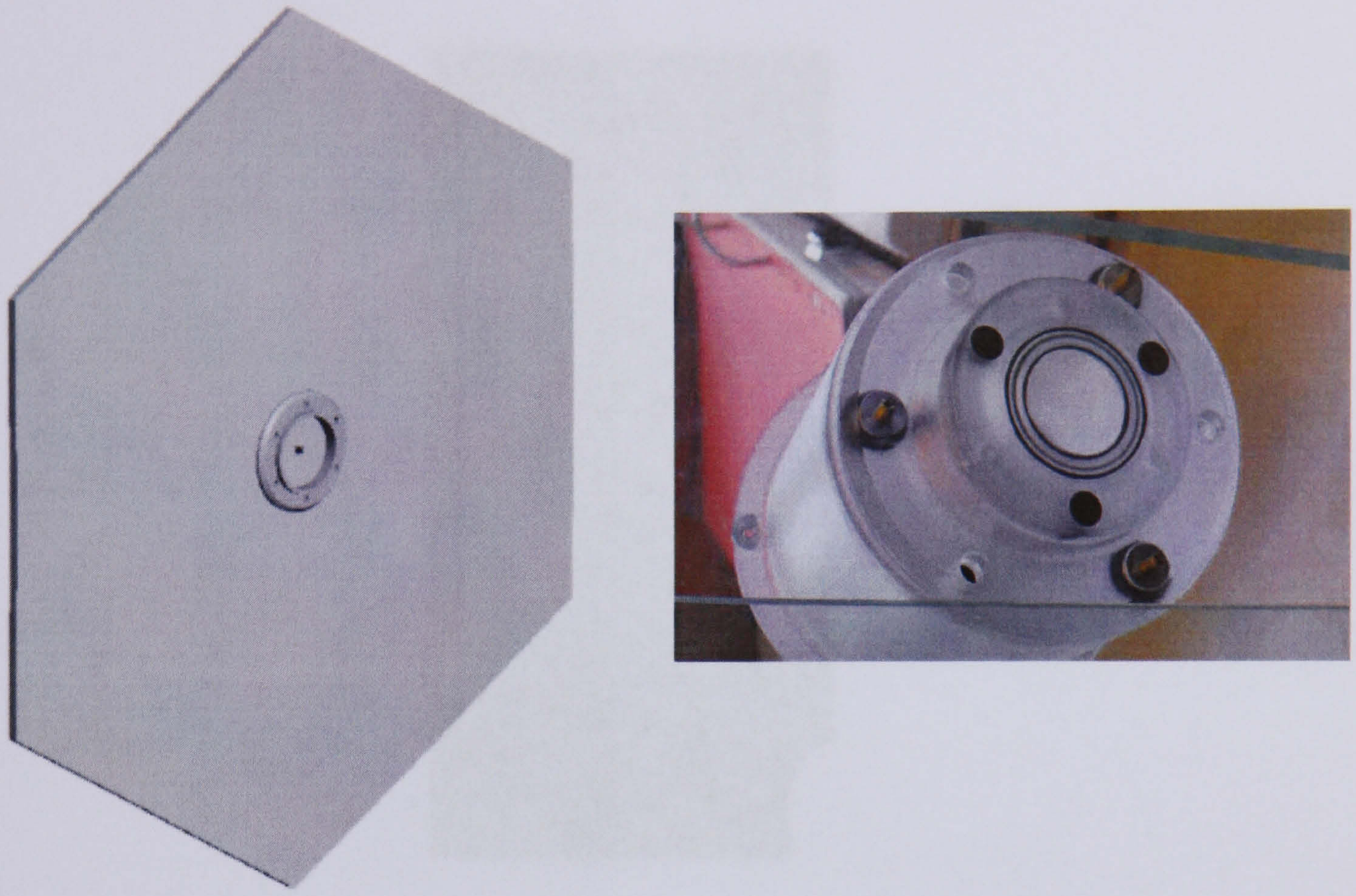

(a) Hexagonal mirror segment with ring attached

(b) Ring bonded on glass plate and mounted on a mirror support

Figure 4.6: Possible key segments that could be monitored [42].

mirror segments, the optical surface at the bond point becomes stressed as the glue dries and contracts. This effect can be clearly seen in figure 4.10 (work done by Christoph Frei).

4.2.4 Alignment System Design Overview

Design Considerations

The driving factors in the design of the Laser Mirror Alignment Monitoring System are to design a laser system that is able to transmit light into multiple single mode 532nm fibres that will travel over a distance of 100m. Each of the fibres should be responsible for monitoring a single mirror segment through the use of a focusing unit and additional reference optics. This section describes the initial design and design considerations for such a system.

Figure 4.7: Mirror supports on sandwich panel [42].

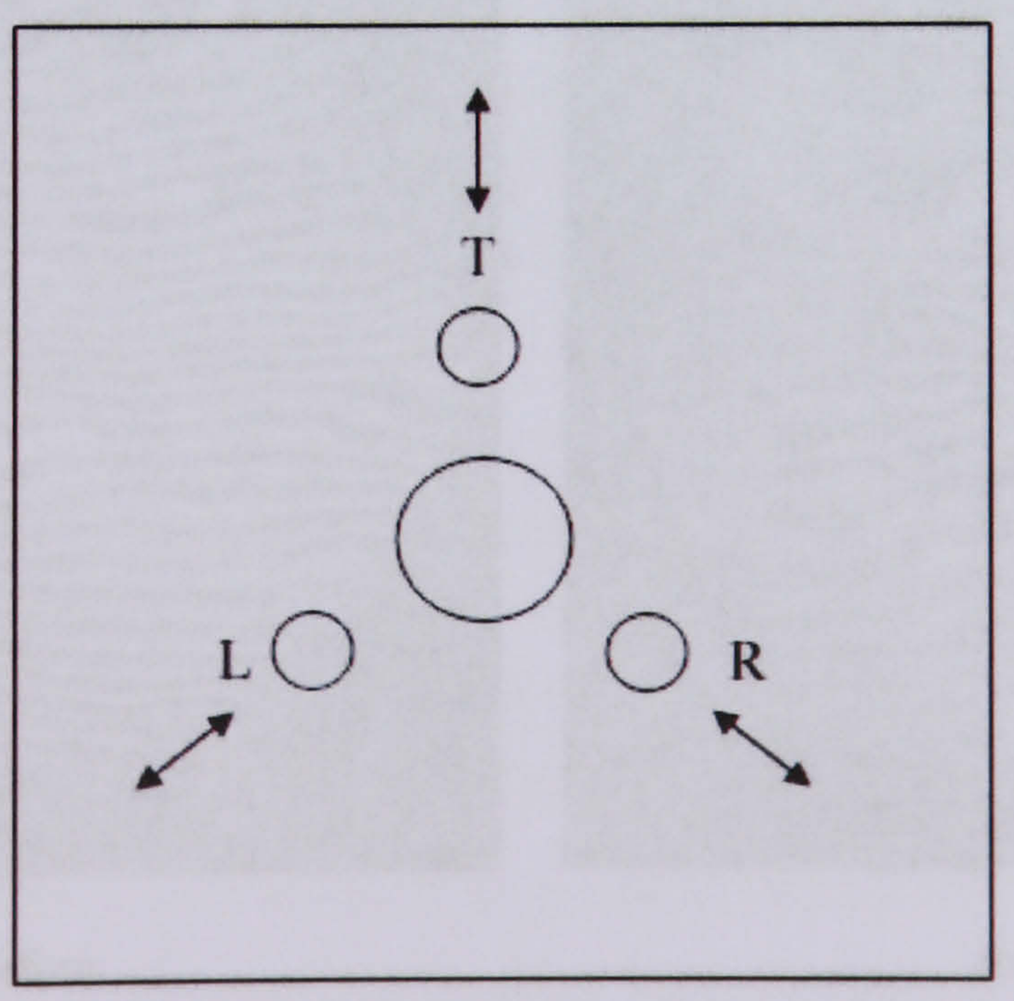

Figure 4.8: Adjustment at the back of the mirror segment support.

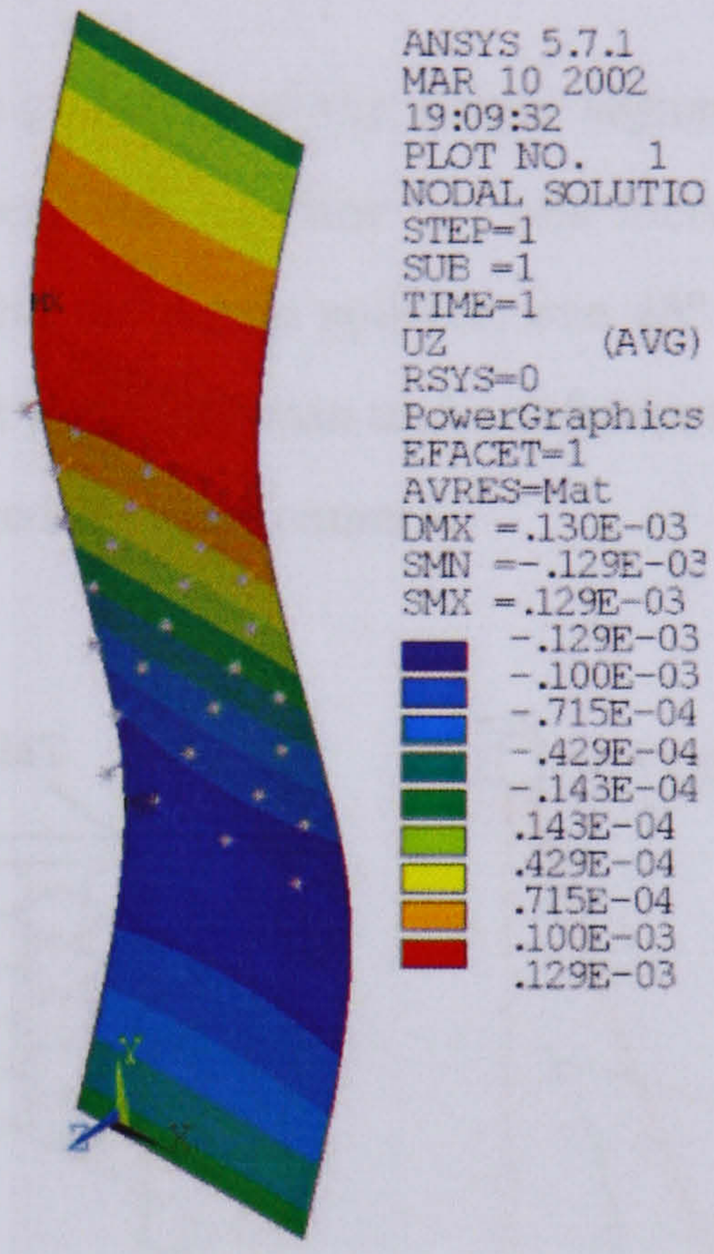

Figure 4.9: Finite Element Analysis of the Sandwich Panels [30, p.13].

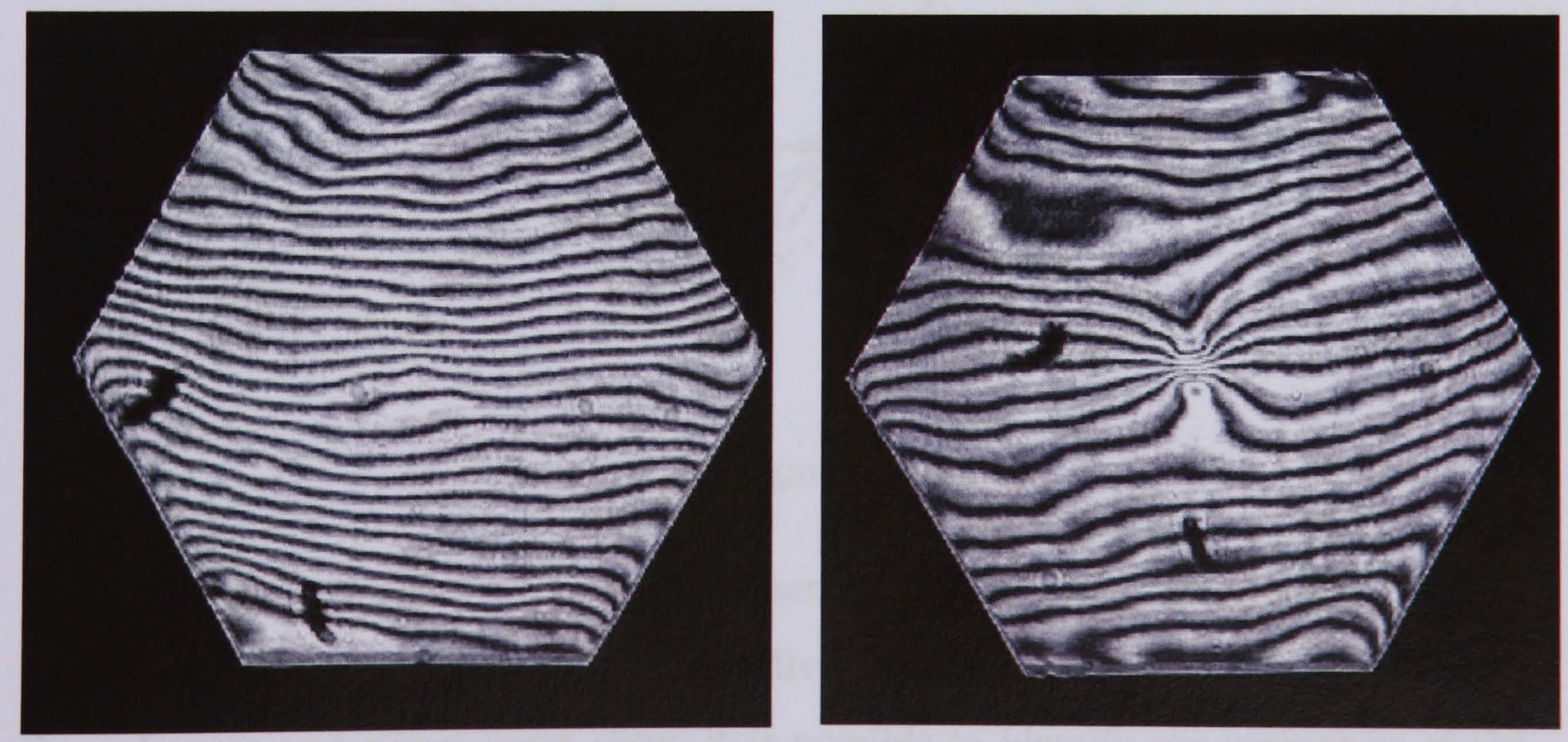

(a) before (b) after

Figure 4.10: A polarised source shows the stresses on the segment from the bonding process [42].

Laser Segment Monitors

The system to monitor the positions of the mirror segments comprises 16 individual segment monitors. Each segment monitor has one focusing unit that focuses light from a fibre optic input, one 45^o beam splitter, one 45^o laser mirror and a camera. These components allow for a signal beam and a reference beam per segment monitor (Figure 4.11) to be measured by each camera.

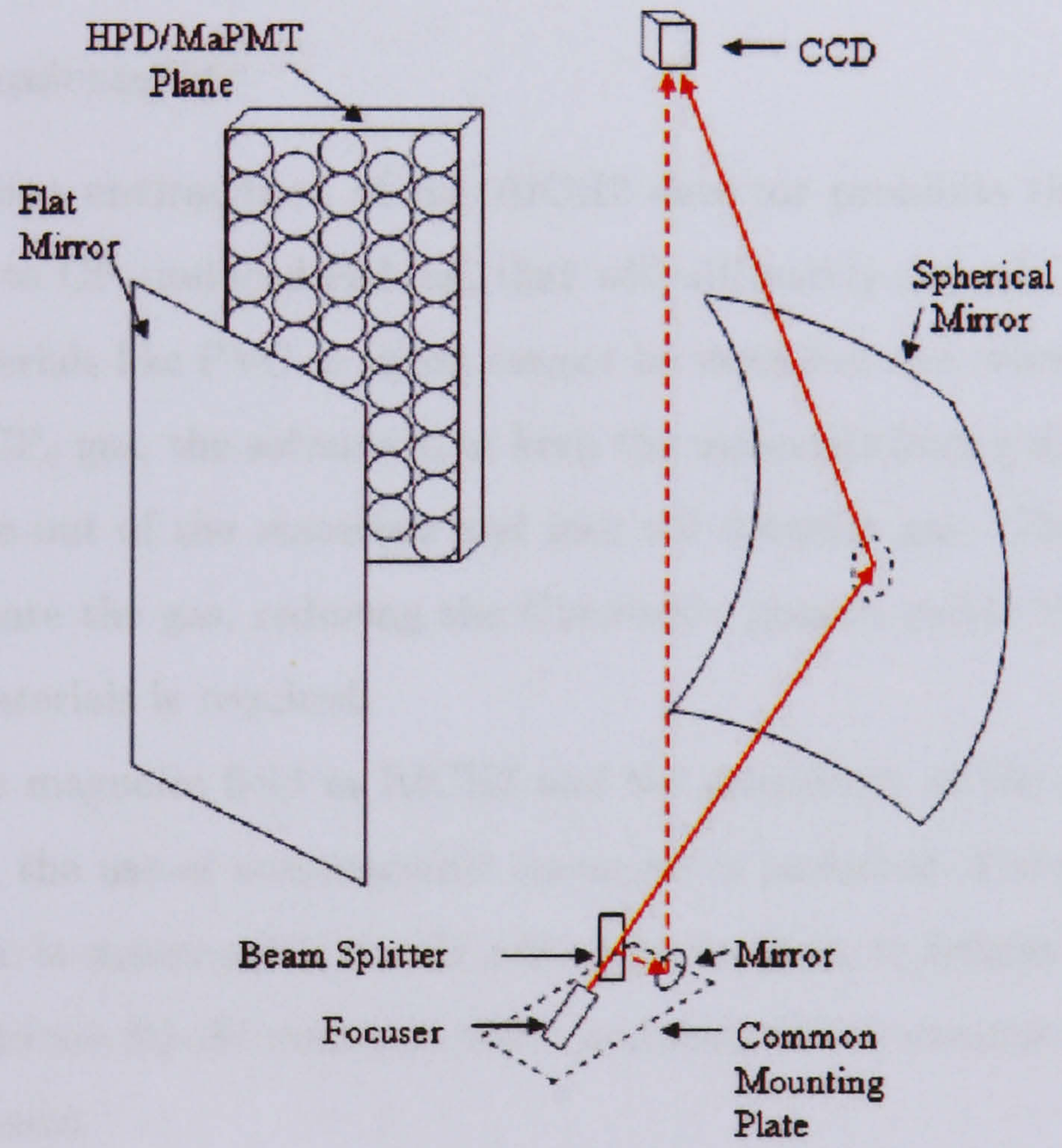

Figure 4.11: Segment Monitor.

The floor components of the segment monitor have a common mounting platform. This ensures that movement between individual components is minimised. Using this reference and signal beam setup it is possible to identify the movement of the individual components of the segment monitor and the mirror segment itself.

Component Mounts

The component mounts of the laser mirror alignment monitoring system comprise two parts: roof mounts for the cameras and floor mounts for the focusing unit, beam splitter and laser mirror. On each side of the detector there is a common top plate for the roof component mounts and a common base plate for the floor component mounts. These common plates reduce the risk of movement between the component mounts.

Material Requirements

The fluorocarbon environment of the RICH2 detector prohibits the use of certain materials due to CF_4-induced etching, that will ultimately degrade the CF_4 gas purity. Also materials like PVC or nylon cannot be used, because when they come into contact with CF_4 gas, the solvents that keep the materials from going brittle ("plastifiers") diffuse out of the materials and into the detector gas. These solvents will thus contaminate the gas, reducing the Cherenkov photon yield. Therefore, careful selection of materials is required.

Due to the magnetic field in RICH2 and the sensitivity of the alignment monitoring system, the use of non-magnetic materials is preferred. Considering that the RICH detector is constructed mainly out of aluminium, it follows that this is the best material to use for the common plates and component mounts in order to avoid additional stresses.

Geometric Range Requirements and Design Constraints

The optical arm of the signal beam (the distance from the centre of the mirror segment and the camera) will be approximately 3.5 m for θ_x segment rotations, and about 1 m for θ_y segment rotations. This means that small angular deviations in the mirror segment positions will result in relatively large movements across the active surface of the camera, especially for θ_x segment rotations where the optical arm is large.

The explanation for this is as follows. Assuming figure 4.4 with a camera placed perpendicular to the exit beam, with its YZ plane in line with the local YZ plane of

the mirror axis, a reduction in $\theta_{c'}$ causes a change in beam position on the camera for dy only (see figure 4.12). Then, to a first approximation, the relationship between a

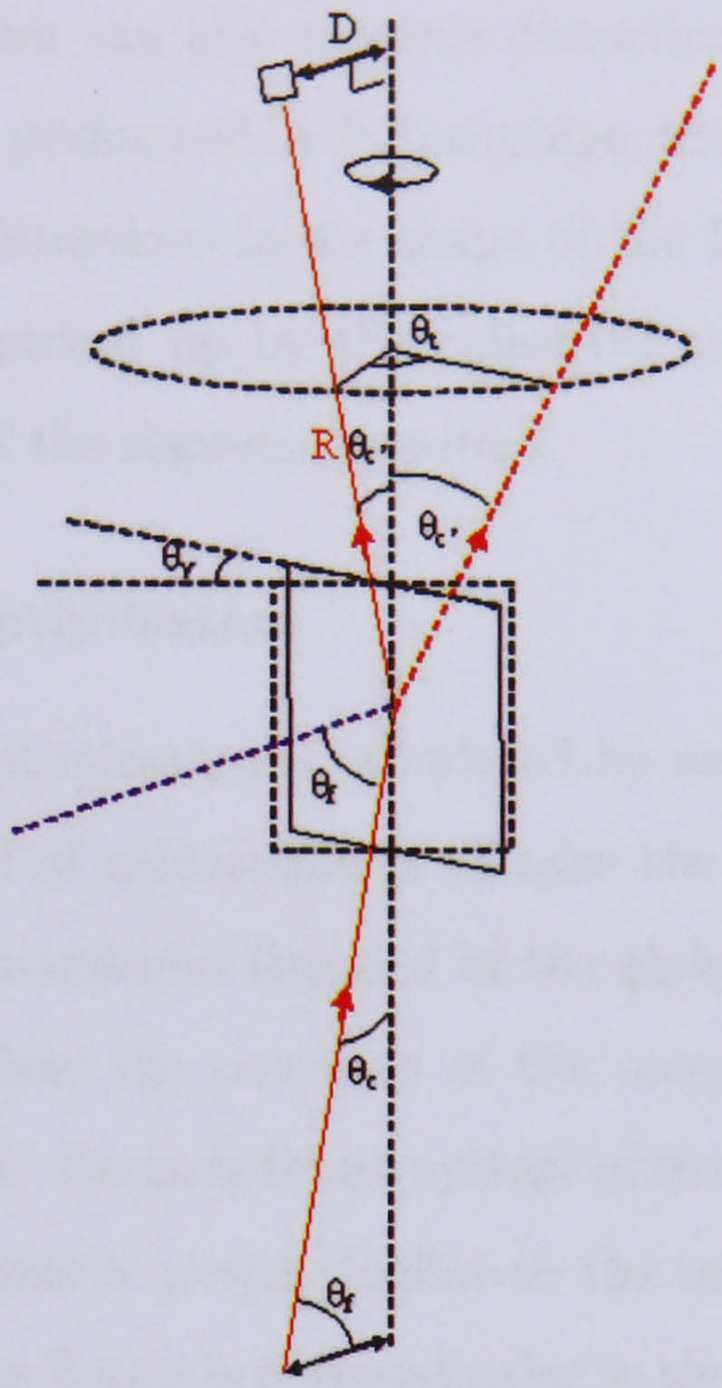

Figure 4.12: Camera placement in Y Rotation.

θ_y segment rotation and the resulting dx movement across the active surface of the camera is therefore:

$$dx = D \tan \theta_t \tag{4.2}$$

where $\theta_t = 2\theta_y$, and $D = R \sin \theta_{c'}$. Similarly for a given θ_x segment rotation, the dy movement across the active surface of the camera will be:

$$dy = Rtan(2\Delta\theta_x). \tag{4.3}$$

where R is the beam length between the mirror segment and the camera, and $\Delta\theta_x$ is the X rotation misalignment of the mirror segment.

Distortion of the RICH2 Super Structure in a Magnetic Field

In addition to monitoring the positions of certain key mirror segments, the laser alignment monitoring system can also monitor distortions in the super structure of RICH2. According to work performed by P. Loveridge, the magnetic field of the dipole magnet will cause minor distortions in the shape of the RICH2 super structure [56]. These distortions can be picked up by the collective analysis of movement in the reference beam positions of the segment monitors.

Component Position Optimisation

The component position optimisation is calculated by an algorithm discussed in the next chapter. The method of calculation is to take the local coordinate system of the mirror segment to be monitored (instead of the global coordinate system of the RICH detector) and calculate the positions of the components needed to monitor that segment with respect to the coordinate system of the segment itself. In the local coordinate system, the Z axis is perpendicular to the mirror segment, while in the global coordinate system the Z axis is perpendicular to the super structure. The main reasons for taking this approach are, firstly, to make the method of calculation the same for all segments monitored, and secondly to make the analysis of mirror movements less complicated, by having a generic solution that remains in the coordinate system of the monitored segment. Thus, the first step is to pick a mirror segment and the second step is to define a point at a distance along the local Z axis of the mirror segment at which to place the focusing unit. However, when using the local coordinate system, one has to take care that the reflected beam does not force the placement of the camera to be within the detector acceptance (figure 4.13).

Thus, the point at the defined distance along the z plane of the segment for the placement of the focusing unit must be with respect to the XZ plane of the global coordinate system of the RICH detector (figure 4.14).

Having defined the Hxz distance (figure 4.15), the placement of the camera will be at the XZ position of this point in the global coordinate system but will have a negative Y position.

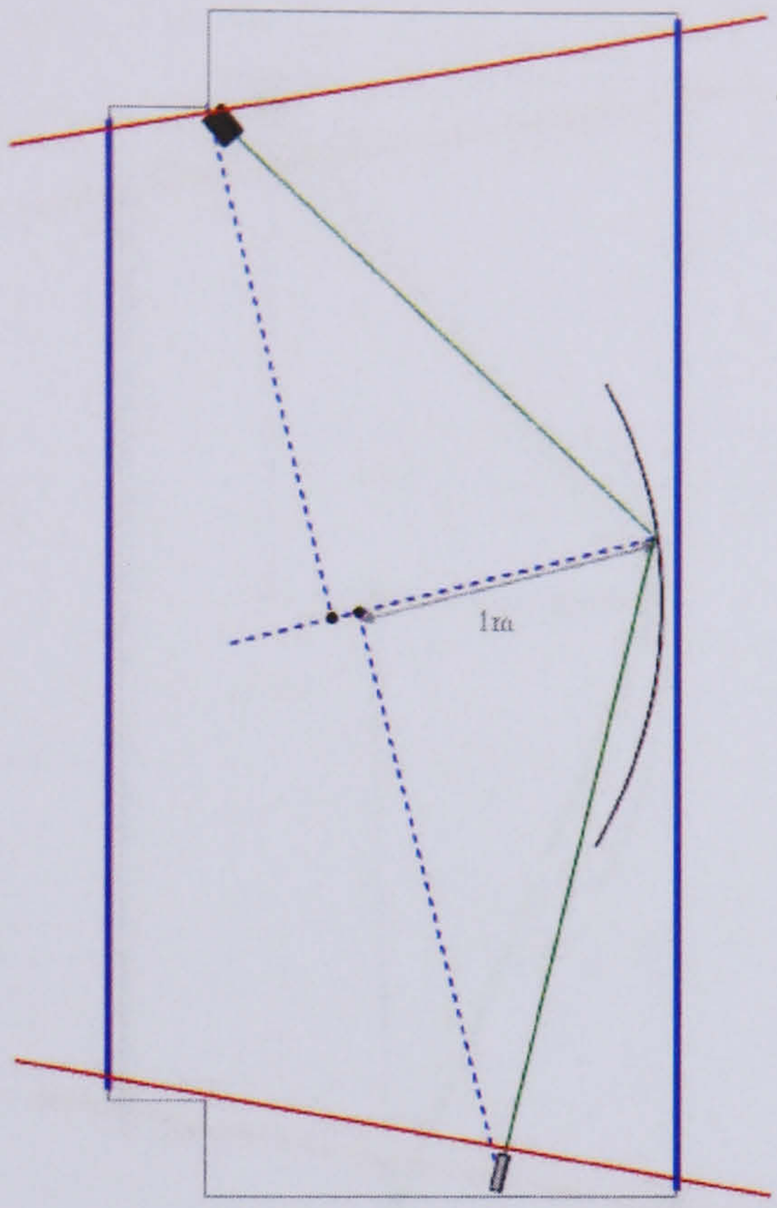

Figure 4.13: Alignment monitoring components are within the red lines of the detector acceptance, by only considering the local coordinate system.

4.2.5 Fibre Optics

The method for supplying a monochromatic coherent light source to each of the segment monitors is to use fibre optics that supply this light from a laser that is 100m away in the control room. The main advantage of supplying laser light in this way as opposed to using small laser diodes within the gas volume of the RICH detector itself is that, in the event of failure, a laser in the control room can be quickly and safely replaced; whereas individual laser diodes placed in the gas volume will have to remain in a state of failure until the LHCb detector is scheduled for maintenance - and this could be a considerable amount of time!

There are a number of ways in which light from the laser in the control room can be delivered to the focusing units in RICH2. One way is to use fibre couplers to split one fibre into two, two into four, four into 8 and so on. However, the efficiency of each coupler is around only 40-50% and they are also very expensive. Another way is to place a fibre bundle in front of the laser and transmit the light to individual focusing

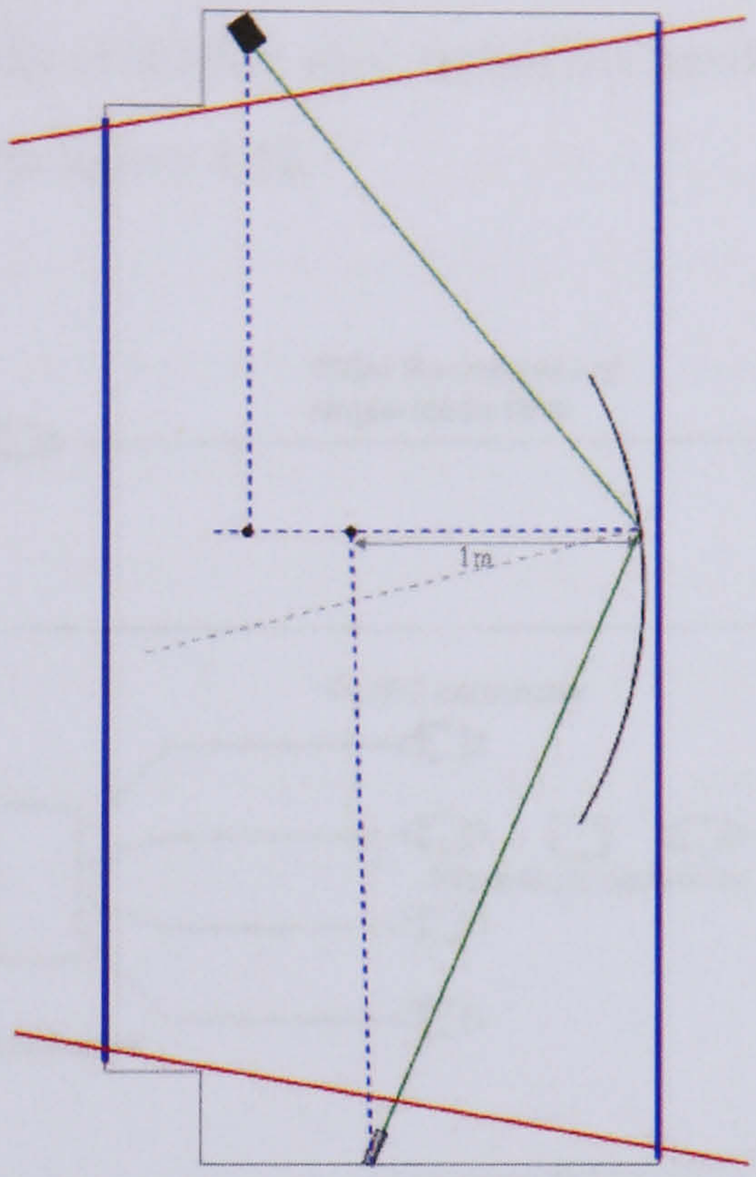

Figure 4.14: Alignment monitoring components are outside the red lines of the detector acceptance, when taking into account the distances in the global coordinate system.

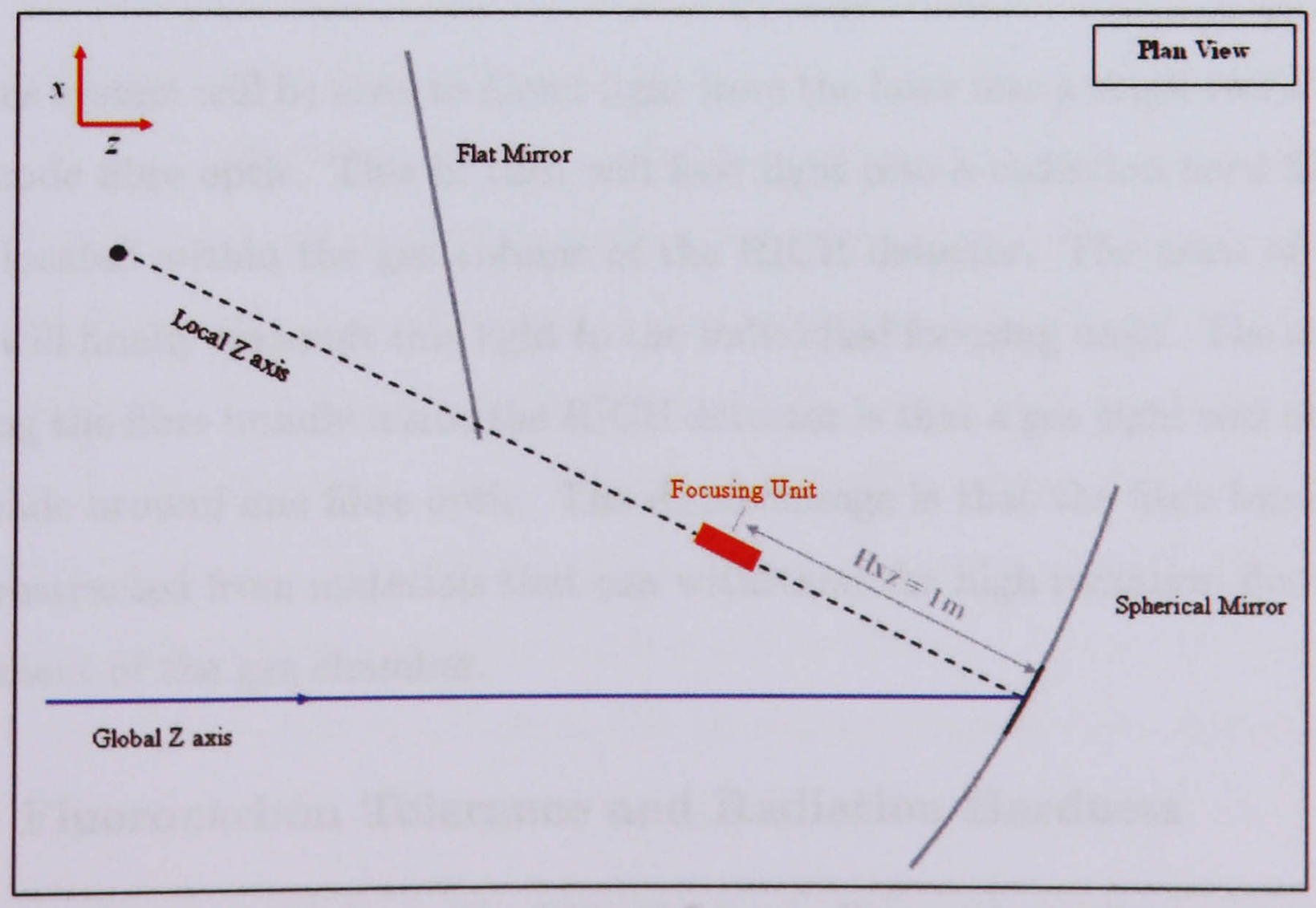

Figure 4.15: Plan view.

units through individual fibres. These fibres will need to be radiation hard to survive the harsh environment of the detector, and radiation hard fibres are expensive. So a final solution is described in figure 4.16.

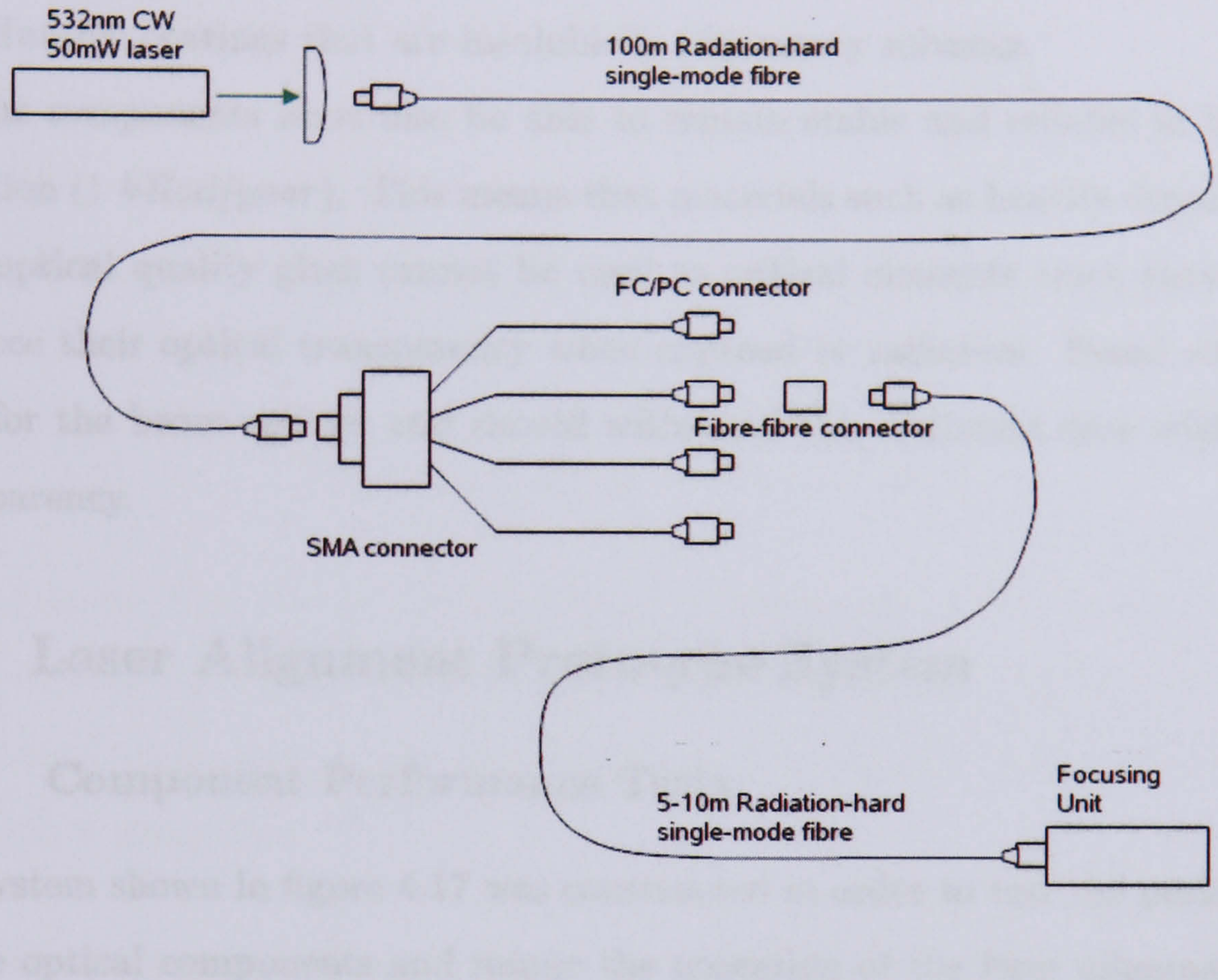

Figure 4.16: Optical Fibre Arrangement.

A lens system will be used to direct light from the laser into a single radiation hard single-mode fibre optic. This in turn will feed light into a radiation hard fibre optic bundle located within the gas volume of the RICH detector. The arms of the fibre bundle will finally transmit this light to the individual focusing units. The advantage of placing the fibre bundle inside the RICH detector is that a gas tight seal only needs to be made around one fibre optic. The disadvantage is that the fibre bundle needs to be constructed from materials that can withstand the high radiation fluorocarbon environment of the gas chamber.

4.2.6 Fluorocarbon Tolerance and Radiation Hardness

All of the components to be used within the laser alignment monitoring system must be able to withstand a pure fluorocarbon environment and have to be chosen carefully.

The cameras that will be used in the final system (see section 4.7) are inside an aluminium casing resistant to fluorocarbon and contain a glass window. The optic fibres will have PVDF (polyvinylidene fluoride), fluorine based plastic jackets compatible with a fluorocarbon environment. The mirrors and beam splitters (see section 4.3.1) have durable coatings that are insoluble in laboratory solvents.

The components must also be able to remain stable and reliable in high energy radiation (1 $kRad/year$). This means that materials such as heavily doped silica and BK7 optical quality glass cannot be used as optical elements since they go cloudy and lose their optical transparency when exposed to radiation. Fused silica will be used for the beam splitter and should withstand this radiation dose without losing transparency.

4.3 Laser Alignment Prototype System

4.3.1 Component Performance Tests

The system shown in figure 4.17 was constructed in order to test the performance of all the optical components and mimic the operation of the laser alignment system. The system consisted of a NuFern 460HP single mode 532 nm fibre optic (with a core diameter of 3.5 μm ± 0.5 μm and 125 μm cladding) coupled to a 532 nm diode pumped Nd:YAG continuous wave 50 mW laser. The optic fibre is attached to an optical focusing unit that houses a single graded lens that is designed to focus the light at a distance of 10 m. The light is focused onto a series of CVI Y2-1025 thin film coated laser mirrors designed to operate at 45^o attached to an optical bench to achieve the desired lever arm. These have durable coatings designed to be insoluble in laboratory solvents [1]. The beam is read out by a $\frac{1}{2}$" analogue Pulnix CCD camera. Each pixel is $13.5\mu m^2$ and contains an active cell of 8.6 $\mu m \times 8.3\mu m$. The pixels form an active area of 10.15 $mm \times 7.86$ mm with an output image of 768×576 pixels. The tests carried out with the prototype system included checking for ghosting (multiple internal reflections) from the film coated laser mirrors and beam splitter. But the primary concern was the ability of the focusing unit to focus light from a fibre optic down to a diameter of 1mm or less at a distance of 10 metres.

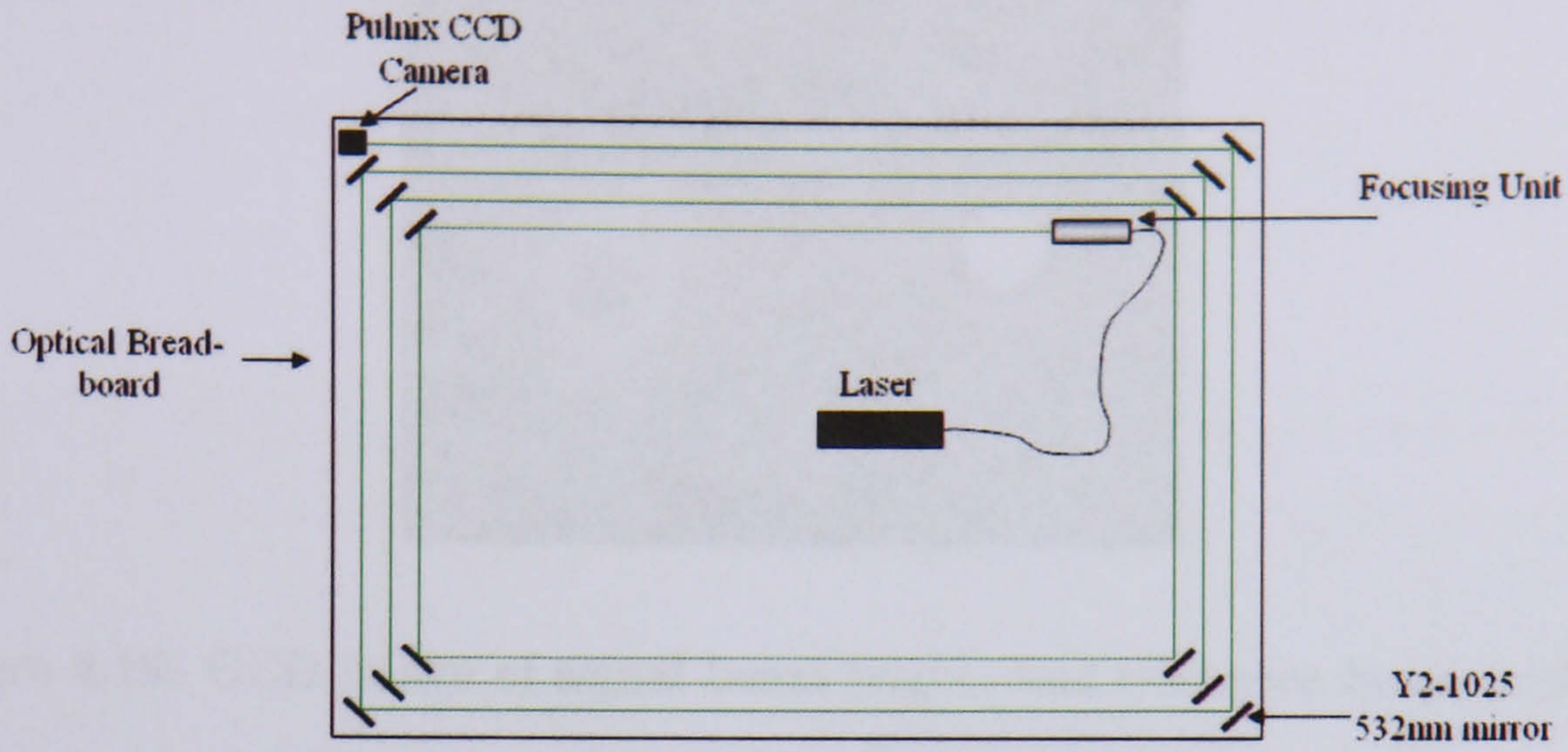

Figure 4.17: Component Test Layout.

The method for testing the convergence performance of the focusing unit was to use mirrors to bounce the transmitted light around the optical bench and monitor the diameter of beam cross-section at various recorded distances along the pathlength of the beam ranging from 5 m to 11 m.

Results/Optical Analysis

The mirrors and beam splitter performed extremely well with no detectable ghosting (figure 4.18) when tested in the setup shown in figure 4.21. Placing the laser mirrors off axis did not result in any detectable ghosting, but their reflective efficiency fell, and a dot on the back wall could be clearly seen with the naked eye as light began to be transmitted through the mirror substrate when the angle differed significantly from 45^o.

The results of the focusing unit performance tests were, however, rather surprising. The initial convergence of the beam from 0 m to 7.5 m suggests that the beam will carry on converging to a point at 10 m (by extrapolating the trend towards a diameter of $0\mu m$). However, at around 7.5 m the beam starts to increase in diameter (see figure 4.19).

A selection of three images shown in figure 4.20, taken at pathlengths of 5 m, 7.5 m and 10 m from the focusing unit give good insight into the reasons for this.

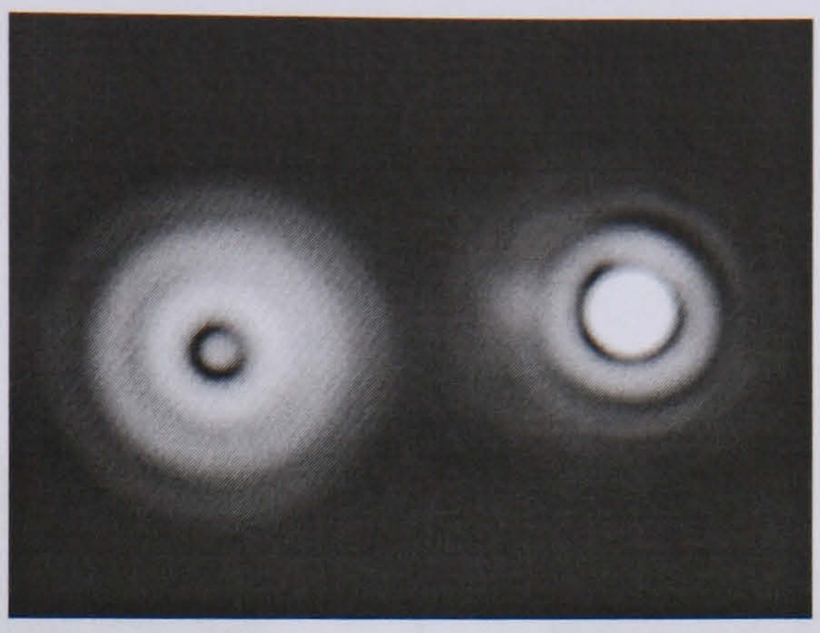

Figure 4.18: CCD image of signal beam (right) and reference beam (right).

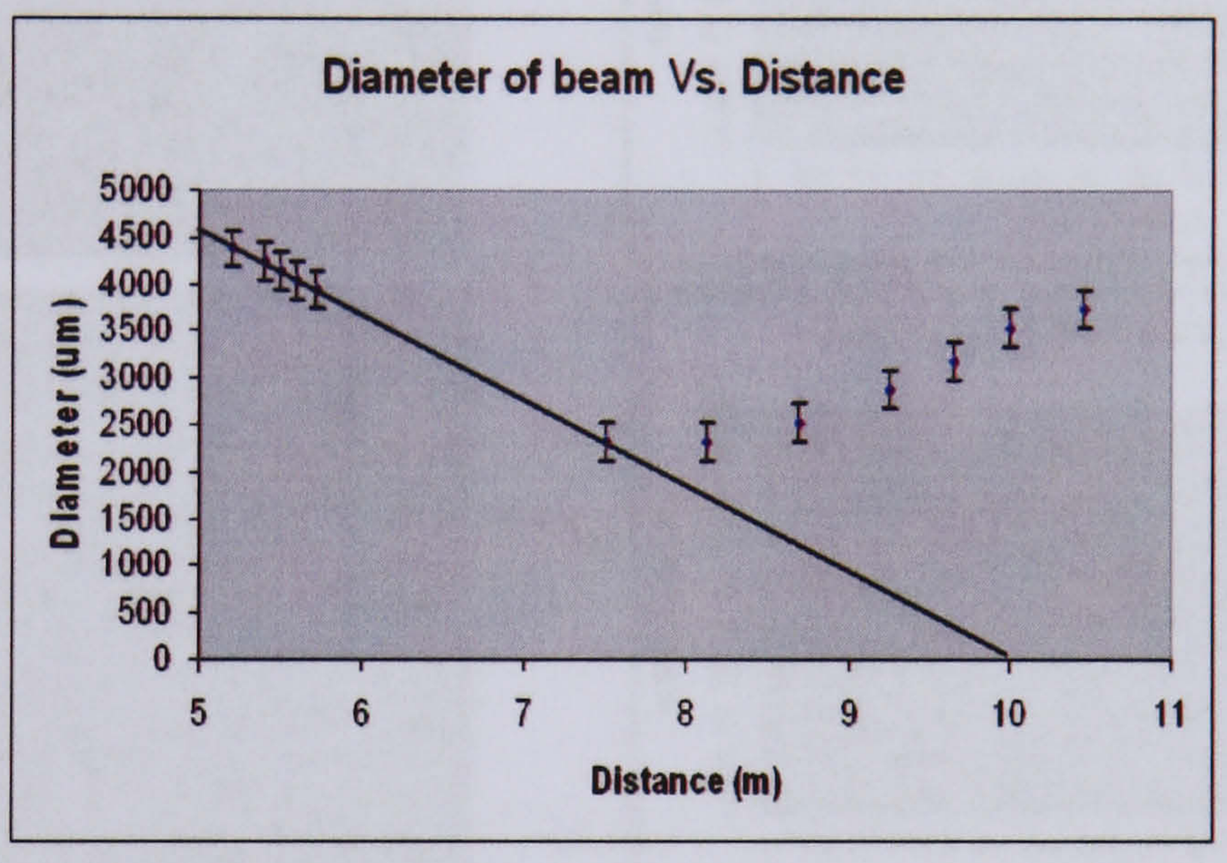

Figure 4.19: Beam convergence over 10.5 m.

High order transverse laser modes can be seen at the shortest recorded pathlength of 5 m. These high order modes can penetrate into the cladding region and also propagate as cladding modes. This produces a complex pattern at the output of the fibre. It is expected that as the fibre length is increased, the cladding modes are reduced. At a distance of 7.5 m the image has changed and is possibly the result of interference between transverse laser modes and the initial evidence for a Fresnel diffraction pattern (most likely originating from the 3.5 μm core of the single mode fibre optic acting as an aperture). At 10 m, any trace of transverse laser modes seems to have been replaced by a pure Fresnel diffraction pattern, with the outer diameter of the final ring extending beyond the diameter of image taken at 7.5 m.

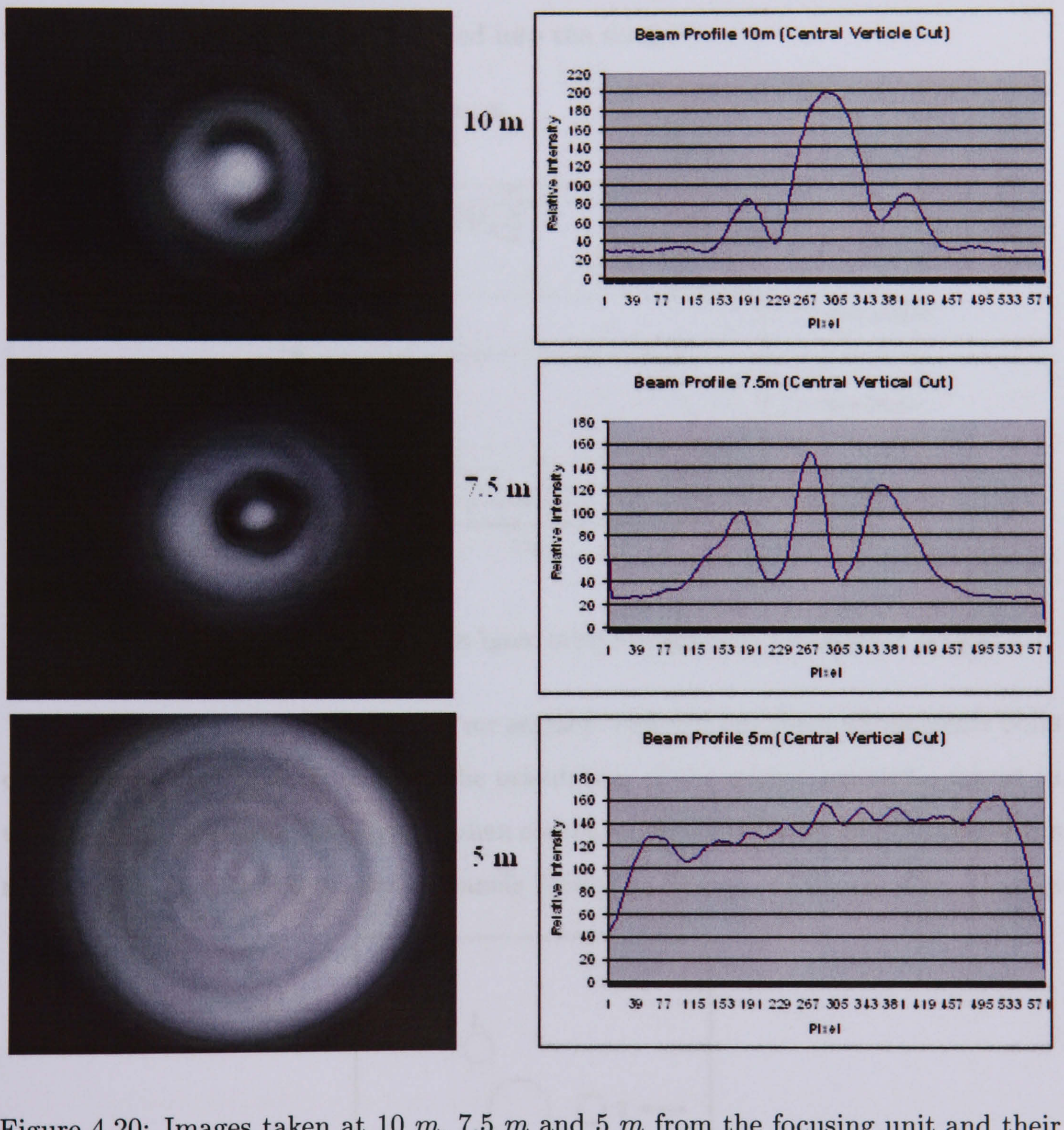

Figure 4.20: Images taken at 10 m, 7.5 m and 5 m from the focusing unit and their profiles.

4.3.2 Prototype Layout

The main objective of the prototype system is to prove the ability of the laser mirror alignment system design to detect mirror segment movements of 0.1 *mrads* or less. The prototype system has been set up as shown in figure 4.21 with one of the RICH2 mirror segment supports also included into the setup.

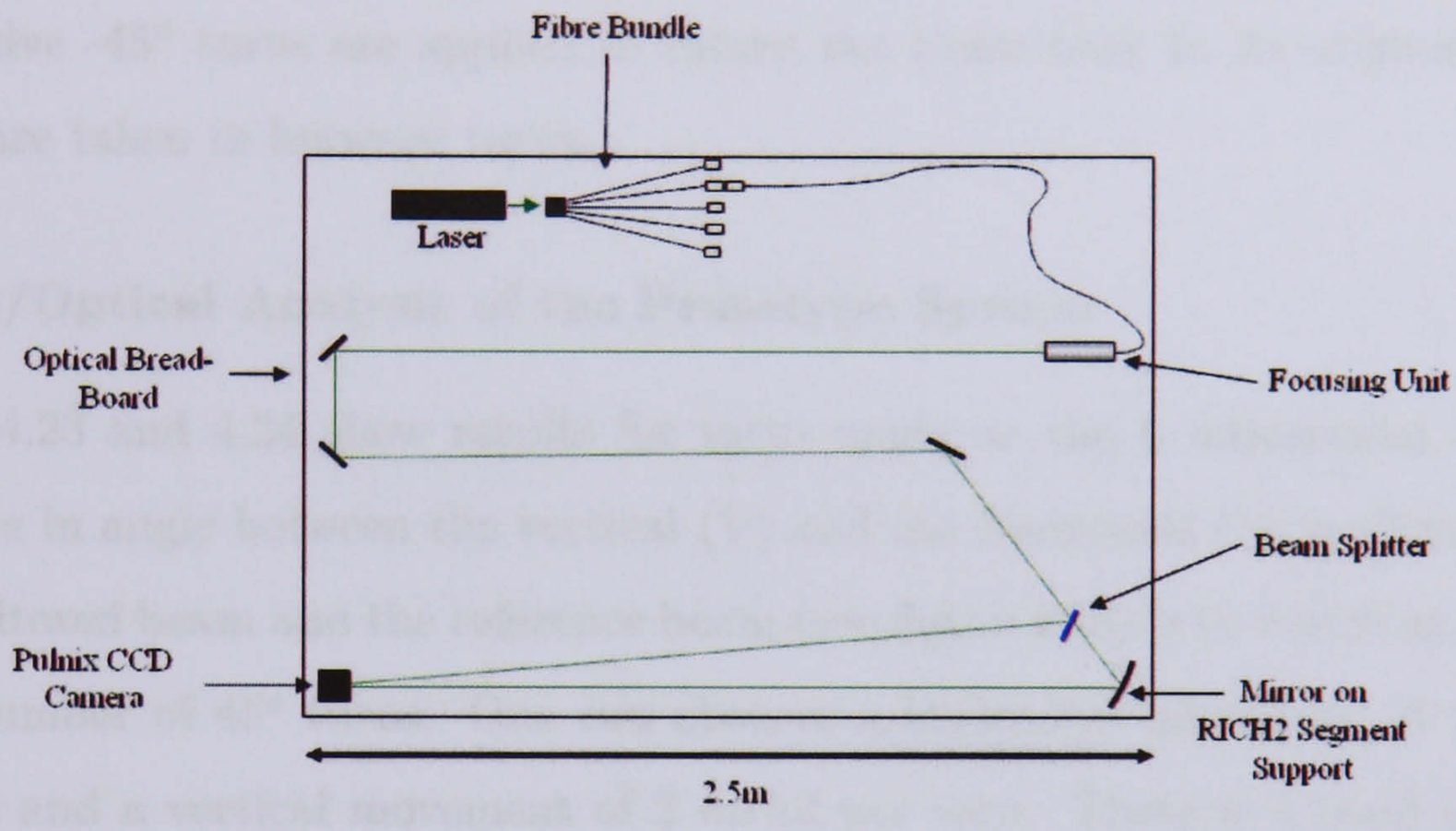

Figure 4.21: The prototype of the laser mirror alignment monitoring system.

As previously mentioned, the mirror segment support has three adjustments bolts on the back labelled L, R and T. The orientation of the mirror segment support in the prototype system differs by 90^o when compared to the orientation of the supports mounted on the RICH2 sandwich panels (compare figures 4.22 and 4.8). This is

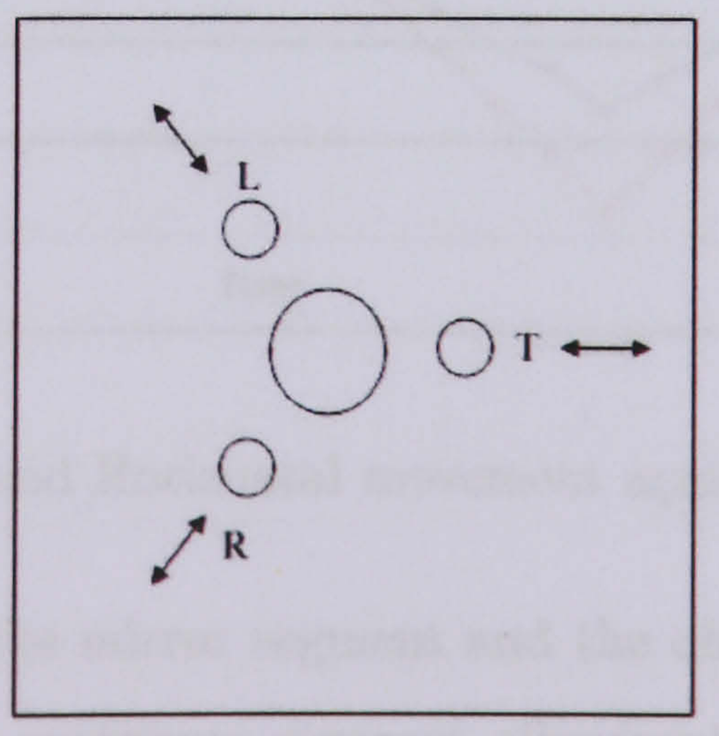

Figure 4.22: Rotated adjustment stage in the prototype system.

because the aluminium block on which the mirror segment support is mounted in the prototype system is physically too high if not properly orientated. Therefore, it has been rotated by 90^o to overcome this problem.

To test the sensitivity and range of the prototype system, each adjustment bolt on the back of the mirror segment support is adjusted by making consecutive 45^o turns until the beam starts to move off the edge of the CCD camera, at which point consecutive -45^o turns are applied to return the beam back to its original position. Images are taken in between turns.

Results/Optical Analysis of the Prototype System

Figures 4.23 and 4.24 show results for turns made on the L adjustment bolt. The difference in angle between the vertical (V) and the horizontal (H) position between the monitored beam and the reference beam (see figure 4.18) is recorded as a function of the number of 45^o turns. One can observe a horizontal movement of 1.33 $mrad$ per turn and a vertical movement of 2 $mrad$ per turn. There is a good correlation

Figure 4.23: Vertical and Horizontal movement against number of turns.

between the movement of the mirror segment and the difference between the signal and reference beam of the prototype segment alignment monitor (figure 4.23). A small amount of hysteresis can be seen (figure 4.24), which could possibly be due to

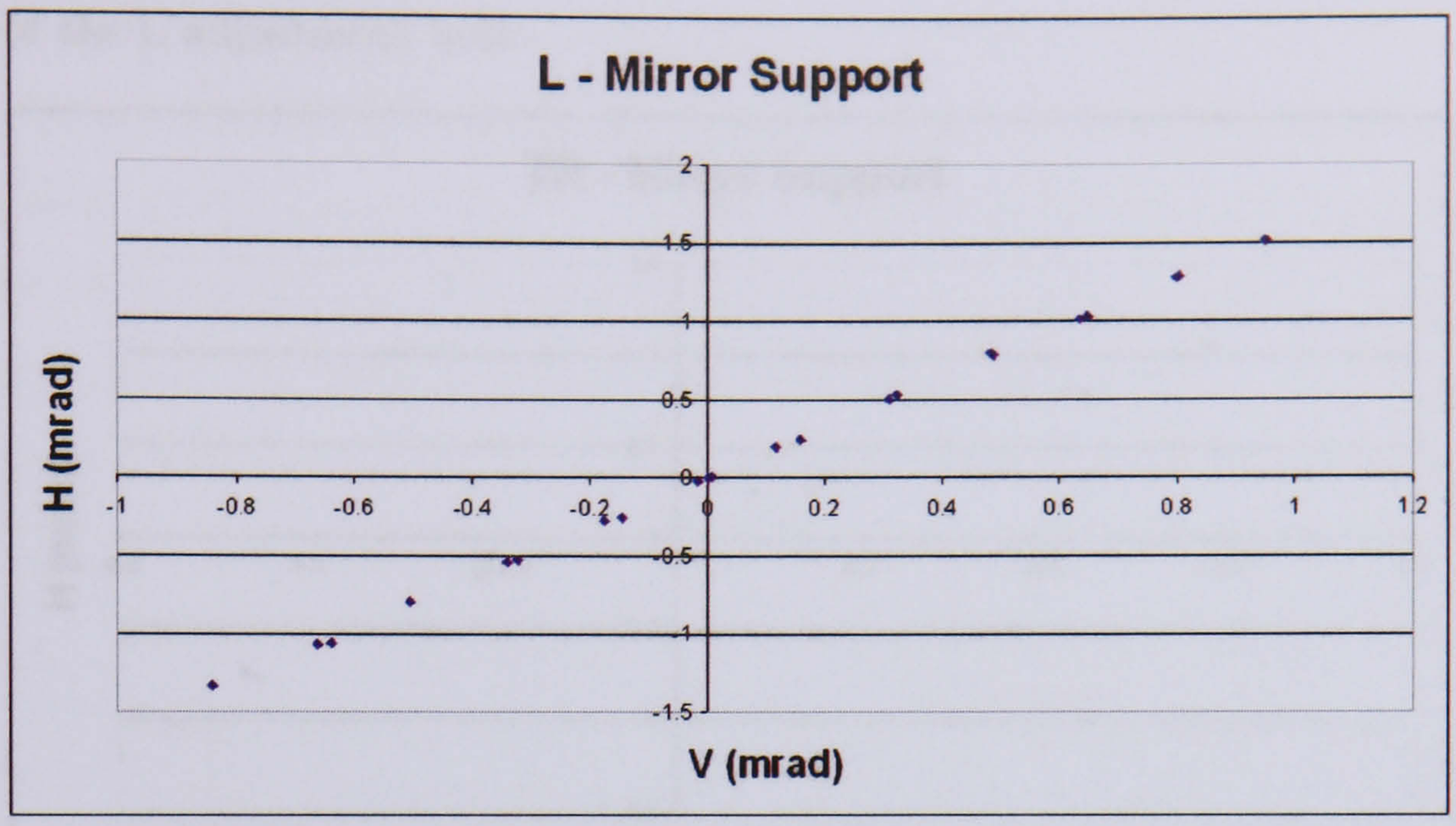

Figure 4.24: L Adjustment hysteresis.

small differences in the 45^o rotations of the L adjustment bolt. The centre of the beam was determined by visually searching for the maximum.

The movement plane of the L adjustment bolt, can also be produced by making equal movements of both the T and R adjustment bolts. Figure 4.25 is a graph showing the relationship of equal 45^o rotations. The ratio of horizontal movement to vertical movement is almost identical, which is expected. There is an increase in

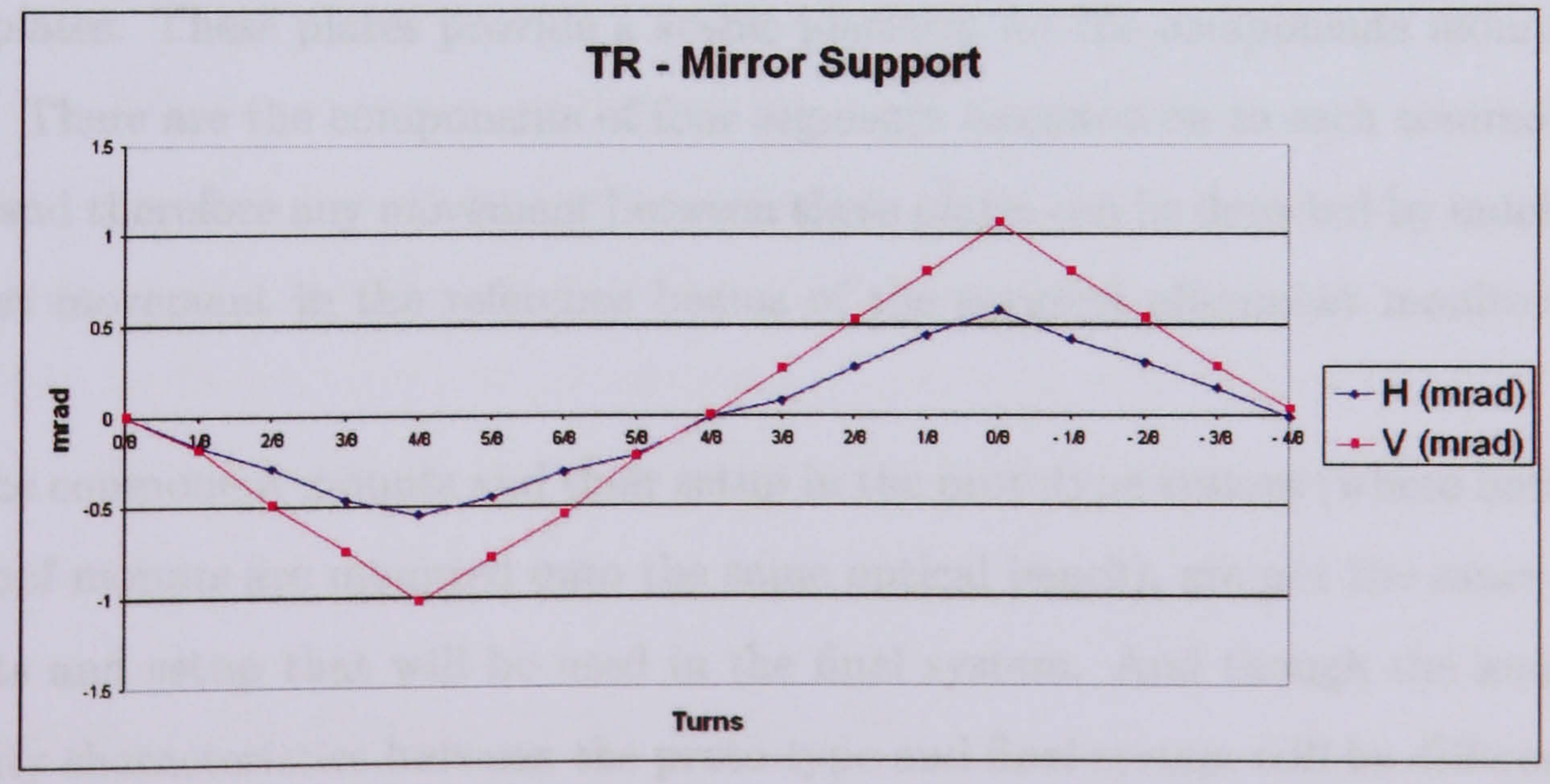

Figure 4.25: vertical and Horizontal movement against turns.

hysteresis (figure 4.26), with the adjustment of two bolts instead of one. However, the correlation between horizontal and vertical movements agrees very well with the

result of the L adjustment bolt.

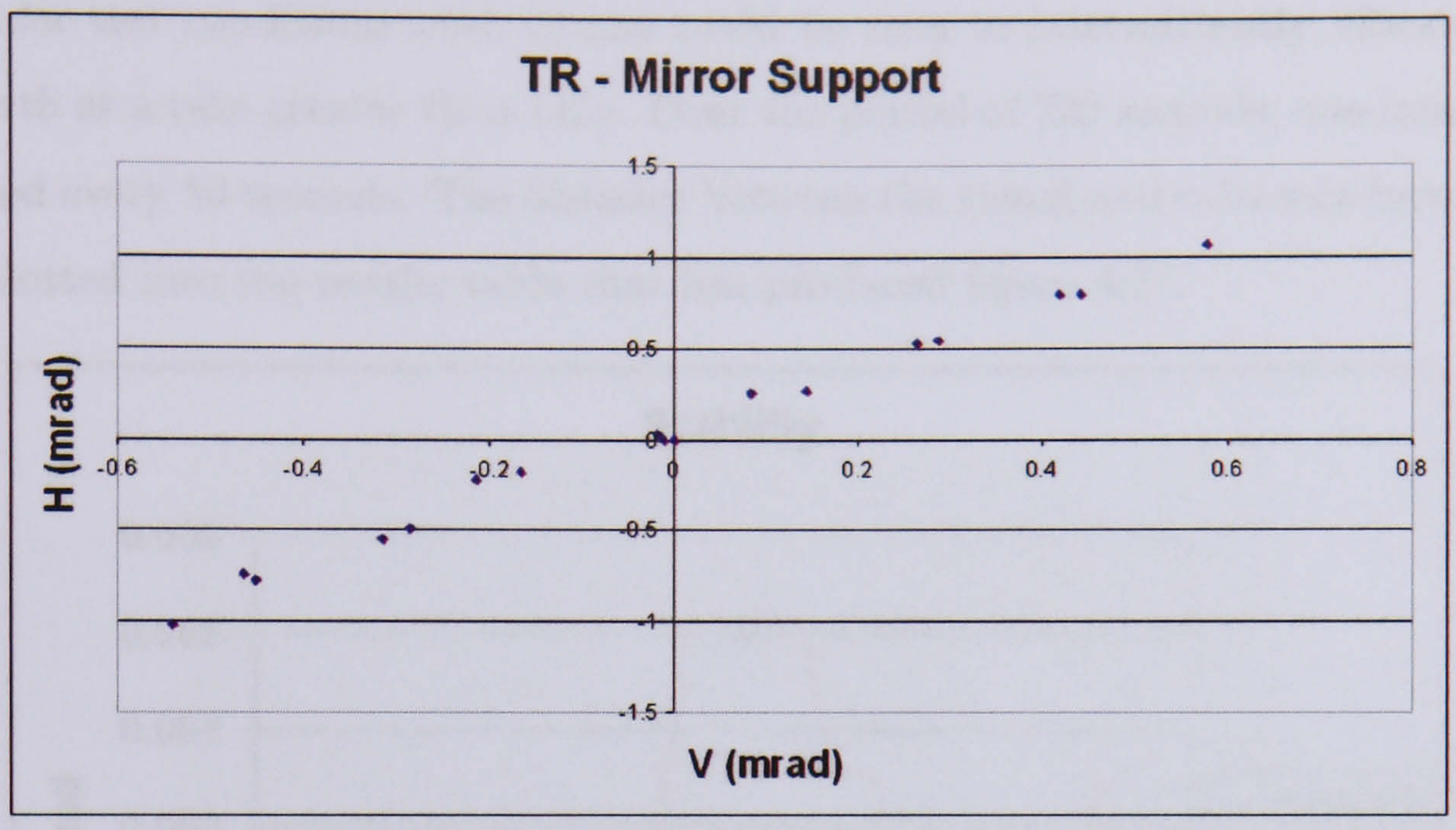

Figure 4.26: TR Adjustment hysteresis.

The stability of the segment alignment monitor is very important. This can be subsectioned into two areas: long term stability, and short term stability. The long term stability of a segment alignment monitor is dictated by the long term stability of the mounts on which the monitoring components are located. In the design of the laser alignment monitoring system, all of the components are mounted onto common base plates. These plates provide a stable platform for the components mounted on them. There are the components of four segments mounted on to each common base plate and therefore any movement between these plates can be detected by monitoring the net movement in the reference beams of the segment alignment monitors they hold.

The component mounts and their setup in the prototype system (where both floor and roof mounts are mounted onto the same optical bench), are not the same as the mounts and setup that will be used in the final system. And though the long-term stability characteristics between the proto-type and final system will be different, the short-term stability can be assumed to be similar. This is because both systems will be subject to vibration and optical anomalies that can cause beam movements. It is therefore important to show that the segment alignment monitors have short term stability (i.e. that the difference between signal and reference beam positions on the

CCD remains stable under test conditions).

Under test conditions both beams could be seen to intermittently vibrate back and forth at a rate greater than $1Hz$. Over the period of 720 seconds, one image was recorded every 30 seconds. The distance between the signal and reference beams was then plotted into the results table that has produced figure 4.27.

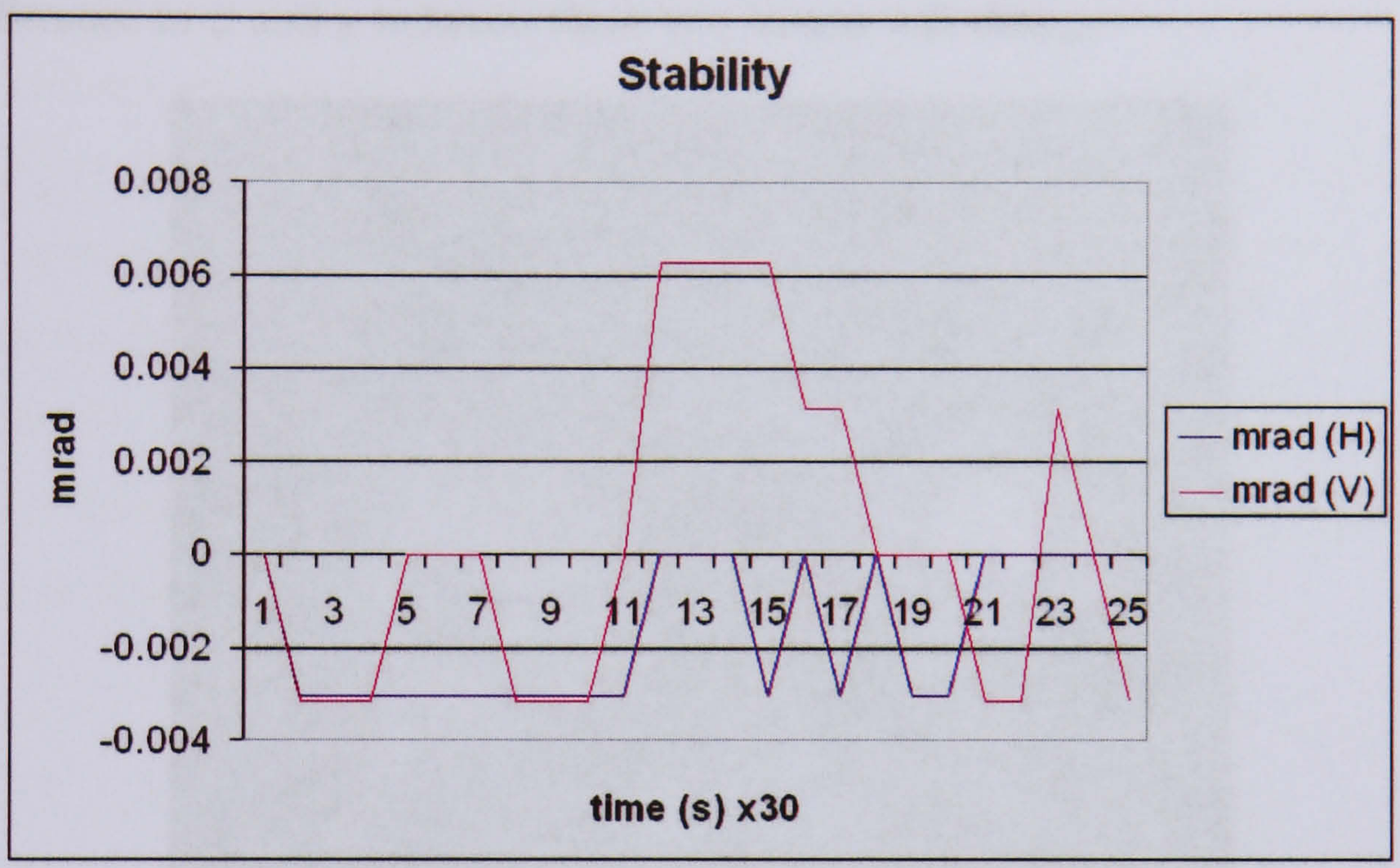

Figure 4.27: The stability of the prototype segment alignment monitor over a period of 720 seconds.

The stability result shows that the movement between the two beams was coherent and that the total movement between the two is relatively small at only 4 pixels. The short term instability results of the prototype segment alignment monitor are negligible, as they contribute an uncertainty in the segment alignment of less than 7 $\mu rads$. The source of the movement could be due to vibration and/or interference from transverse laser modes.

Recovering a Misaligned Mirror Segment

The method for finding the distance the beam has moved across the active surface of the camera for any given change in mirror rotation has already been discussed. This section deals with the reverse order (i.e. finding out the change in mirror rotations for given distances that the beam has moved across the active surface of the camera).

Before any calculations can be made, the positions of the signal and reference beams must first be extracted from the images retrieved from the camera. This process is described in the following section under Image Analysis Software.

Once the initial beam spot positions of the signal and reference beams are known, the difference between them can be recorded (figure 4.28). As the signal beam moves, the difference in x and y between these two beams will change.

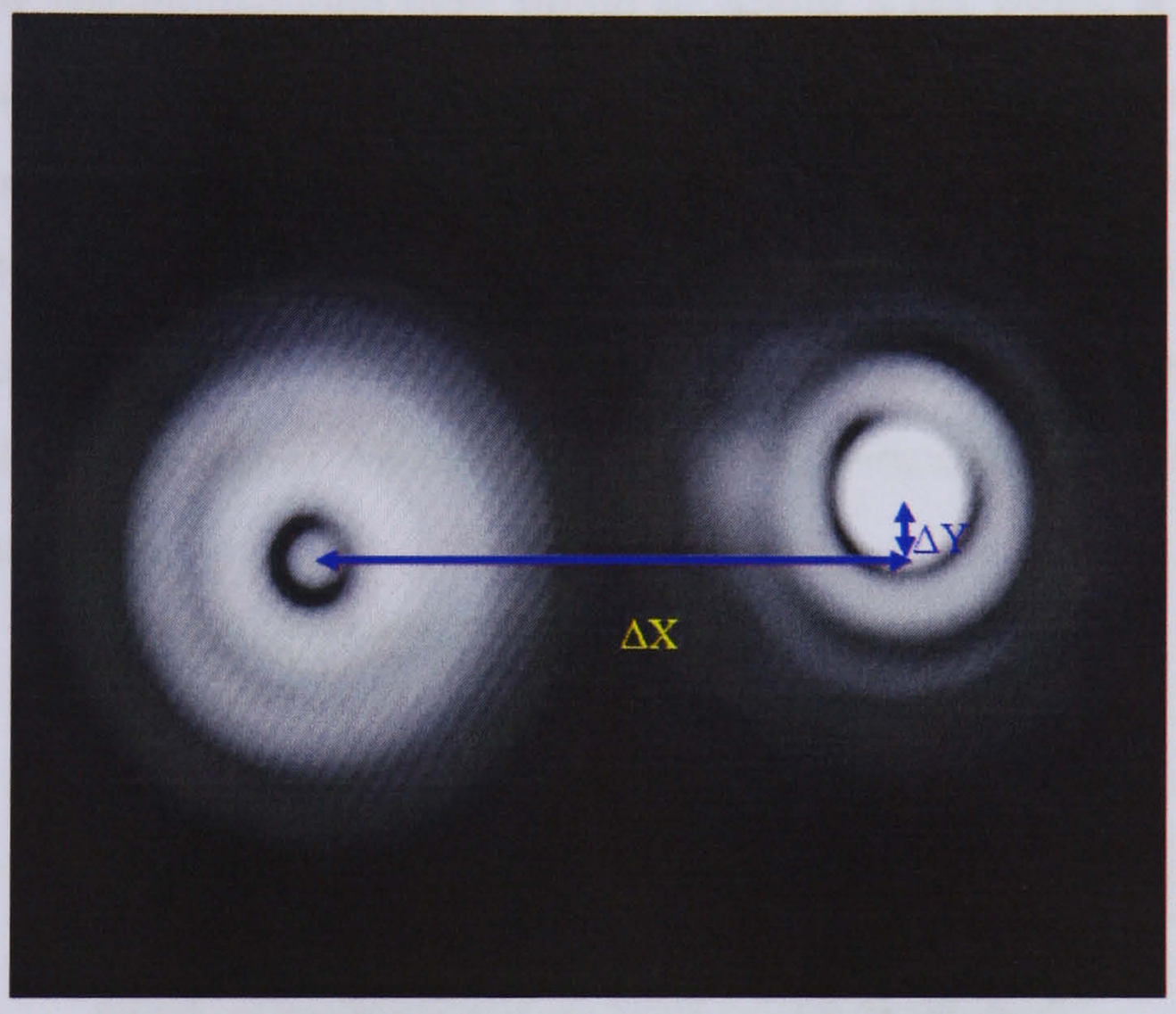

Figure 4.28: Measurement of the difference between x and y of the signal and reference beams.

Multi-mode Fibre Tests

The large beam spot of the prototype segment alignment monitor is believed to be largely due to diffraction caused by the small 3.5 μm core diameter of the single mode fibre and transverse modes from the laser. To test the theory the Fresnel diffraction pattern can be reduced in size by increasing the size of the end of the optical fibre. Therefore a 200 μm multi-mode fibre has been tested to check for a Fresnel diffraction pattern. The tests have been carried out with the setup shown in figure 4.17 but with a Lumenera LE-175 CMOS APS camera (described in section 4.7) instead of

the Pulnix PE2005 CCD camera. According to the optics equation

$$m = \frac{-s'}{s} \tag{4.4}$$

where s is the distance between the object and the lens and s' is the distance between the image and lens. The magnification of the end of the 200 μm multi-mode fibre will be about 250 when s is 0.04 m and s' is -10 m. Therefore, at 10 m the spot size supplied by the multi-mode fibre would be about 5 cm which is far larger than the CMOS active surface of the camera. Thus, in order to fit the image on the active surface and test the beam characteristics of the multi-mode fibre the distance between the fibre and the lens needs to be increased such that the object is focused at a distance of 0.5 m. The magnification at 0.5 m is about 12.5 and therefore the image is expected to be about 2.5 mm. An example beam spot image at this distance is given in figure 4.29.

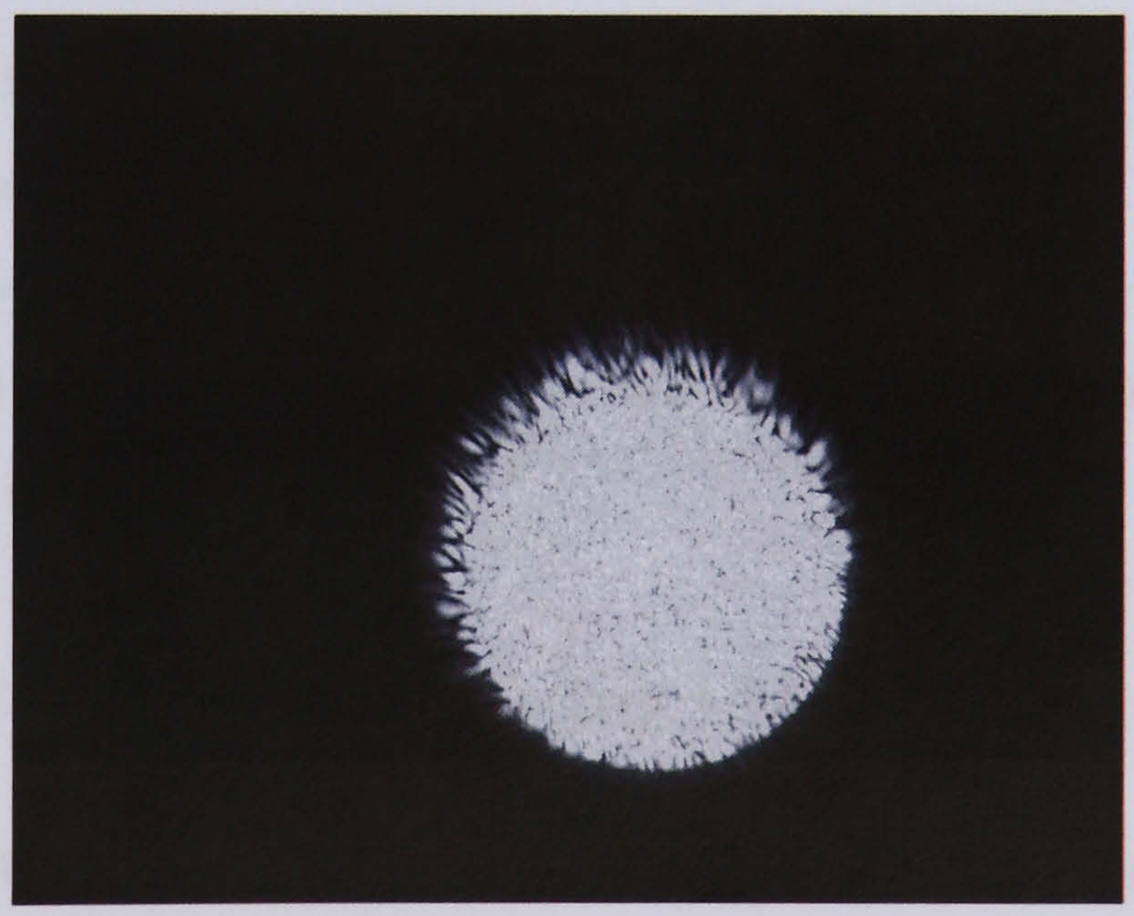

Figure 4.29: A beam spot image of a 200 μm multi-mode fibre at a focal point of 0.5 m.

There is no evidence of a diffraction pattern forming around the image. This suggests further evidence that the rings surrounding the images at the focal point of 10 m with the single-mode fibre are Fresnel diffraction rings. A plot of the beam diameter against the distance from the CMOS camera is given in figure 4.30.

The smallest beam diameter is at 0.5 m. The diameter of the beam spot image at this distance shown in figure 4.29 spans about 435 pixels of the Lumenera LE-175

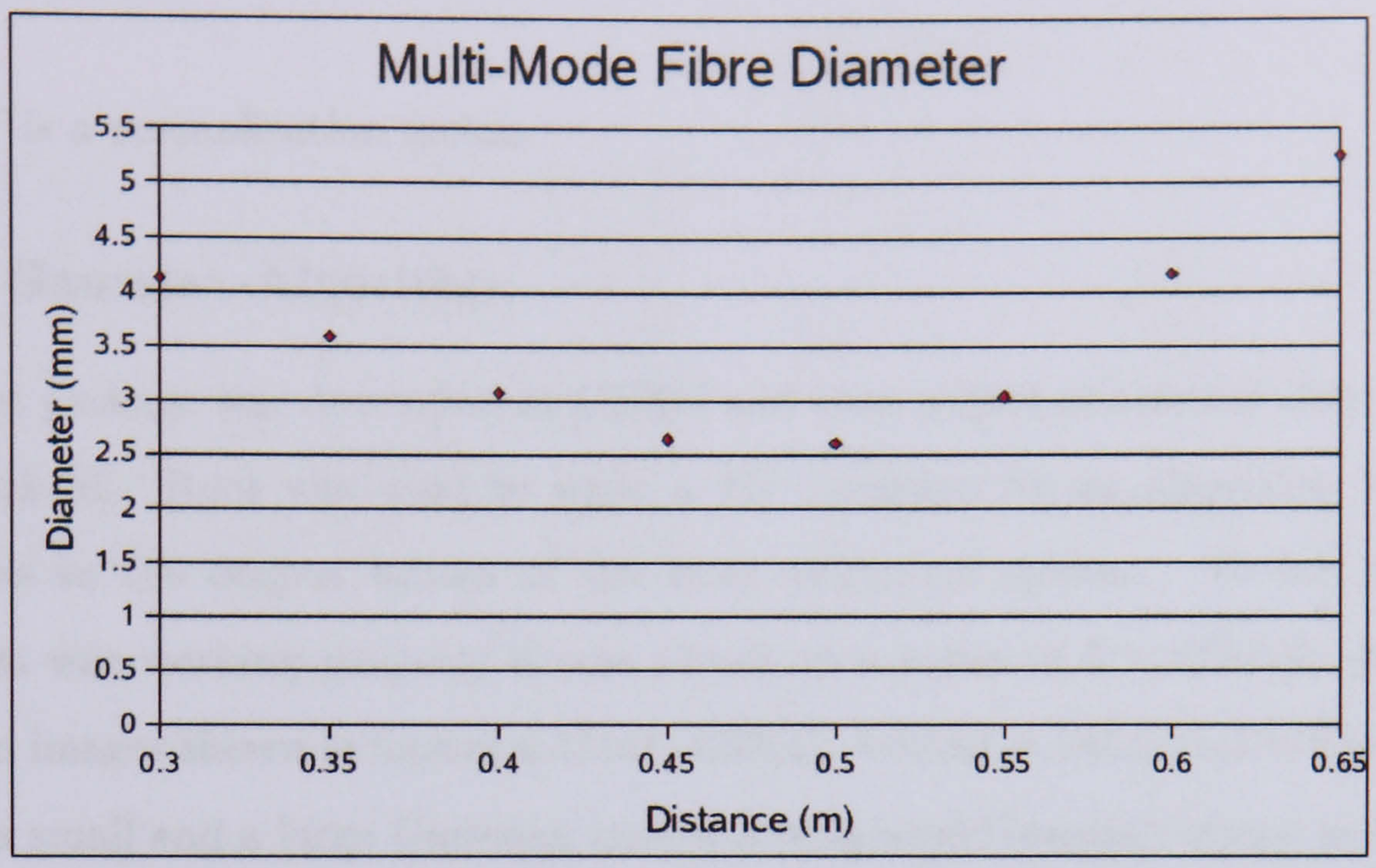

Figure 4.30: The focused 200 μm multi-mode fibre beam spot diameter over a distance of 0.3 m to 0.65 m.

CMOS camera with pixel dimensions of 6 μm^2, this equates to 2.6 mm, which is close to the expected magnified value of 2.5 mm.

Thus, it has been shown that a multi-mode fibre with large aperture (i.e. 200 μm) cannot be focused on a 1/2" APS, so we will use single-mode fibres for the laser alignment monitoring system.

4.4 Beam Spot Tracking using the Gaussian Fit Method

The requirement of finding the difference between the beam spot centres produced by the laser mirror alignment system means that an accurate automated measurement method must be utilised. The Gaussian fit method is an established method of fitting to a beam that has a Gaussian profile. The equation of the elliptical 2D Gaussian function for the two dimensional variates x and y, means μ_x and μ_y and variances σ_x^2 and σ_y^2 is

$$f(x,y) = Ne^{-\left[\frac{(x-\mu_x)^2}{2\sigma_x^2}+\frac{(y-\mu_y)^2}{2\sigma_y^2}\right]}, \tag{4.5}$$

where N is a normalisation factor.

4.4.1 Gaussian Algorithm

The Root package was developed at CERN and is an object-orientated data analysis framework [6]. Root was used to write a 2D Gaussian fitting algorithm to fit 2D Gaussians to the output beams of the laser alignment system. To test that the algorithm was working properly it was tested on a series of 5 artificially generated Gaussian images shown in figures 4.31(a), 4.32(a). 4.33(a), 4.34(a) and 4.35(a), which include a small and a large Gaussian image, a truncated Gaussian image and a small and large Gaussian image on the edge of the field of view.

With the exception of the edge and off-edge tests, the results shown are for the fit algorithm output when its start location was at the centre the image. The edge and off-edge tests failed to converge unless the Root algorithm was given an initial starting place within a few pixels of the centre of the beam.

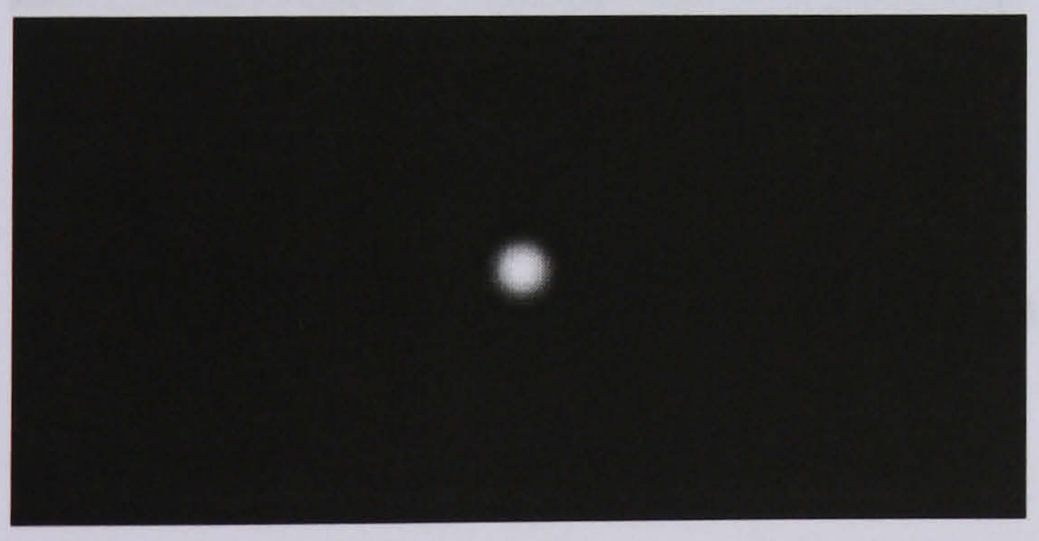

(a) A small simulated Gaussian image.

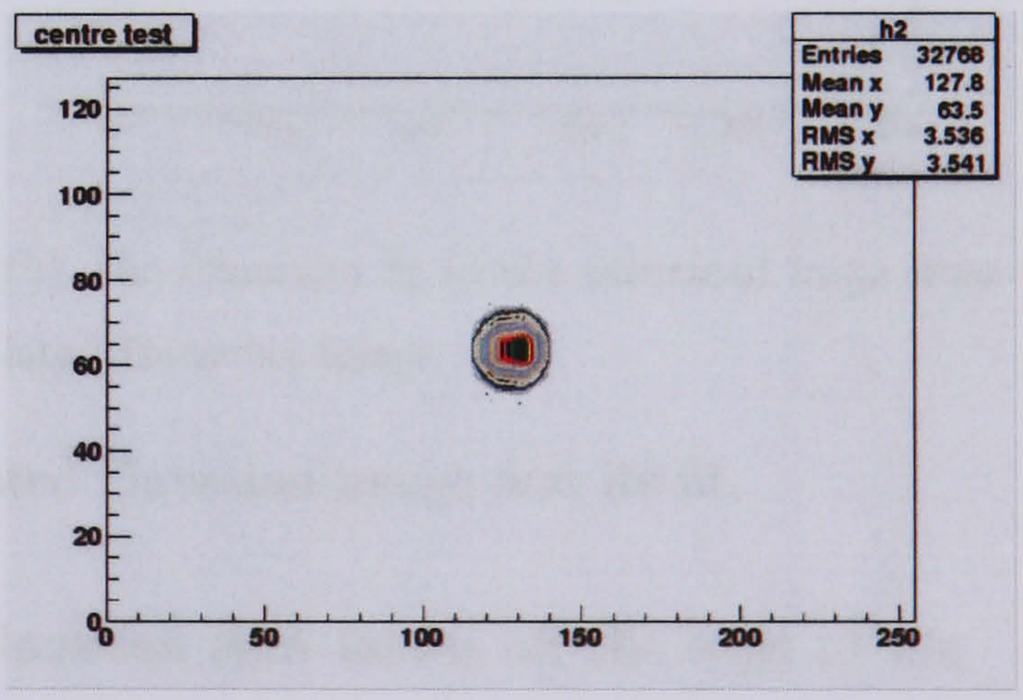

(b) The Gaussian fit to the small simulated Gaussian image.

Figure 4.31: Small simulated Gaussian image and its fit.

The results in figures 4.31(b), 4.32(b) and 4.33(b) and table 4.1 show that the algorithm works well at finding the centre of the Gaussian profile under normal conditions. However, the table of results also shows that when the beam is on the edge of the image, even though a start location for the fit is given that is directly on the centre of the spot, the Gaussian fit does not correctly find the centre (see figure 4.34(b)).

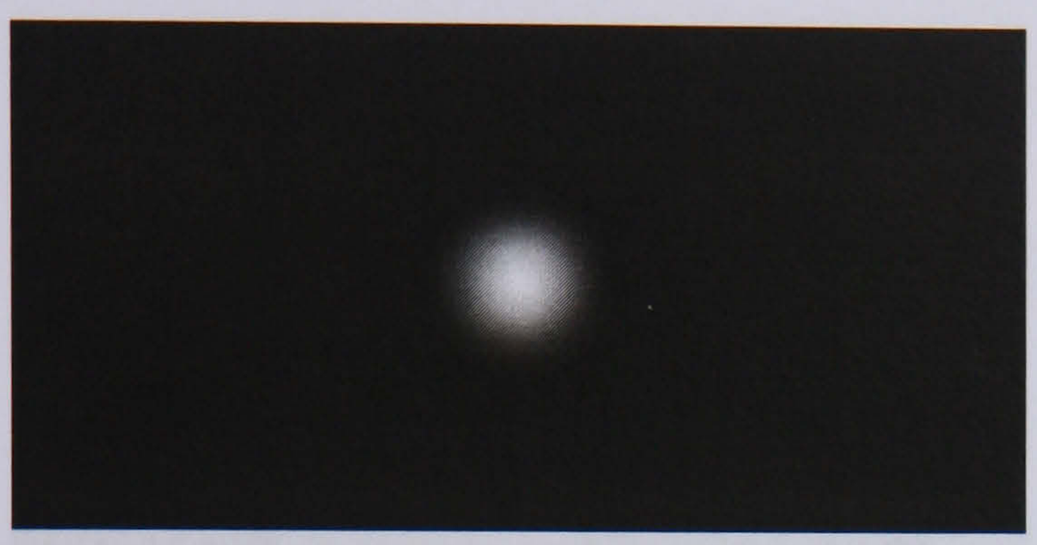

(a) A large simulated Gaussian image.

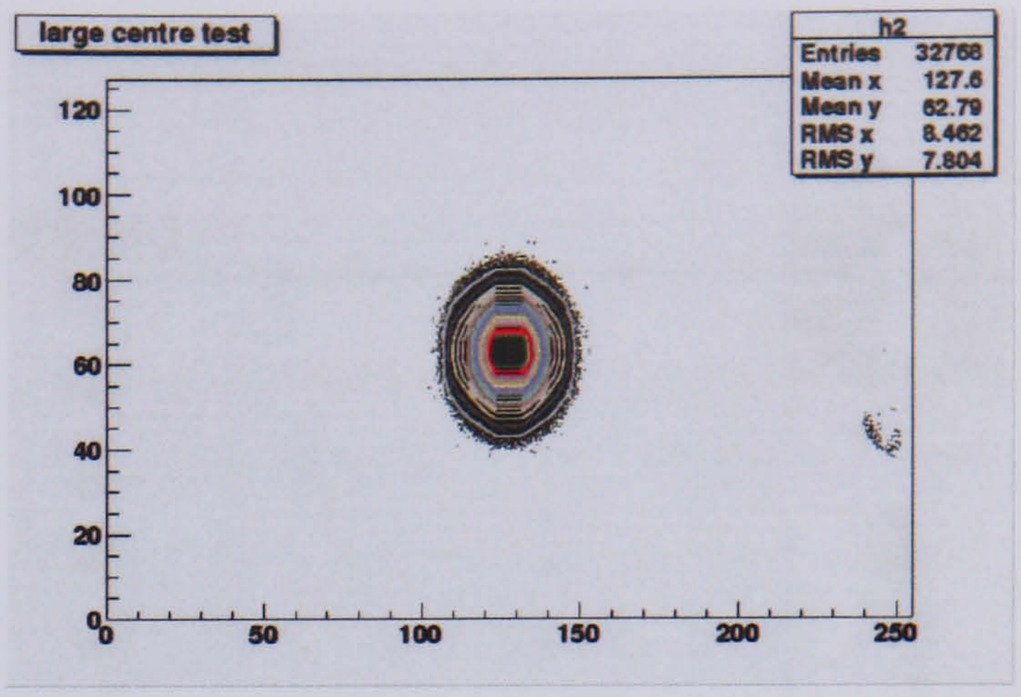

(b) The Gaussian fit to the large simulated Gaussian image.

Figure 4.32: Large simulated Gaussian image and its fit.

(a) A saturated large simulated Gaussian image.

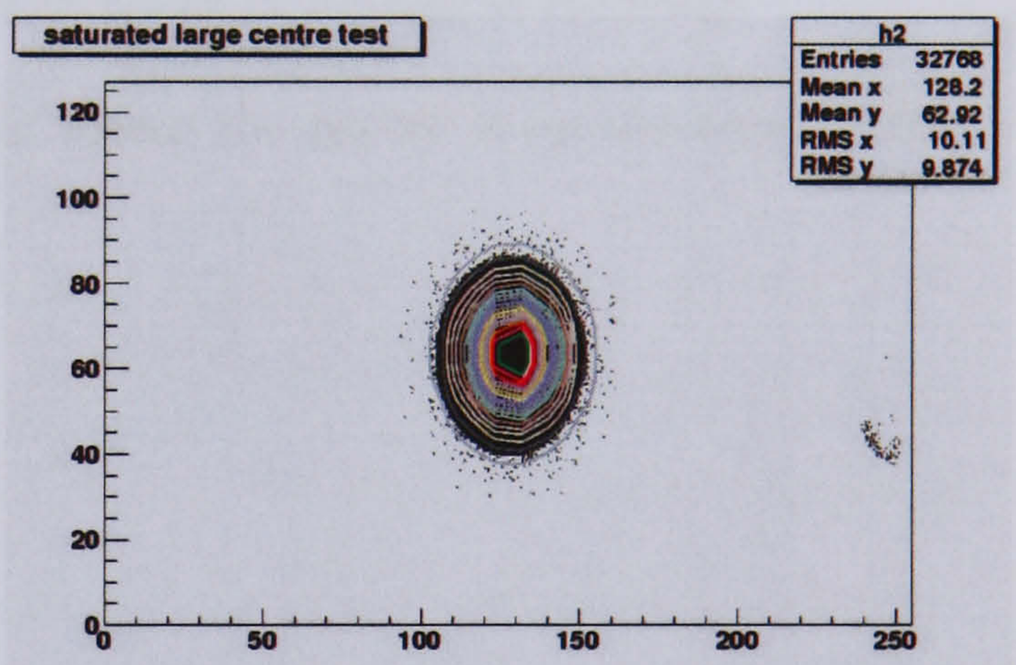

(b) The Gaussian fit to the saturated large simulated Gaussian image.

Figure 4.33: Saturated large simulated Gaussian image and its fit.

The result gets worse if the centre of the Gaussian spot moves off the edge of the image (see figure 4.35(b)).

4.4.2 Tests with Real Data

The profiles of the beams produced by the laser system are not really Gaussian in shape, and so the Gaussian fit method has been tried with different values for the parameters σ_x^2, σ_y^2, N and initial μ_x and μ_y. The 2D Gaussian fit was applied to a reference beam image and then to a signal beam image (see figures 4.37(a) and 4.36(a) respectively). Due to the non-ideal shape of the beam spot profiles, the fits took 50

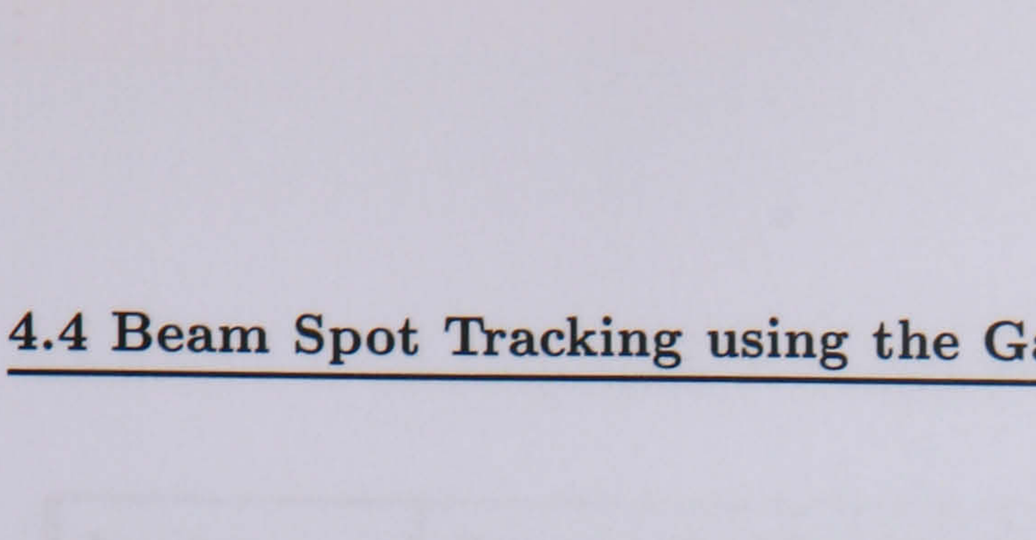

(a) A small simulated Gaussian profile where the centre is on the edge of the image.

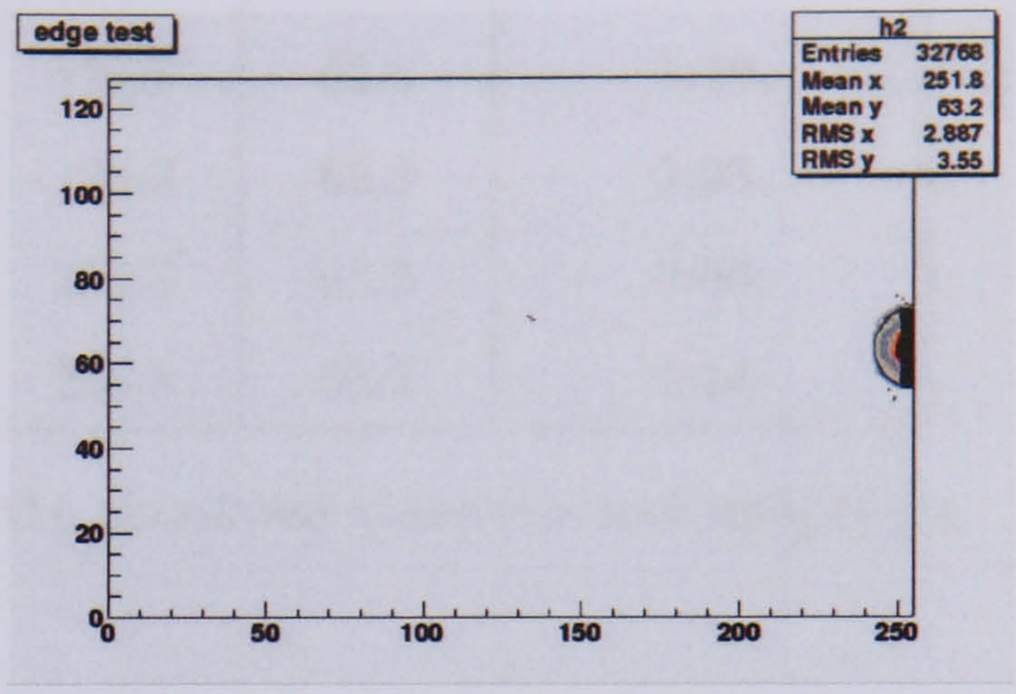

(b) The Gaussian fit of the small simulated Gaussian profile on the edge of the image.

Figure 4.34: Small simulated Gaussian profile where the centre is on the edge of the image and its fit.

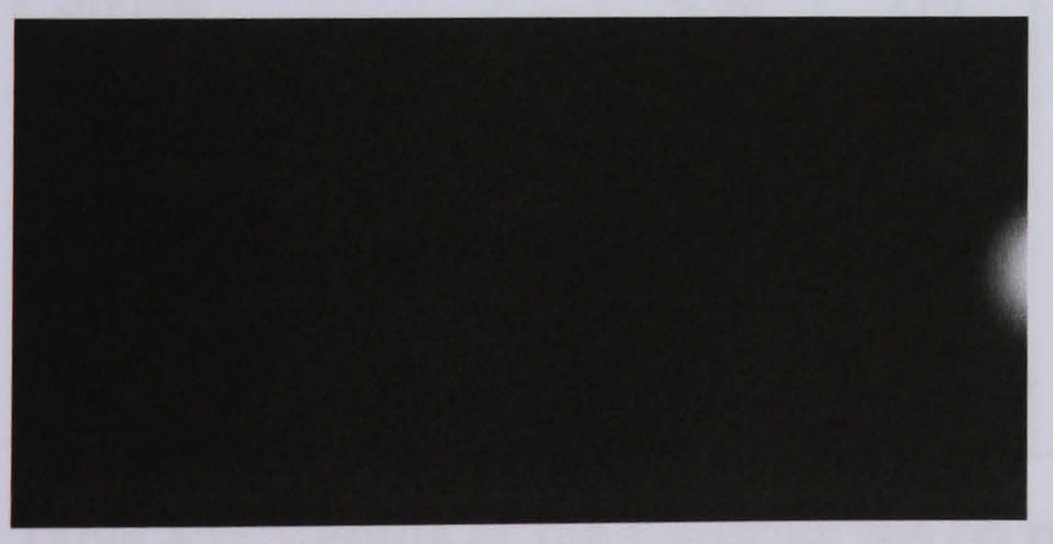

(a) A large simulated Gaussian profile where the centre is off the edge of the image.

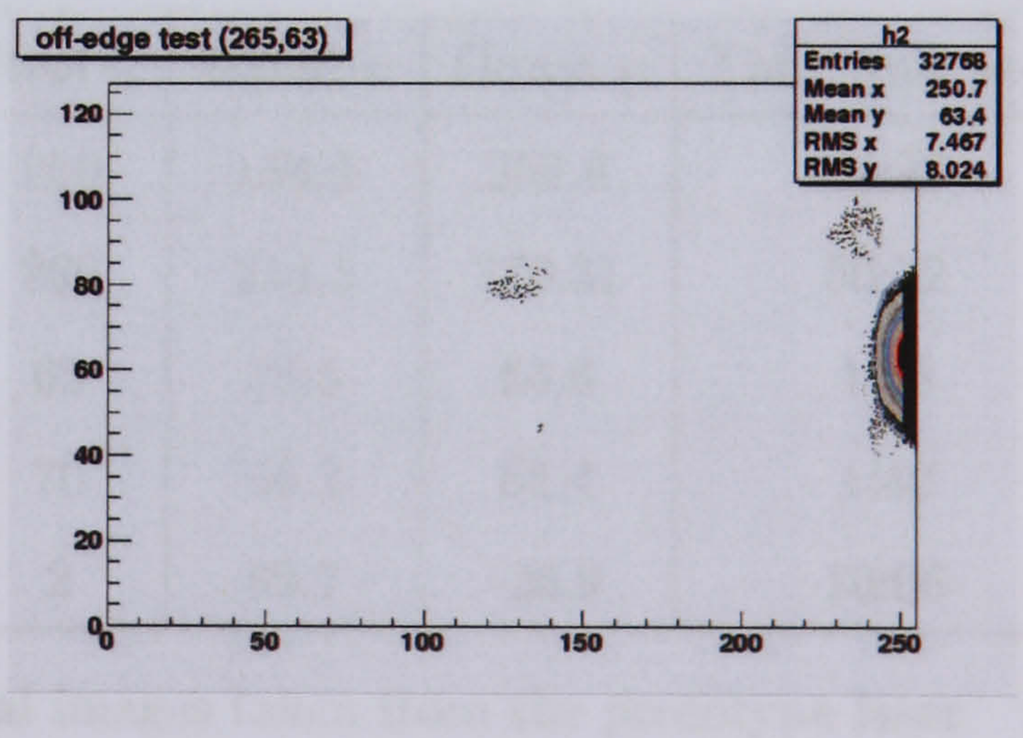

(b) The Gaussian fit to the large simulated Gaussian profile where the centre is off the edge of the image.

Figure 4.35: Large simulated Gaussian profile where the centre is off the edge of the image and its fit.

Image	Figure	Real x	Real y	Gauss x	Gauss y	Time (min:sec)
Small centre	4.31	127	63	127.8	63.5	2:19
Large centre	4.32	127	63	127.6	62.8	1:40
Saturated	4.33	128	64	128.2	62.9	1:23
Edge	4.34	255	63	251.8	63.2	2:00
Off-edge	4.35	265	63	255.8	63.2	2:14

Table 4.1: Results of the Gaussian fits on the simulated Gaussian test images (in pixel number).

minutes 12 seconds and 34 minutes 23 seconds of CPU time respectively.

Table 4.2 shows that the reference beam result was 11.5 pixels out in the x direction and 10.3 pixels out in the y direction. Similarly the signal beam result was 23 pixels out in the x direction although it was only 0.2 pixels out in the y direction. To reduce the processing time, the images were resized to 1/4 of their original size. The Gaussian fit was then applied to the 1/4 sized images. The reference beam converged after 1 minutes 40 seconds and the signal beam took 1 minute 55 seconds to converge.

Image	Figure	Real x	Real y	Gauss x	Gauss y	Time (min:sec)
Signal	4.36	178	260	154.9	259.8	34:23
Reference	4.37	203	260	214.5	270.31	50:12
1/4 size signal		45	65	38.5	64.6	1:55
1/4 size reference		46	70	46.2	66.4	1:40
1/4 size signal (edge)	4.38	80	2	69.7	-25.9	10:06

Table 4.2: Results of the Gaussian fits on real images taken from the prototype laser mirror alignment system.

The results for the quarter sized images 1/4 *size signal* and 1/4 *size reference* in table 4.2 show that the Gaussian fit method is sensitive to changes in resolution when the profile is already not ideal. The reference beam Gaussian fit location has now moved below the real location in the y direction, where as for the full size image

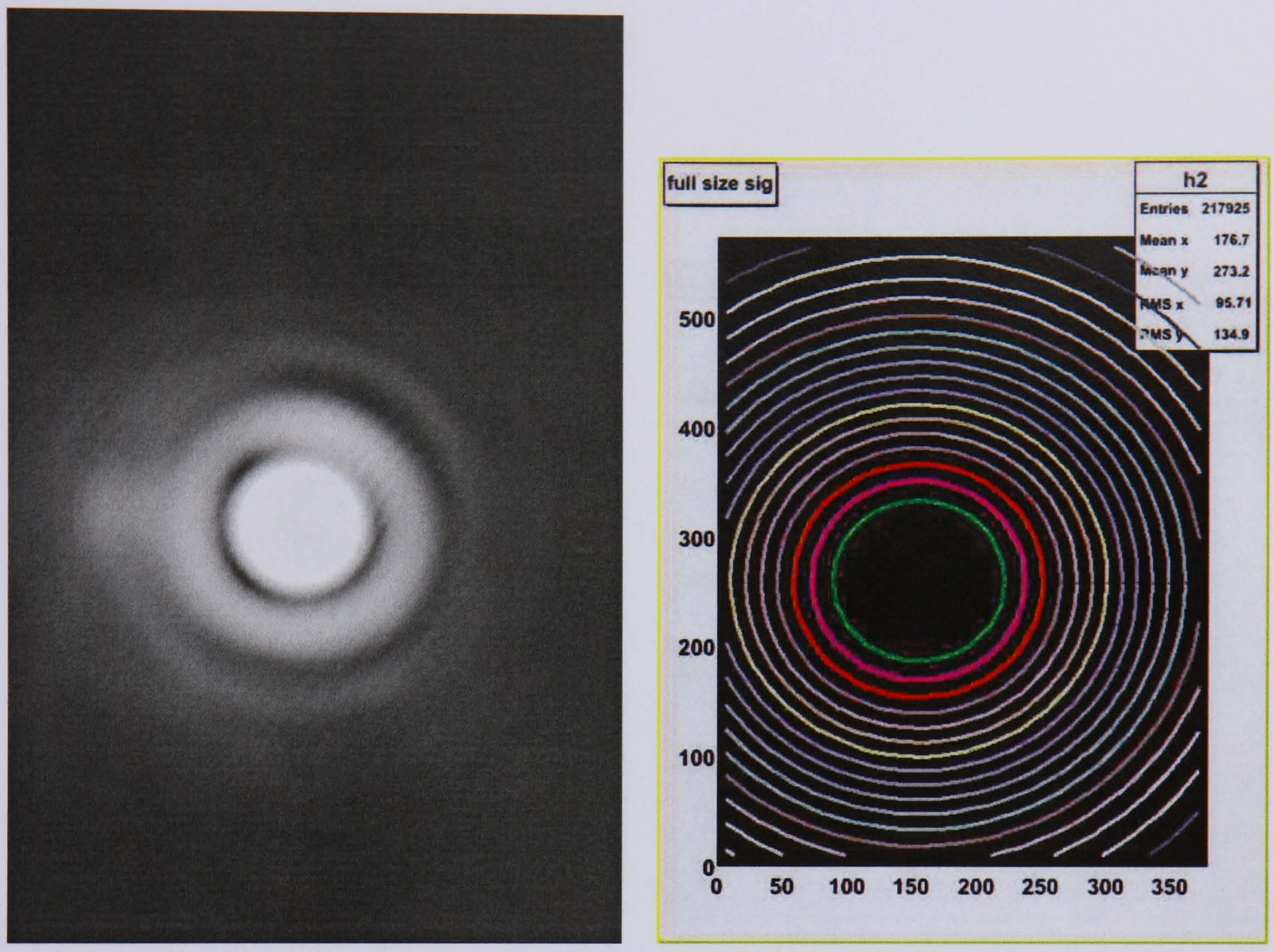

(a) A full size signal image (b) The Gaussian fit of the full size signal image

Figure 4.36: A quarter sized image and a Gaussian fit of the full size image.

the Gaussian fit location was above the real centre in the y direction. The result for the signal beam has scaled nicely. However, the results show that the signal beam is 6.5 pixels out in the x direction and the reference beam is 3.6 pixels out in the y direction. This is equivalent to deviations of 13 pixels and 7.2 pixels respectively for a full size image.

Since the signal beam centre is not Gaussian, it was thought that a good test would be to see how the 2D Root algorithm copes when some of the image surrounding the centre is removed. Therefore, the 1/4 *size signal* (*edge*) image in figure 4.38 was tested and the results are also included in table 4.2. The fit failed to converge unless a lower cut of 1% was applied to remove some of the background noise. Even with some of the background removed, the fit took a very long time to converge and the result was extremely poor. The Gaussian fit output locations are -25.9 in the y

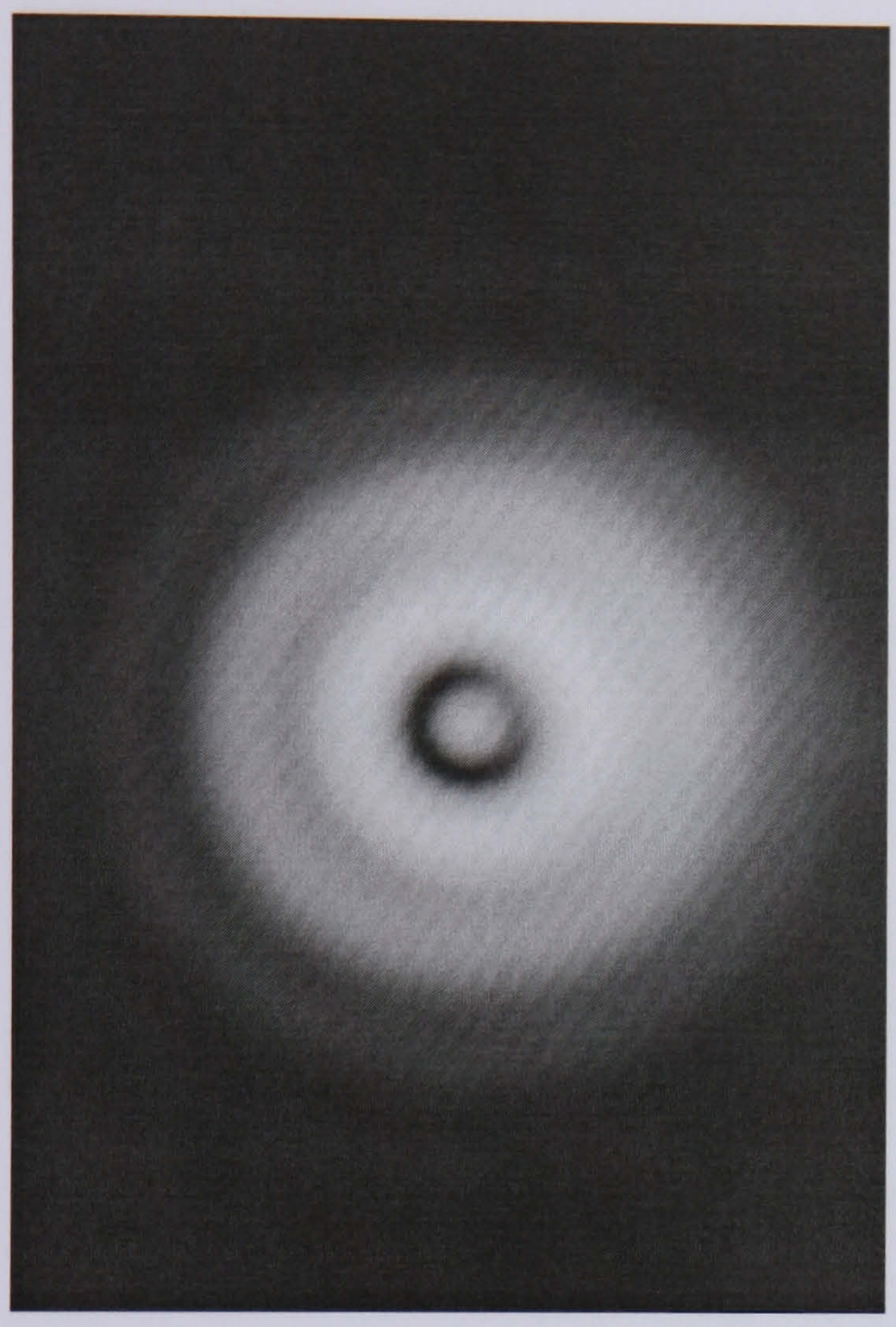

(a) A full size reference image (b) The Gaussian fit of the full size image

Figure 4.37: A quarter sized signal image and a Gaussian fit of the full size image.

direction and 69.7 in the x direction, this is a deviation from the centre of 27.9 pixels in y and 10.3 pixels in x.

The 1/4 *size signal* (*edge*) image no longer provides enough useful information to make an accurate fit. Changing the input parameters of the Gaussian fit method to further optimise the fits for the quarter sized images failed to make a significant improvement to the processing time or fit accuracy.

Gaussian Fit Summary

The Gaussian fit method is a very reliable and established way of fitting to Gaussian distributions and Gaussian image profiles. The initial results in this section have shown that for Gaussian images, the Root 2D Gaussian fit method was very accurate, with a reasonable processing time. The latter results in this section however, have

(a) A quarter sized signal beam profile on the edge of the image.

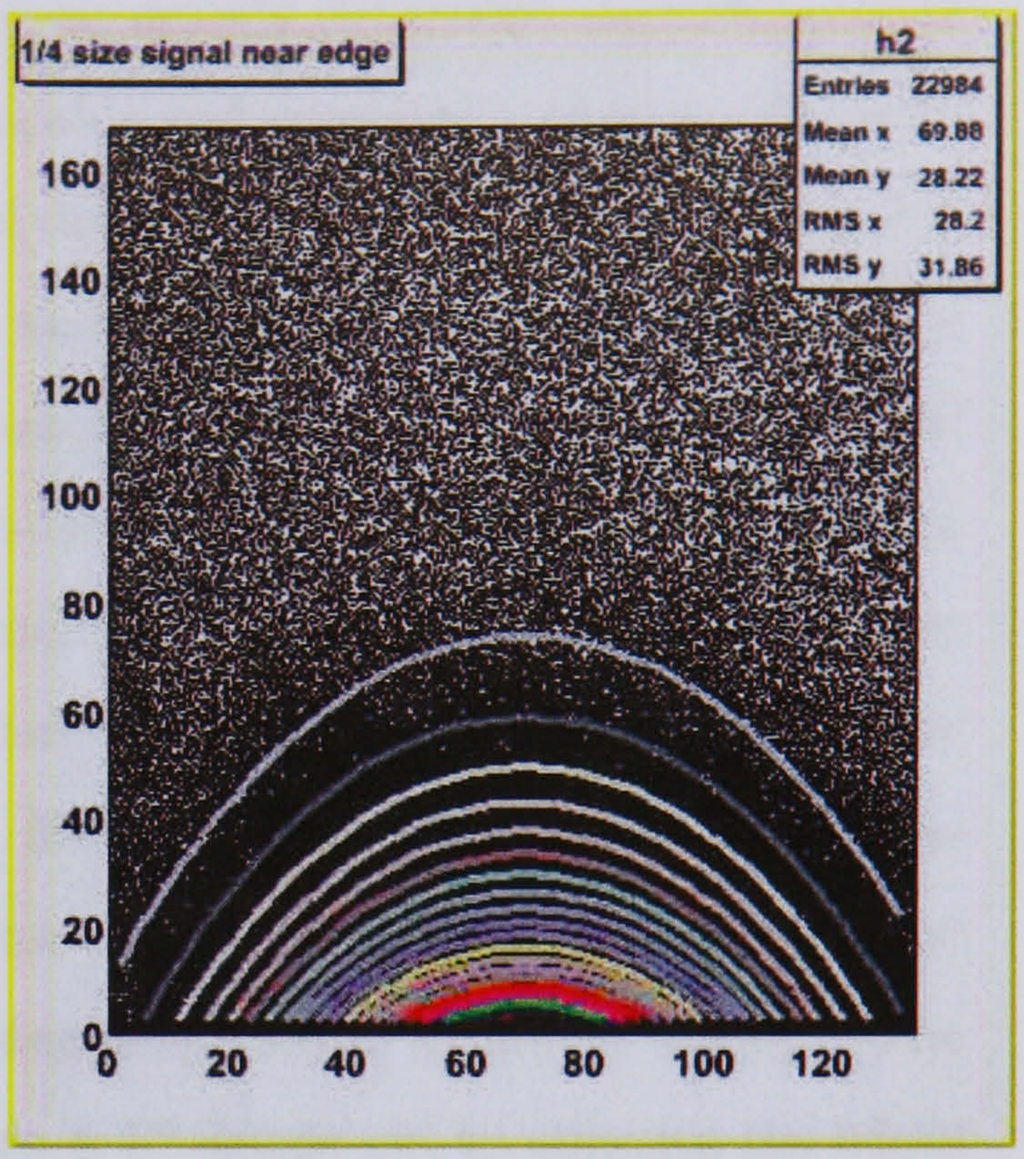

(b) The Gaussian fit of the quarter sized signal beam profile on the edge of the image.

Figure 4.38: A quarter sized signal beam profile on the edge of the image and its fit.

shown that for images that do not have a perfect Gaussian profile or where a large degree of saturation occurs, the Gaussian fit method takes a large amount of time to converge and the accuracy of the fit is compromised. Decreasing the image size to improve the processing time does not improve the fit accuracy but does reduce the fitting time. The poor performance of the Root 2D Gaussian fit method when applied to the laser alignment system images provoked the development of another method of finding the beam spot centres.

4.5 Image Analysis Software

Following the results of the 2D Gaussian fit method for finding the beam spot centres, another method was developed to find the centres of the beam spots using methods borrowed from image analysis techniques. With this Image Analysis Software method, changes in the positions of the monitored mirror segments can then be tracked. This

section of the thesis describes the design and results of the Image Analysis Software. The role of the Image Analysis Software is to accurately determine the difference in distance between the two beam spots in a reliable and consistent manner. The software needs to accommodate beam profiles of diverse characteristics (e.g. diffraction profile, asymmetries, non-Gaussian shapes) and needs to be robust so that it may operate automatically while the system monitors the alignment. Assuming optical stability of the laser alignment monitoring system, a change in distance between these two beams will point to a movement in the angular position of the monitored mirror segment. The image analysis software therefore needs to be able to locate primarily the two beams spots in the image, and then find their centres. A difference calculation between these two points can then be made. In order to accurately locate the centres of the beam spots, the image processing is applied in a number of steps. The first stage is to apply a smoothing filter, then a 1^{st} image cut to enhance the edges of the image, then a Sobel mask edge detection algorithm, a Hough accumulator to determine the centre of the edges, a 2^{nd} image cut in conjunction with an anomaly removal algorithm to remove spurious peaks, a spot location algorithm to extract the real peaks and, finally, a weighted centre of mass calculation to determine the centre of the peaks. These steps will now be considered in turn.

4.5.1 The Smoothing Filter

An example of a typical image taken from the prototype system is given in figure 4.39.

One of the steps of the image analysis process is to use a Sobel Mask [35] edge detector. Although the principle behind this edge detection technique will be considered shortly, it is useful to mention its use in order to understand the need of the smoothing filter. It can be clearly seen in figure 4.39 that there is a pixel aliasing effect in the form of evenly spaced parallel diagonal lines that run across the image. If these lines are not filtered out, then they will be considered as edges by the Sobel Mask edge detector, and will thus cause unwanted difficulties in the determination of the two beam spot centres. It is therefore necessary to apply a smoothing filter to remove them.

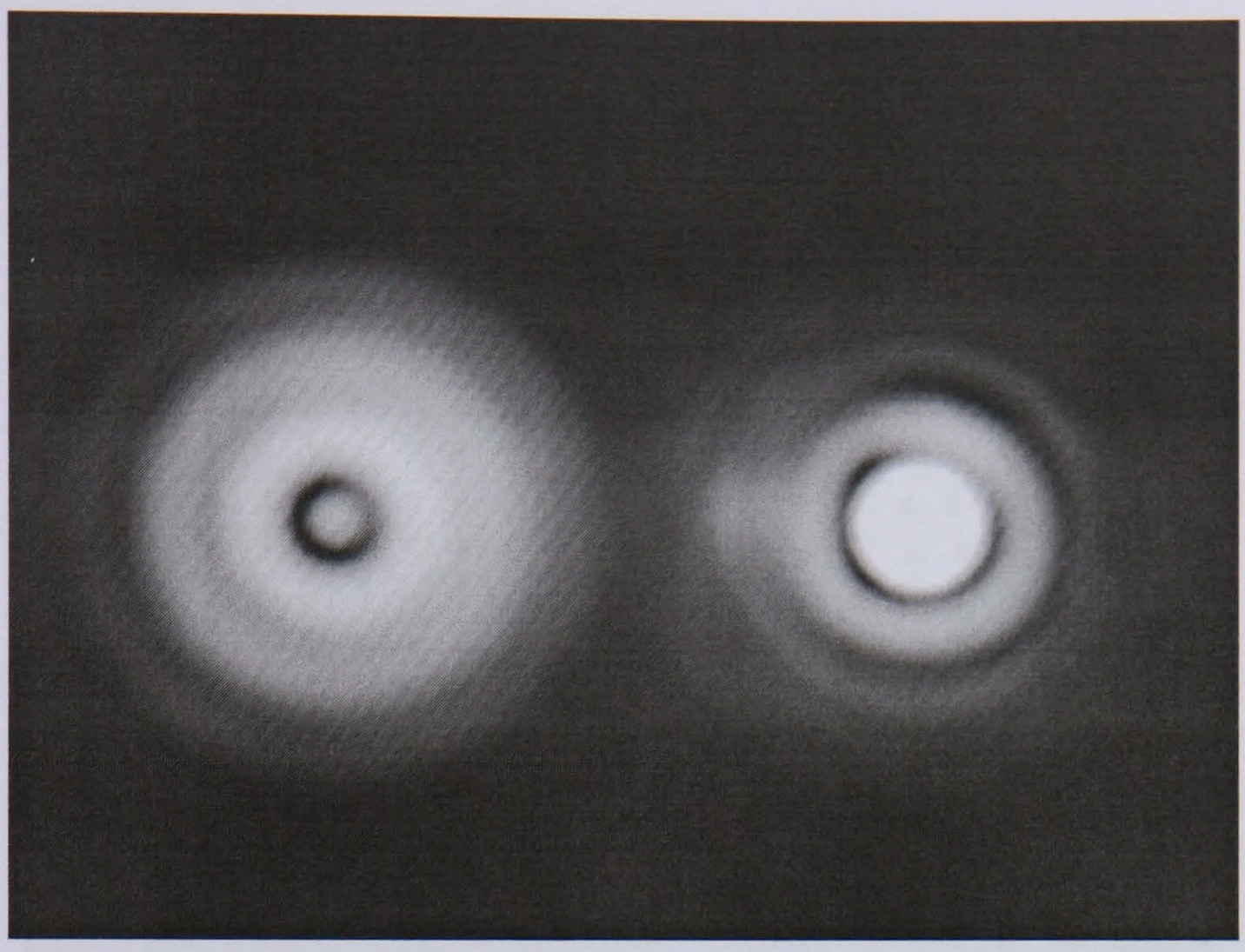

Figure 4.39: An example of a typical image taken from the prototype laser mirror alignment monitoring system.

Method

The smoothing filter used in the image analysis software is a 5×5 pixel averager that can be applied multiple times. Ignoring a two pixel border around the edge of the image, the 5×5 pixel mask is placed over every pixel in the image (figure 4.40).

The average of the pixels in each mask is written to an output file (figure 4.41). Note that the border pixels are ignored, but instead are written unchanged to the output file. The reason for not discarding completely the border pixels will be considered later on.

The method of averaging the pixels in the pixel mask is as follows. Taking a 5×5 mask as shown in figure 4.42, the sum of the pixel values within the mask is divided by the number of pixels in the mask such that

$$Average = (a1 + a2 + a3 + ...an)/n. \tag{4.6}$$

The average value is then written out to the pixel location in the output image that is in the equivalent location of mask pixel $a13$ in the image.

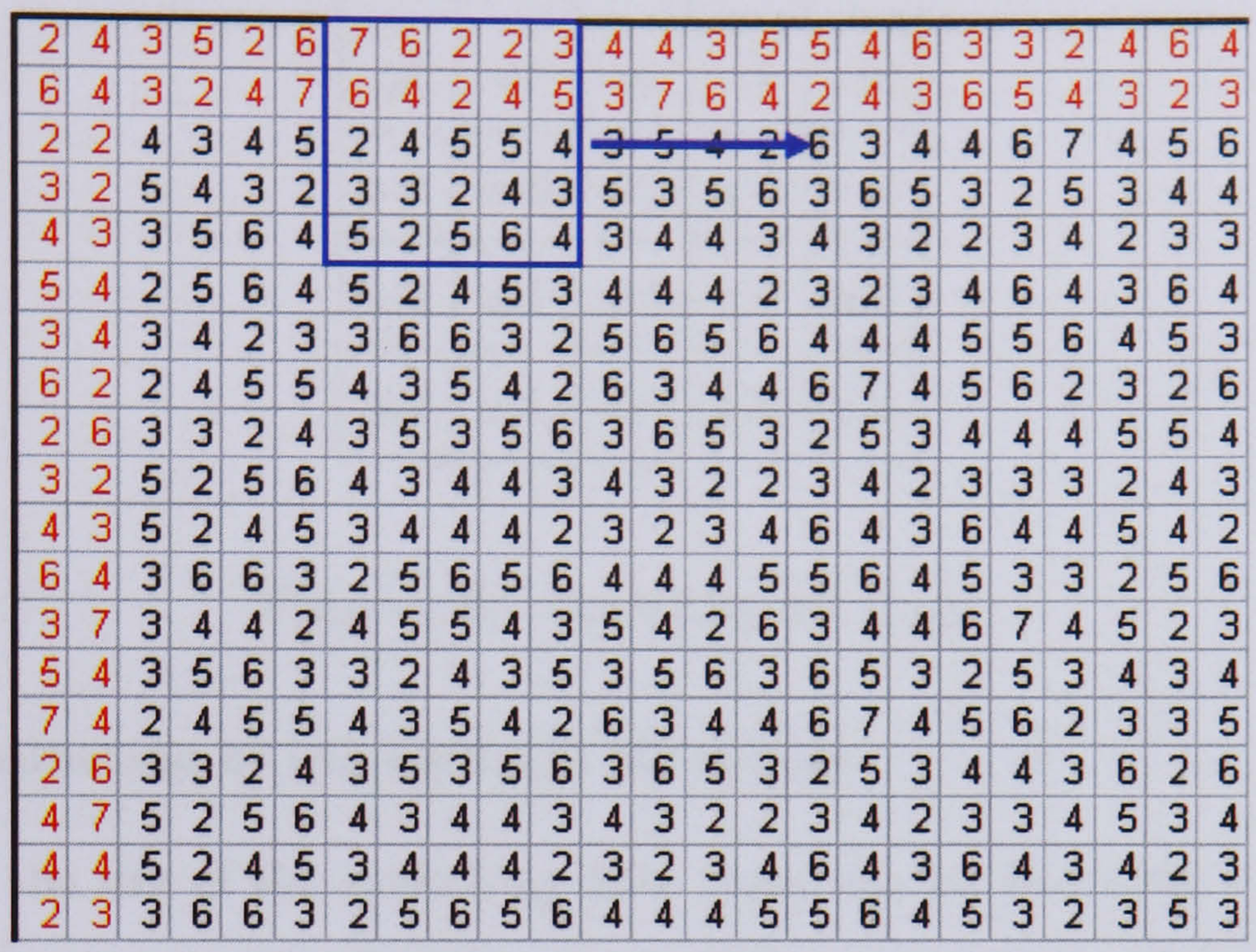

Figure 4.40: A section of image taken at the top left of the image with the 5×5 pixel mask applied. The number on each pixel depicts the brightness level for the pixel.

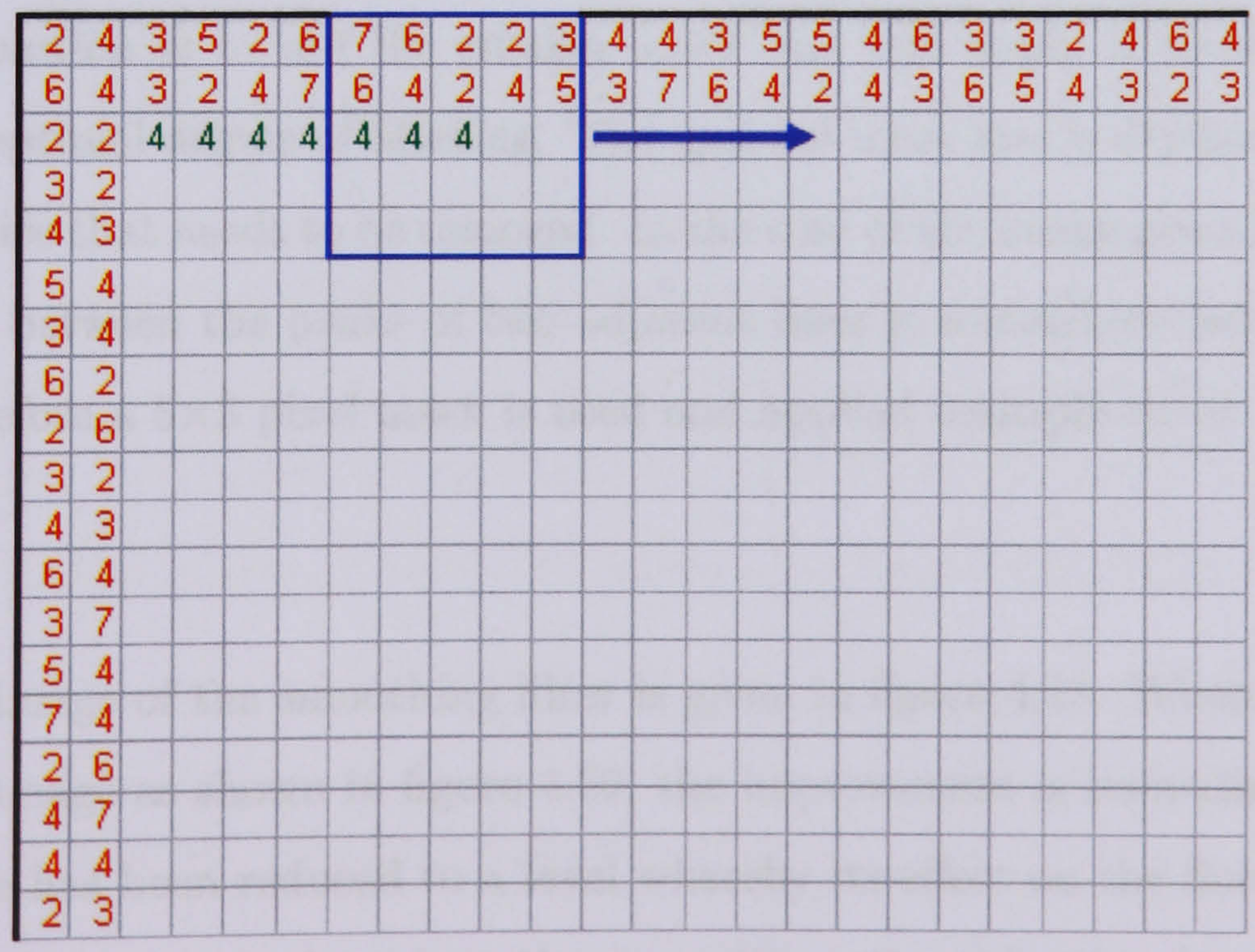

Figure 4.41: The averages of each mask are written to the output image file.

a1	a2	a3	a4	a5
a6	a7	a8	a9	a10
a11	a12	a13	a14	a15
a16	a17	a18	a19	a20
a21	a22	a23	a24	a25

Figure 4.42: The 5×5 pixel mask.

The Determination of the Optimal Mask Size

In principle, the size of the smoothing filter mask can be decreased or increased in size, giving finer or coarser degrees of smoothing respectively. If the mask is too small, its effect on the image will be negligible, but if the mask is too large, as well as removing noise it will also degrade the image by introducing fuzziness and loss of clarity.

It is possible that one application of a given filter mask is not sufficient to remove the aliasing noise. Also, if the mask is too large then it applies too much filtering. Thus, the solution is to use the smaller mask size and apply it multiple times to achieve the optimal degree of filtering. The optimal mask size is dependent upon the size of the noise that needs to be removed. In the case of the image given in figure 4.39, the distance between the peaks of two adjacent lines is somewhere between 5 and 6 pixels. Therefore a 5×5 pixel mask is used and applied multiple times.

Results

The output image of the smoothing filter is given in figure 4.43. When compared to the original image as shown in figure 4.39, the improvement is immediately evident.

The noise has been reduced to a level whereby its effect on the Sobel mask edge detector will be minimised, and at the same time, the reduction in clarity on the image is minimal.

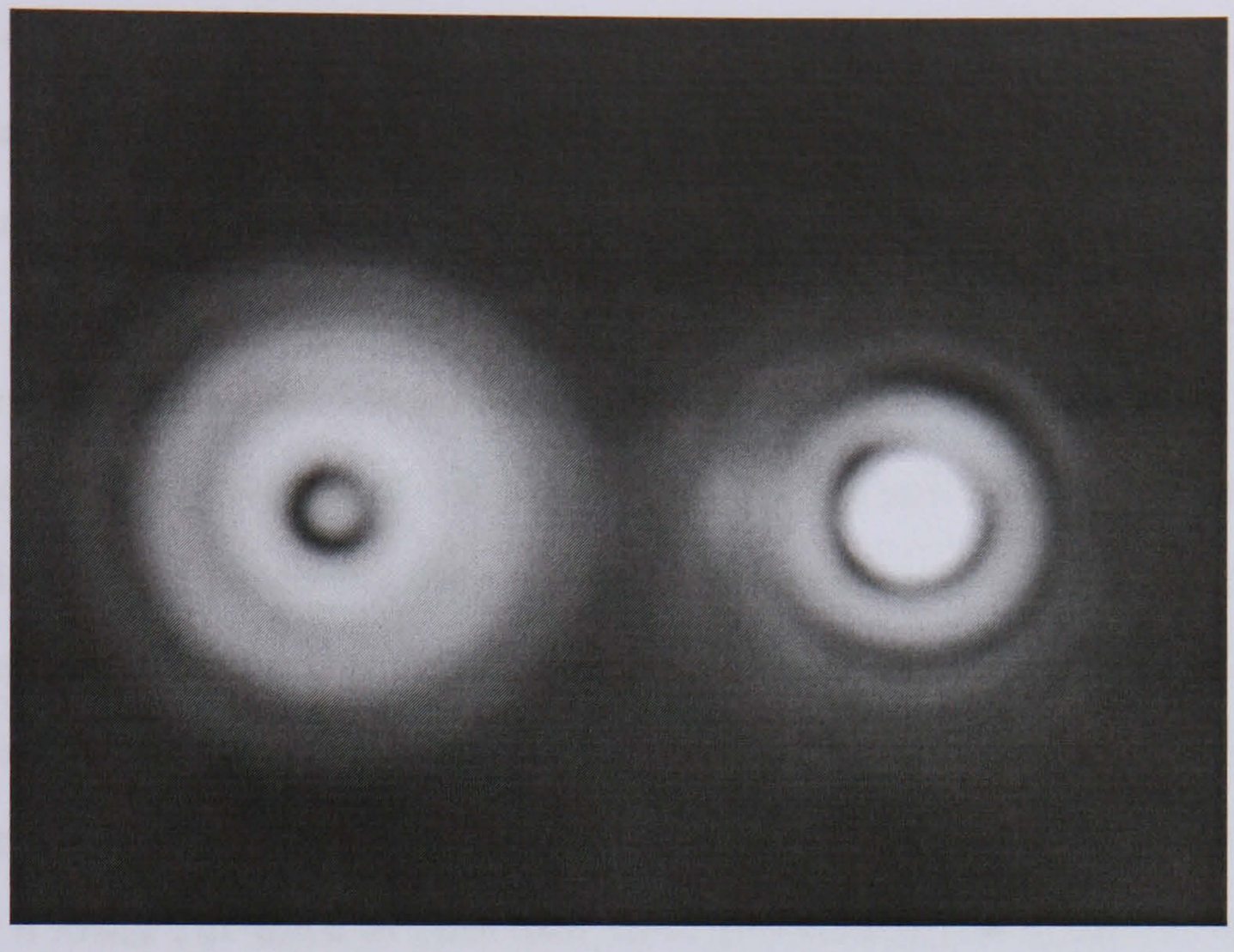

Figure 4.43: The output image of the pixel averaging smoothing filter.

4.5.2 The 1^{st} Image Cut

In order for the Sobel Mask edge detector to work efficiently, it is necessary to supply strong edges. Therefore a cut needs to be made. The method of applying the cut must take into consideration the intensity range of the image so that an optimal cut can be made. To illustrate this point, if an absolute cut level is applied to the image with respect to the maximum measurable range of the camera pixels (i.e. 0-255 for an 8 *bit* pixel), then as the relative intensity of the beam spots changes over time (due to a reduced transmission rate in the fibre optics through accrued radiation damage), then the position at which the cut is made with respect to the beam spot intensities will also change. It is therefore important to match the cut to the intensity range of the beam spots and not to the absolute measurable range of the camera pixels.

Method

The method of applying the cut follows two steps:

1. Find the intensity range of the beam spots within the image;
2. Apply the upper and lower cuts to the image relative to the intensity range of the beam spots

In the first part of the method, the cut algorithm scans the image for the highest value and the lowest value. In the final system, over time, the cameras will experience radiation damage. This damage may cause some pixels to stay permanently at values of 255 or 0. However, because the image that the cut algorithm receives is already averaged, dead pixels in the image are already accounted for. Therefore this method of finding the intensity ranges of the beam spots is still valid and applicable. Without the image filter, dead pixels on the camera would cause the cut algorithm to make a bad judgement with respect to finding maximum and minimum intensities.

In the second part of the method, the cut algorithm applies upper and lower cuts to the image based upon the result of the intensity range found in the image. For example, for a lower cut limit of 60% and an uppercut limit of 80%, the cut algorithm would make all pixels that have values below 60% of the intensity range equal to the 60% intensity range value and all pixels that have a value greater than 80% of the intensity range equal to the 80% value.

Results

The results of the cut are given in figure 4.44. Clear edges are visible, giving a good input for the Sobel Mask edge detector.

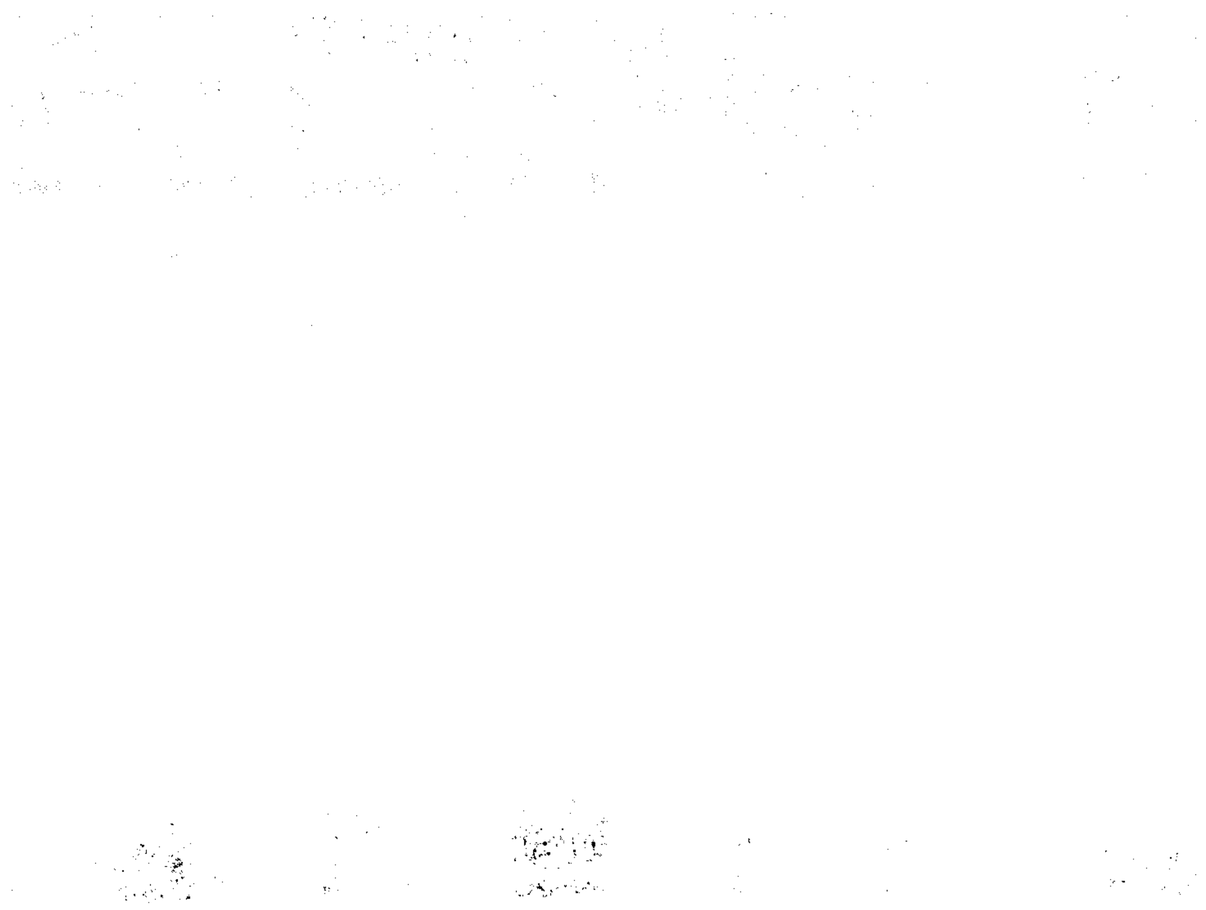

Figure 4.44: The output image after the 1^{st} cut has been applied to the smoothed image.

4.5.3 Sobel Mask Edge Detection

The Sobel Mask method [35] of edge detection is a well defined method of finding edges in images. It works by performing 2-D spatial gradient measurements across the image using a 3×3 pixel mask that is made up of two 3×3 convolution masks. Regions of high spatial gradient found by this method correspond to edges.

Method

The two convolution masks of the Sobel operator are shown in figure 4.45.

-1	0	+1
-2	0	+2
-1	0	+1

(a) Gx

+1	+2	+1
0	0	0
-1	-2	-1

(b) Gy

Figure 4.45: The convolution masks of the Sobel operator.

These masks are designed to have optimal response to vertical and horizontal edges respectively relative to the pixel mask. The Gx operator measures the vertical spatial gradient value of the mask, and the Gy operator measures the horizontal spatial gradient value of the mask. The definitions of magnitude for the Gx and Gy spatial gradient operators are

$$|Gx| = |(a3 + 2a6 + a9)| - |(a1 + 2a4 + a7)| \tag{4.7}$$

and

$$|Gy| = |(a1 + 2a2 + a3)| - |(a7 + 2a8 + a9)|. \tag{4.8}$$

By combining the two convolution masks together, the absolute Sobel magnitude of the pixel mask can be found. This value is the total spatial gradient that the pixel mask contains and is given by

$$|G| = \sqrt{Gx^2 + Gy^2} \tag{4.9}$$

or by approximation

$$|G| = |Gx| + |Gy|. \tag{4.10}$$

The direction of the total spatial gradient is given by the Sobel angle θ (see figure 4.46) where,

$$\theta = tan^{-1}(Gy/Gx). \tag{4.11}$$

From the Sobel Mask calculations, the image analysis software produces two arrays, one for the absolute Sobel magnitude values and one for the correlating Sobel angle. When creating the array for the absolute Sobel magnitude, the Sobel algorithm applies a cut so that only the top 95% of the Sobel magnitude values are recorded, the remaining values are set to zero. Both the Sobel magnitude array and the Sobel angle array are required as inputs to the Hough Transform accumulator (see below).

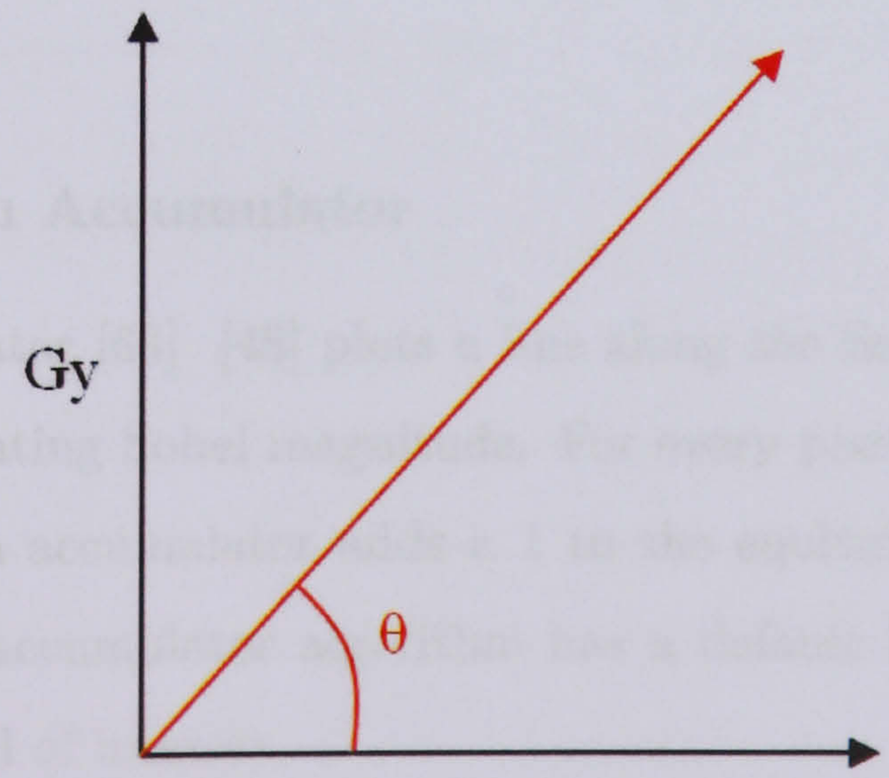

Figure 4.46: The Sobel gradient direction.

Results

The output image shown in figure 4.47 is a plot of the array containing the Sobel magnitude values after the cut has been made. For each pixel shown there is a correlating Sobel angle stored in a separate array.

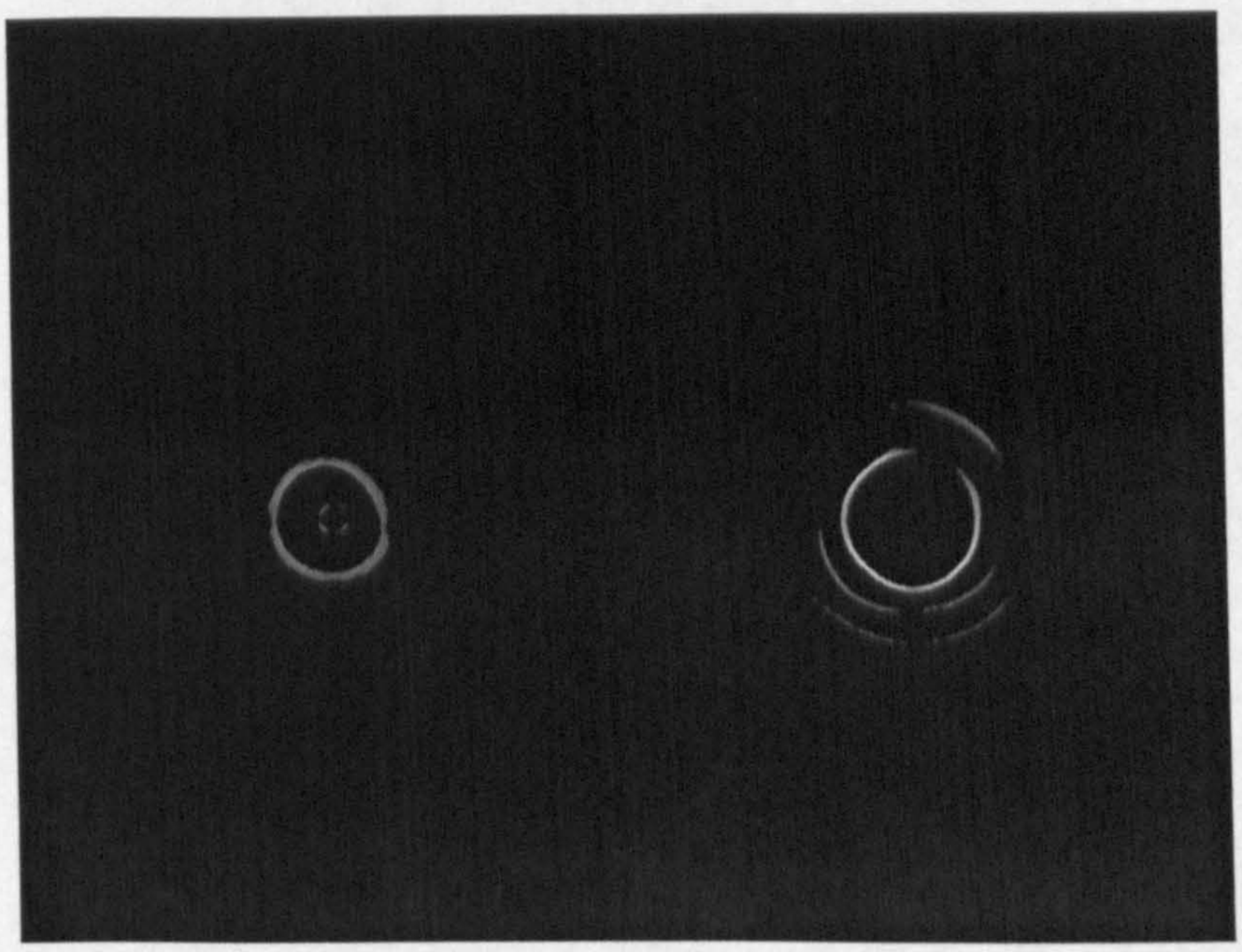

Figure 4.47: The output image of Sobel Mask edge detector when applied to the cut image.

4.5.4 The Hough Accumulator

The Hough Accumulator [63] [48] plots a line along the Sobel angle from the pixel location of the correlating Sobel magnitude. For every pixel that the line traverses, the Hough Transform accumulator adds a 1 to the equivalent pixel on the output image. The Hough Accumulator algorithm has a default line length of 100 pixels either side of the pixel of interest.

Method

To give an example of the method for the Hough Transform accumulator, take the image shown in figure 4.48(a). The red pixel points represent high Sobel edge magnitudes at the point in the image at which they are located and the arrows represent

the direction given by the Sobel Angle. When the Hough Accumulator is applied, an accumulation arises at the crossing point of the two lines. This is represented by figure 4.48(b), which also includes the pixel values to show the principle that applies to the accumulator.

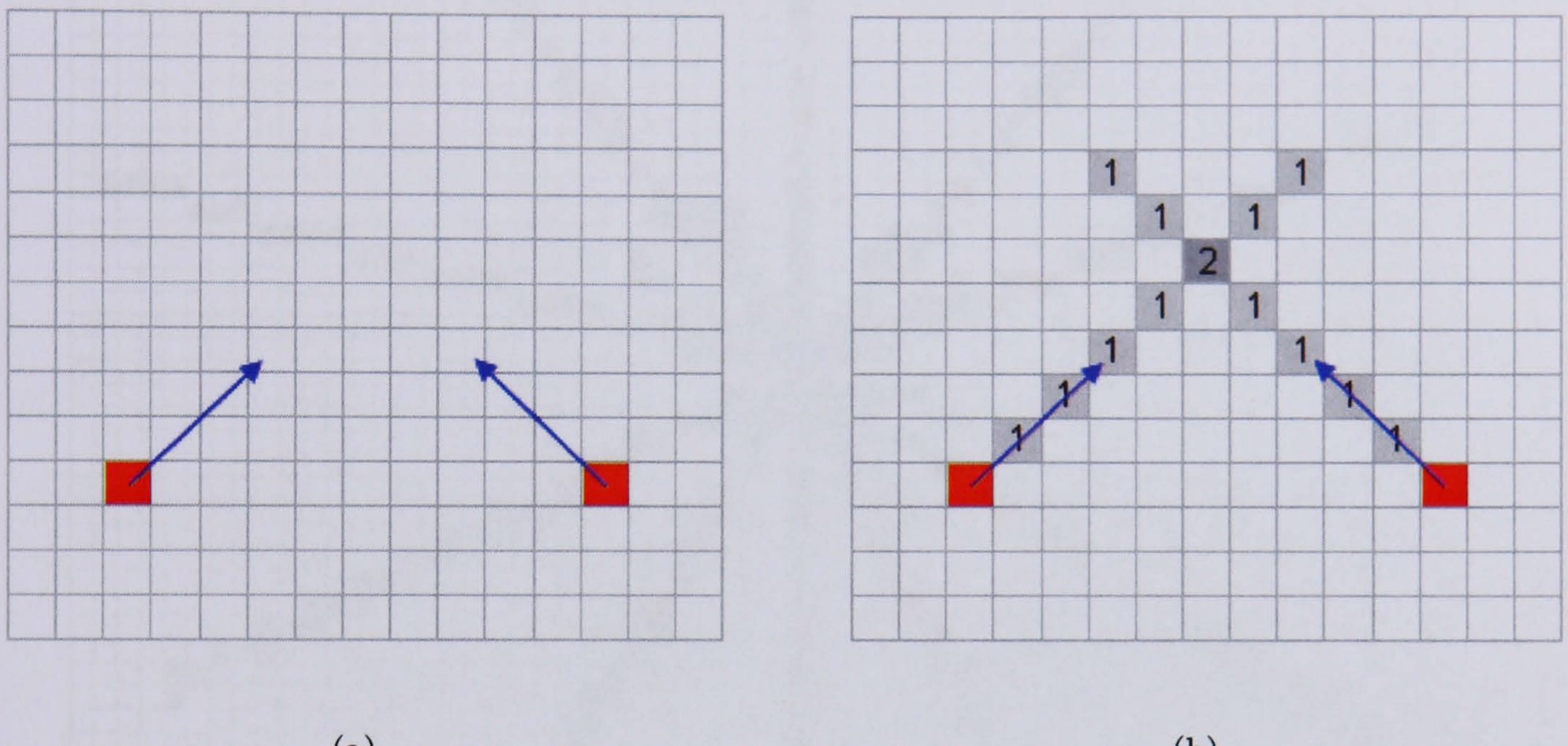

(a) (b)

Figure 4.48: The method of applying the Hough Accumulator to an image with Sobel magnitudes and Sobel angles.

If this principle is applied to a few points of a circle in a larger image as shown in figure 4.49, a central accumulation arises. Figure 4.48(a) shows an example Hough Transform accumulation of a hypothetical small number of Sobel magnitude and Sobel angle inputs.

It may be noted that the accumulator lines drawn in figure 4.49 have been drawn in both directions from the pixels of Sobel magnitude. This is because when the Hough Accumulator is applied to an image with a circular diffraction pattern, the gradient direction on a fringe going from a peak to a trough will be in the opposite direction to the centre of the circle. Therefore, it is necessary to also apply the Hough Accumulation in the opposite direction of the Sobel angle.

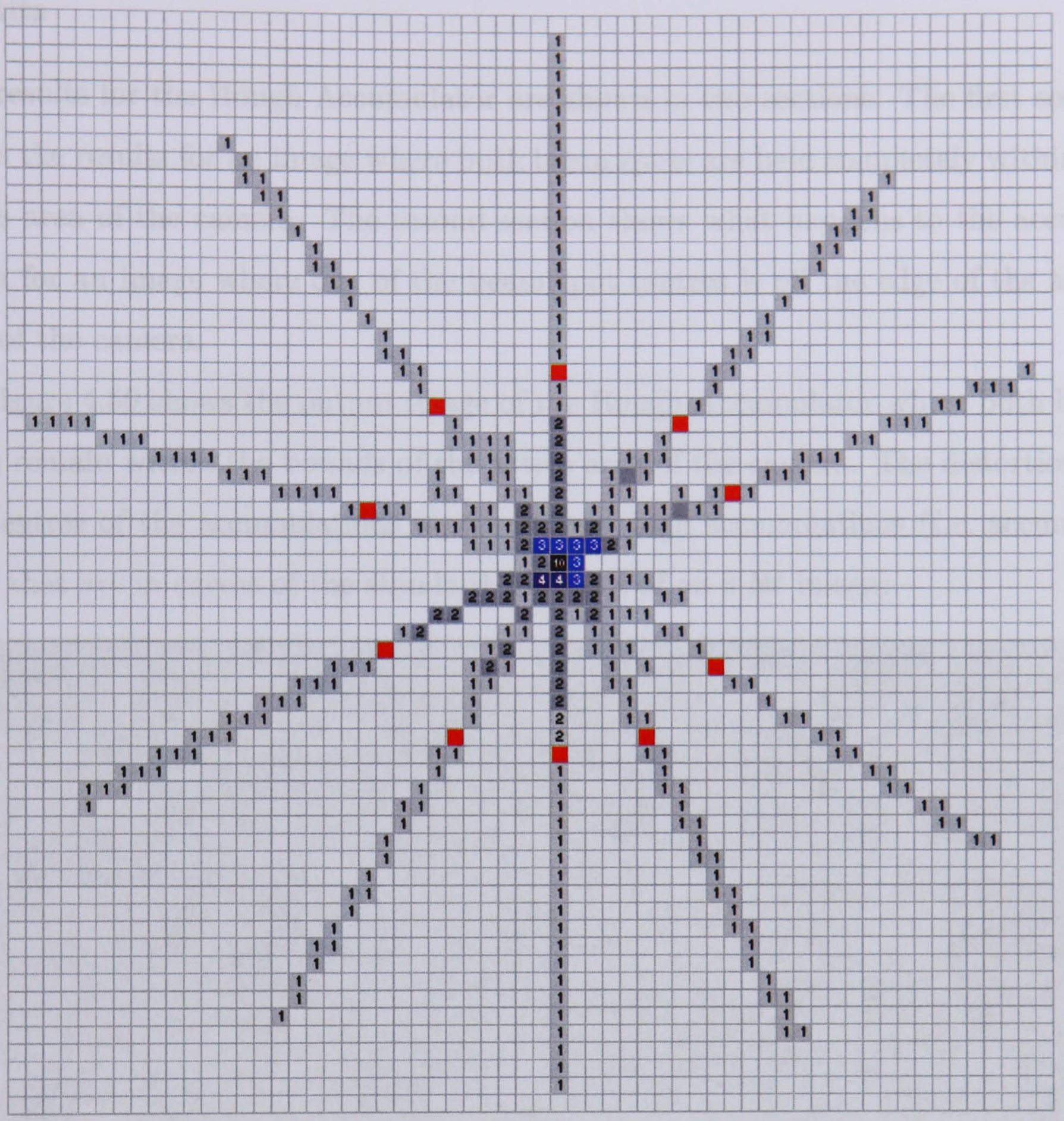

Figure 4.49: A Hough Accumulation for a small number of points in a circle.

It is also interesting to note that if a beam spot starts to move off the edge of the image, in principle, it is still possible to track the centre of the spot. As long as there is a circular edge on the image, the edge will always point to the centre of the spot, and therefore an accumulation will gather there and the centre can be found. For this reason, the Hough Accumulators output image is larger than the input images, so that the beam spot centres can be tracked when they are off the edge of the image.

Results

The results for the Hough Accumulator are shown in two sections. The first section shows the results for an image where both beam spots are held completely within the active area of the camera. The second section shows what happens to the accumulation for an image where one of the beam spot centres is off the edge of the active area of the camera.

Figure 4.50 shows the output image of the Hough Accumulator where both beam spots remain within the bounds of the active area of the camera. The distortions at the centres of the accumulations represent very high accumulations (*i.e.* accumulations that are in excess of the standard 255 limit of an 8 *bit* image).

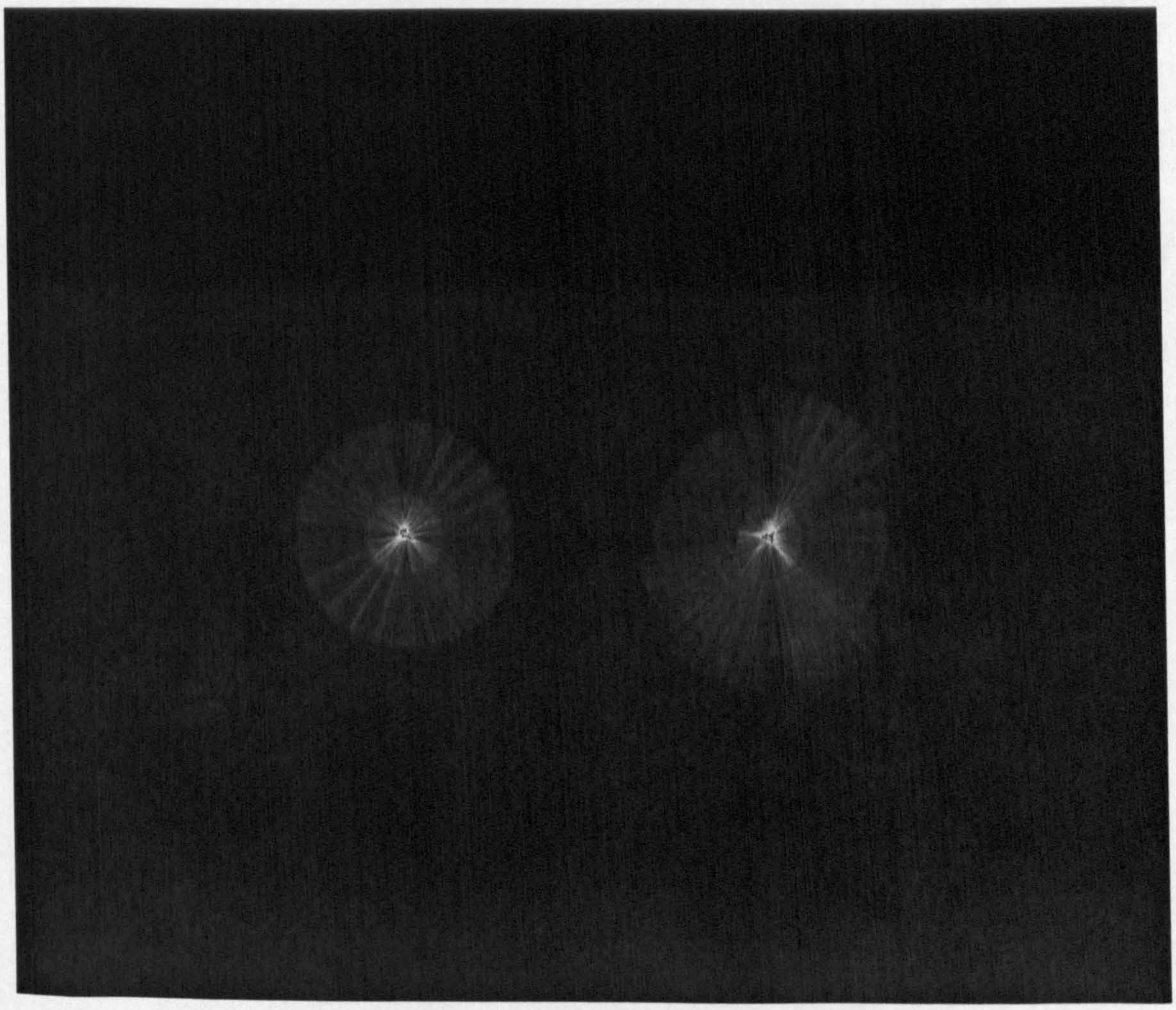

Figure 4.50: The output image of the Hough Accumulator.

The output images from the Hough Accumulator algorithm are 400 pixels larger

in both x and y directions when compared to the output images of the previous algorithms of the Image Analysis software. They are therefore shown as larger images in this chapter. Figure 4.51 shows the Hough Accumulator output when one of the beam spot centres moves off the edge of the active area of the camera. To illustrate this point further, the output image of the smoothing filter has been super-imposed onto figure 4.51 to show the boundaries of the output image from the camera.

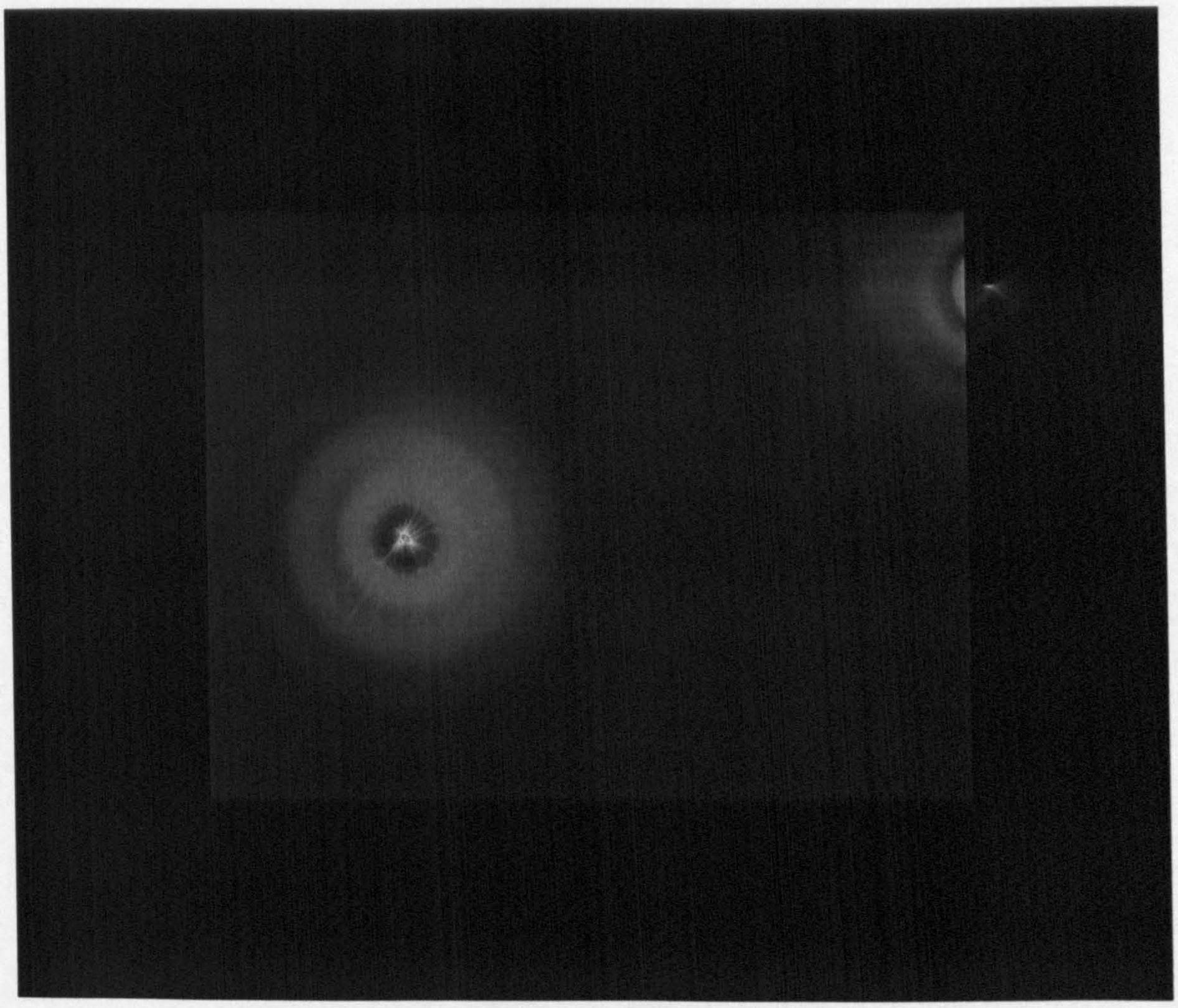

Figure 4.51: The output image of the Hough Accumulator superimposed with the output image of the Smoothing Filter.

The central accumulation intensities between the two beam spots differ due to the reduced amount of edge that the second spot has. This highlights the point that a careful cut will need to be made on the Hough Accumulator output if the second beam spot is to remain trackable after the cut has been made.

4.5.5 2^{nd} Image Cut

The cut that is made to the Hough Accumulator output is referred to as the 2^{nd} cut. This cut removes unwanted low value accumulations, leaving only the higher value accumulations for processing. Without this cut it is very difficult to process the image to find the centres of the two beam spots. By making the cut, the two accumulations will be better defined and therefore easier to process.

Method

The 2^{nd} cut works on a similar principle to the 1st cut in that it first finds the intensity range in the image and then applies a cut relative to that range. However, the intensity range on the output of the Hough Accumulator can be far greater than the maximum range of 0-255 that an 8 *bit* greyscale image should have. Nevertheless, the code used in the 1^{st} Cut algorithm is able to cope with this and is therefore also used for the 2^{nd} Cut algorithm to find the intensity range. After the intensity range in the image has been found, and the optimal cut range calculated, the two cut algorithms begin to differ in their implementation.

As with the 1^{st} Cut algorithm, the 2^{nd} Cut algorithm is able to take a slice through the intensity range of the image. However, this approach does not work as well as simply only applying a lower cut limit. The reason for this is that the points of highest accumulation are also the points that should have the highest accuracy and therefore applying a cut to them does not make sense. The lower cut limit is calculated using the intensity range and an arbitrary percentage cut limit value set by the user. For example, if the percentage cut limit value is set to 70%, then anything below that 70% value will be rejected. The method of applying this cut is to take 70% of the maximum range value from every pixel in the image. Once this has been done, there will be pixels in the image that have a negative value. These negative values are found within the image and set to a value of zero. The percentage cut limit should be set high enough so as to remove accumulation lines visible in figure 4.50, but low enough so as not to remove the low centre accumulation that occurs when a spot centre moves off the edge of the active surface of the camera.

Results

As with the results for the Hough Accumulator, the results in this section are placed into two sections. The first section shows the result of the 2^{nd} Cut applied to the Hough Accumulator output where both beam spots are clearly within the boundary of the active surface of the camera. The second section shows the result of the 2^{nd} cut applied to the Hough Accumulator output where one of the beam spot centres has moved off the edge of the active surface of the camera. Figure 4.52 shows the resulting output image of the cut applied to the Hough Accumulator output when the lower cut limit is set at 70%. The beam spot centres are clearly better defined, enabling a more efficient spot location process.

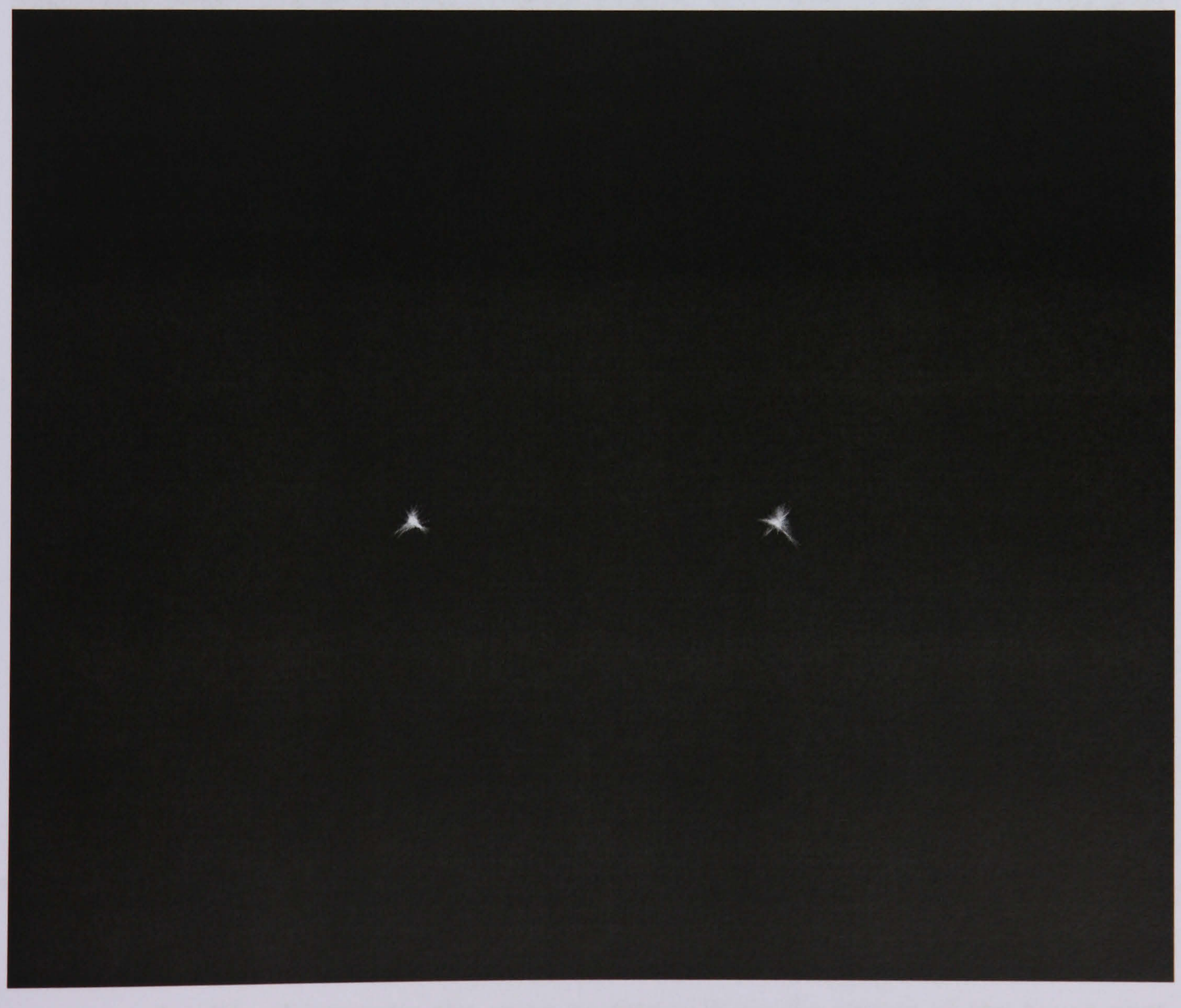

Figure 4.52: The output image of the Hough Transform accumulator after the 2^{nd} cut has been applied.

Figure 4.53 shows the resulting output image of the cut applied (with a lower cut limit of 70%) to the Hough Accumulator output when one of the beam spot centres has moved off the edge of the active surface of the camera.

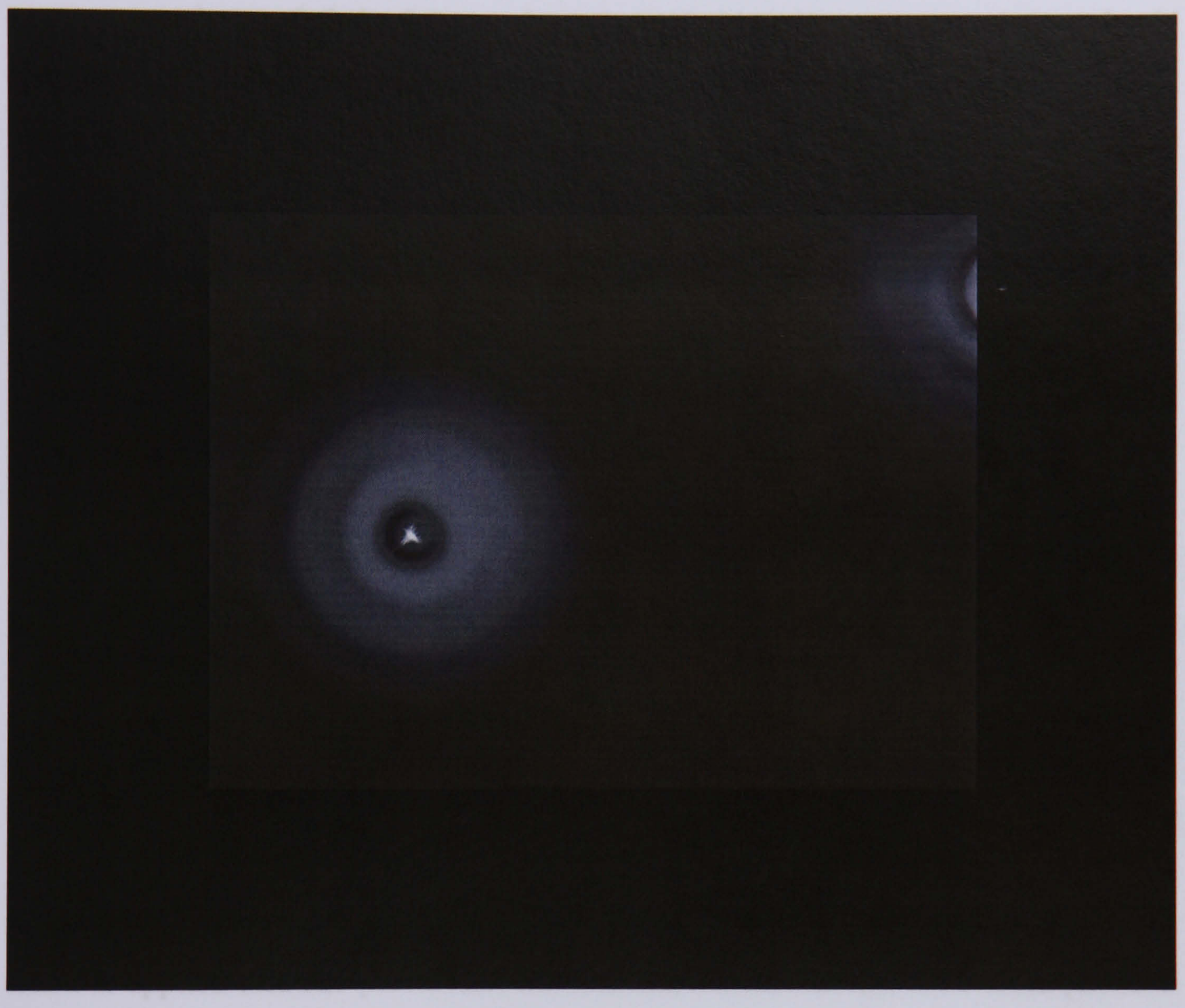

Figure 4.53: The output image of the 2^{nd} Cut algorithm superimposed with the output image of the Smoothing filter.

The beam spot centre of the 2^{nd} spot, though still there has become faint. This suggests that if the beam spot centre is still to be tracked when the beam spot moves further off the edge of the active surface of the camera, then the lower limit cut level will need to be lowered. However, the smaller the edge that the Hough Accumulator has to work with, the greater the error in determining the centre of the beam spot. Therefore, a small study has been made at the end of this chapter to show the correlation between the distance that the beam spot centre has moved off the edge of

the active surface of the camera and the associated error in the determination of the beam spot centre. The results of this study will help to determine the optimal lower cut limit. If the error due to low centre accumulation causes the resolution of the segment monitor to fail the 0.1 *mrad* requirement, then the segment monitor should be made redundant, and the lower cut limit should be set to reflect this cut off point.

4.5.6 Anomaly Removal

Anomaly removal is an important stage of the image analysis. We define an anomaly as a local spurious maximum that may mimic the centre of a spot. As a result of the cut on the Hough Accumulator output, it is most likely that small accumulations will remain in the image that are not connected to the main accumulations located at the centres of the beam spots. Therefore, if the spot location algorithm is run without anomalies being removed first, the spot location algorithm may find more than two spots.

Method

Figure 4.54 shows the three masks that are used in the Anomaly Removal algorithm. The first image, figure 4.54(a), is a 3×3 pixel mask and is the first mask that is applied. The pixel denoted by the letter 'p' is the pixel of interest around which the mask is applied and the pixels that are marked with an 'x' are the border pixels of the mask.

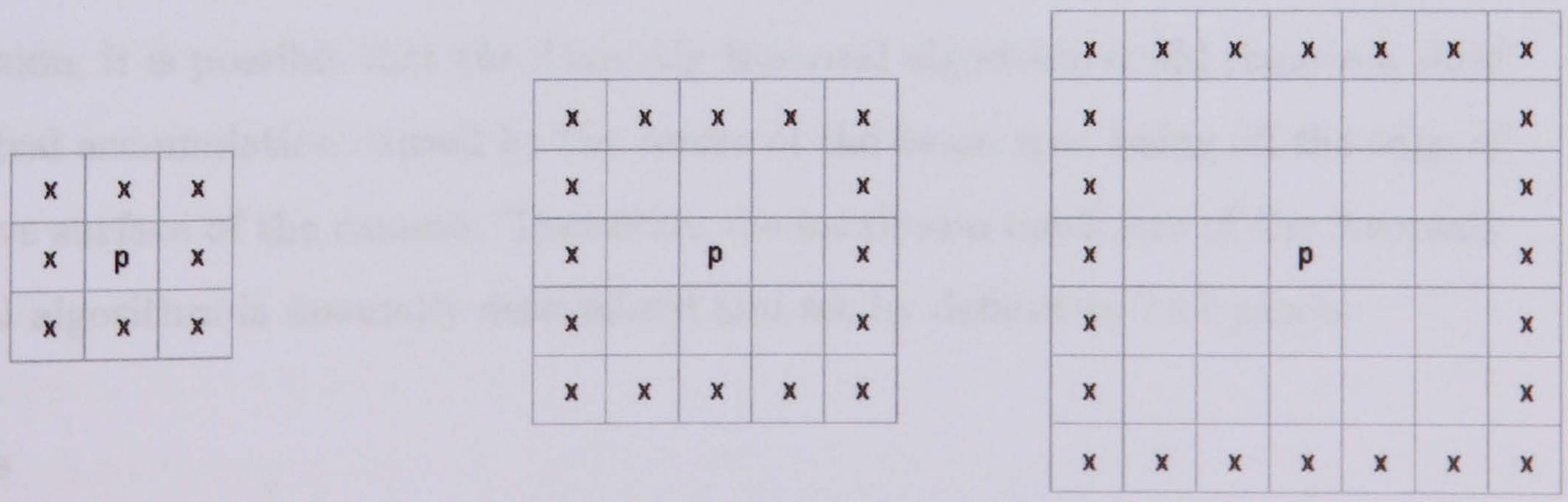

(a) (b) (c)

Figure 4.54: Anomaly removal masks.

The Anomaly Removal algorithm scans every pixel in the image (except for a 1 pixel wide border) and applies the first mask around each pixel that has a value greater than zero. Each time the mask is applied the algorithm asks an anomaly check question "Are all the border pixels zero?". If the answer is yes, then pixel p is given a zero value, if the answer is no, then pixel p is ignored and the algorithm moves on to the next pixel.

When the whole image has been scanned the process is repeated with the larger mask sizes shown in figures 4.54(b) and 4.54(c). With these larger masks of 5×5 and 7×7 pixels, if the answer is yes to the anomaly check question, and all the border pixels are zero, then not only is pixel p given a zero value but also are all the pixels within the borders of the mask.

The maximum size of anomaly that can be removed by a mask size of $n \times n$ pixels is $m \times m$ pixels, where $m = (n - 2)$. By applying these three masks to the image with a maximum mask size of 7×7 pixels, any small accumulation with an area of 5×5 pixels or less in size will be removed. It should be noted that if the mask size is 5×5 pixels, then the mask can be applied to any pixel in the image except for those that are contained within a 2 pixel wide border around the image. Similarly, if the mask size is 7×7 pixels, then the mask can be applied to any pixel in the image except for those that are contained within a 3 pixel wide border around the image.

It is possible that the maximum mask size used by the Anomaly removal algorithm could be determined in an automated manner by imposing that it contain the largest accumulation in the image. However, by making the process automated in this fashion, it is possible that the Anomaly Removal algorithm could remove a valid low central accumulation caused by the centre of the beam spot being off the edge of the active surface of the camera. Therefore, the maximum mask size of the Anomaly Removal algorithm is manually determined and set by default to 7×7 pixels.

Results

Figure 4.55 shows a blown up image of the right hand beam spot taken from figure 4.52. The blue squares outline areas that contain non-zero pixels when all of the blue pixels are equal to zero. Each of the areas highlighted are recorded as spot

centres in addition to the centre of mass location if the Anomaly Removal algorithm is not applied.

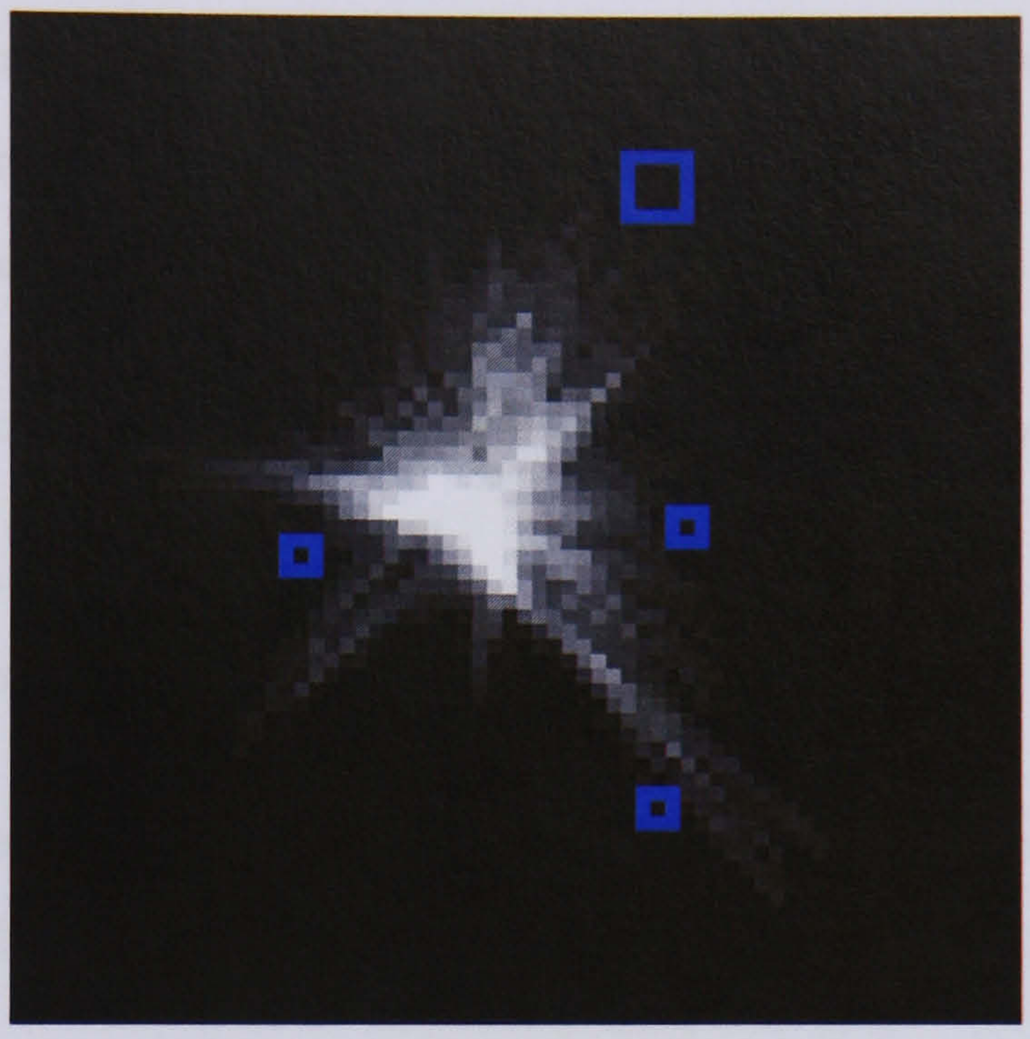

Figure 4.55: Anomaly Removal from the right hand beam spot of figure 4.52.

4.5.7 Spot Location

The Spot Location algorithm uses masks that are based on the same principle as those used in the Anomaly Removal algorithm. By scanning the image until a non-zero pixel is found, the algorithm begins the process of incrementally increasing the mask size until it encapsulates the whole of the beam spot. This process continues for each non-zero pixel found in the image. The algorithm will ignore any non-zero 'pixel of interest' encountered that is determined not to be a pixel at the centre of an accumulation but instead a pixel that is located on the edge of the accumulation. In the method of locating the beam spot accumulations, the Spot Location algorithm must determine whether or not the pixel of interest is adjacent to the centre of the accumulation. In order for the algorithm to run in a concise manner, the first section of the method assumes that the pixel of interest is adjacent to the centre until it determines otherwise.

Method

The spot location algorithm starts with a mask size of 9×9 pixels. It will then begin to scan the whole image with this mask column by column, row by row (except for a 4 pixel wide border) . Eventually, the mask will find non-zero pixels. At this point the algorithm asks two centre determination questions in order:

1. Are there non-zero pixels on opposing sides or diagonally opposing corners of the mask?

2. Are all of the border pixels zero?

In the example shown in figure 4.56, by asking the first centre determination question, the algorithm will determine that it has found an edge pixel because the answer will be no.

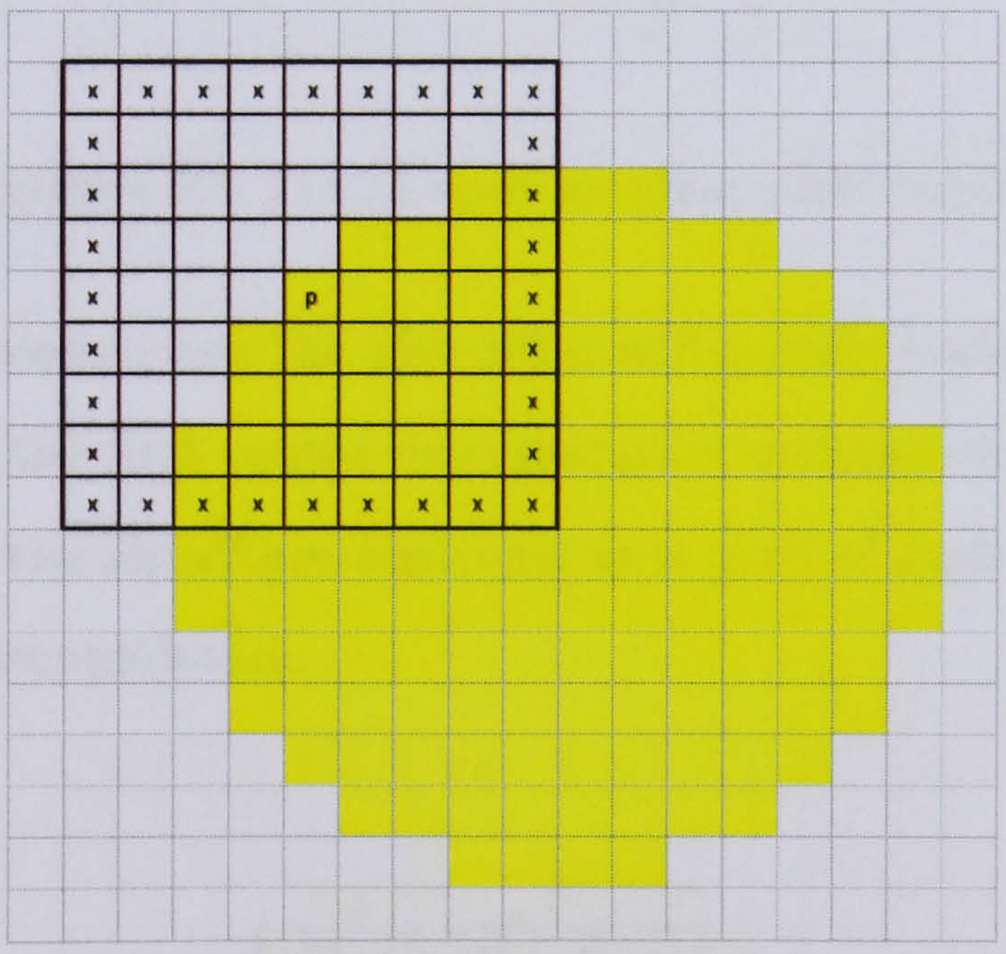

Figure 4.56: 9×9 spot location pixel mask.

However, at this point, the algorithm cannot be entirely sure that it really does have an edge pixel, since the only information that the algorithm has at this stage is contained within the mask. As far as the algorithm understands, it may be that, if it increases the mask size by one increment around its current location, the whole accumulation could then be contained within the borders of the mask. Therefore the algorithm will increase the mask size by one increment from 9×9 to 11×11 (fig-

ure 4.57). The algorithm will then ask the second centre determination question and if the answer is no then the algorithm will conclude that the pixel of interest cannot be a centre pixel and will therefore ignore that pixel and move on to the next. Every time the algorithm moves to a new pixel of interest, the mask size returns to a square of 9×9 pixels.

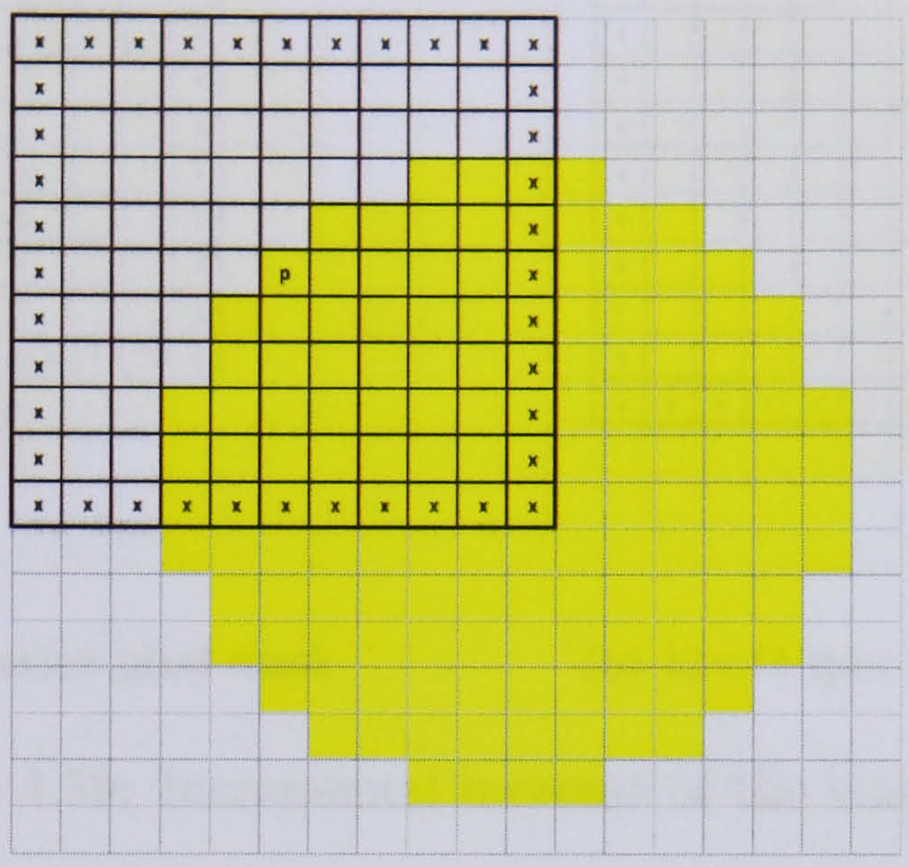

Figure 4.57: 11×11 spot location pixel mask.

Following the above process, the algorithm will quickly come to a pixel of interest where the answer to the first centre determination question is yes. In the example shown in figure 4.58, the algorithm has come to a pixel of interest p that is adjacent to the centre of the accumulation.

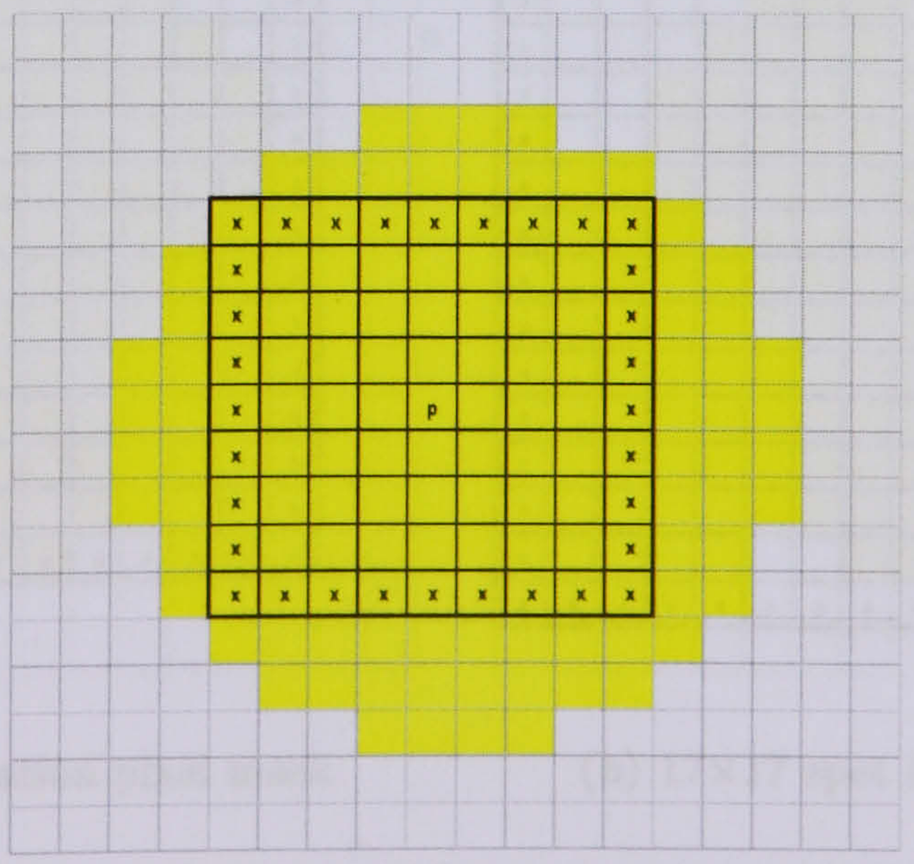

Figure 4.58: 9×9 spot location pixel mask.

As the mask size increases in size as in figures 4.59(a) and 4.59(b), the number of non-zero pixels on opposing sides and diagonally opposing corners decreases.

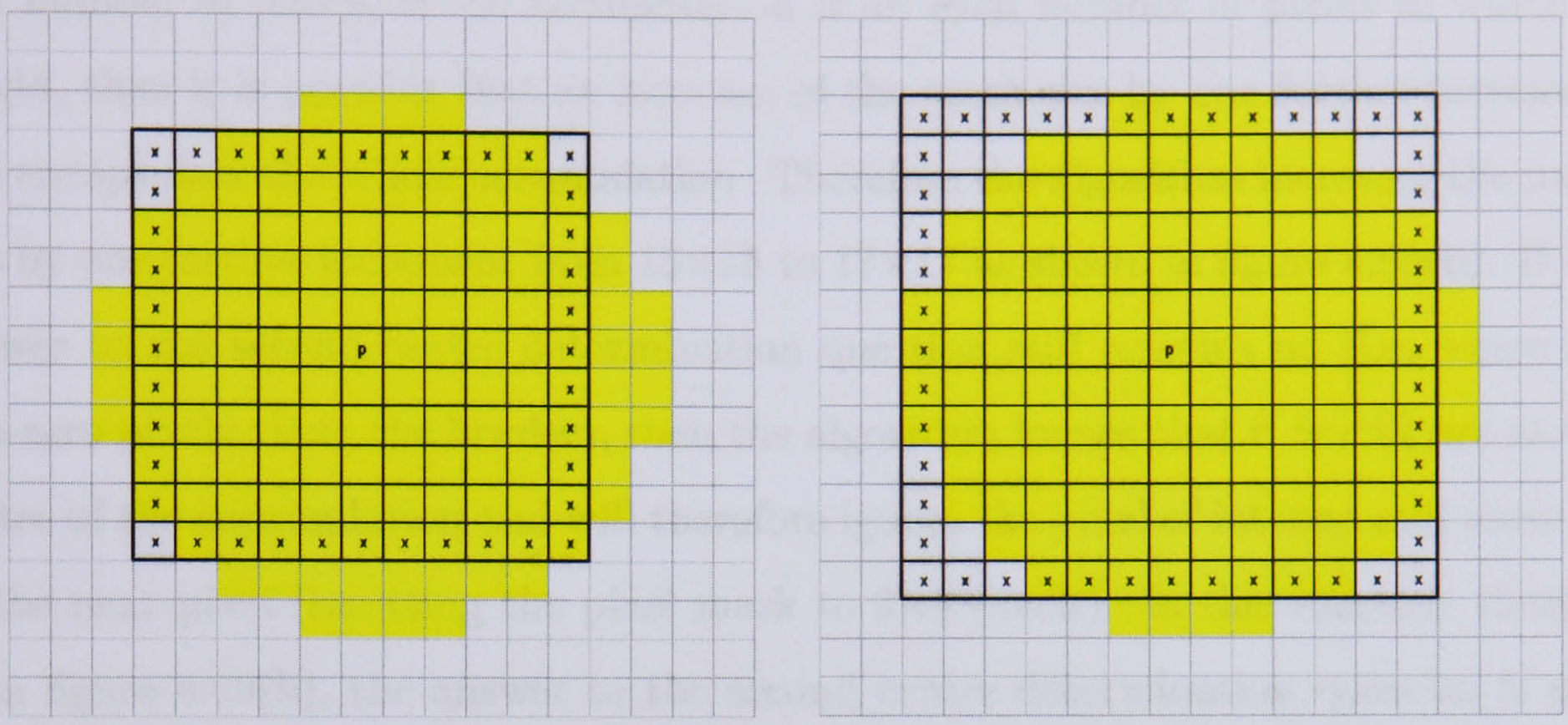

(a) 11×11 spot location pixel mask (b) 13×13 spot location pixel mask

Figure 4.59: Incremental increase of the mask size.

When the mask size has increased to a sufficient size, diagonally opposing corners and opposing sides will contain pixels of zero value. However, the mask size may still not be large enough for all of the pixels to be contained within the borders of the mask (figure 4.60(a)). Then the algorithm asks the second centre determination

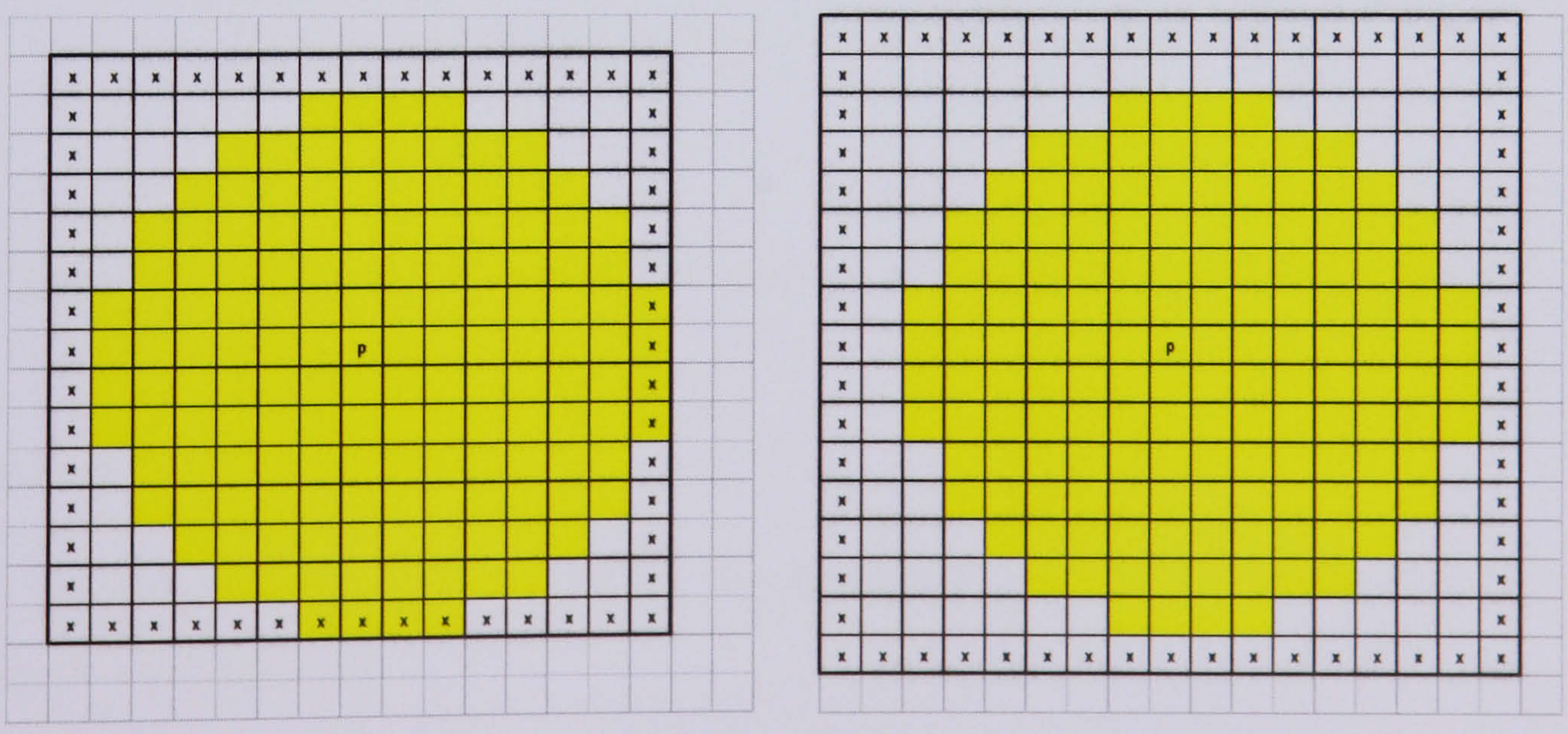

(a) 15×15 spot location pixel mask (b) 17×17 spot location pixel mask

Figure 4.60: Continued incremental increase of the mask size.

question. In the case of figure 4.60(a), the answer to this second question is no.

However, at this stage the algorithm cannot decide whether the pixel width and/or height of the accumulation is even or odd. Given the fact that the pixel mask is an odd number of pixels, if the accumulation is an even number of pixels in width or height, then it is possible that an increase of the mask size by one further increment will encapsulate the whole accumulation. Therefore the algorithm increases the mask size by one further increment from 15×15 to 17×17 as shown in figure 4.60(b). If the answer to the second centre determination question still remains no (i.e. there are non-zero pixels along the border), then the algorithm knows that it is still not at the centre of the accumulation and will therefore ignore the pixel of interest and move on to the next pixel (resetting the pixel mask to 9×9 pixels). In this example though, from figure 4.60(b), the answer to the second centre determination question is now yes and it has found a region fully containing the centre of accumulation. It can now proceed to find the centre of the beam spot by applying a centre of mass calculation to the mask, writing the result to the output array and then continuing to search the image for further accumulations.

4.5.8 Weighted "Centre of Mass" Calculation

By taking the mask shown in figure 4.60(b) one can calculate the column and row totals (numbers in blue) from the grey-scale values of each pixel. For example, pixel 7(p) has a value of 7, the (p) shows that it is the pixel of interest and is thus the central pixel in the mask.

x →

y ↓	1	2	3	4	5	6	7	8	9	10	11	12	13	14	15	16	17	
1	x	x	x	x	x	x	x	x	x	x	x	x	x	x	x	x	x	0
2	x																x	0
3	x							1	1	1	1						x	4
4	x					1	1	1	1	1	1	1	1				x	8
5	x				1	1	1	2	2	2	2	1	1	1			x	14
6	x			1	1	1	2	2	2	2	2	2	1	1	1		x	18
7	x			1	1	2	2	2	5	5	2	2	2	1	1		x	26
8	x		1	1	2	2	2	5	5	5	5	2	2	2	1	1	x	36
9	x		1	1	2	2	5	5	7 (p)	7	5	5	2	2	1	1	x	46
10	x		1	1	2	2	5	5	7	7	5	5	2	2	1	1	x	46
11	x		1	1	2	2	2	5	5	5	5	2	2	2	1	1	x	36
12	x			1	1	2	2	2	5	5	2	2	2	1	1		x	26
13	x			1	1	1	2	2	2	2	2	2	1	1	1		x	18
14	x				1	1	1	2	2	2	2	1	1	1			x	14
15	x					1	1	1	1	1	1	1	1				x	8
16	x							1	1	1	1						x	4
17	x	x	x	x	x	x	x	x	x	x	x	x	x	x	x	x	x	0
	0	0	4	8	14	18	26	36	46	46	36	26	18	14	8	4	0	

Figure 4.61: Column and row totals used to calculate the two centres of mass.

Method

The method of finding the values for the centres of mass in the x or y directions is given by the equations:

$$WeightedX = \frac{\Sigma(x_1 \times R_1 + x_2 \times R_2 + ...x_n \times R_n)}{N} \tag{4.12}$$

and

$$WeightedY = \frac{\Sigma(y_1 \times C_1 + y_2 \times C_2 + ...y_n \times C_n)}{N} \tag{4.13}$$

where x_n is the row number, R_n is the row total for row x_n, y_n is the column number, C_n is the column value at y_n and

$$N = (R_1 + R_2 + ...R_n) = (C_1 + C_2 + ...C_n). \tag{4.14}$$

These equations give the centre of mass position with respect to the top left corner of the mask. The centre of mass can also be expressed with respect to the pixel of interest (pX, pY), as follows

$$pX = WeightedX - \frac{(M+1)}{2} \tag{4.15}$$

and

$$pY = WeightedY - \frac{(M+1)}{2} \tag{4.16}$$

where M is the mask size. Thus the centre of mass location (X_{out}, Y_{out}) to be written to the output image is

$$X_{out} = x_{image} + pX \tag{4.17}$$

and

$$Y_{out} = y_{image} + pY \tag{4.18}$$

where x_{image} and y_{image} are the x and y locations of the pixel of interest in the image. In the example in figure 4.61, $X_{out} = 9.5$ and $Y_{out} = 9.5$.

Following the method given for the Spot Location algorithm, the same accumulation may be found more than once by different pixels of interest. However, once the weighted centre of mass calculation has been made, the ultimate location result of the beam spot centre with respect to the output image will be the same for each instance in which the accumulation is found, regardless of the pixel of interest.

The accuracy of the measurement depends upon size, but for typical beam spot images we observe an accuracy with regard to the geometric centre of under 5 pixels.

4.5.9 Image Analysis Software Results

The net result for the joint use of the Anomaly Removal, Spot Location and Weighted Centre of Mass algorithms is an output image that only has two non-zero pixels. Each non-zero pixel represents the centre of a beam spot. The result of applying these algorithms to figure 4.52 is given in figure 4.62. The two non-zero pixels are highlighted by blue crosses.

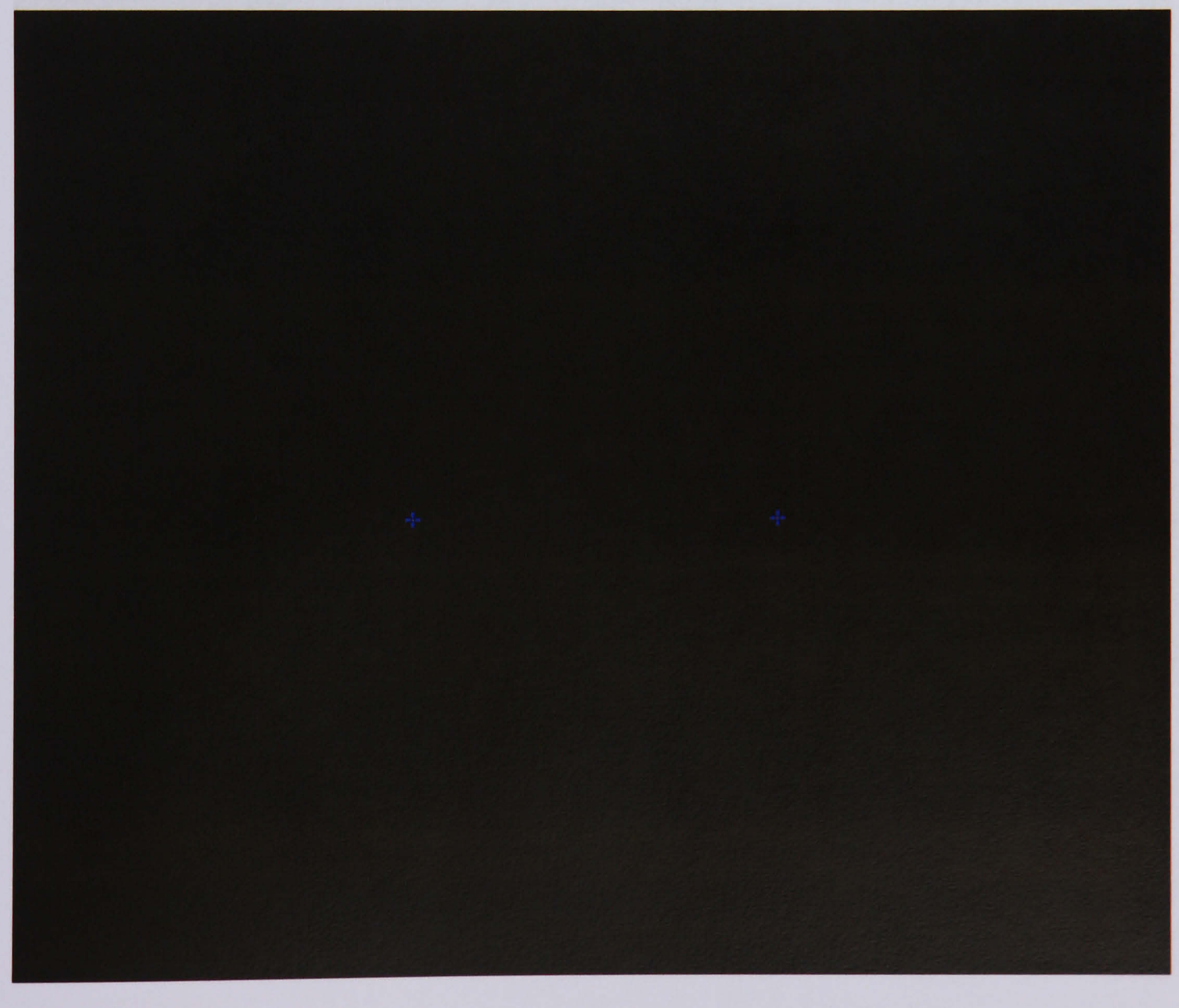

Figure 4.62: The result of the centre of mass calculations for the two centres of mass.

Figure 4.63 shows the final result superimposed with the 2^{nd} cut and smoothing filter output images (figures 4.52 and 4.43). These two points are required as repeat-

able reference points so that accurate calculations of the difference between the two beam spots can be made. However, the Image Analysis software produces a result that visibly supplies an accurate representation of the two beam centres.

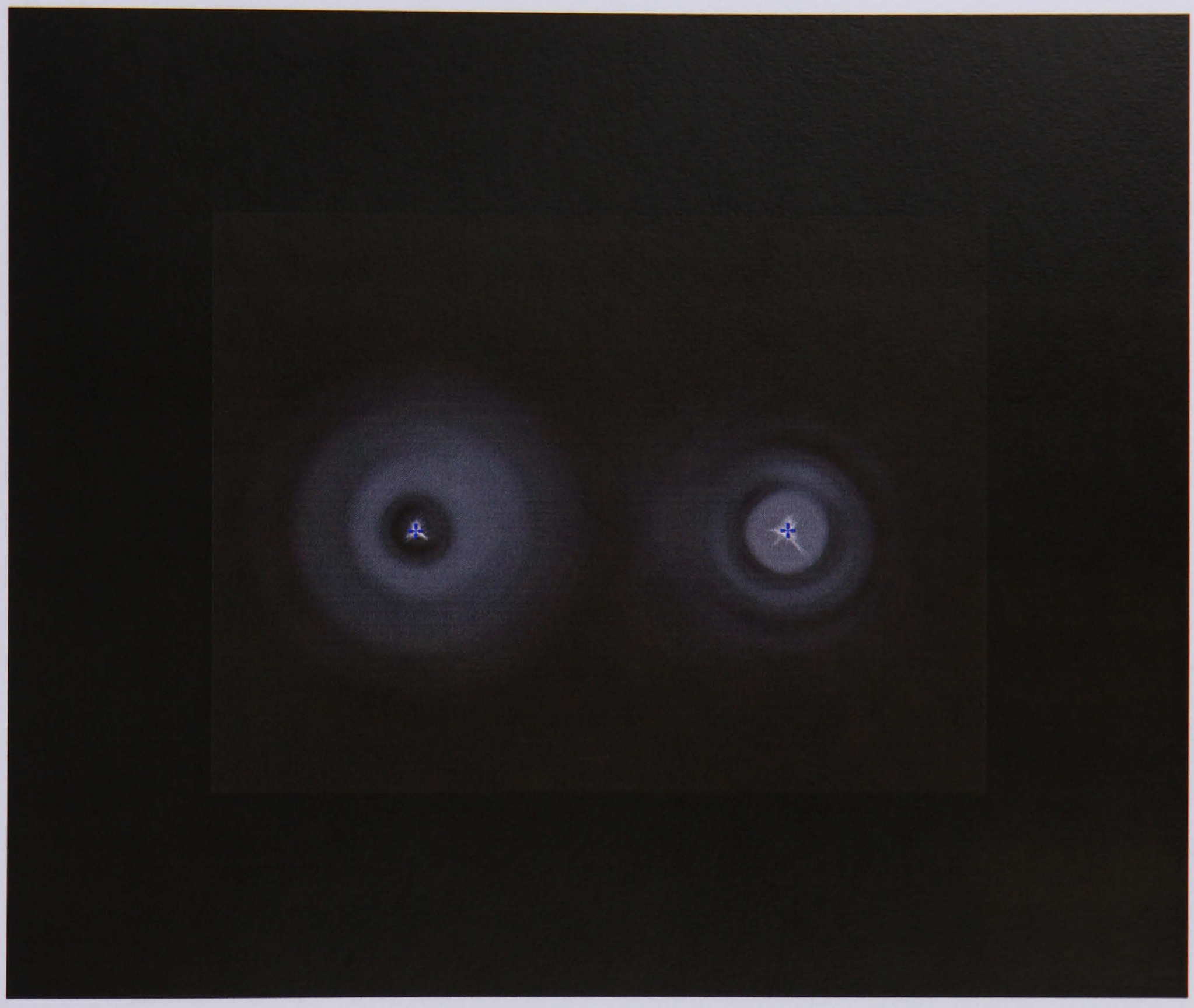

Figure 4.63: Final image analysis result.

4.5.10 Beam Spot Tracking off the Edges of the Cameras Active Surface

This final section of the Image Analysis software is a short study of how the accuracy of the image analysis software degrades as one of the beam spots moves off the edge of the active surface of the camera. This is not designed to be a comprehensive study, but an indicator of what to expect. The results in figures 4.64 and 4.65 have been produced by editing an image so that the second beam spot can be moved by a known

quantity. The second spot (the signal spot located on the right side of the image) was placed at the right hand side of the image first minima was on the edge. The beam spot was then moved by known quantities in the horizontal direction only to the right such that the beam moved off the edge of the active surface of the camera. Each time a movement was made, the image was analysed by the Image Analysis Software. The final position of the beam spot is given in figure 4.51. The results in figures 4.64 and 4.65 show that the error in tracking the image increases as the beam moves further off the edge.

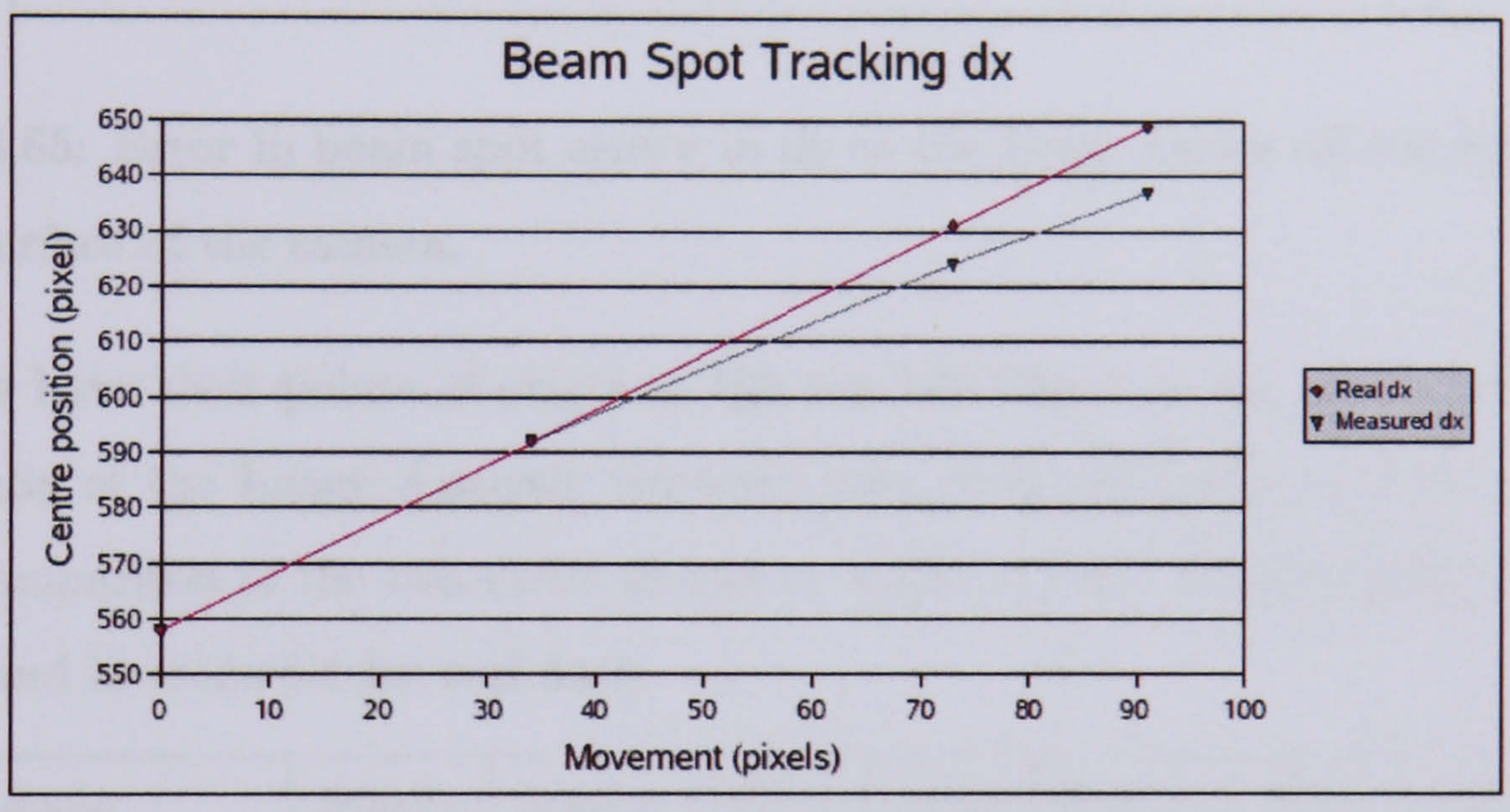

Figure 4.64: Error in beam spot centre in dx as the beam moves off the edge of the active surface of the camera.

4.6 Comparison Image Analysis Software and Gaussian Fit Method

This section of the thesis is a direct comparison of the Gaussian fit method and Image Analysis Software. The following results are for the same images, on exactly the same computer. The computer used is a PIII 1GHz with 384MB of RAM. Tables 4.3 and 4.4 show the real x, y centre for each beam spot for each image, and the centres given by the Gaussian fit method (GFx,GFy) and the Image Analysis Software ($IASx$,$IASy$). The x axis and y axis of the Gaussian fit method have their points of origin at the bottom left corner of the image, where as the x and y axis of the Image Analysis

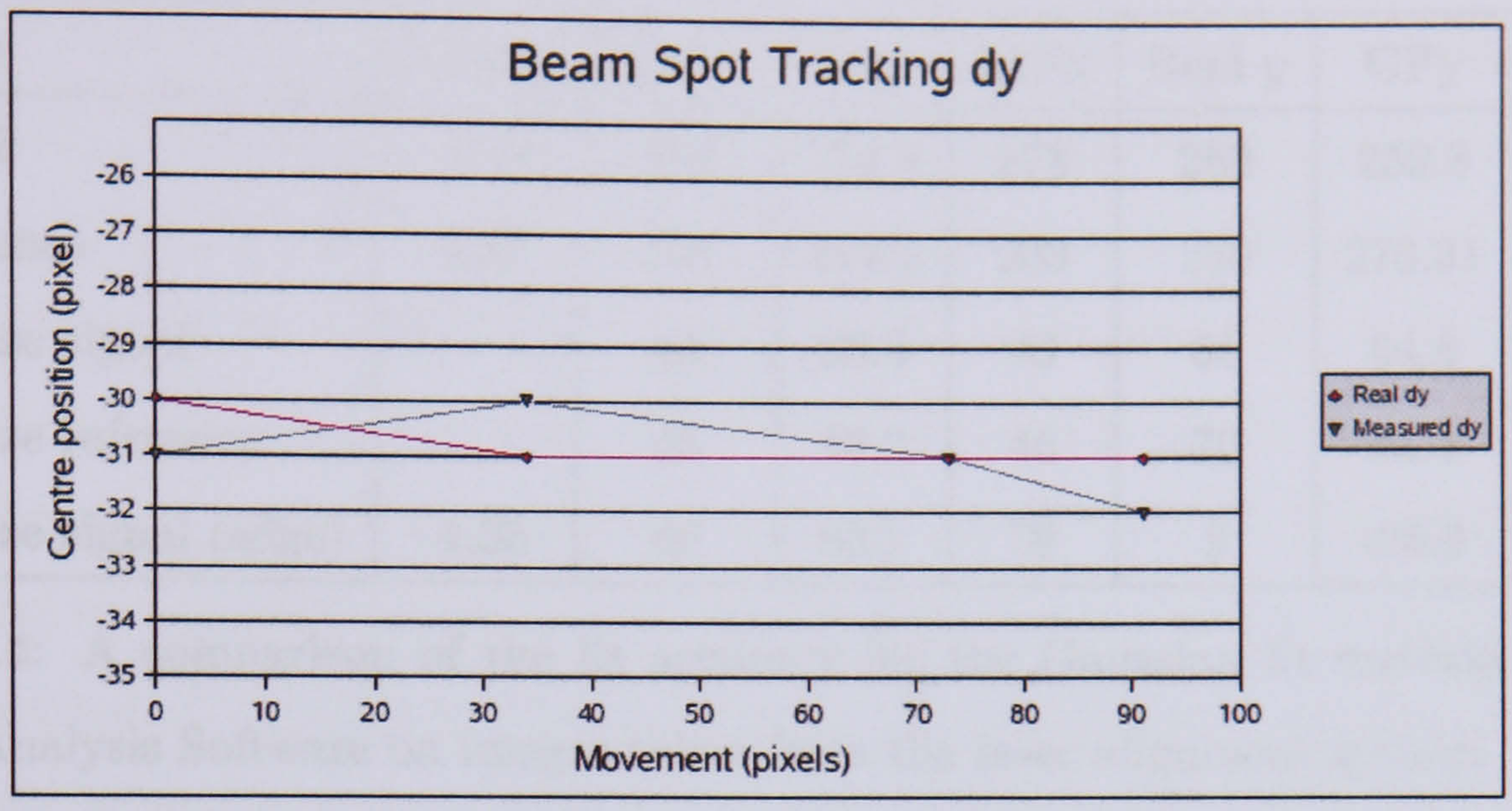

Figure 4.65: Error in beam spot centre in dy as the beam moves off the edge of the active surface of the camera.

Software have their points of origin at the top left corner of the image. Therefore, the results of the Image Analysis Software have been vertically inverted so that a direct comparison of the two methods can be made in table 4.3 for perfect Gaussian images and in table 4.4 for real data.

Image	Figure	Real x	GFx	IASx	Real y	GFy	IASy
Small centre	4.31	127	127.8	127	63	63.5	63
Large centre	4.32	127	127.6	127	63	62.79	64
Saturated	4.33	128	128.2	128	64	62.92	64
Edge	4.34	255	251.8	254	63	63.2	64
Off-edge	4.35	265	255.8	263	63	63.2	63

Table 4.3: A comparison of the Gaussian fit method and the Image Analysis software on Gaussian test images (in pixel number).

The results show that for real Gaussian images, both the Gaussian fit method and the Image Analysis Software perform very well under normal conditions. However, when the Gaussian spot moves off the edge of the image, the Gaussian fit method does not correctly find the centre of the spot, whereas the Image Analysis software continues to perform very well.

Image	Figure	Real x	GFx	IASx	Real y	GFy	IASy
Signal	4.36	178	154.9	178	260	259.8	263
Reference	4.37	203	214.5	203	260	270.31	263
1/4 size signal		45	38.5	43	65	64.6	65
1/4 size reference		46	46.2	46	70	66.4	67
1/4 size signal (edge)	4.38	80	69.7	79	2	-25.9	0

Table 4.4: A comparison of the fit accuracy for the Gaussian fit method and the Image Analysis Software on images taken from the laser alignment system.

As can be seen from table 4.4, the Image Analysis Software is a more accurate method of finding the beam spot centre for the non-Gaussian images produced by the laser alignment system. Table 4.5 shows the results of the comparison of processing time for the two fit methods.

Data	Image	Figure	GF time (min:sec)	IAS time (min:sec)
Simulated	Small centre	4.31	2:19	0:01
	Large centre	4.32	1:40	0:01
	Saturated	4.33	1:23	0:01
	Edge	4.34	2:00	0:01
	Off-edge	4.35	2:14	0:01
Real	Signal	4.36	34:23	0:06
	Reference	4.37	50:12	0:06
	1/4 size signal		1:55	0:02
	1/4 size reference		1:40	0:02
	1/4 size signal (edge)	4.38	10:06	0:02

Table 4.5: Results of the Gaussian fits on the simulated Gaussian test images (top) and real data (bottom).

The processing time for the Image Analysis Software is significantly faster than the Gaussian fit method when used with the Gaussian test images. When compared

using real full size images from the laser alignment system, the processing time for the Gaussian fit method greatly increases. In contrast, the Image Analysis Software continues to be a fast and reliable algorithm under all test conditions.

The Gaussian fit method for centroid location works very well when the profile being fitted is Gaussian in shape and within the bounds of the image. However, the performance of the fitting method degrades significantly both in accuracy and processing time when used on full size images that deviate from a perfect Gaussian representation. Furthermore, the Gaussian fit method fails to accurately locate the centres of the profiles as they move off the edge of the image. This handicap reduces the effective measurement range of the alignment system. Under the consideration that there are 16 segment monitors that will each produce an image for processing, the poor performance of the Gaussian fit method with the alignment system images drove the development of the Image Analysis Software with the aim of creating a method of centroid location that remains robust and accurate under the varying possible circumstances of the alignment system (such as when the beams start to move off the edge of the image).

The Image Analysis Software in all of the tests has shown itself to fulfill all expectations. It is robust, very fast and more accurate than the Gaussian fit method when used with real images from the prototype laser alignment system. The error is never more than a few pixels. For this reason it is the software of choice for the final laser mirror alignment monitoring system.

4.7 Sensor Technologies

Charged Coupled Devices (CCD's)

A CCD is a pixelated silicon based photon sensing device that stores charge from a signal produced by an incident photon on the silicon. When a photon of greater than 1.26 eV is absorbed into the photosensor of a pixel by an electron in the valence band of a silicon atom, the electron becomes excited into the conduction band and is thus free to move in the silicon crystal lattice. A small electric field guides the electron to the corresponding charge bucket for that pixel.

CCD's are read out row by row. To read out a row of a CCD, the charge of the rightmost bucket is measured and stored into memory. The charges in each of the remaining buckets in the row are then shifted one pixel to the right and the process is repeated until the whole row has been read out. Upon completion of the readout of the row, the charges in each of the remaining rows are read out until the whole image has been obtained [47]. For most applications this method of readout is robust, however, a charge bucket badly damaged by radiation can cause a severe loss of data through in efficient charge passing as charges are transported through it. For this reason, CCD's are generally considered to be radiation soft.

Complementary Metal Oxide Semiconductor (CMOS) Sensors

Like CCDs, CMOS Active Pixel Sensors (APS) include an array of photo-sensitive diodes, one diode within each pixel. However, in contrast to the CCD, each pixel in a CMOS sensor has its own individual integrated amplifier and hence this type of sensor is referred to as an "active pixel sensor". Each pixel can be read directly on an x,y coordinate system, rather than the sequential readout process of a CCD. While the charge of a CCD pixel is always transferred to an adjacent pixel until it can be read out, the charge held by a CMOS pixel is read out directly [65]. This means that a CMOS pixel damaged by radiation will not affect the readout of neighbouring pixels and thus the damage is contained. This makes the CMOS APS a more radiation hard solution.

There are additional benefits of CMOS APS technology. When exposed to high light intensities CCD sensors suffer from artefacts caused by charges flowing to neighbouring pixels, that in turn change the information of the whole column in the image. This effect is known as blooming. Because CMOS APS pixels are read out directly they are more resistant to blooming. In addition to this, logarithmic compression such as Photonfocus' LINLOG^{TM} can be used on a CMOS APS at the pixel level to further reduce blooming effects and even allow in-scene contrasts of over 120 dB [5].

Electronic Shutters

There are two types of electronic shutter that can be found in both CCD and CMOS APS technologies. These are known as electronic rolling and electronic global (frame) shutters.

In the case of the electronic rolling shutter, the rows of the sensor are exposed in a staggered timed sequence, starting at the top row and ending at the bottom row, such that each row is exposed for the same amount of time. While the other rows are still being exposed the readout sequence starts at the top row of the sensor and starts to make its way down the sensor. The electronic rolling shutter provides a high speed, high frame rate through-put of data, however it is susceptible to the incorrect capture of high speed movements.

With the electronic global shutter the whole sensor is exposed at the same time for a fixed period. Once exposure of the sensor is complete, the read out process can begin. Because there is no simultaneous readout of parts of the sensor while other parts are being exposed, capture of a single image takes longer than it does with the electronic rolling shutter. However, the advantage of the electronic global shutter is that the sensor correctly captures images where high speed movements are involved. Due to the increased circuitry required at the pixel level for the electronic global shutter to function, devices that use these shutters tend to have larger pixels.

Sensor Choice

In this application, it is important to choose a sensor that is radiation hard with a small pixel size for high resolution measurements. The expected radiation dose in the RICH2 region is 1 $kRad$ (10 Gy) per year. CMOS sensors have been shown to be radiation tolerant up to 0.6 kGy [37]. The sensor chosen for the laser alignment monitoring system is the Lumenera LE-175 CMOS APS camera.

The Lumenera LE-175 [2] utilises the MT9M001 CMOS active pixel sensor [3]. This sensor has a 5.2 μm $\times$ 5.2 μm pixel size with an 800 nm spacing between pixels. The number of pixels in the active surface are 1312 $\times$ 1048 pixels. The first 16 and last 7 columns and the first 8 and the last 7 rows are black pixels. The black pixel

data is used internally by the sensor for automatic black level adjustment. There is then a 4 pixel border of active pixels and an additional column and row of active pixels that are not included in the SXGA image. The remaining pixels form the 1280 $\times$ 1024 SXGA output image. Each SXGA frame takes 33.34 ms to read out using an electronic rolling shutter.

4.8 Results with the Final System and Software

The final prototype system and software tests used the optical components and camera that will be used in the final RICH2 Laser Mirror Alignment System. The setup differs from the previous prototype setup in geometry and in the replacement of the Pulnix CCD with a Lumenera LE-175 CMOS APS camera with a resolution of 1280 $\times$ 1024 pixels and effective pixel size of 6 μm^2. The Lumenera LE-175 also features an ethernet connection and so the shutter and gain functions can be controlled remotely.

4.8.1 Beam Characteristics

Before the final prototype system was setup, beam characteristics of the single-mode fibre were obtained using the setup shown in figure 4.66.

Single-mode Fibre Tests

Using the above setup the beam characteristic tests in section 4.3.1 have been repeated in further detail using the Lumenera LE-175 CMOS camera. The two areas in this test are the repetition of the measurement of beam diameter against distance from the focusing unit and to examine the bare fibre with no focusing unit to check for a Fresnel diffraction pattern. Figure 4.67 shows the result of the beam diameter measurements from 4.5 m to 10.5 m. The plot closely agrees with figure 4.19 with a projected focal point at 9.9 m

Figure 4.68 shows the beam spot image of the 3.5 μm single-mode fibre without the focusing lens at about 12 mm ± 1 mm away from the APS camera. There are some faint rings surrounding the beam spot that are consistent with Fresnel diffraction.

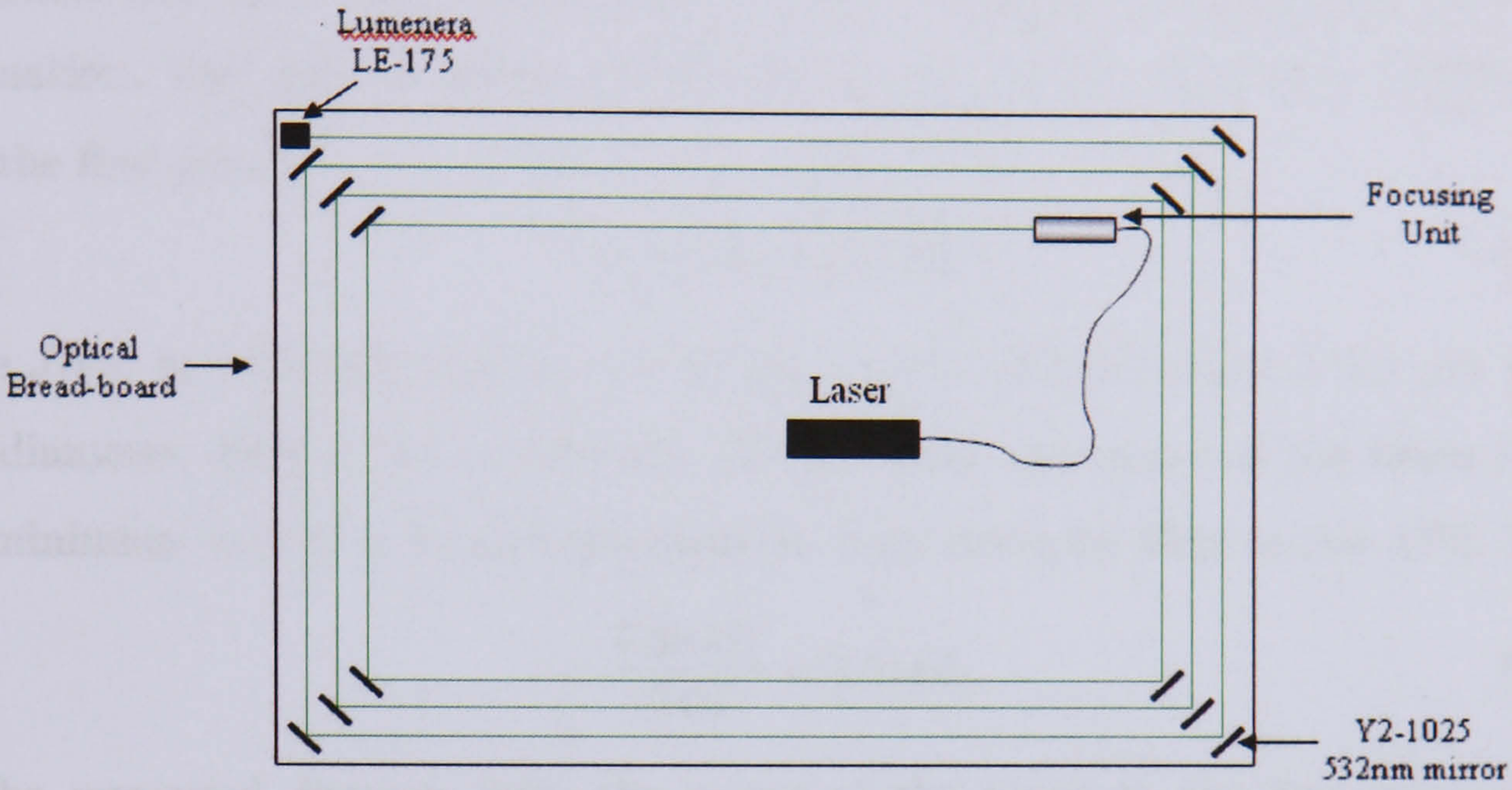

Figure 4.66: Beam characteristic test station.

Figure 4.67: A plot of beam diameter against distance for the single-mode fibre after the focusing unit.

We will approximate the Fresnel diffraction pattern for the simpler Fraunhofer diffraction and show that the ring minima in the image are consistent with this explanation. The zeros of the Fraunhofer diffraction pattern are when: $\left|\frac{J_1(x_0)}{x_0}\right| = 0$, with the first zero at:

$$x_0 = 2\frac{\pi}{\lambda} a \sin\theta = 3.83, \tag{4.19}$$

where $J_1(x)$ is a Bessel function, $\lambda = 532\ nm$ is the wavelength, $a = 3.5\ \mu m$ is the fibre diameter, $\sin\theta = l/D$, with l the distance from the center of the beam to the first minimum, and $D = 12\ mm$ the distance from the optic fibre to the APS. Thus:

$$l = \frac{3.83\lambda D}{2\pi a} = 1.1mm. \tag{4.20}$$

The measured distance from the centre of the beam to the first minimum is $1.17\ mm$. This is consistent with the calculated value of $1.1\ mm$, since the calculated value with $D = 13\ mm$ is $1.2\ mm$. Figure 4.69 shows a plot of the beam diameter against distance for the bare fibre. The plot suggests that the distance value of $12\ mm$ for the first image taken (figure 4.68) is out by about $1\ mm$, making the real value about $13\ mm$. The angle of divergence is 6.1^o.

Figure 4.68: A beam spot image at a distance of 12 mm from the end of a bare single-mode fibre.

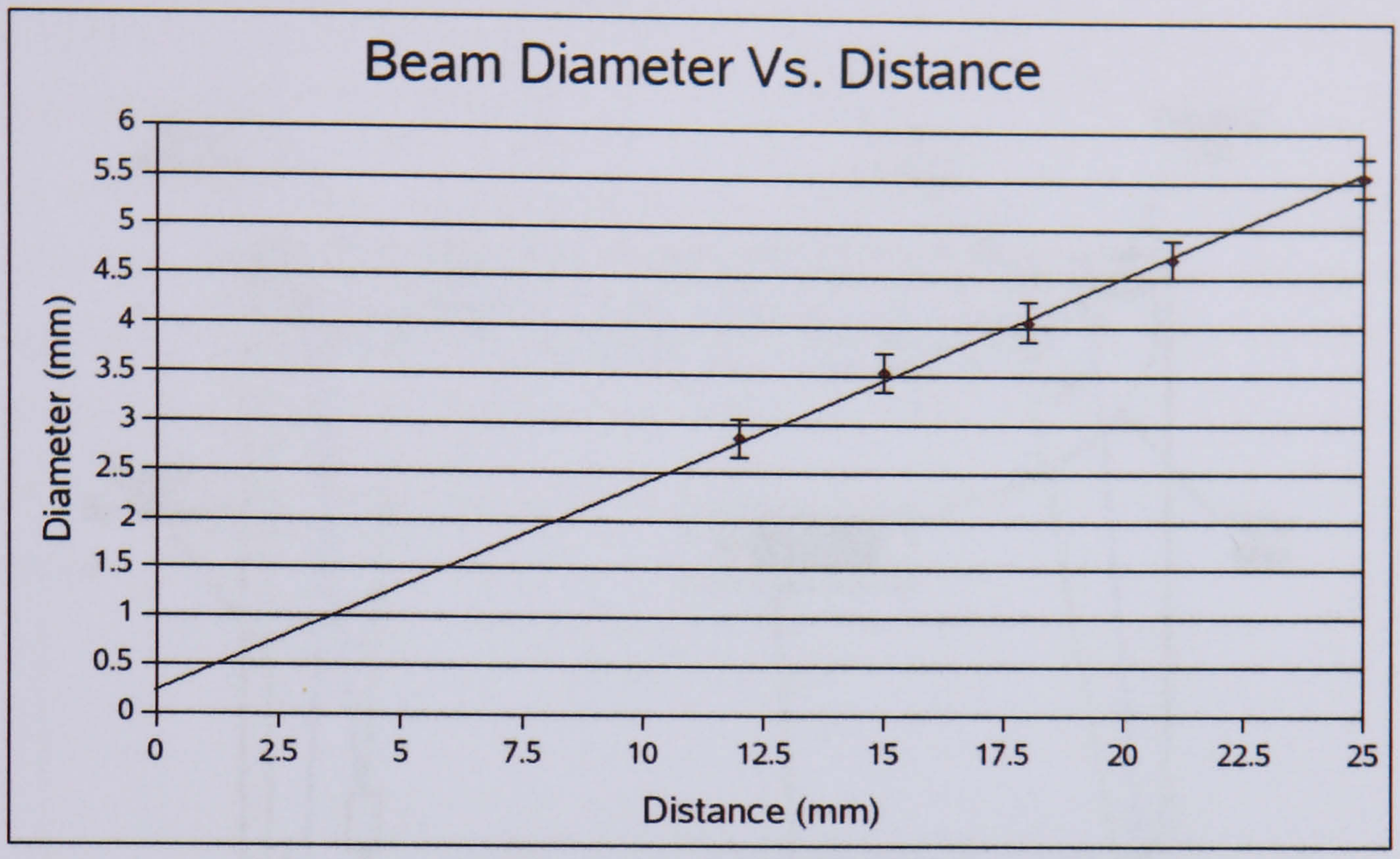

Figure 4.69: A plot of beam diameter against distance for the single-mode fibre with no focusing unit.

4.8.2 Final Prototype Setup

The geometric setup of the final prototype system is shown in figure 4.70, where the blue beam is the reference beam and the green beam is the signal beam.

The distance along the signal beam from the focusing unit to the signal mirror (a small spherical mirror with a centre of curvature of 8.6 m mounted on a RICH2 mirror support, shown in red in figure 4.70) is 2.96 m and the distance from the signal mirror to the CMOS camera is 1.893 m. The incident angle of the signal beam on the signal mirror is 37.9^o and the total path length of the signal beam from the focusing unit to the CMOS camera is 4.853 m. The total path length of the reference beam from the focusing unit to the CMOS camera is 5.039 m. An example image captured in this setup is shown in figure 4.71.

Stability Measurements

Stability measurements were performed to test the consistency of the system with the Image Analysis software in tracking the difference between the two beam spots. With

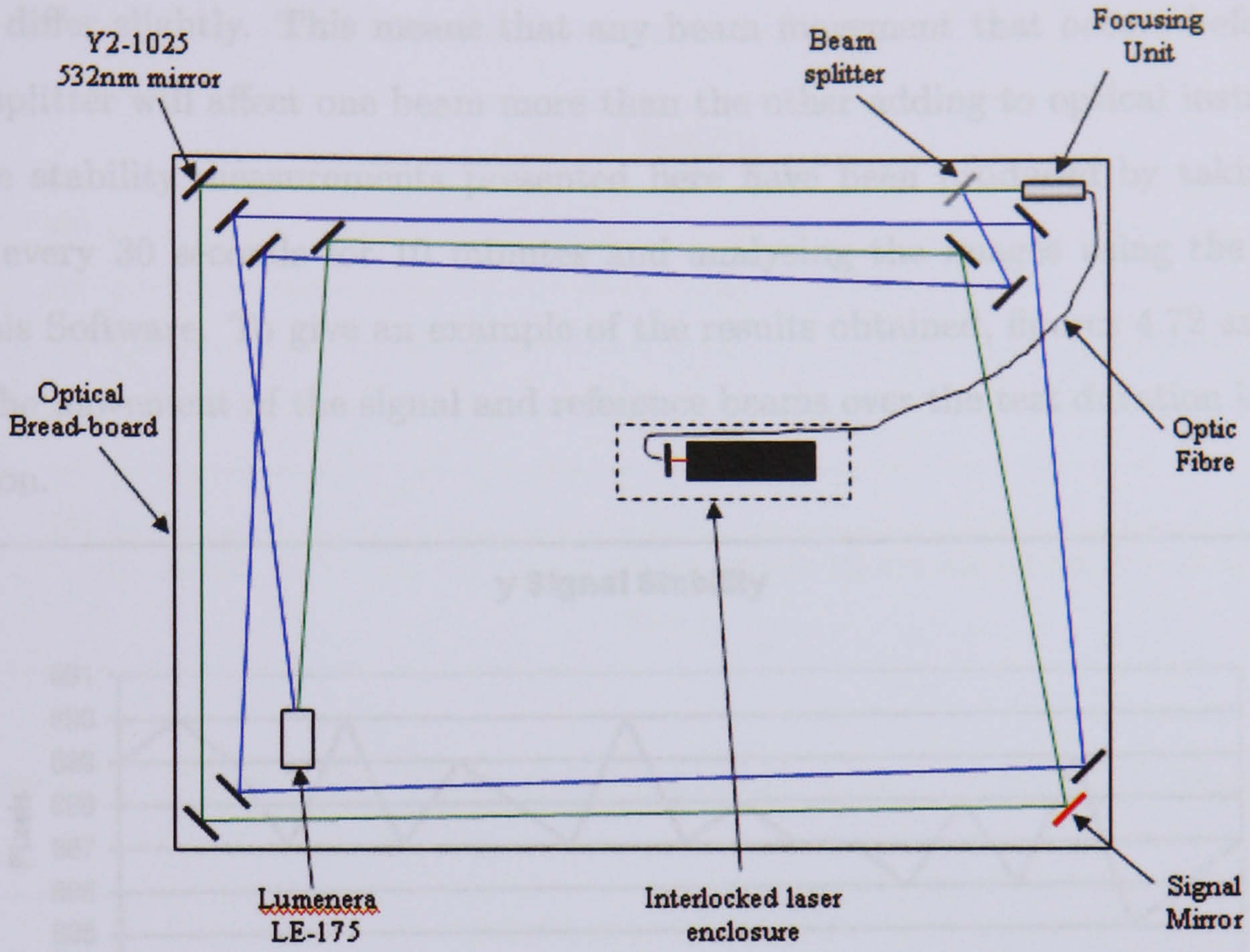

Figure 4.70: Final prototype system setup.

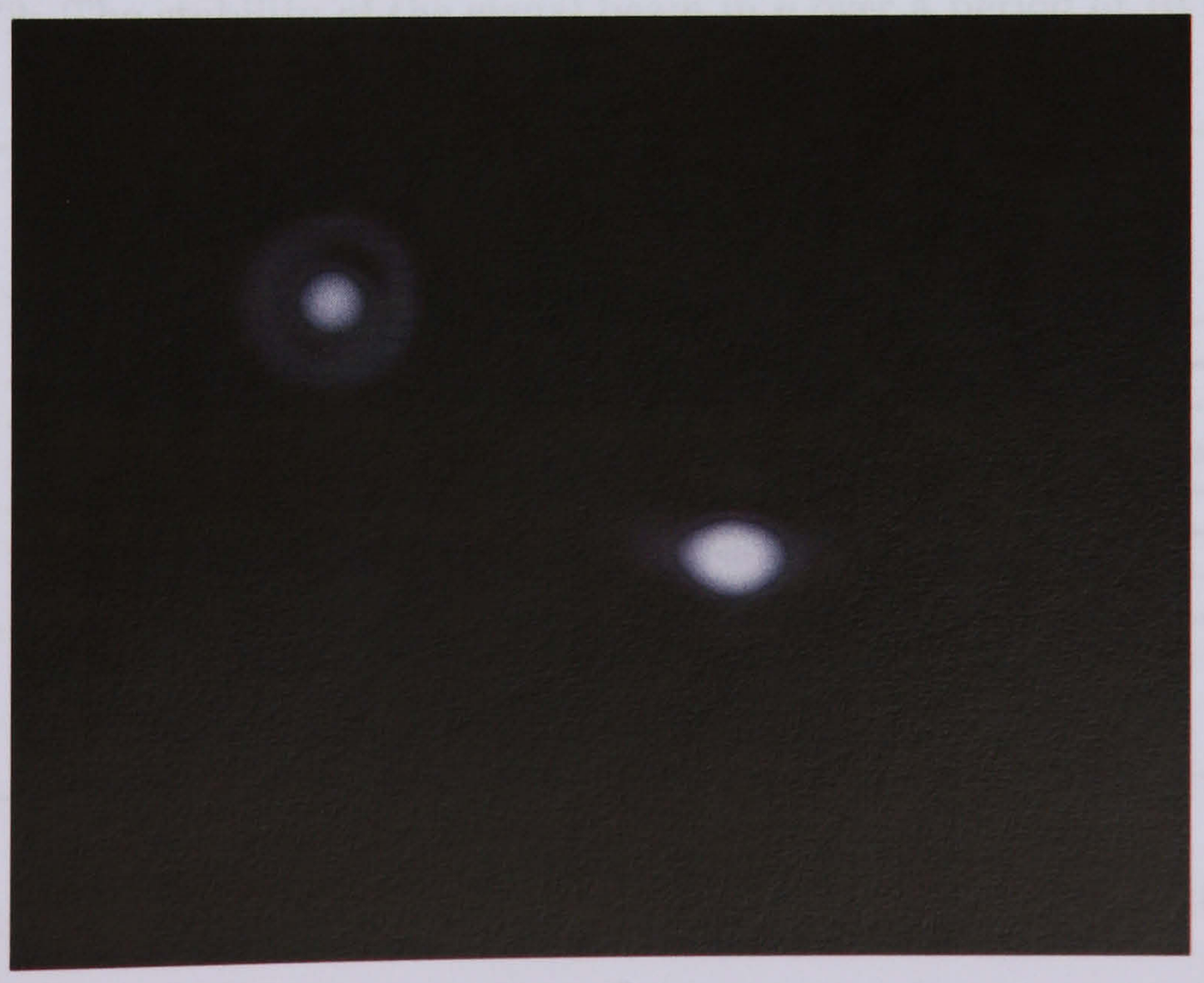

Figure 4.71: Final prototype system setup.

the optical set-up shown in figure 4.70, the path lengths of the signal and reference beams differ slightly. This means that any beam movement that occurs before the beam splitter will affect one beam more than the other adding to optical instability.

The stability measurements presented here have been produced by taking one image every 30 seconds for 10 minutes and analysing the images using the Image Analysis Software. To give an example of the results obtained, figures 4.72 and 4.73 show the movement of the signal and reference beams over the test duration in the y direction.

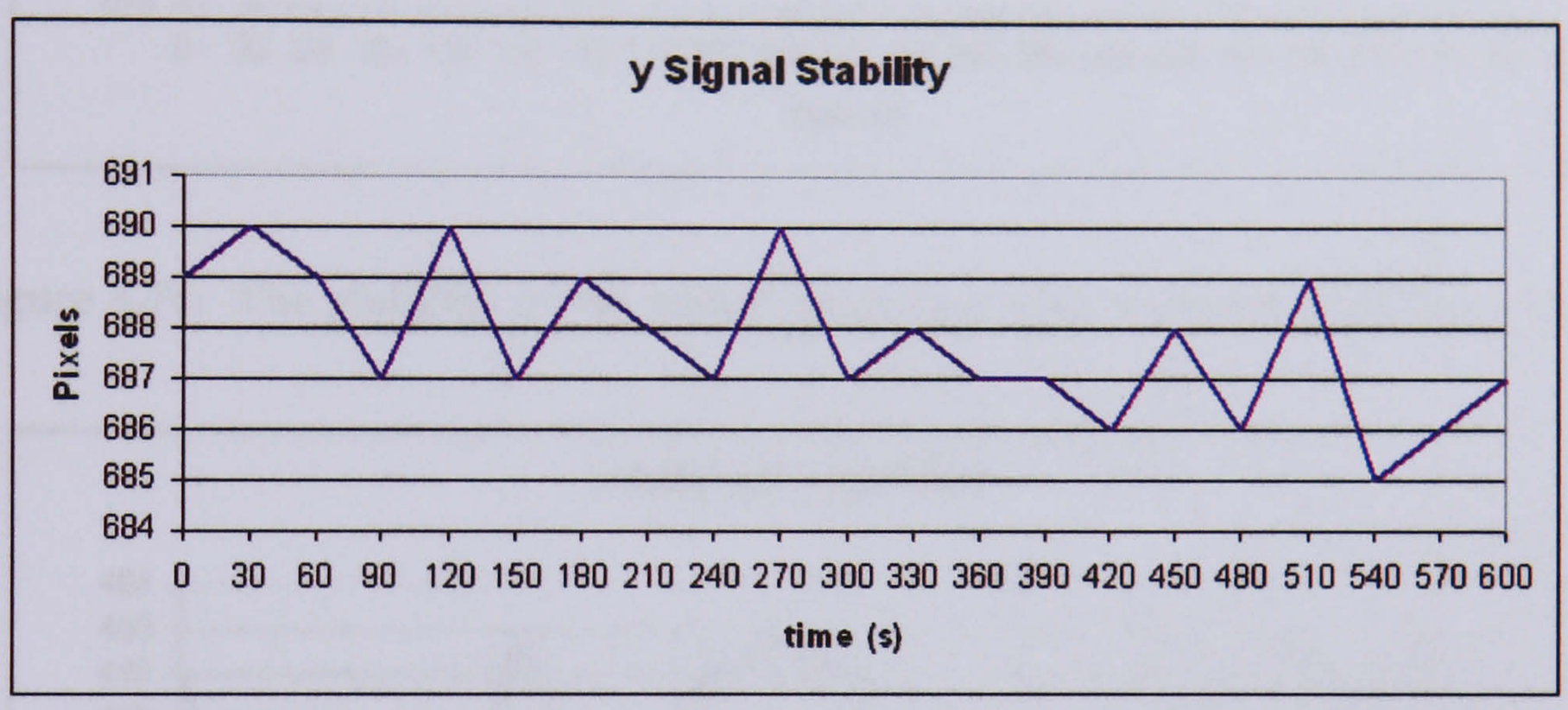

Figure 4.72: The stability of the signal beam in y over a period of 10 minutes.

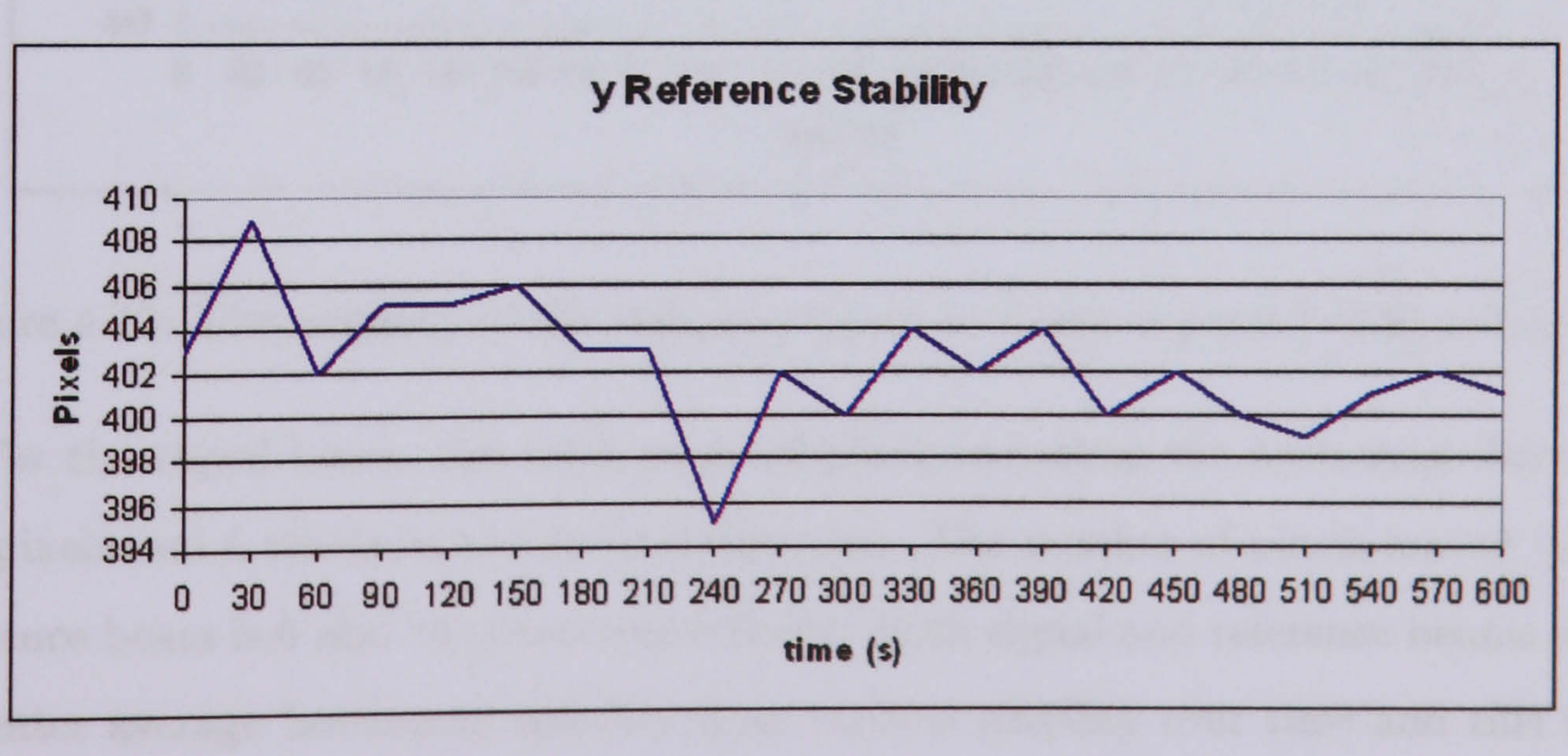

Figure 4.73: The stability of the reference beam in y over a period of 10 minutes.

Though there is very small movement from one measurement to the next, both signal and reference beams show a general downward trend, suggesting correlated

movements. We attribute this possibly to a temperature effect from the heating of the optical bench by the laser head as a function of time.

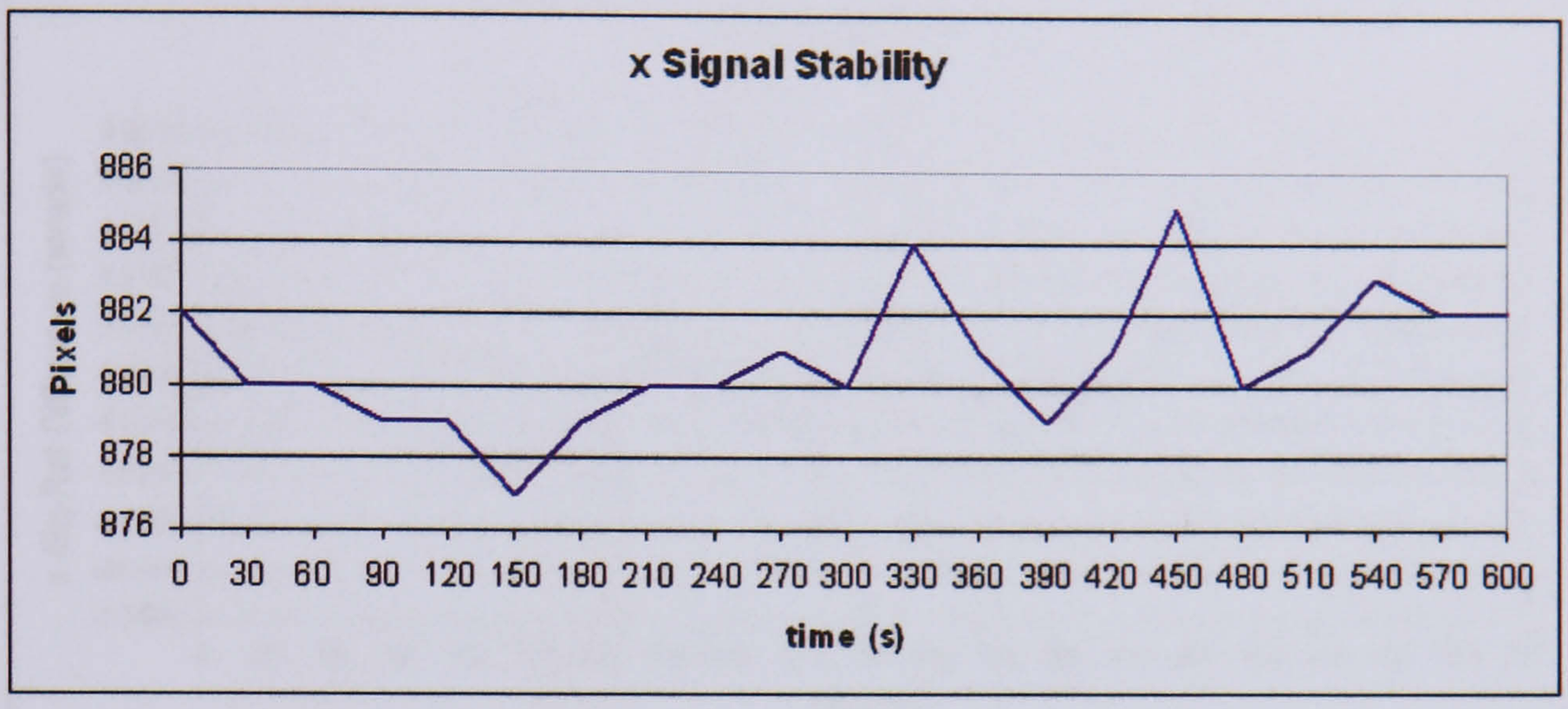

Figure 4.74: The stability of the signal beam in x over a period of 10 minutes.

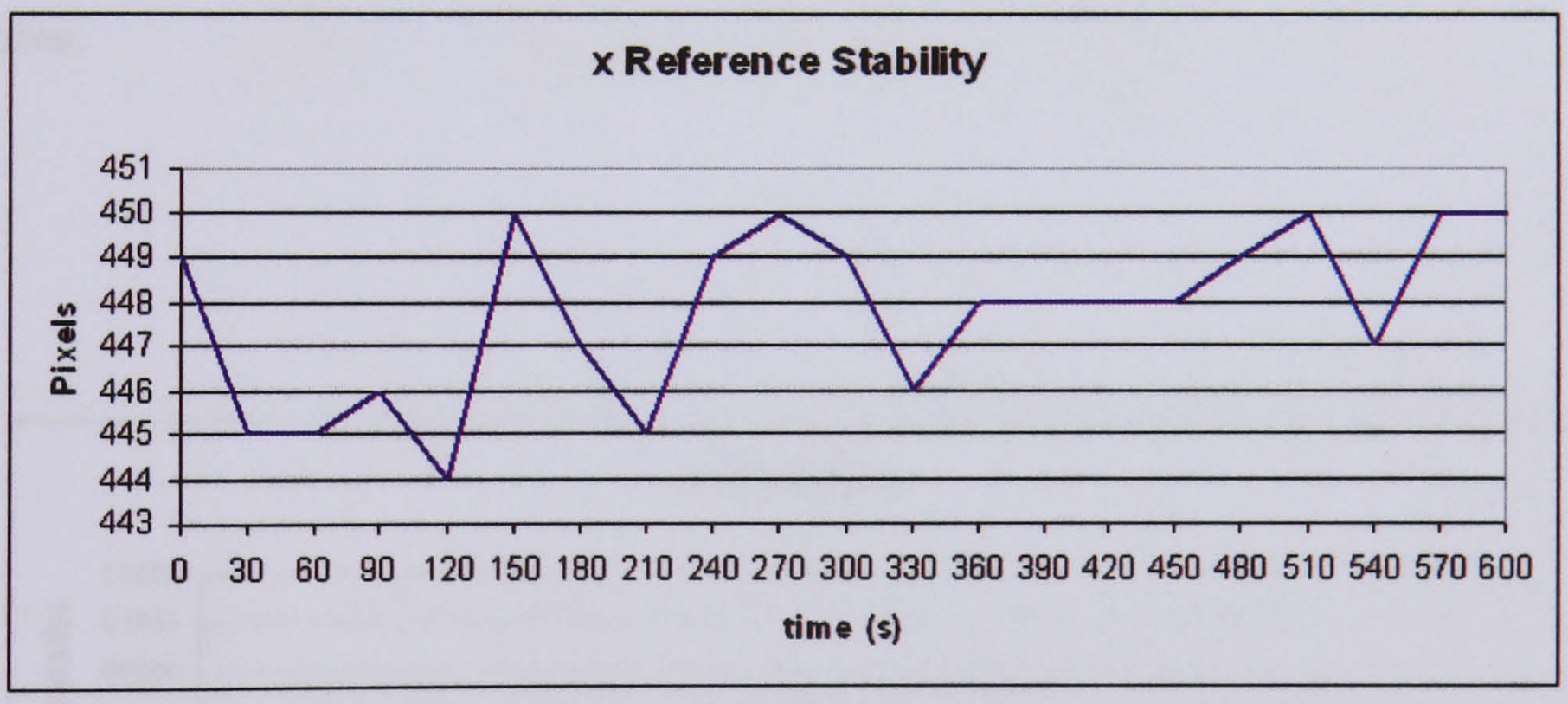

Figure 4.75: The stability of the reference beam in x over a period of 10 minutes.

For the signal beam, the total range of pixels moved in the horizontal direction is 6 pixels and 5 pixels in the vertical direction. The number of pixels moved in the reference beam is 6 and 14 pixels respectively. Both signal and reference beams show a greater average horizontal stability than vertical stability over time and this is to be expected when considering a new setup with the effects of gravity. The system has been designed to only acknowledge differences between the signal and reference beams. Therefore the final stability results are given as difference results (figures 4.76 and 4.77).

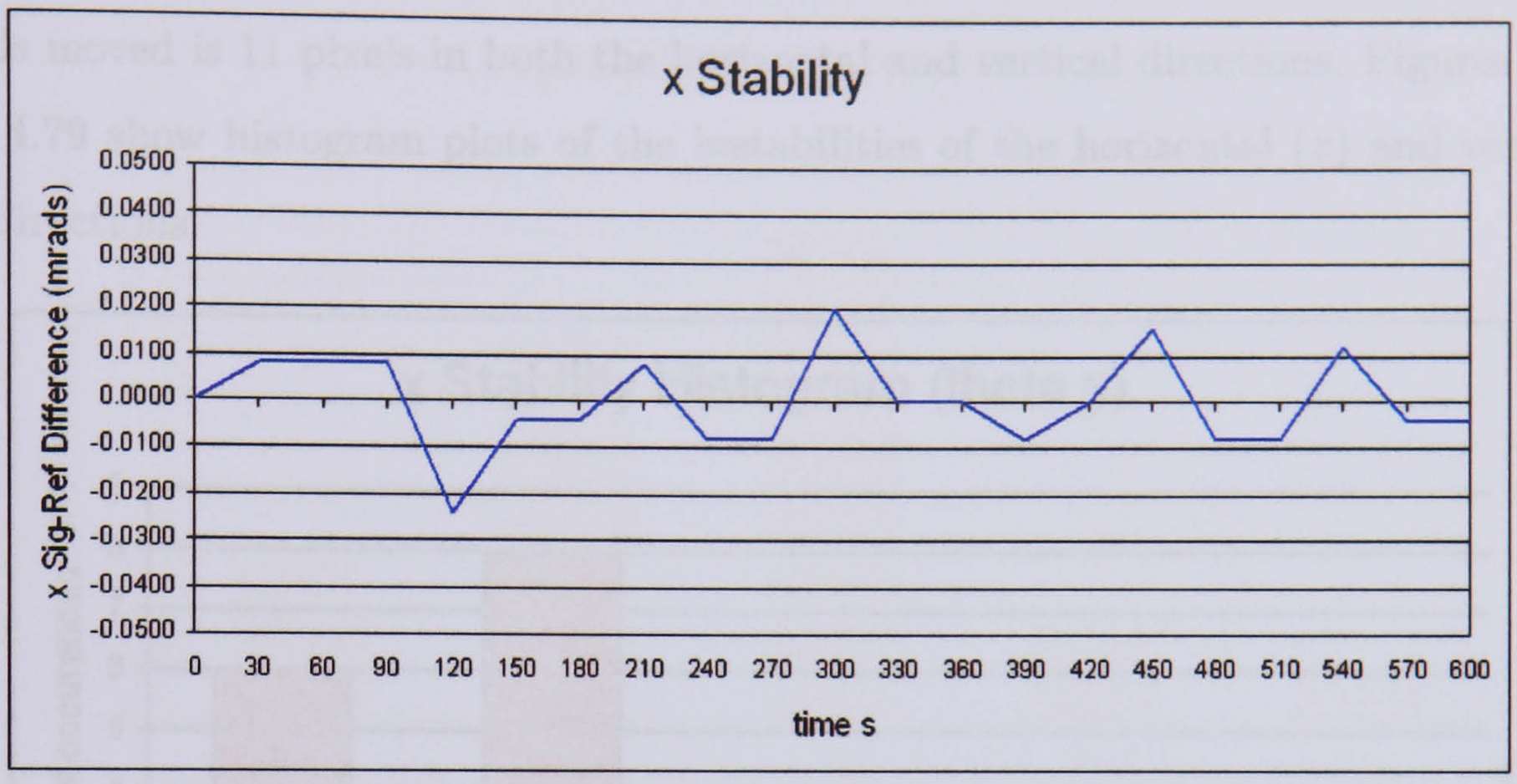

Figure 4.76: The stability of the difference measurement for x over a period of 10 minutes.

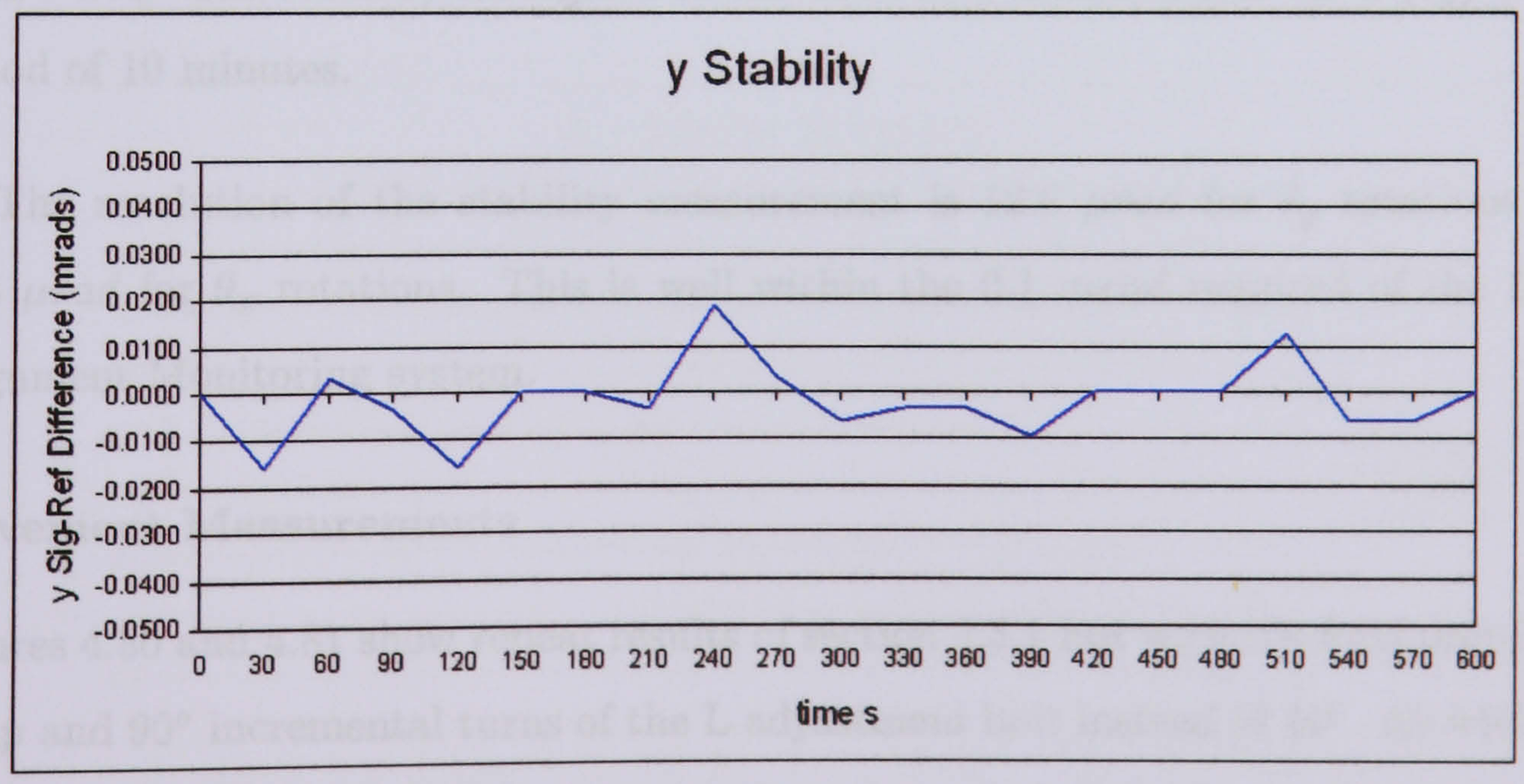

Figure 4.77: The stability of the difference measurement for y over a period of 10 minutes.

For the difference measurement, both the horizontal and vertical movements show good stability with no detectable downward movement over time. The total range of pixels moved is 11 pixels in both the horizontal and vertical directions. Figures 4.78 and 4.79 show histogram plots of the instabilities of the horizontal (x) and vertical (y) directions.

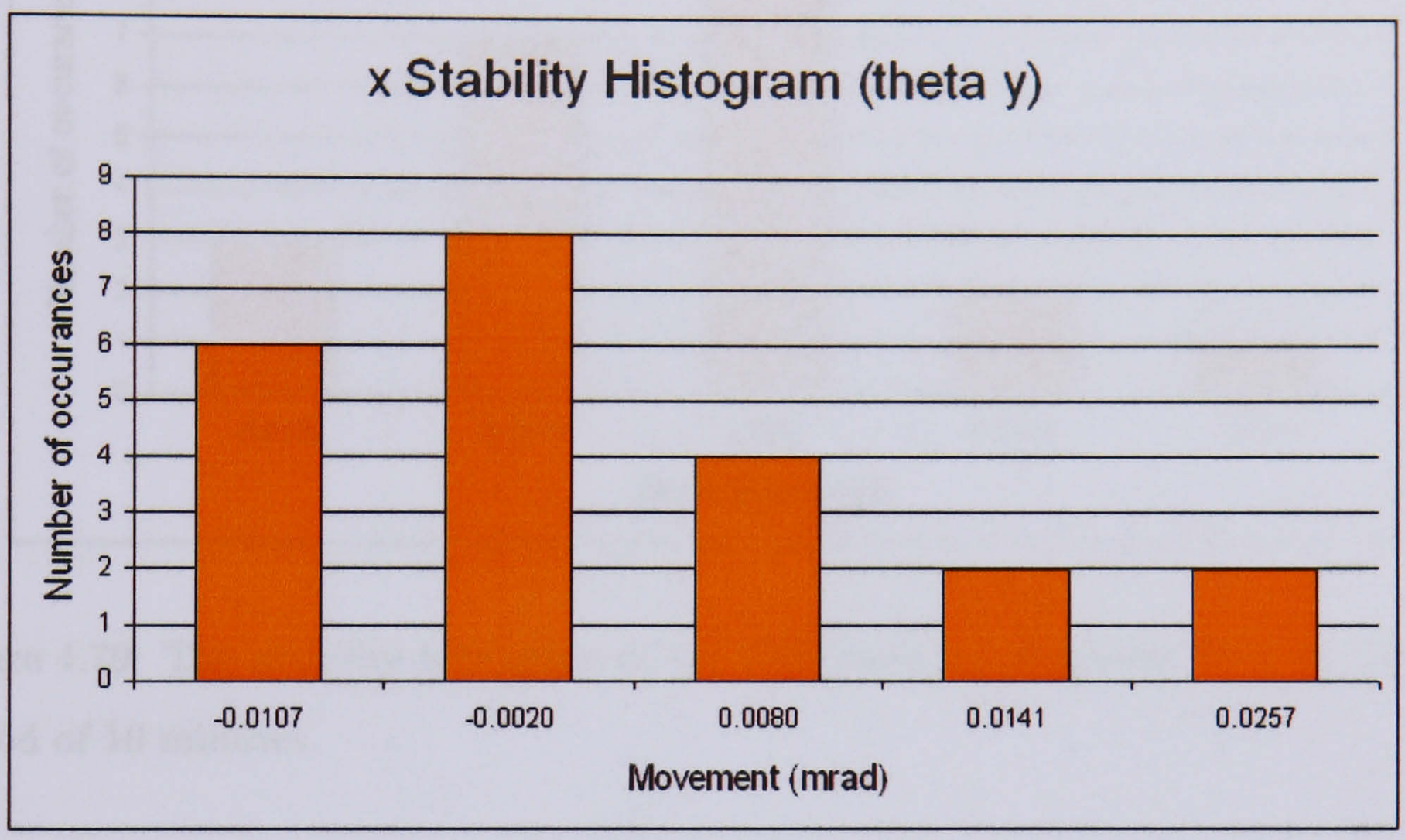

Figure 4.78: The stability histogram of the difference measurement for x (θ_y) over a period of 10 minutes.

The resolution of the stability measurement is 12.6 μrad for θ_y rotations and 12.8 μrad for θ_x rotations. This is well within the 0.1 $mrad$ required of the Laser Alignment Monitoring system.

Movement Measurements

Figures 4.80 and 4.81 show repeat results of section 4.3.1 but with the final prototype setup and 90^o incremental turns of the L adjustment bolt instead of 45^o. As with the original results, one can observe a vertical movement of about 2 $mrad$ per turn and a horizontal movement of 1.33 $mrad$ per turn.

A small amount of hysteresis can be seen in figure 4.81 which is possibly due to small differences in the 90^o rotations of the L adjustment bolt.

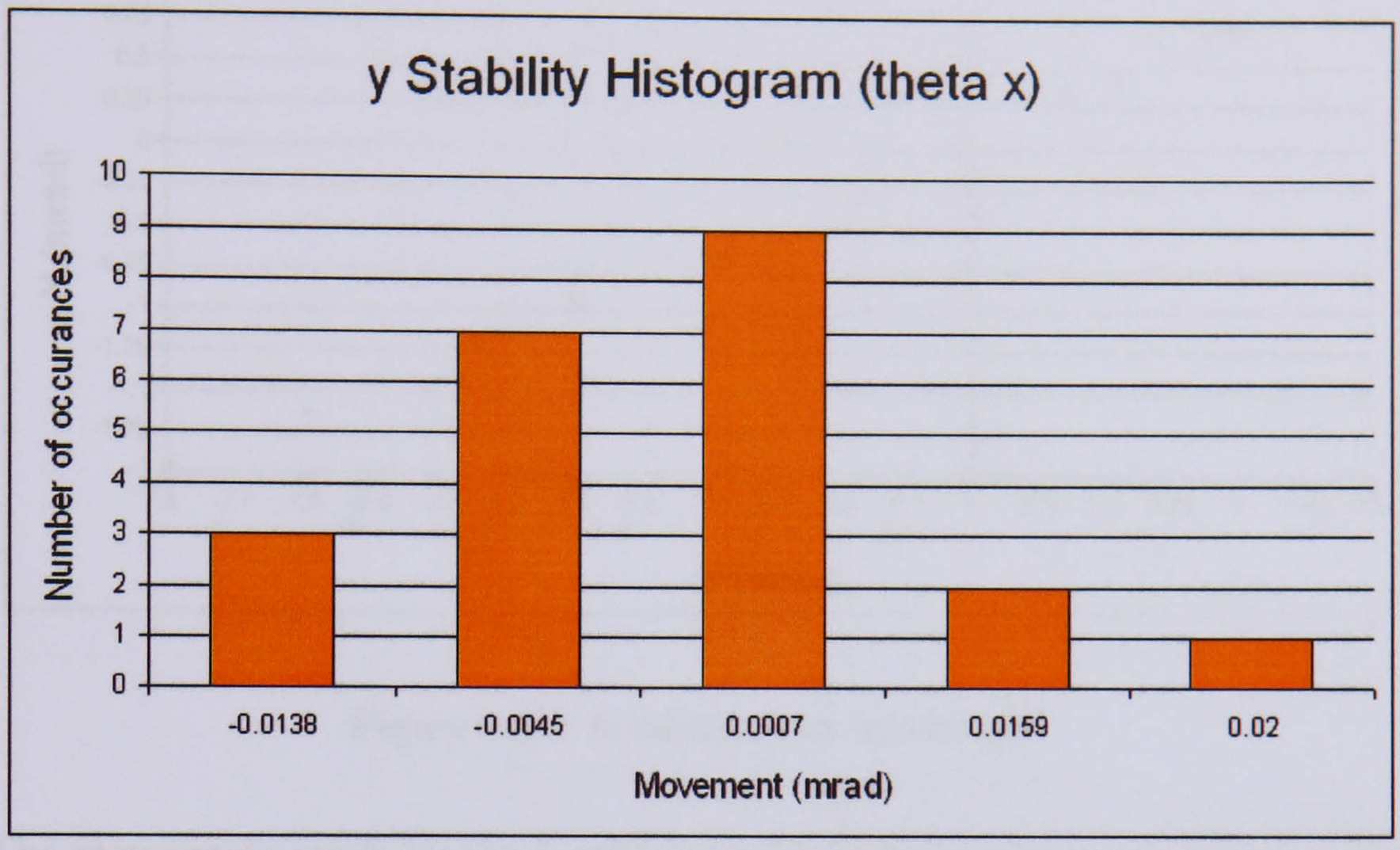

Figure 4.79: The stability histogram of the difference measurement for y (θ_x) over a period of 10 minutes.

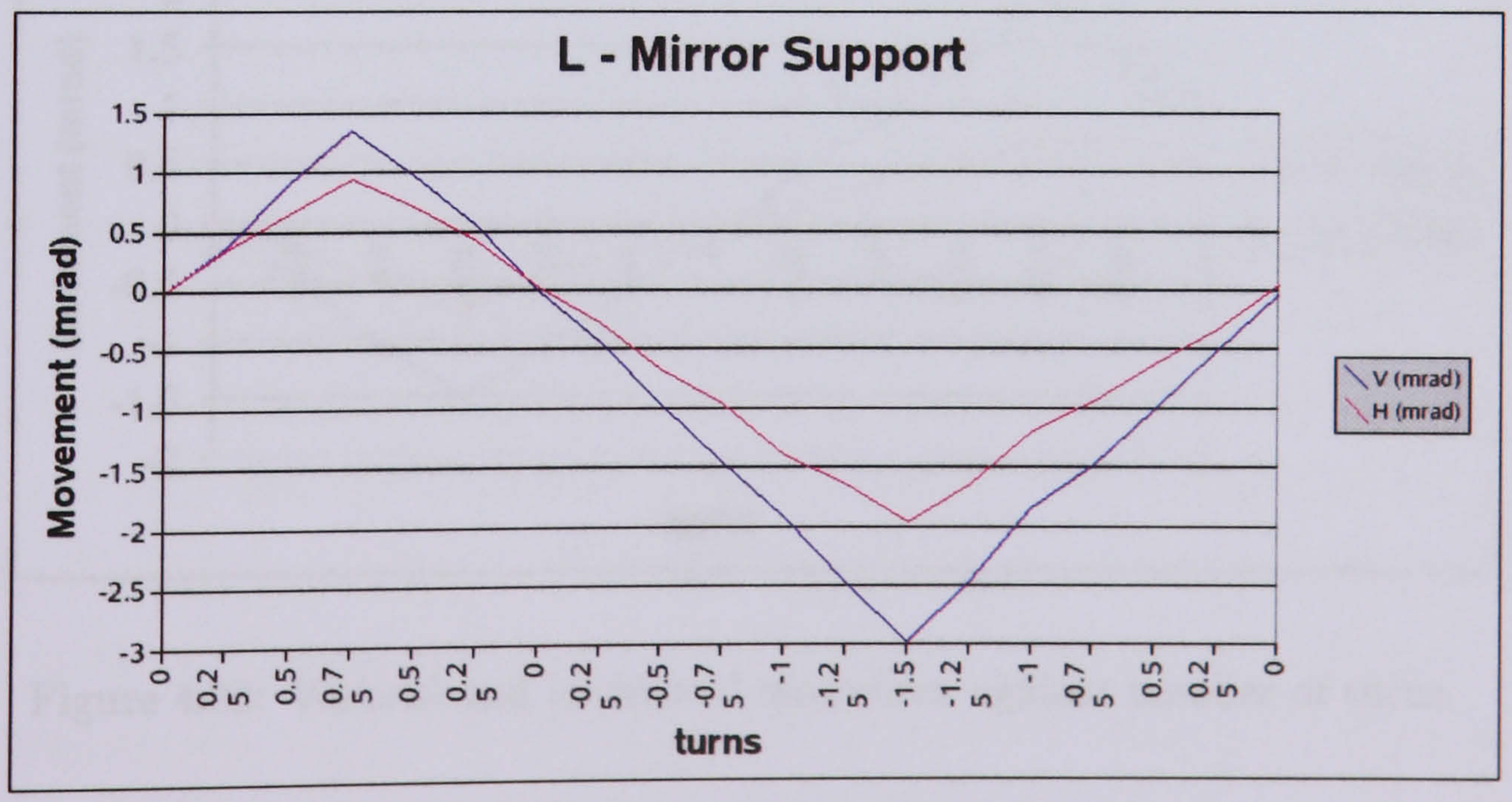

Figure 4.80: Vertical and horizontal movement against number of turns.

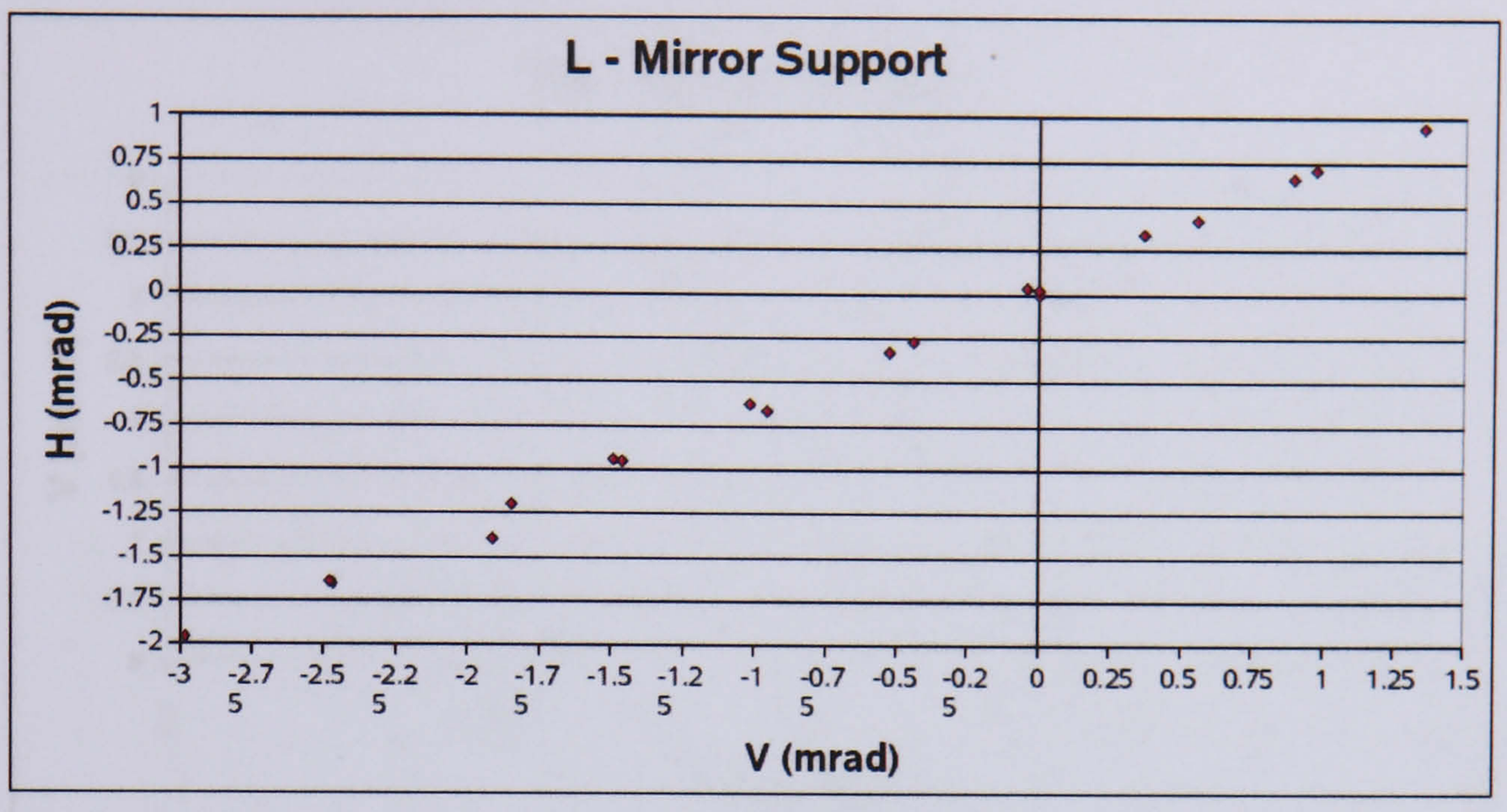

Figure 4.81: L adjustment hysteresis.

The movements made by the L adjustment bolt have been reproduced by making equal turns of the T and R adjustment bolts. The results of this reproduction are given in figure 4.82 and 4.83.

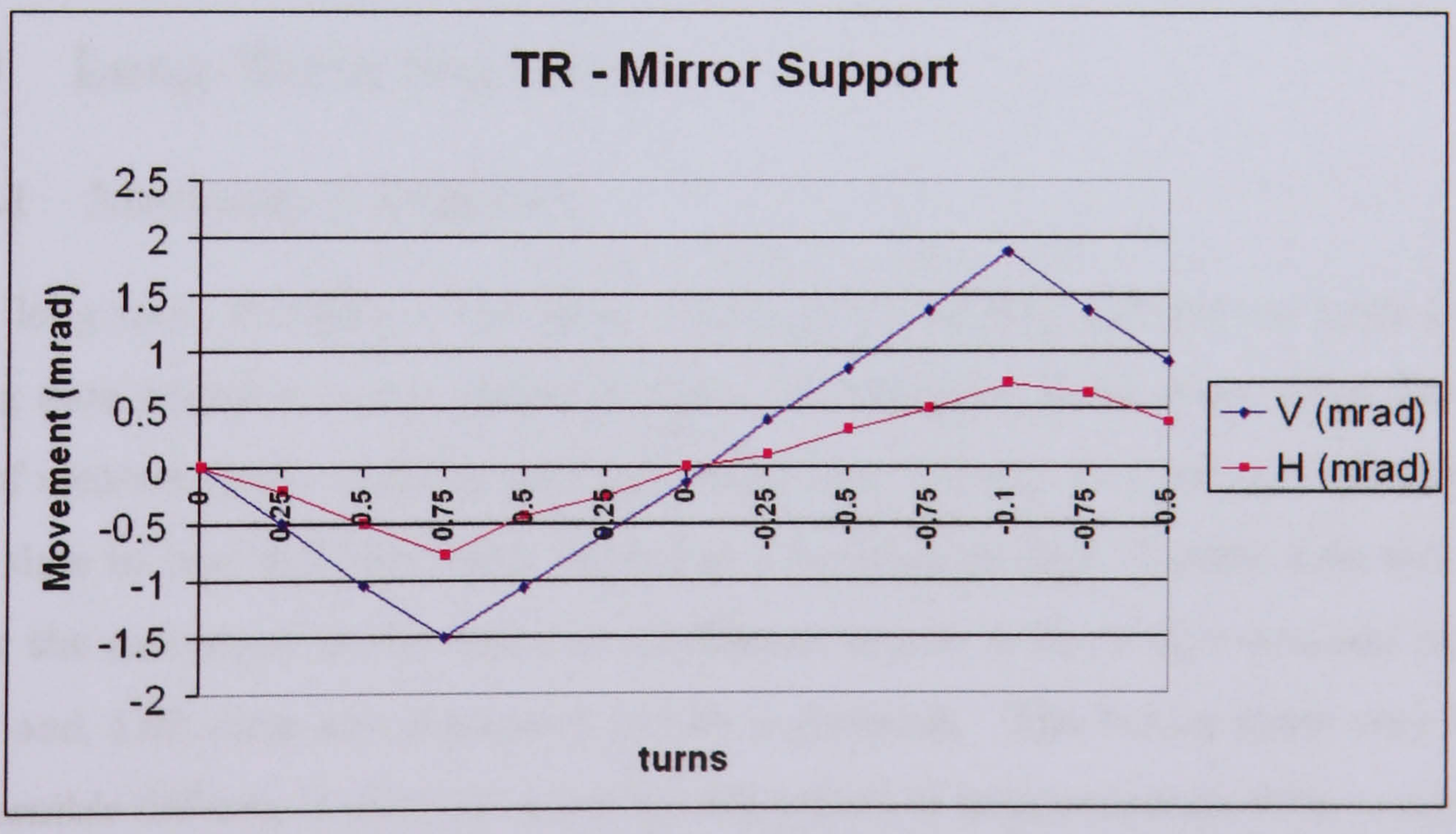

Figure 4.82: Vertical and horizontal movement against number of turns.

The correlation between horizontal and vertical movements agrees very well with the result of the L adjustment bolt (see figure 4.82). The results show a small increase in hysteresis over the full cycle, with respect to the L-mirror adjustment. This is due

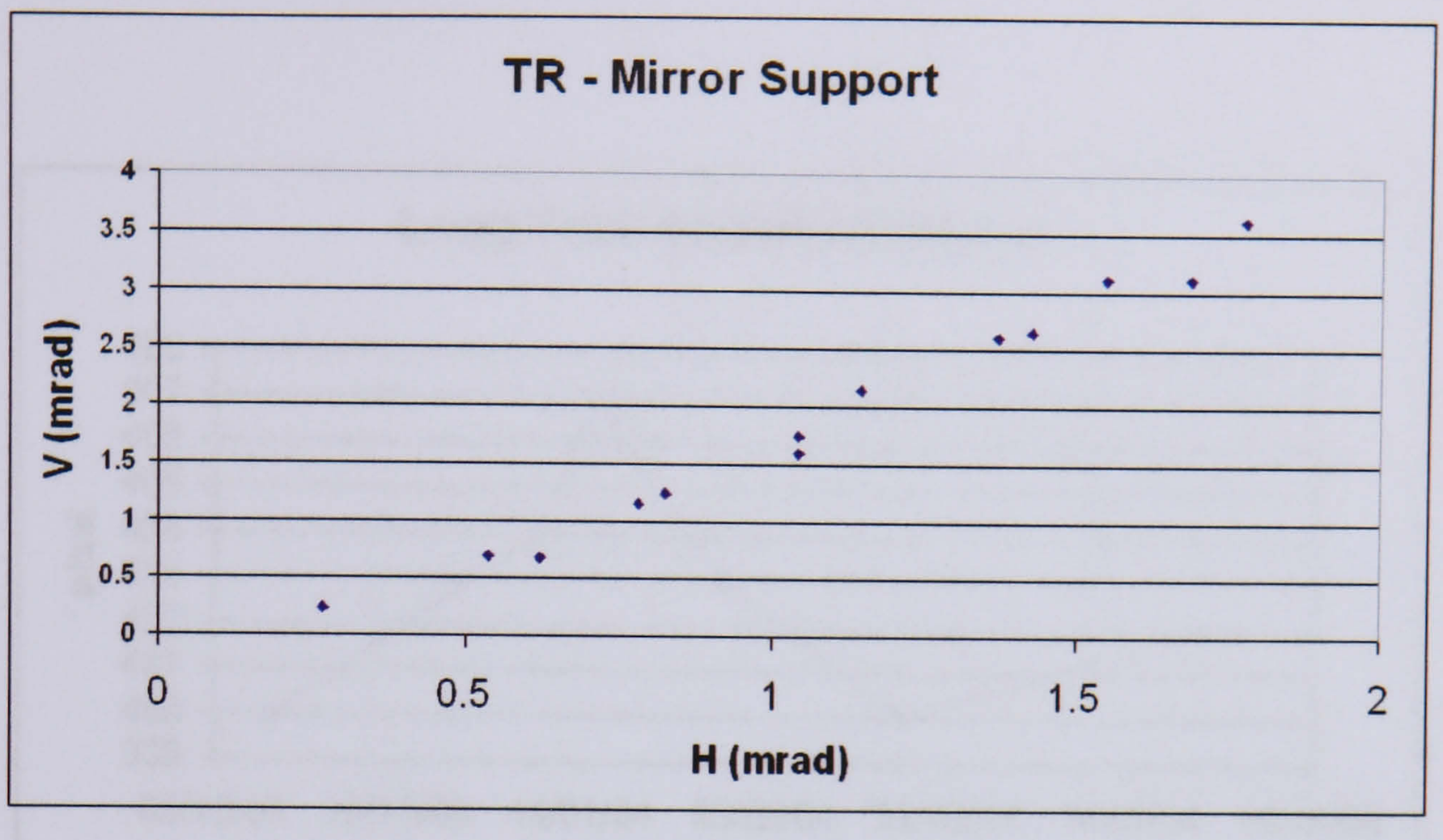

Figure 4.83: TR adjustment hysteresis.

to the simultaneous use of two adjustment bolts when moving T and R, instead of one bolt in the case of the L-movement (see figures 4.83 and 4.81).

4.9 Long Term Stability

4.9.1 Mechanical Stability

The long term stability of the laser alignment monitoring system has been tested using data acquired over a period of just over 3 months. Data taken using the first set of measurements acquired each day (soon after turning the laser on, before it has had time to heat up) have been plotted as a function of date. Figures 4.84 and 4.85 show the movement in the signal and reference beams in the x direction and figures 4.86 and 4.87 show the movement in the y direction. The beams show very little discernible differences over the three month period of measurements, with maximum drift in the x direction of 7 pixels and 4 pixels in the signal and reference beam respectively, and maximum drift in the y direction of 15 pixels and 9 pixels in the signal and reference.

The results in figures 4.88 and 4.89 show that the maximum difference between signal and reference translate into an angular stability of 20 μrad in the θ_x (RMS

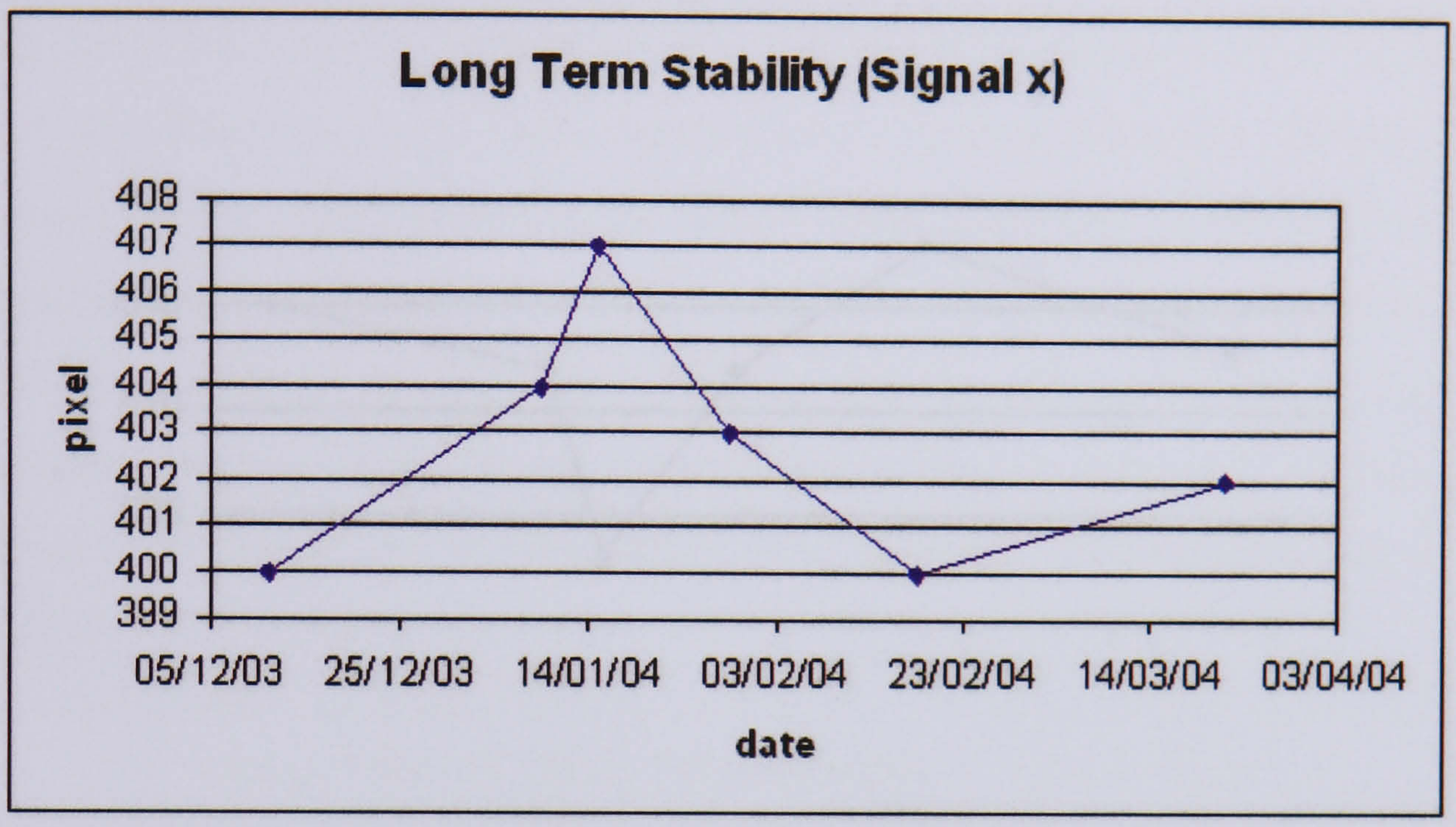

Figure 4.84: The long term stability of the signal beam in x.

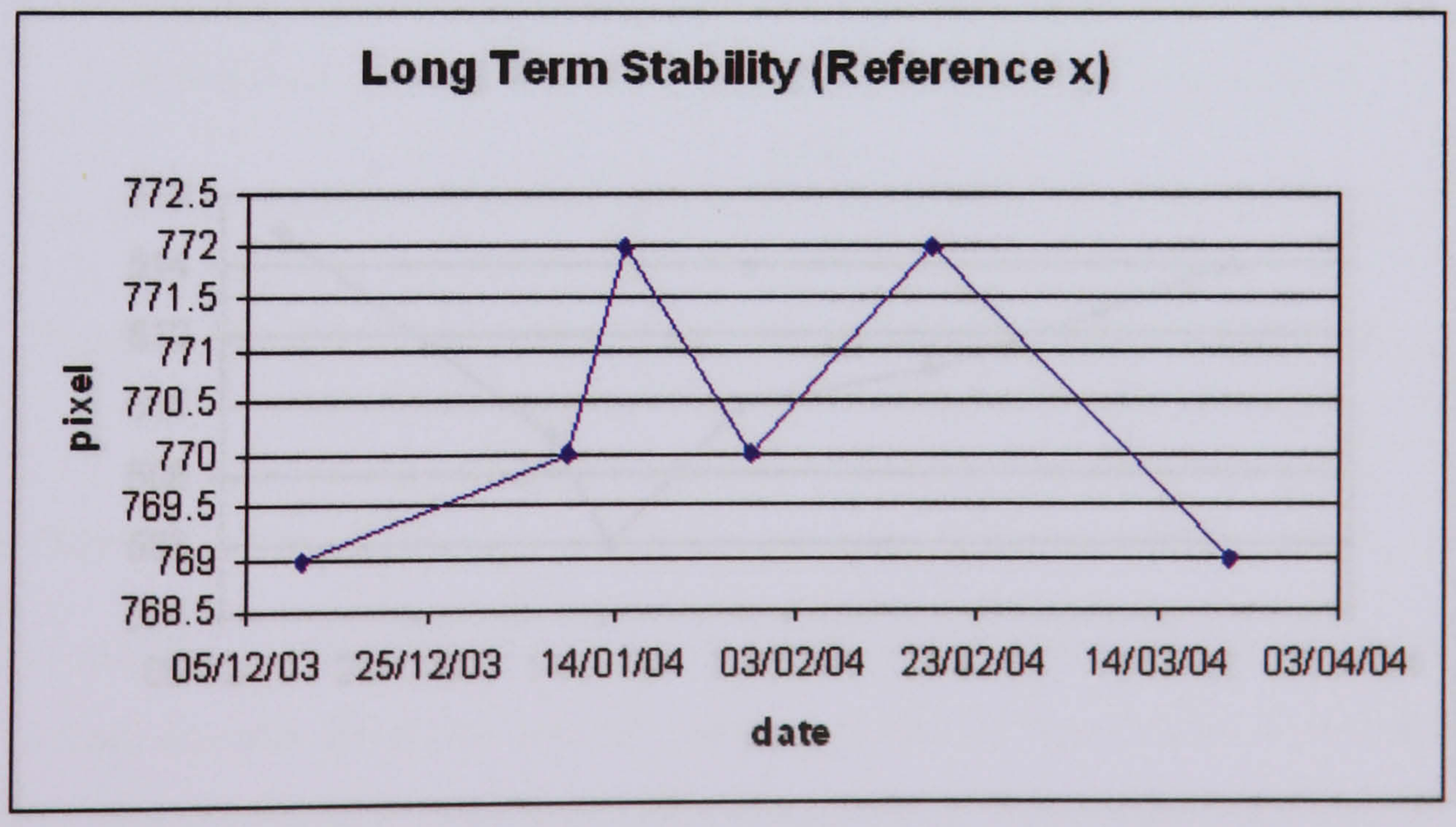

Figure 4.85: The long term stability of the reference beam in x.

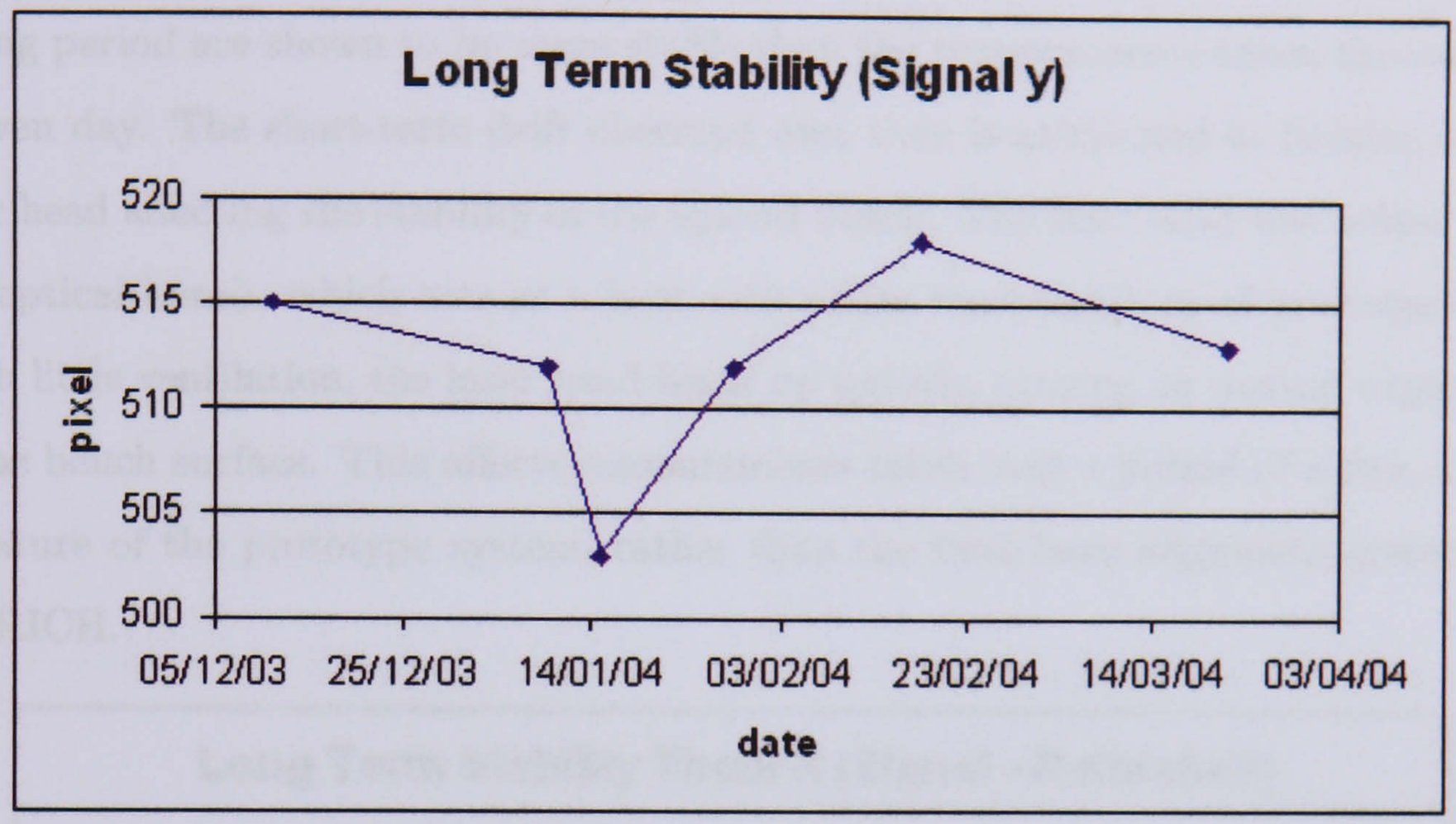

Figure 4.86: The long term stability of the signal beam in y.

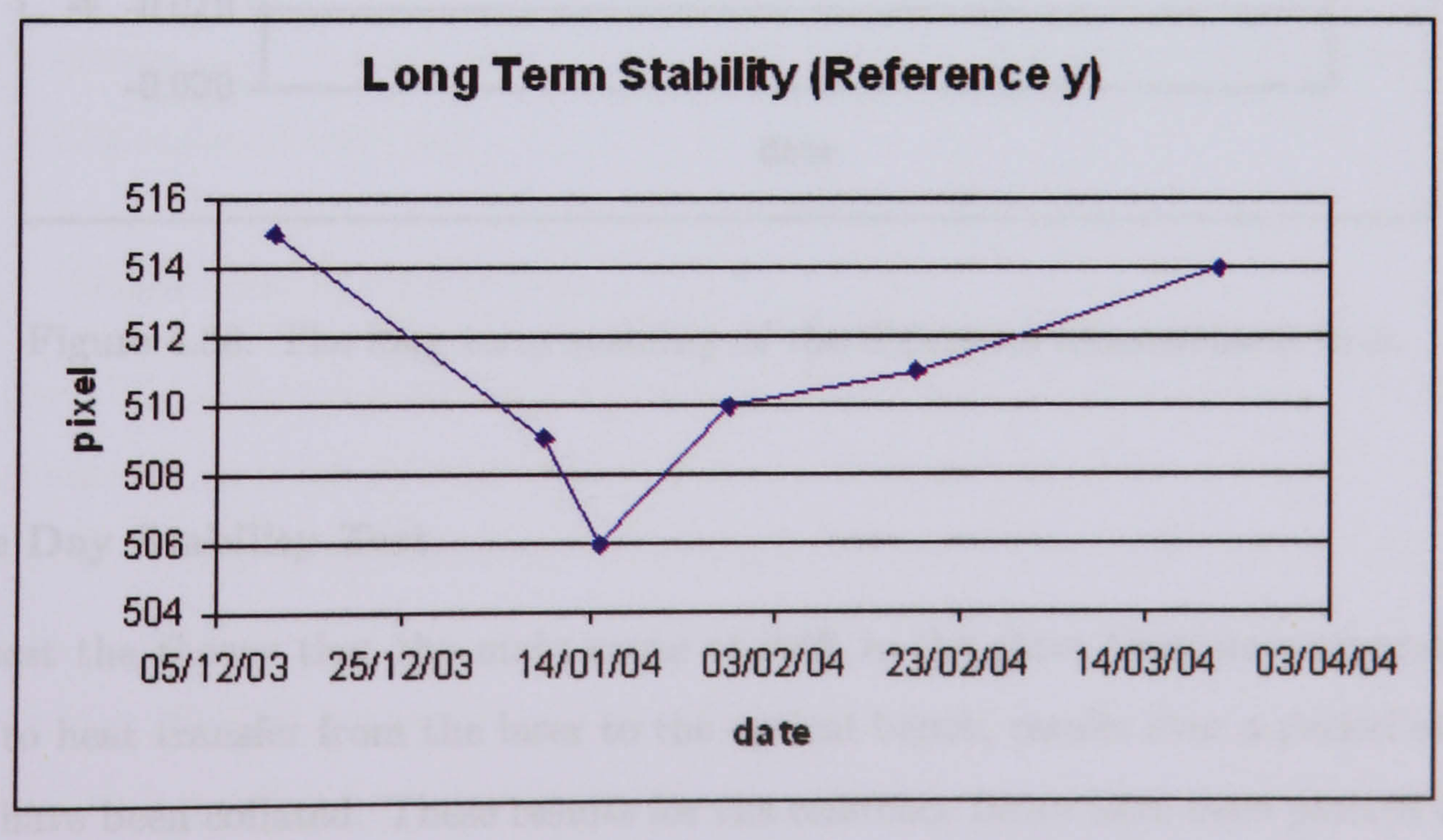

Figure 4.87: The long term stability of the reference beam in y.

$\theta_x = 6.4\ \mu rad$) and 40 μrad in θ_y (RMS $\theta_y = 13.7\ \mu rad$) over the full measurement period of three months. Long term measurements at the beginning of each data taking period are shown to be more stable than the measurements taken throughout a given day. The short-term drift observed over time is attributed to heating of the laser head affecting the stability of the optical bench. The laser head was bolted onto the optical bench, which acts as a heat sink under the conditions of prolonged use. With little ventilation, the laser head heats up quickly, causing an uneven expansion of the bench surface. This affects measurements taken over a period of a day, and is a feature of the prototype system, rather than the final laser alignment system for the RICH.

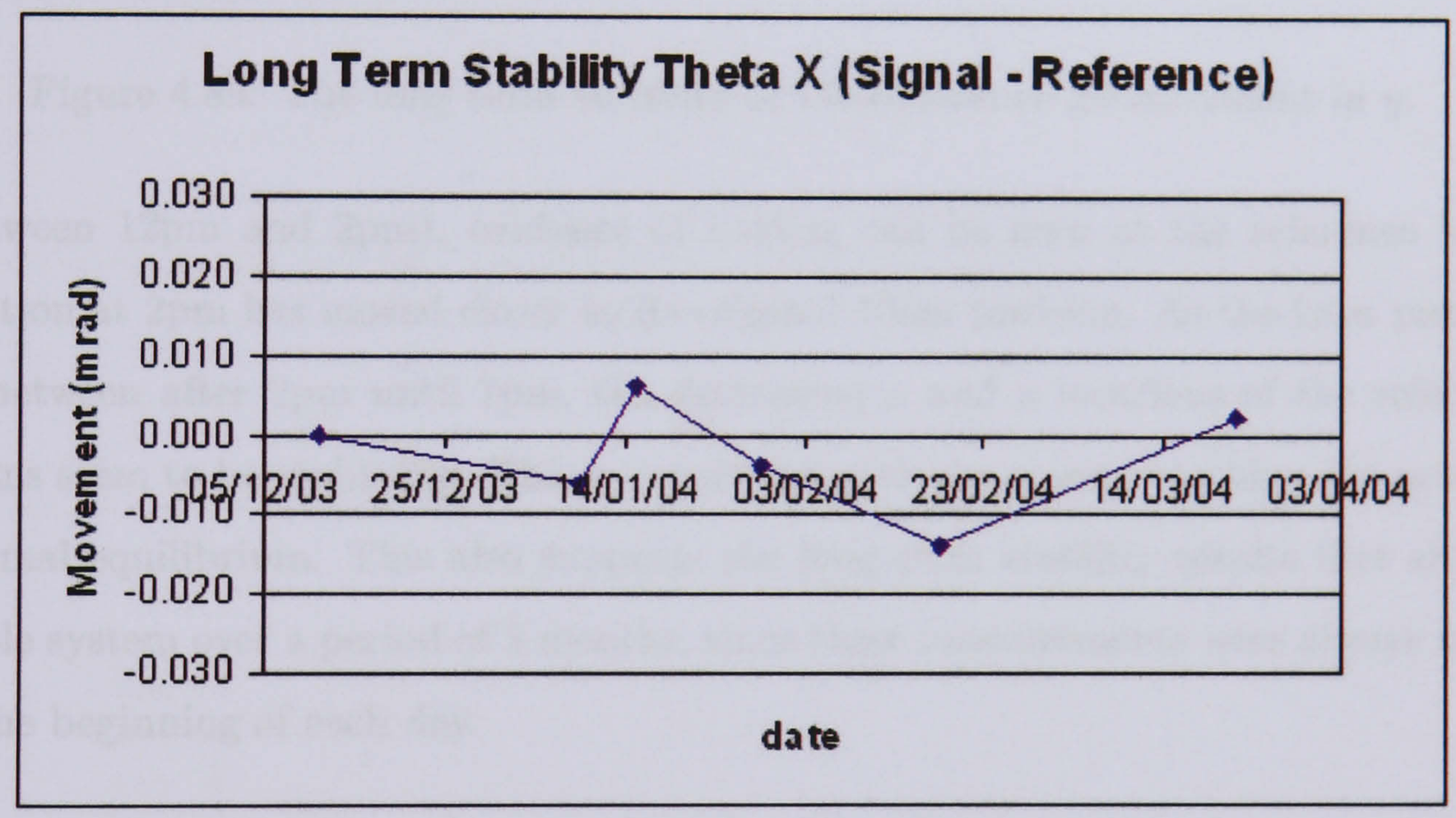

Figure 4.88: The long term stability of the difference measurement in x.

One Day Stability Test

To test the theory that the main cause of drift in the short term measurements is due to heat transfer from the laser to the optical bench, results over a period of one day have been collated. These results for the reference beam have been plotted for x and y directions in figures 4.90 and 4.91 respectively. The results show that for the first period between 10am and 12pm, the reference beam location gradually decreases in both x and y locations. Over the lunch period when the laser was switched off

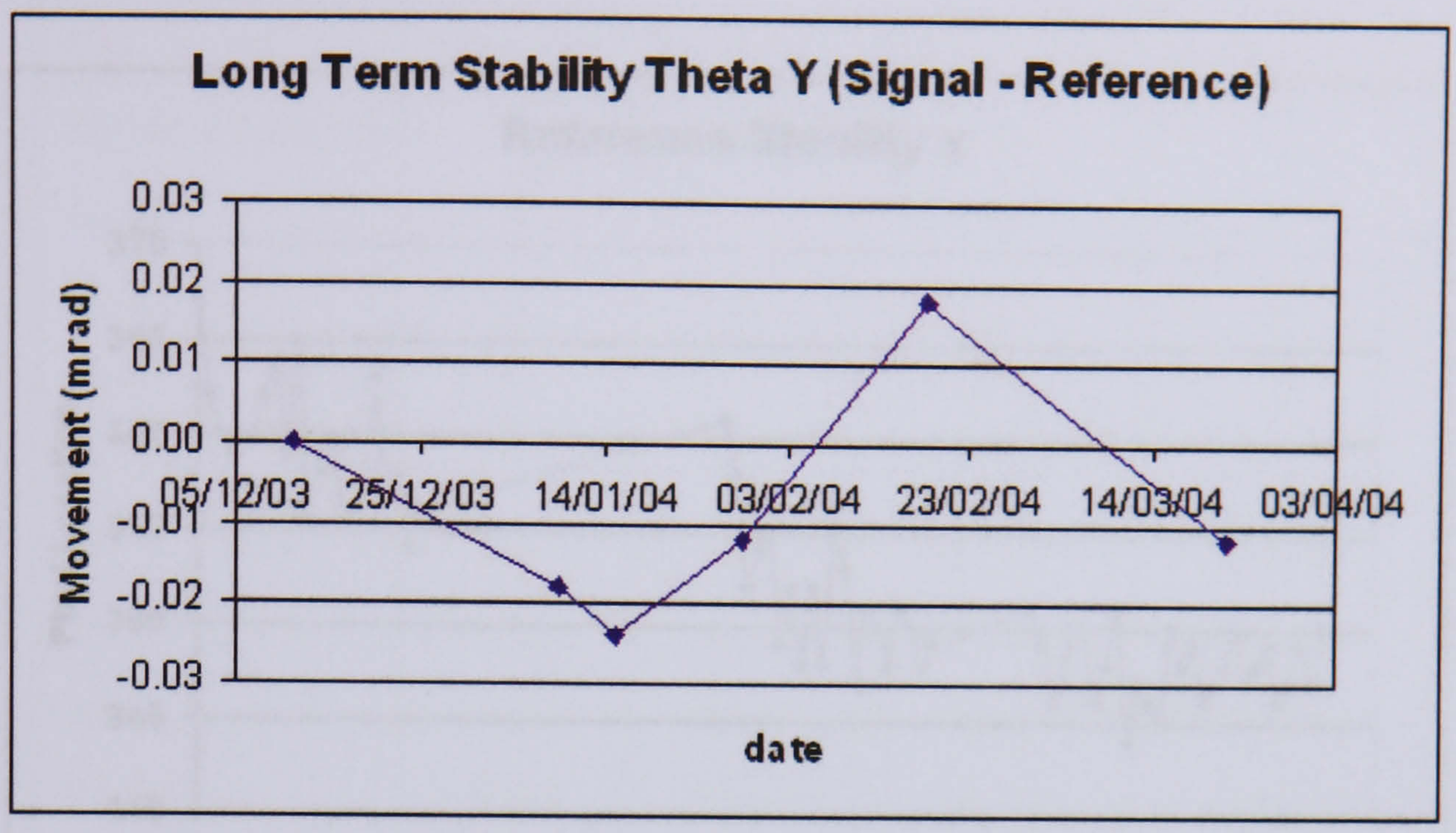

Figure 4.89: The long term stability of the difference measurement in y.

(between 12pm and 2pm), evidence of cooling can be seen as the reference beam location at 2pm has moved closer to its original 10am position. As the laser remains on between after 2pm until 7pm, the decreasing x and y locations of the reference beams seem to be stablising. This is consistent with the system reaching the point of thermal equilibrium. This also supports the long term stability results that show a stable system over a period of 3 months, since these measurements were always taken at the beginning of each day.

4.9.2 Algorithm Stability

The stability of the algorithm was tested by varying the range of the 1st image cut parameters. The results of the tests are shown in table 4.6.

The algorithm is very stable at recovering X rotations, moving less than 0.005 $mrad$, however, a movement of 0.10 $mrad$ is detected in the Y direction as the cut range is moved from 65-100% to 40-75%. This is because the lower cut limit of 40% includes pixels with lower Sobel gradients that do not project to central accumulations. This means that without changing program variables, large spurious accumulations are created near the central accumulation and are not removed in the anomaly removal stage. The spot location stage expands its mask to include the spurious accumula-

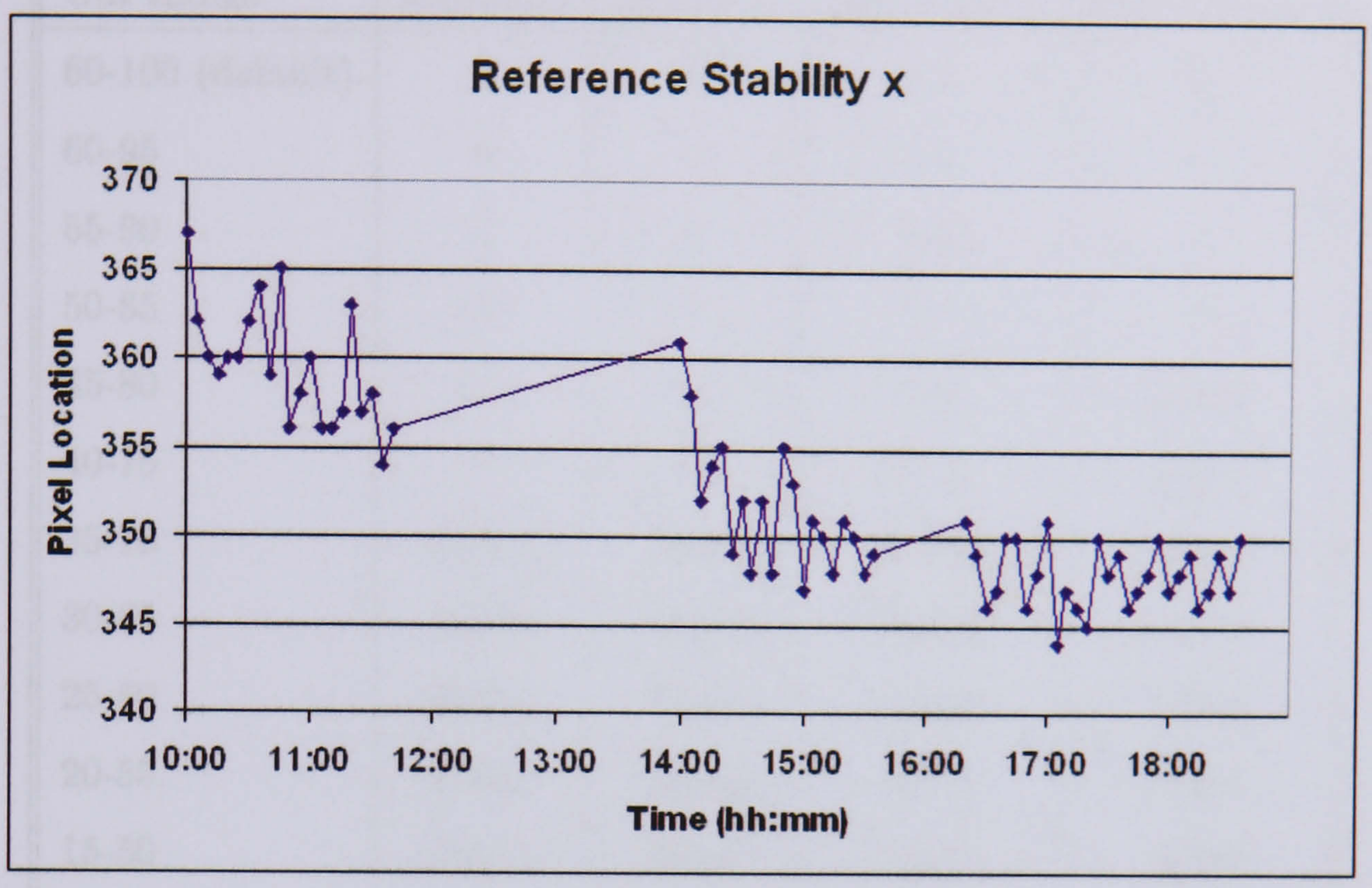

Figure 4.90: A one day stability measurement of the reference beam in the x direction.

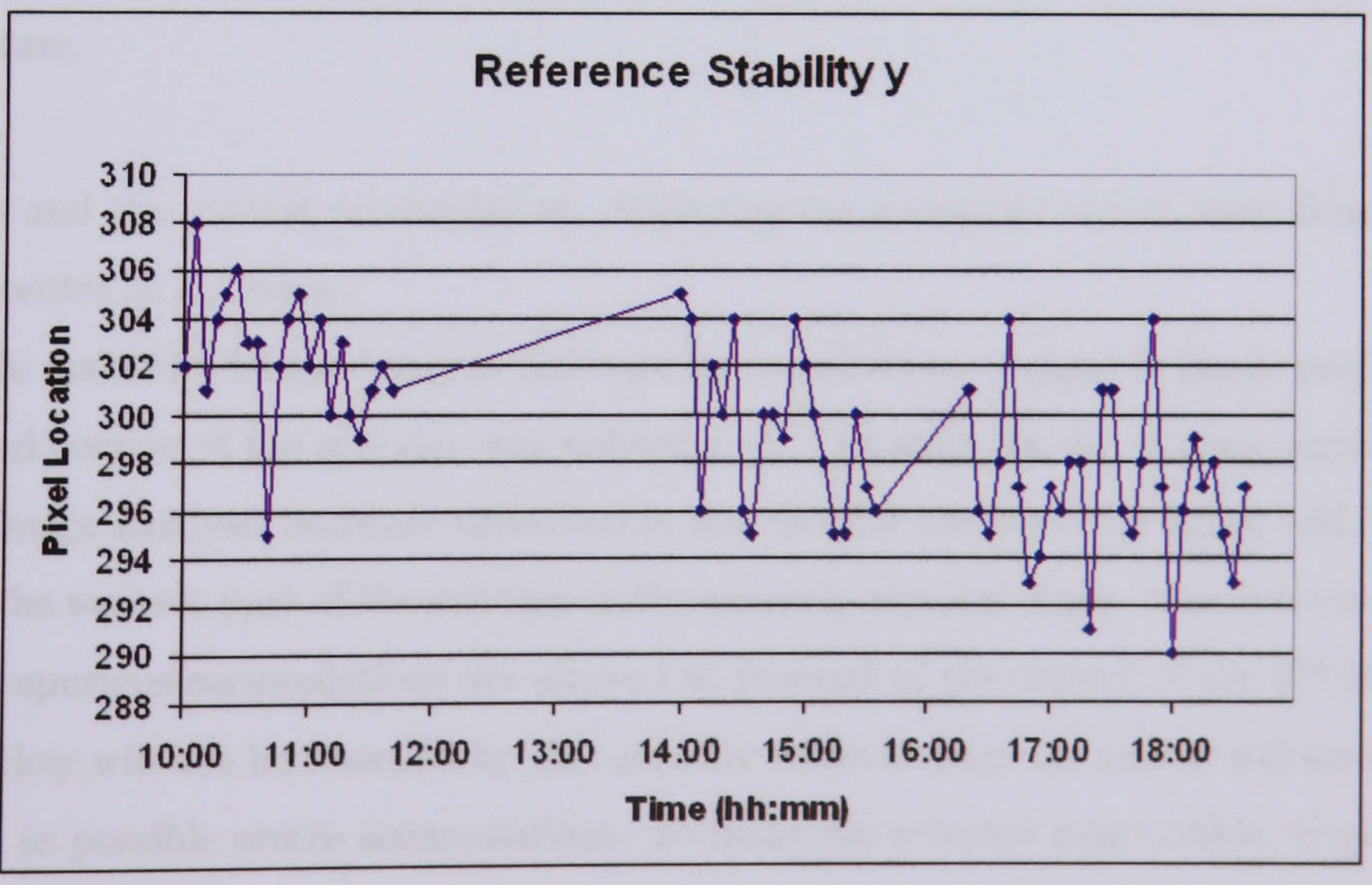

Figure 4.91: A one day stability measurement of the reference beam in the y direction.

Cut Range	$x(pixels)$	$y(pixels)$	$\Delta\theta y\ (mrad)$	$\Delta\theta x\ (mrad)$
60-100 (default)	0	0	0	0
60-95	0	0	0	0
55-90	3	0	0.02	0
50-85	0	0	0	0
45-80	11	2	0.07	0.004
40-75	17	2	0.10	0.004
35-70	failed	failed	failed	failed
30-65	failed	failed	failed	failed
25-60	failed	failed	failed	failed
20-55	failed	failed	failed	failed
15-50	failed	failed	failed	failed
10-45	failed	failed	failed	failed
5-40	failed	failed	failed	failed
0-35	failed	failed	failed	failed

Table 4.6: Stability results for varying cut levels for version 1 of the image analysis software.

tions and the central accumulation, displacing the measured centre away from the real centre of the beam.

To make the Image Analysis Software less sensitive to changes in image profile, a second version of the software was redeveloped. The steps for the original version of the Image Analysis Software described in this chapter are shown in figure 4.92.

The weakest part of the software is the anomaly removal stage. This is because if large spurious accumulations are allowed to proceed to the output of the 2^{nd} image cut, they will not be removed by the anomaly removal stage because it will consider them as possible centre accumulations. To make the software more stable, version 2 of the Image Analysis Software does not use the anomaly removal stage but instead uses a different method of removing spurious accumulations. Figure 4.93 shows the program steps for version 2 of the Image Analysis software.

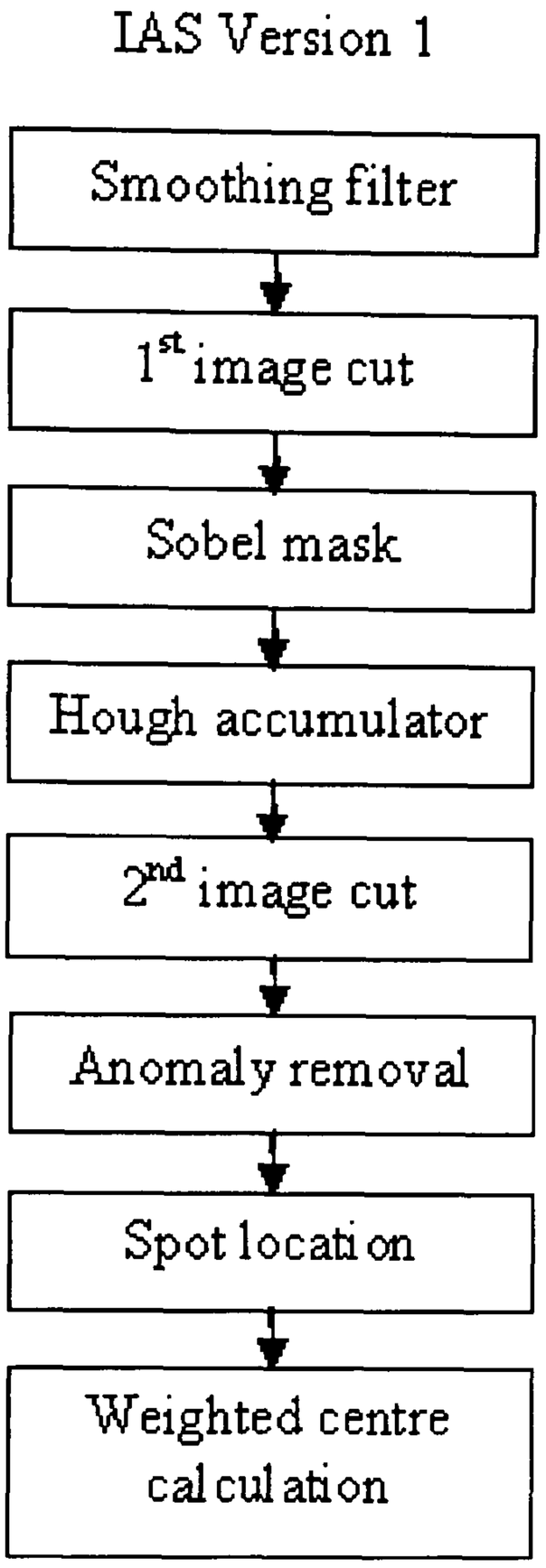

Figure 4.92: Steps of version 1 of the Image Analysis Software.

In version 2, the Hough accumulator output is copied and a 2^{nd} smoothing filter is applied to the copy. The 2^{nd} smoothing filter (3×3 multipass filter) reduces the height of the large spurious accumulations such that when the 2^{nd} image cut(2) is applied, the large spurious accumulations are no longer high enough to get past the cut threshold. Therefore, the output of the 2^{nd} image cut(2) only contains a smoothed version of the real central accumulations. The spot location stage is then applied to this output. It generates a mask for each central accumulation and records the mask location for each beam.

The masks are then applied to the unfiltered output from the 2^{nd} image cut(1),

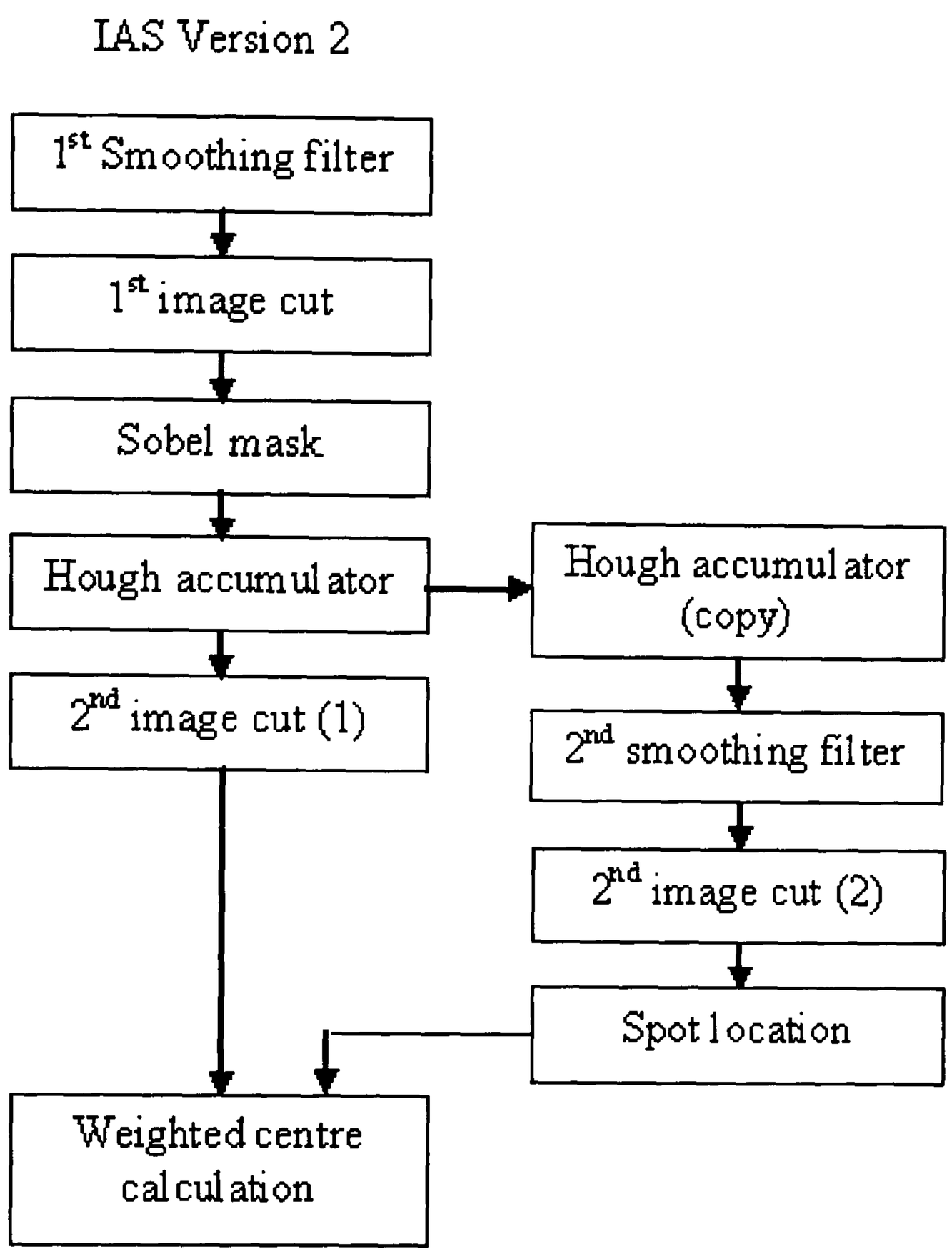

Figure 4.93: Steps of version 2 of the Image Analysis Software.

since the filtered output might bias the position of the centres. The end result is that the 2nd version of the Image Analysis Software has improved the stability in finding the position of the centre, as can be seen from table 4.7. It should be noted that it is unlikely that the real system will experience such changes in input images. The range in which the software has been tested in this section is equivalent to the profile ranging from an extremely saturated beam to a beam with very low intensity.

Version 2 of the algorithm was applied to the stability measurements in section 4.8.2. The results in figures 4.76 and 4.77 remain unchanged with respect to the default parameters of version 2 of the algorithm. Hence, the stability observed is

0.013 *mrad* in the x direction (θ_y) and 0.013 *mrad* in the y direction (θ_x).

Cut Range	$x(pixels)$	$y(pixels)$	$\Delta\theta y$ $(mrad)$	$\Delta\theta x$ $(mrad)$
60-100 (default)	0	0	0	0
60-95	0	0	0	0
55-90	0	0	0	0
50-85	-4	5	-0.02	0.01
45-80	-1	5	0.07	-0.01
40-75	6	0	0.04	0
35-70	11	-4	0.07	-0.008
30-65	7	-4	0.04	-0.008
25-60	13	-11	0.08	-0.022
20-55	18	-16	0.11	0.032
15-50	14	-17	0.08	-0.034
10-45	19	-20	0.11	-0.04
5-40	21	-19	0.13	-0.038
0-35	27	-24	0.16	-0.048

Table 4.7: Stability results for varying cut levels for version 2 of the image analysis software.

4.10 Summary

The RICH detectors of LHCb play a vital role in the identification of particles leading to constraints upon the CKM matrix. The mirrors of RICH2 are segmented and can potentially move over time. Therefore to maintain optimal performance of RICH2, the angular positions of these segments must be monitored in order to recover performance lost due to random misalignment. The solution to the monitoring of mirror segments comes in two parts, a data based alignment monitoring system, and a laser based alignment monitoring system that feeds alignment reference points to the data based system. The basic design of the laser based system has been shown to be

successful in the determination of the change in angular movements of a mirror segment. The short term stability measurements that define the accuracy capability of the system have a resolution of 0.013 $mrad$ for both θ_y and θ_x rotations. The long term stability measurements have a resolution of 0.014 $mrad$ in θ_y and 0.006 $mrad$ in θ_x. Both results are better than the required 0.1 $mrad$ resolution.

Chapter 5

The Laser Alignment System Simulation

5.1 Introduction to Simulation

The software framework of LHCb is called GAUDI [18] and it is the skeleton structure on which the simulation and reconstruction software of LHCb is based. The aim behind GAUDI is to provide a familiar standardised development environment of classes and interfaces written in C++, by which all GAUDI based packages can communicate. In practice, this software structure also allows for individuals to easily plug in and run their own code within the framework with the advantage of being able to access all of the available framework tools.

Integration of non-GAUDI based packages is done through the use of GAUDI based interface packages such as GiGa [21] [11], the GEANT4 [20] [45] interface to GAUDI. GEANT4 is a toolkit developed by high energy physicists to simulate the passage of particles through matter. The use of such a tool in LHCb is imperative for accurate simulation and reconstruction of events. GiGa has been developed at CERN to be a seamless communication interface that acts between GEANT4 and the GAUDI based simulation and reconstruction packages of LHCb.

The simulation package for the LHCb experiment is called GAUSS [55]. it is based on the GAUDI framework and heavily uses the GEANT4 toolkit. Figure 5.1 shows

the working of Gauss in its simplest form.

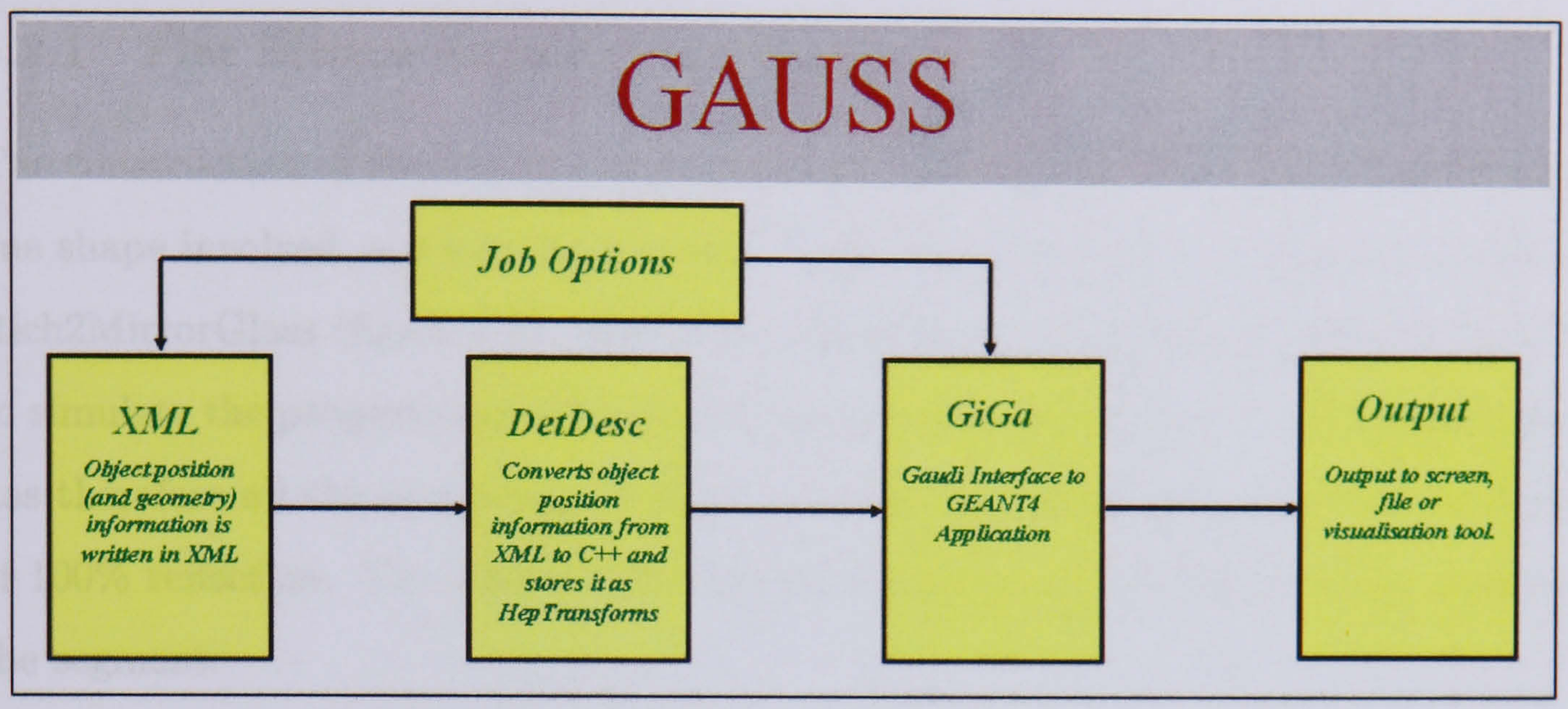

Figure 5.1: A simple view of Gauss.

All of the composition and position information about any part of the detector is held in the XML database. There is one logical volume for each type of created object. The logical volume for an object will have parameters such as size, shape and the material it is made from. The XML code for each object is then converted into C++ using a package called DetDesc. The advantage of creating objects in this way is evident, in that it would be very difficult and time consuming for the developer to directly write the C++ code for each object. For example, the C++ code for a complex shape such as a sphere could run into hundreds of lines, whereas the XML equivalent may be written in only a few lines.

In order for a logical volume to be physically placed in the simulation, it must have at least one physical volume. The physical volume holds the information for the placement of the logical volume. Therefore it has such parameters as translation, rotation and scale. For each physical volume, a copy of the object referred to in the objects logical volume is created and placed with the position information contained in its physical volume.

5.2 Mirror Segment Geometry

5.2.1 Flat Mirror Segment Construction

The construction of the flat mirror segment in XML is very simple since there is only one shape involved, a 6 mm thick square of dimensions 410 mm × 380 mm made of Rich2MirrorGlass (figure 5.2). Rich2MirrorGlass, is a hypothetical material created to simulate the properties of glass with a coated reflective surface. Rich2MirrorGlass has therefore all the properties of glass, but with the additionally specified property of 100% reflection. The centre of the logical volume is at the centre of the inside of the segment.

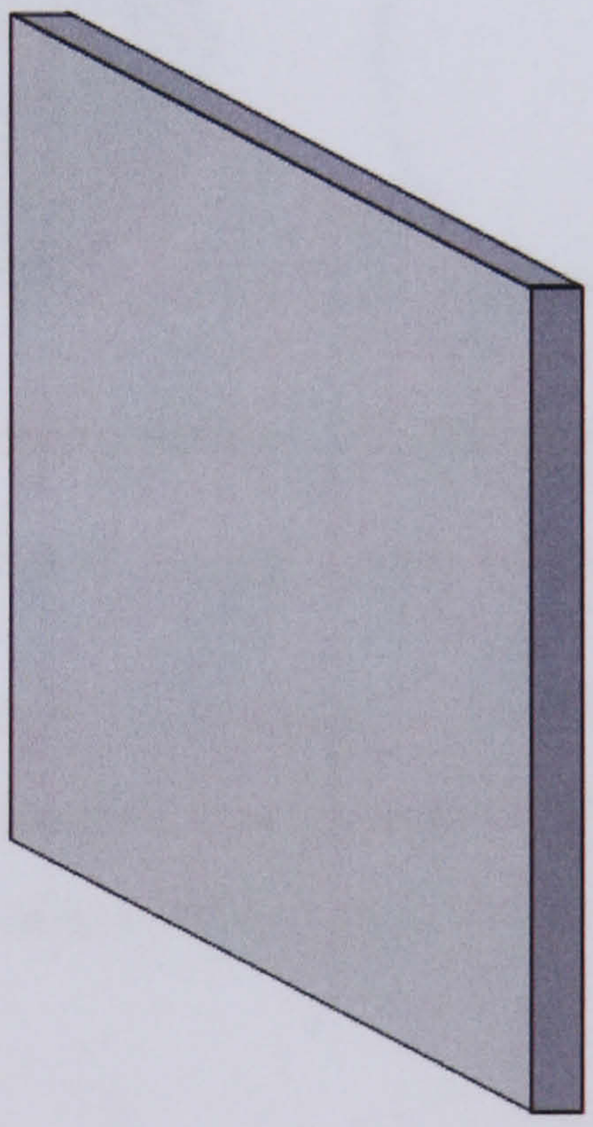

Figure 5.2: Logical Volume of the Flat Mirror Segment.

When all twenty of the mirror segments are put together to a flat mirror, the total reflectivity of the mirror drops to 98.4%, with a 1.2% loss due to clearances between segments and a further loss of 0.4% due to the chamfers on the edge of each segment.

5.2.2 Spherical Mirror Segment Construction

The construction of the spherical mirror segment is far more complex than the flat mirror segment. The basic spherical mirror segment is created by taking the product of two shapes, a large hollow sphere and a hexagon with a finite depth.

The large hollow sphere is constructed by creating a sphere of radius 8606 mm and subtracting from its inside a sphere of radius 8600 mm. The product is a large hollow sphere with inner radius 8600 mm and outer radius 8606 mm (figure 5.3).

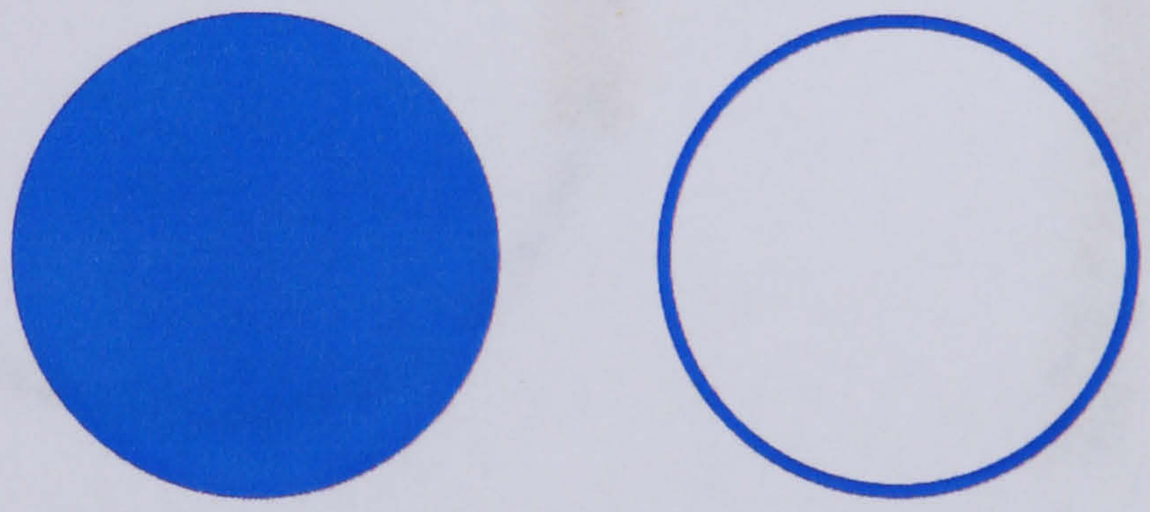

(a) Sphere before subtraction (b) Sphere after subtraction

Figure 5.3: The creation of a large hollow sphere through subtraction

The hexagon is constructed by creating a cuboid of dimensions 441.7 $mm\times$ 441.7 $mm\times$ 50 mm, and subtracting four rotated cuboids from its corners, leaving a hexagon with the dimensions of 441.7 mm between any two parallel faces (figure 5.4).

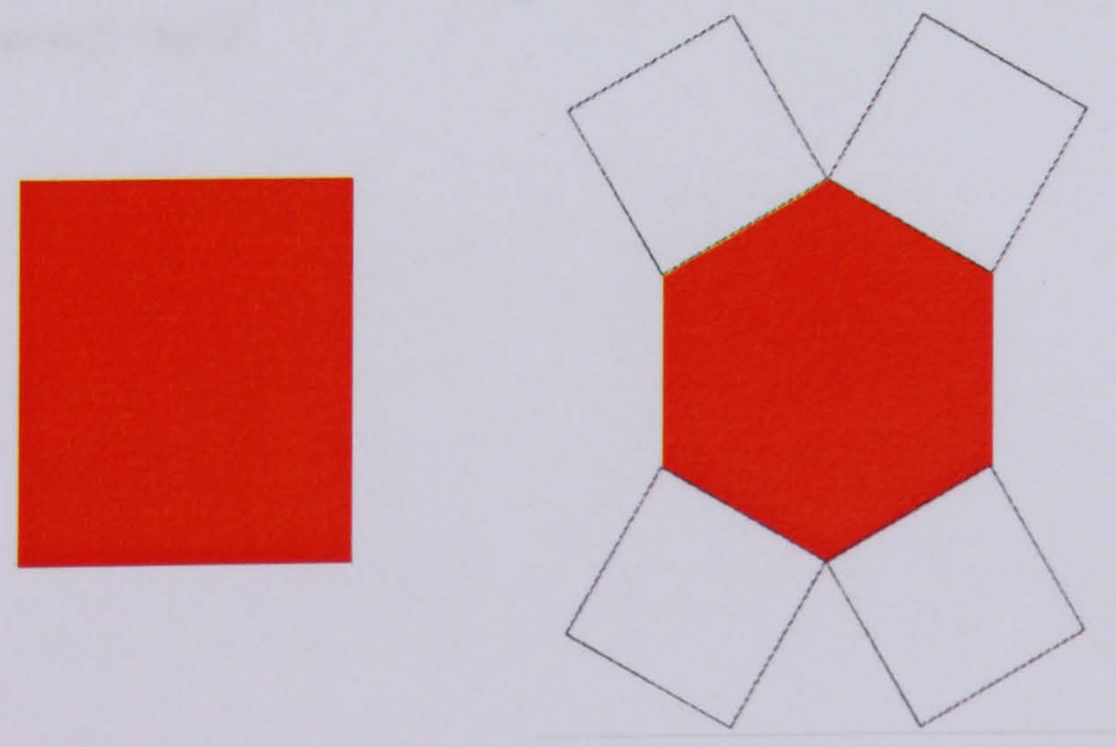

Figure 5.4: The subtraction of four rotated cuboids to create a flat hexagonal segment

These two shapes are placed together at the edge of the sphere (figure 5.5(a)). Any part of the subsequent volume that is not a product of the two volumes is then subtracted away, leaving a hexagon with a concave surface(figure 5.5(b)).

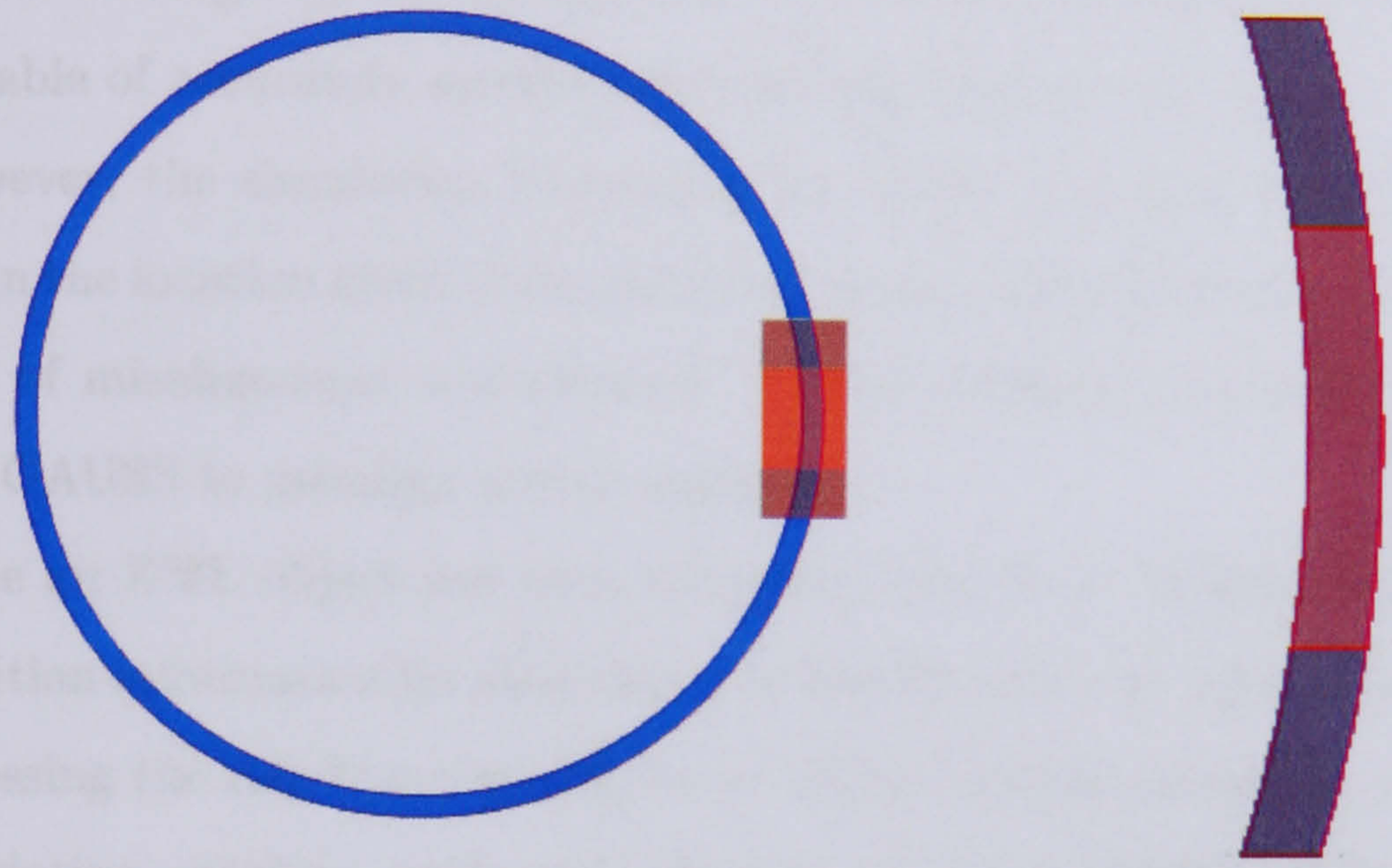

(a) The overlap of volumes before subtraction

(b) The overlap of volumes after subtraction

Figure 5.5: The creation of a hexagonal concave (spherical) segment through the subtraction of logical volumes

Unlike the flat segment, the centre of the logical volume for the spherical mirror segment is at the centre of the original sphere that created the volume, and not at the centre of the segment itself.

5.3 Coordinate Systems

5.3.1 Misaligning Mirror Segments

In the simulation of the laser mirror alignment monitoring system, it is necessary to be able to misalign the mirror segments in order to show that the segment monitors are capable of accurately monitoring small segment rotations.

However, the simulation framework for LHCb only allowed for an object to be placed in the location given in its physical volume in the XML database, no additional process of misalignment was allowed. It was therefore necessary to find a way of forcing GAUSS to misalign mirror segments.

Once an XML object has been converted into C++ by the DetDesc package, all the position information for that object is held by a matrix called a HepTransform3D. By accessing the HepTransform3D for an object, 3-dimensional changes can be made to translation, rotation, scale and reflection. If any misalignment is to be done, it is important that it is done at this stage, before the HepTransform3D is passed onto GiGa, the GAUDI interface to GEANT4 (figure 5.6).

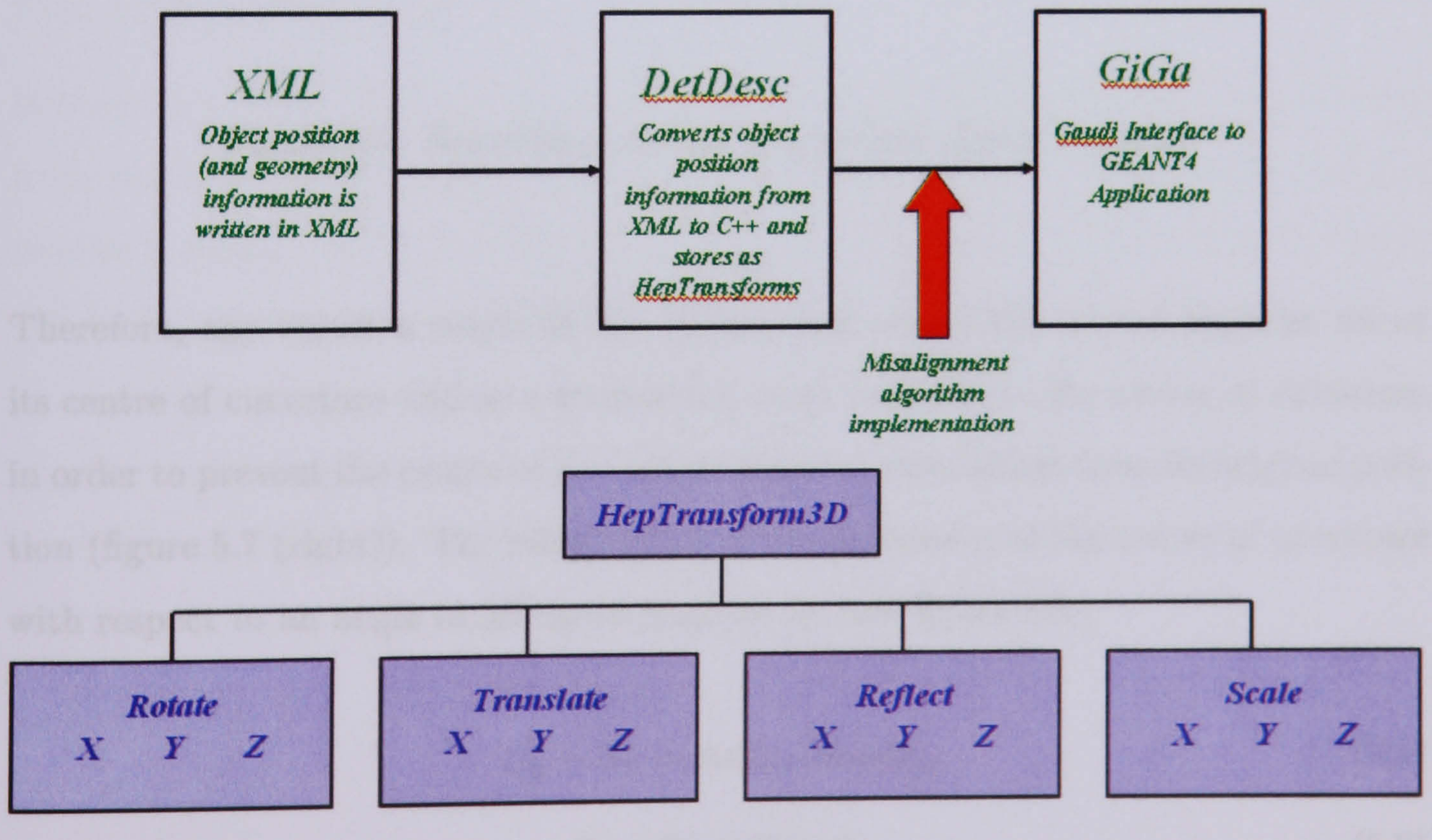

Figure 5.6: Implementation point of the misalignment algorithm.

Spherical Mirror Segments

Due to the nature of the construction of the spherical mirror segments in the XML, it is intrinsically difficult to simply rotate them. This is because the centre of the logical volume is the centre of the sphere they are constructed from (Cx, Cy, Cz), and not the centre of the mirror segment itself (Sx, Sy, Sz). Therefore, if the HepTransform3D for a spherical segment is changed only with respect to rotation, the mirror segment will also experience a translation (figure 5.7 (left)), since the rotation will be made around its centre of curvature (the centre of the sphere).

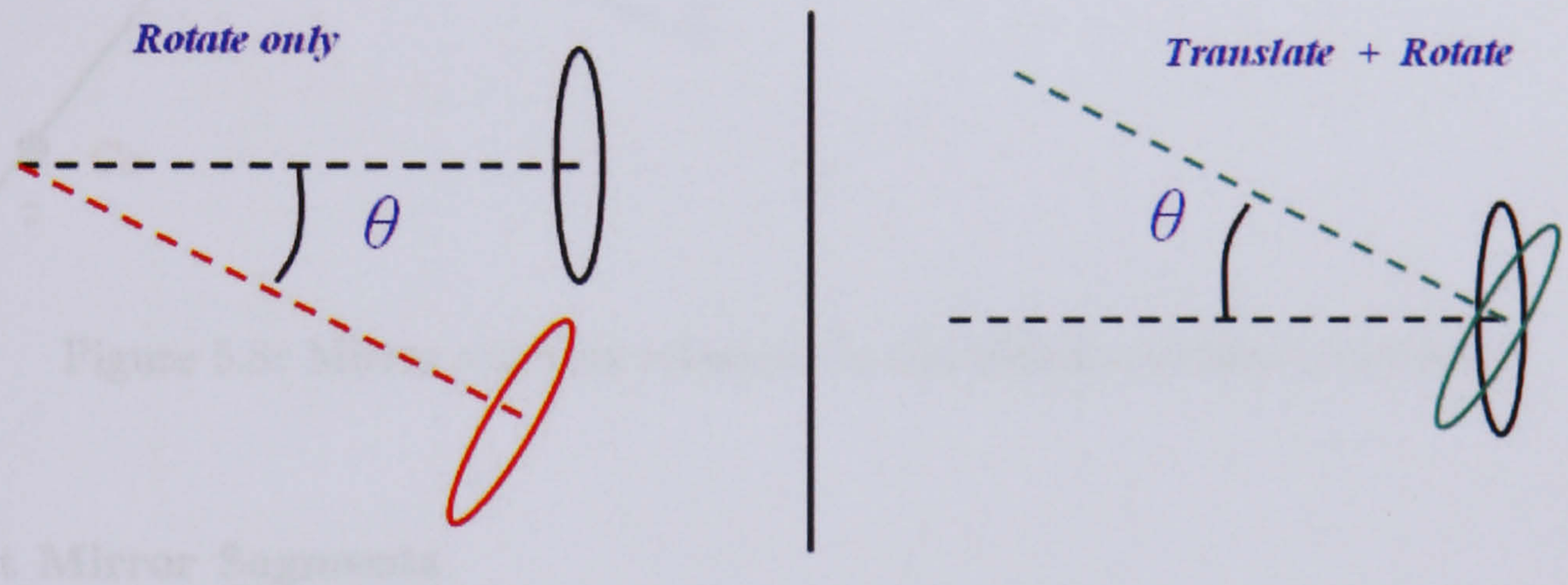

Figure 5.7: Rotation point for a spherical mirror segment.

Therefore, any rotation made to the volume will rotate the mirror segment about its centre of curvature and so a translation must be made to the centre of curvature in order to prevent the centre of the mirror segment translating from its original position (figure 5.7 (right)). The relationship of the movement of the centre of curvature with respect to an angle in 3D space is given by (see figure 5.8):

$$C_x - S_x = sin\theta_{xz}.Rcos\theta_{yz} \tag{5.1}$$

$$C_y - S_y = Rsin\theta_{yz} \tag{5.2}$$

$$C_z - S_z = cos\theta_{xz}.Rcos\theta_{yz}, \tag{5.3}$$

where θ_{xz}, θ_{yz} are the rotations around the y axis and the centre of curvature respectively, and R is the radius of curvature.

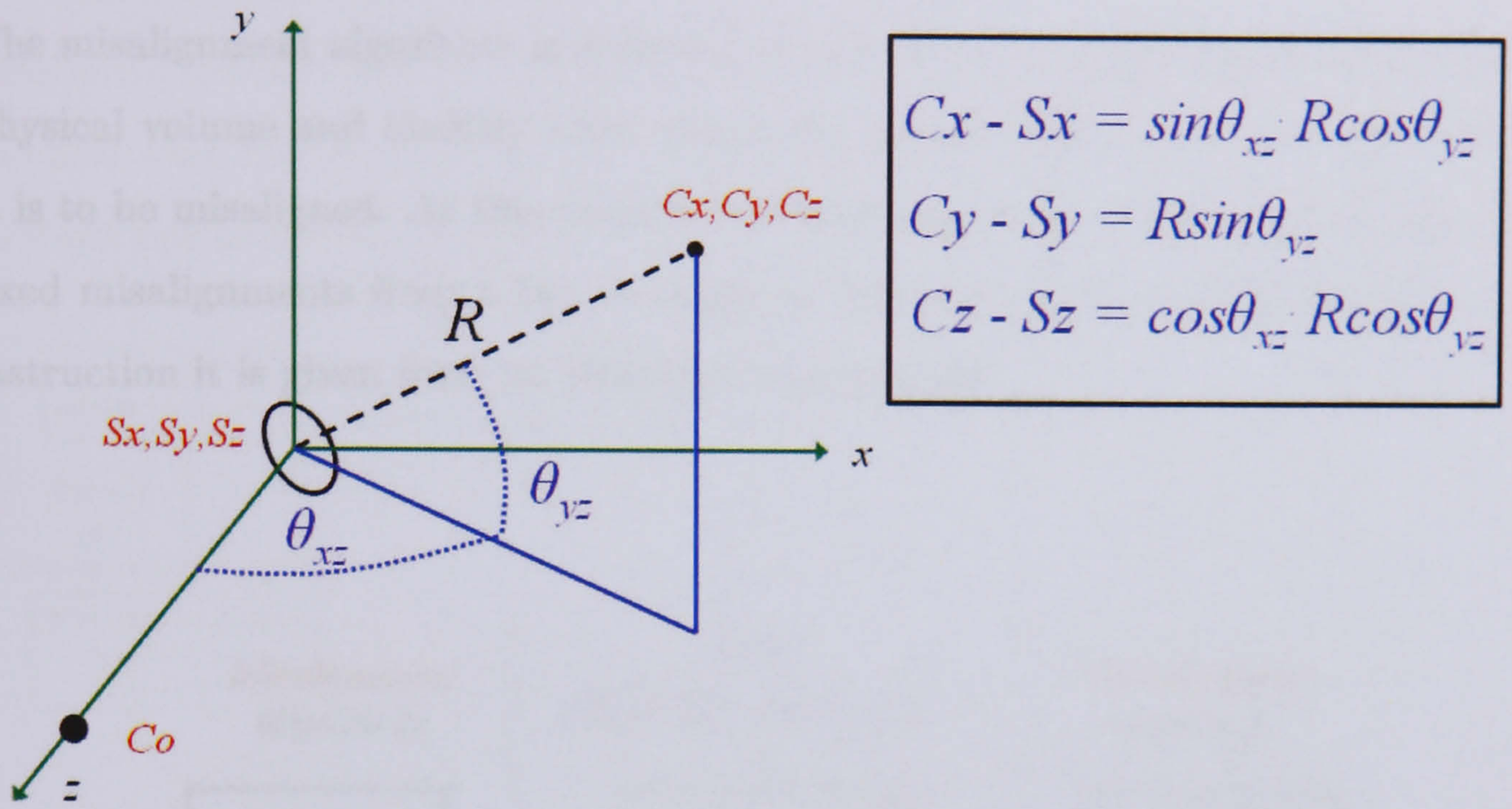

Figure 5.8: Mirror segment rotations in the global coordinate system.

Flat Mirror Segments

Because the centre of the reflective surface of the flat mirror segment is only 3 mm from the centre of its logical volume, any rotation of the logical volume does not require a translation, since the centre of the reflective surface of the mirror segment will have only moved by a negligible amount for rotations in the order of 1 $mrad$.

5.3.2 The Misalignment Algorithm

Software Architecture

The misalignment algorithm is designed to read in the original Heptransform3D of a physical volume and identify what object the volume refers to, and whether or not it is to be misaligned. At this point it will either apply a random misalignment, call fixed misalignments from a file, or apply no misalignment at all, depending on the instruction it is given from its MisAlignment.opts file.

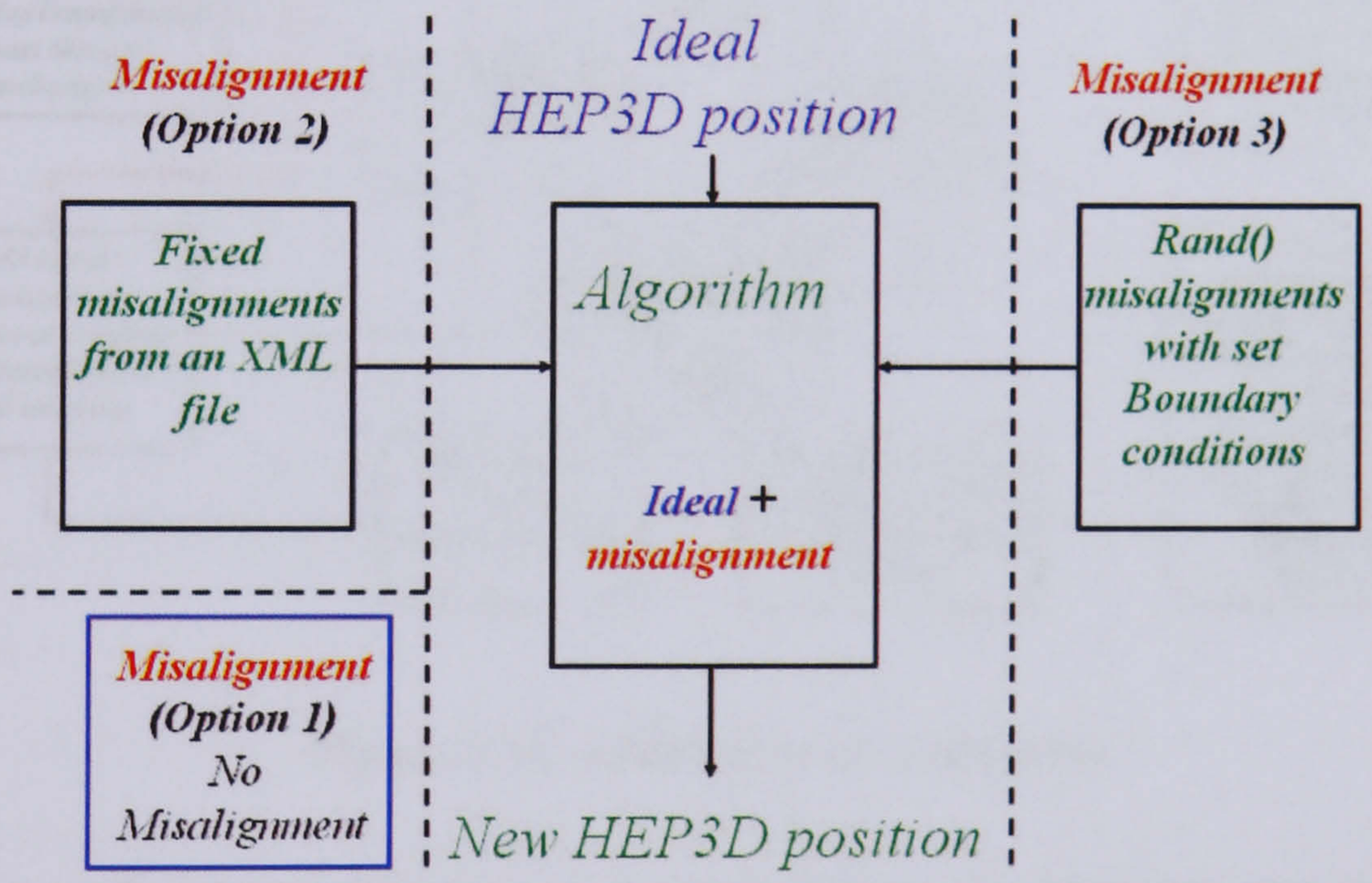

Figure 5.9: Misalignment Algorithm.

Algorithm Overview

The algorithm itself implements a number of checks and changes. The standard method of making a change to a HepTransform3D is to multiply it by another 3D transform matrix that contains the change by which the object should be moved. However, the non-inverted HepTransform3D does not give its position with respect to the origin $(0, 0, 0)$, but the position of the origin with respect to itself. Thus a change made to the HepTransform3D could have an undesired effect.

In order to avoid unwanted changes, the misalignment algorithm first reads the HepTransform3D, keeps the inverted matrix values in memory and applies the opposite non-inverted matrix values to the original HepTransform3D. This returns all the position and rotation information back to 0. The reason for this cancellation is firstly to check that the algorithm is handling properly the HepTransform3D, and secondly to limit unwanted errors when applying the new HepTransform3D values.

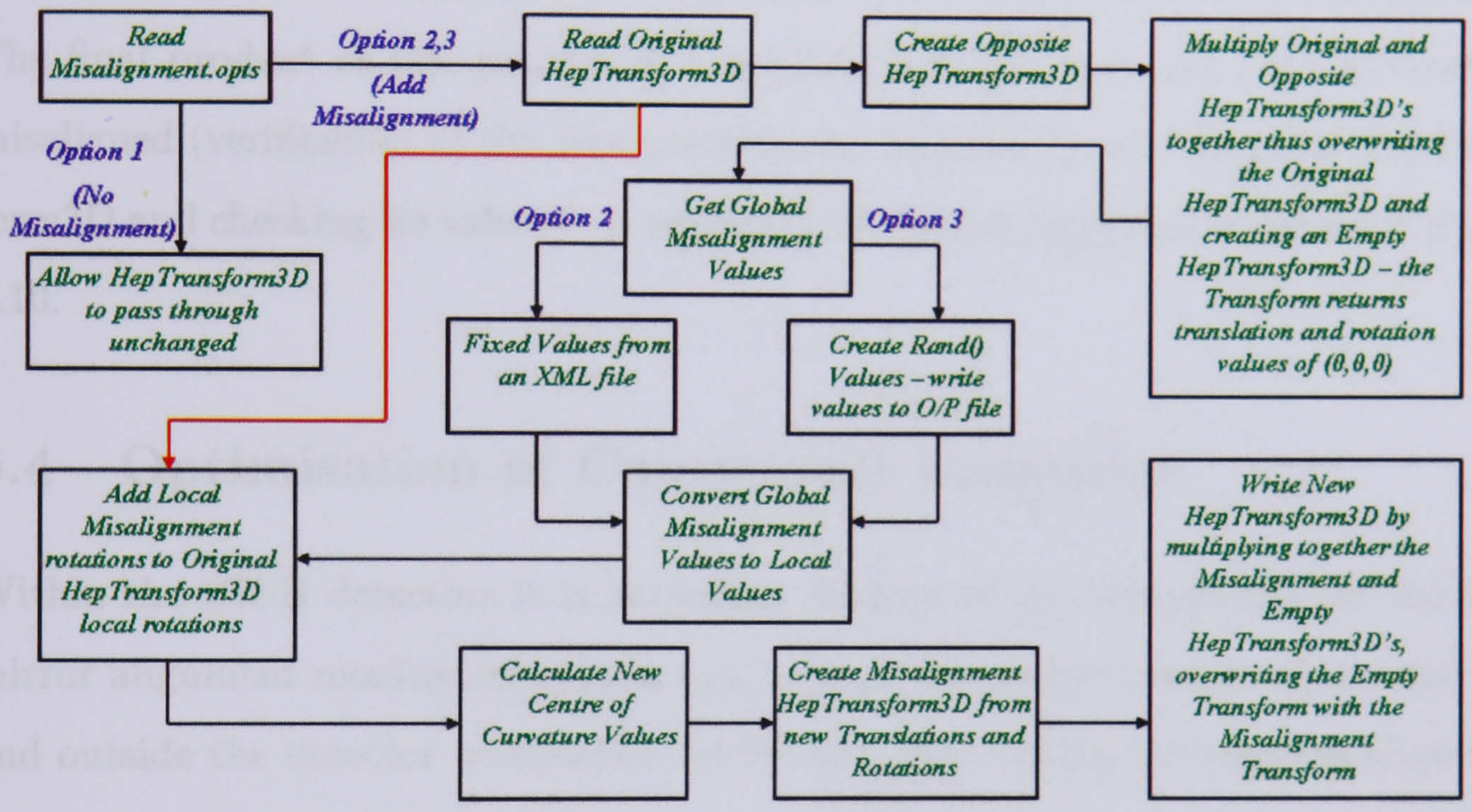

Figure 5.10: Misalignment Algorithm.

Before applying any changes to the original values stored in memory, the algorithm reads its options file (MisAlign.opts) to find out what type of misalignment to make. The options are (see Figure 5.9):

1. Fixed misalignment from file.
2. Random misalignment (seed supplied in file).
3. No misalignment.

The rotation information for fixed misalignments is presently held within the MisAlign.opts file itself and is split into four sections (Spherical X rotation, Spherical Y rotation, Flat X rotation and Flat Y rotation). Each mirror segment has its own fixed misalignment value.

For random values, a simple uniform randomiser is implemented that starts its number generation from a given seed value. This means that random values can be reproduced. The range of the random number generator can be restricted with respect to minimum and maximum allowed values.

For both fixed and random values, the algorithm takes the misalignment value and adds it to the original value kept in memory. It then creates a misalignment HepTransform3D with the new values and multiplies it with the empty HepTransform3D. The final product of this process is a HepTransform3D that has been successfully misaligned (verification of the new position can be made by recalling the HepTransform3D and checking its values). A schematic of the full algorithm is shown in Figure 5.10.

5.4 Optimisation of Component Locations

Within the RICH detectors it is important that all of the components for the laser mirror alignment monitoring system can be kept within the bounds of the detector and outside the detector acceptance, whilst still allowing for the segment alignment monitors to be optically sensitive.

In a plan view, the closer the APS camera is to the mirror segment, the less sensitive the segment aligment monitor is going to be to changes in the Y rotation of the segment being monitored.

For monitored mirror segments that are not at a translation of $y = 0\ mm$, the path of the light from the focusing unit to the mirror segment and the mirror segment to the APS camera are no longer equal in length or symmetrical in geometry (see Figure 5.11). With a given starting point, the destination of the light after reflection can be calculated.

The aim of the component location algorithm is to find suitable positions for the key components of the laser mirror alignment monitoring system. The suitability of the positions are determined by the sensitivity of the segment alignment monitors and the feasibility of the physical positions of the components within the RICH detector.

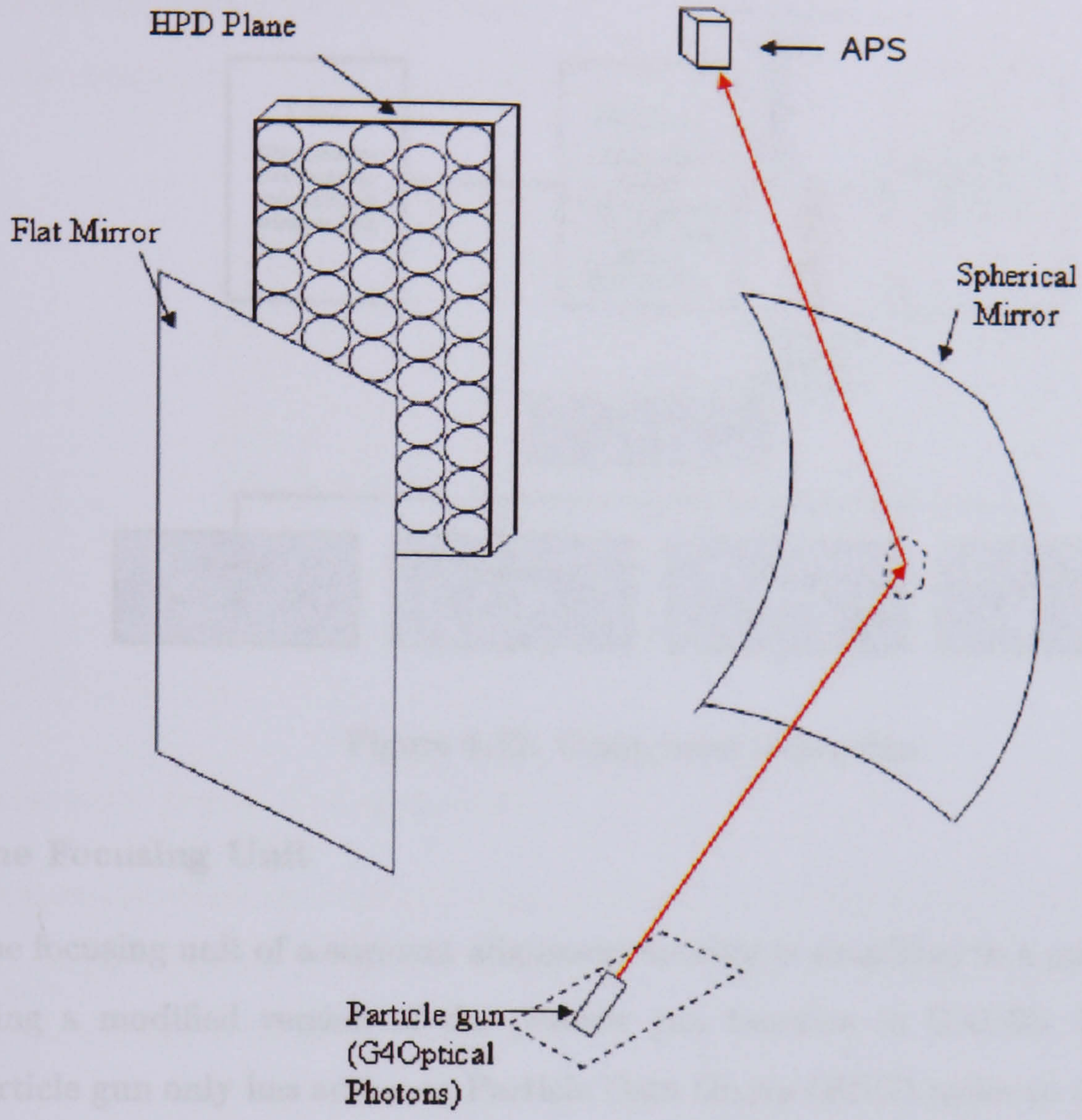

Figure 5.11: Misalignment Algorithm.

5.4.1 Software Architecture

Since it is the job of the component location algorithm to find the ideal locations of the components for the laser mirror alignment monitoring system, it should be activated at a time when all of the mirrors are in their ideal locations in the simulation process. Therefore, within the software structure, the component location algorithm must by necessity come before any misalignment of the mirror segments occurs (i.e. before the misalignment algorithm), as shown in Figure 5.12.

5.4.2 Component Creation

The simulation of the key components of the laser mirror alignment monitoring system are each considered in turn.

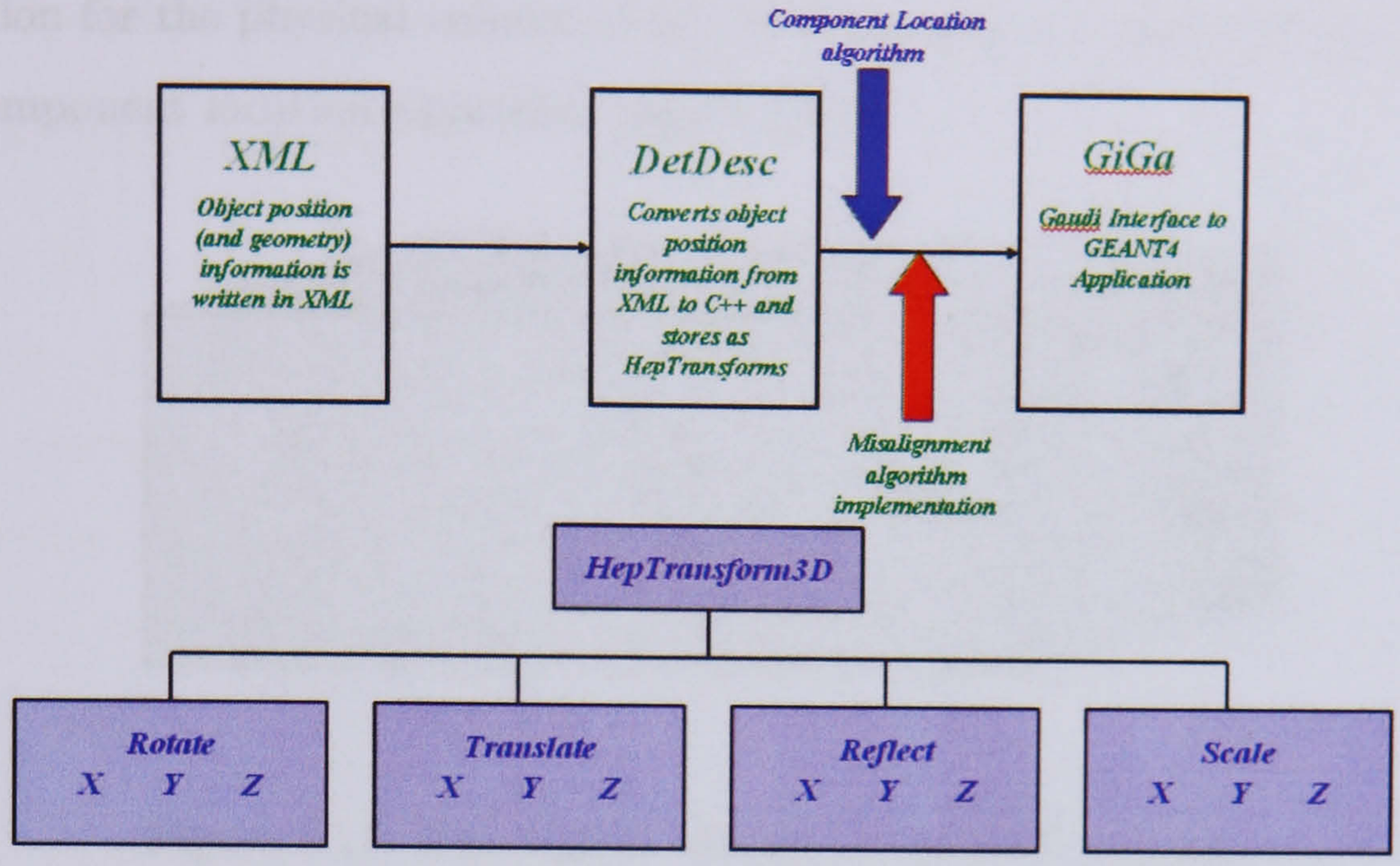

Figure 5.12: Component Algorithm.

The Focusing Unit

The focusing unit of a segment alignment monitor is simplified to a point light source using a modified version of the particle gun function in GAUSS. By default the particle gun only has access to Particle Data Group (PDG) codes to select a particle to be generated by the particle gun. Although there is a PDG code for a photon, it is a high energy photon (non-optical), and therefore cannot be used to simulate the reflections of visible wavelength photons. However, GEANT4 can simulate optical photons, and because the photon energy can be specified within the particle gun options, the problem can be solved by writing a line of code into the GiGa package, that says "if a PDG code photon is selected and its energy is below 3 MeV, change it to a G4OpticalPhoton".

By making this change, the particle gun can now be used to produce optical photons and act as the focusing unit. These are located at the base of the RICH2 detector, as shown in Figure 5.11.

The APS Camera

The XML logical volume construction for the APS camera in the simulation is a simple aluminium block of dimensions 100 $mm\times$ 50 $mm\times$ 50 mm. The positional

information for the physical volume of the APS Camera is acquired from the output of the component location algorithm (figure 5.13).

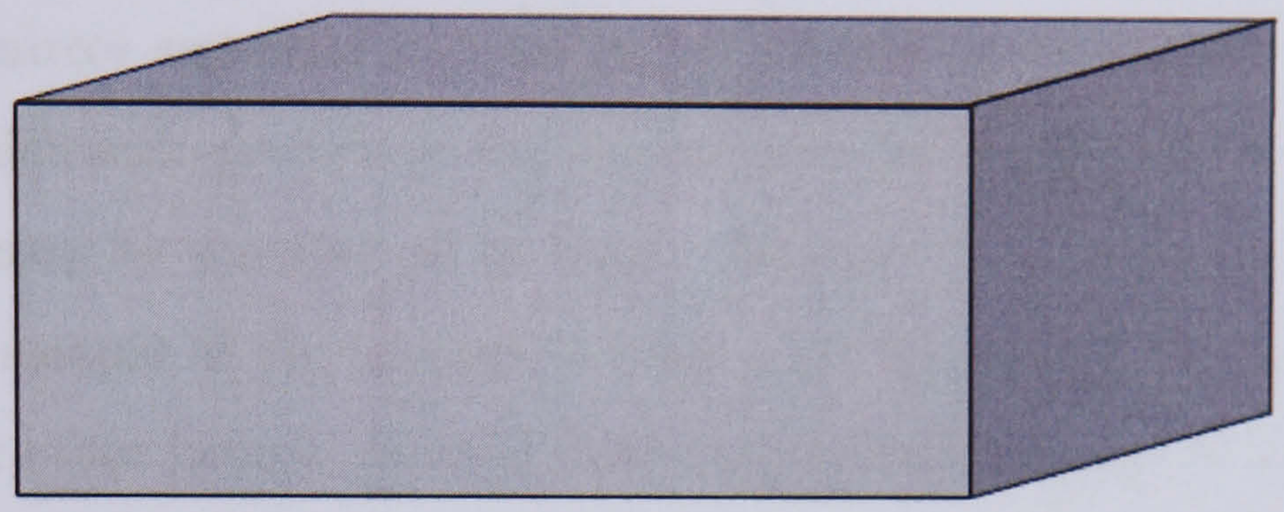

Figure 5.13: The logical volume of the APS camera.

Reference Beam Components

Because the reference beam component mounts are designed such that they can direct the reference beam to wherever the APS camera is placed, it is not necessary to calculate their optimal positions.

5.4.3 Optimal Geometry

Choice of Mirror Segments

There are 96 mirror segments in total in RICH2 (56 spherical and 40 flat). Since the software alignment procedure will perform the final alignment of the segments, it is not necessary to monitor all of them. However, it is necessary to monitor a representative sample of the mirrors to keep track of changes due to pressure and temperature or other factors. We will limit the number of segments to be monitored to sixteen (four per mirror) due to cost constraints and to simplify the complexity of the system. It is therefore important to make a careful selection on which mirror segments should be monitored.

The most useful mirrors to select are those that are heavily used in the reflection of Cherenkov Photons. These mirrors are closest to the beam pipe at $y = 0$. These mirrors also offer a more ideal geometric position with respect to incident and reflected alignment beam angles.

If a flat mirror segment is selected that is too far above $y = 0$ (figure 5.14(a)), then the focusing unit will need to be positioned further back in the detector to prevent an inevitably short optical arm for the Y axis of the mirror (a short optical arm (L) will produce a low sensitivity).

Similarly, if a flat mirror segment is selected that is too far below $y = 0$ (figure 5.14(b)), then the focusing unit will need to be placed further towards the mirror segment to prevent the resultant extended reflected beam hitting the exit window. Since the exit window is within the acceptance, components cannot be placed within this region.

Unlike the flat mirror segments, the curvature of the spherical mirror causes the reflected beam geometry to differ from that of flat mirror segments. If a spherical mirror segment is selected that is too far below $y = 0$ (figure 5.15(a)), the resultant XZ optical arm will be very short and the sensitivity will be very low. This is because the mirror segments have an inherent X rotation associated with them, that causes the reflected beam angle to be significantly different.

If a spherical mirror segment is selected that is too far above $y = 0$ (figure 5.15(b)),

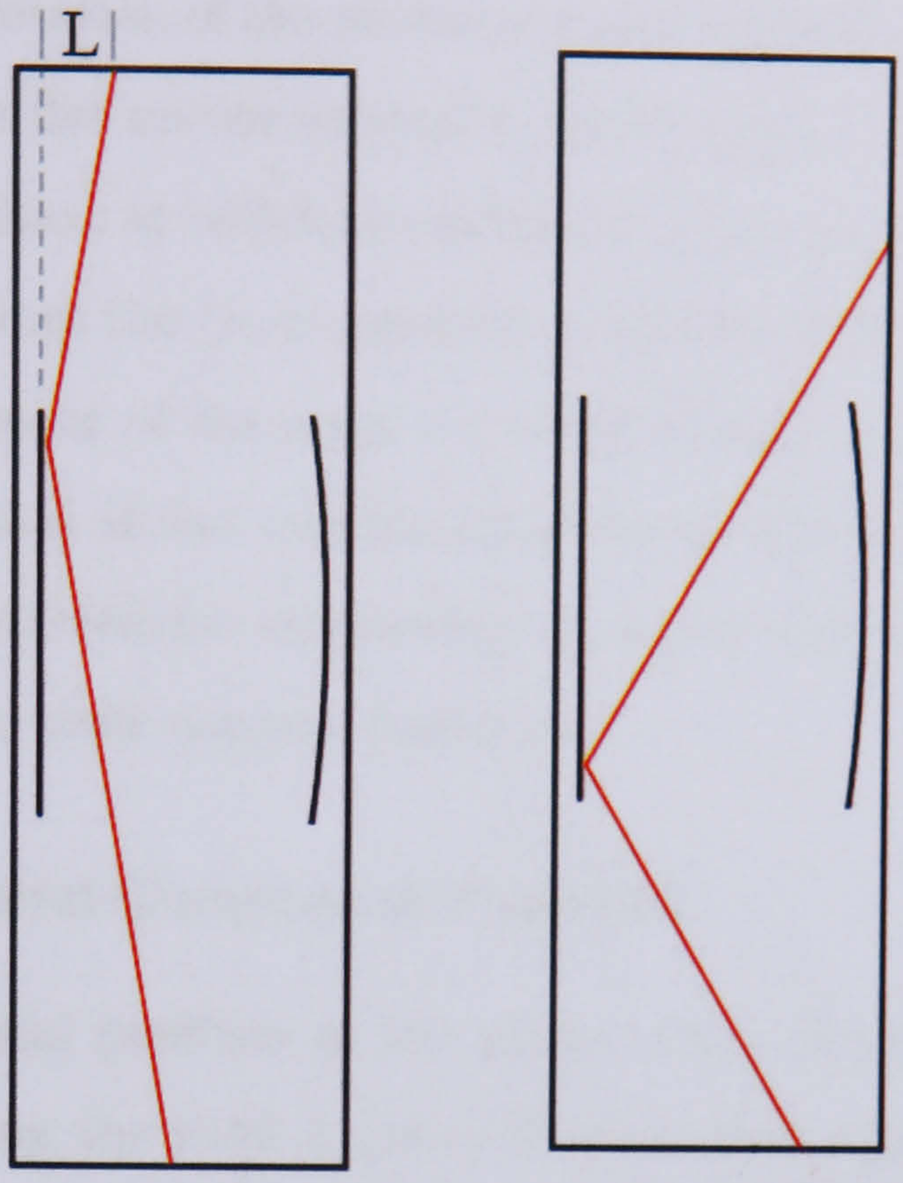

(a) Monitored segment is far above $y = 0$

(b) Monitored segment is far below $y = 0$

Figure 5.14: Flat segment alignment beam reflections

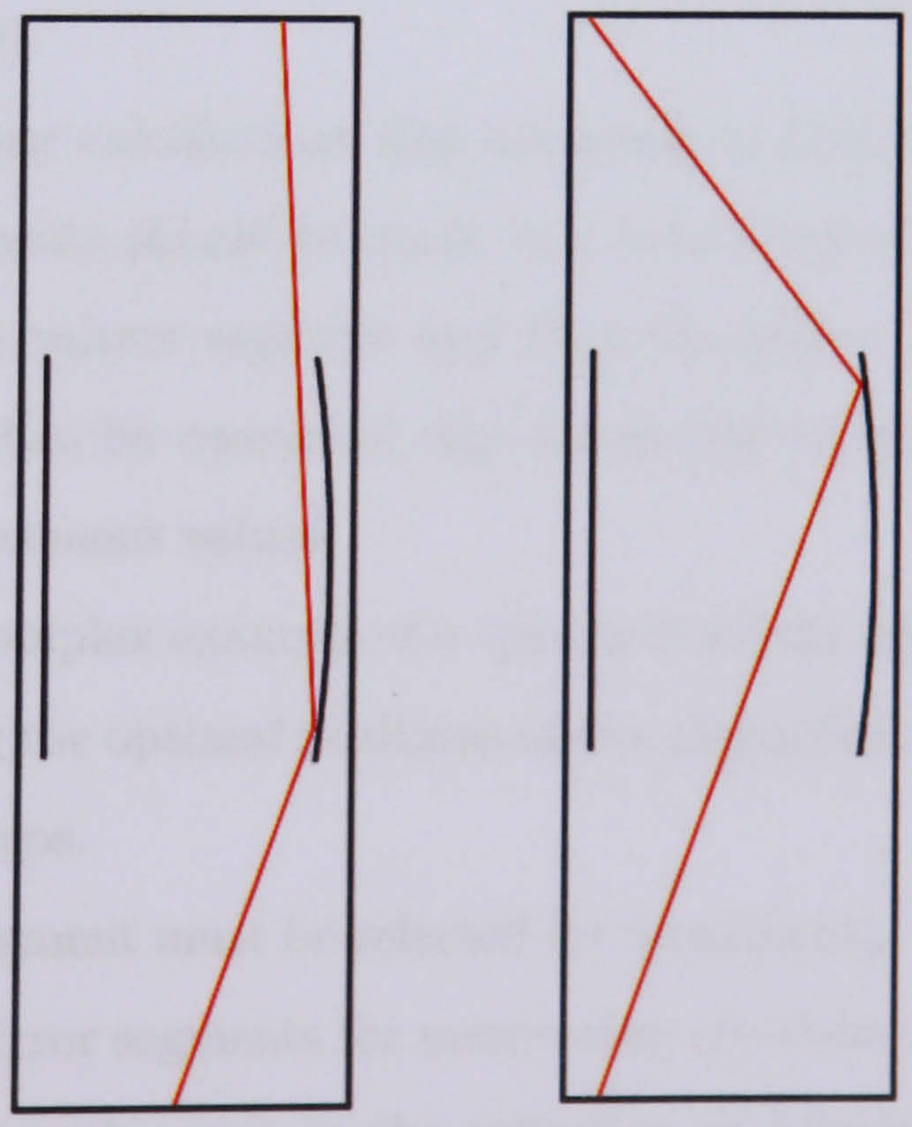

(a) Monitored segment is far below $y = 0$

(b) Monitored segment is far above $y = 0$

Figure 5.15: Spherical segment alignment beam reflections.

then, although the X rotation of the mirror segment prevents a short XZ optical arm, as is the case with the flat mirror segments, another less obvious potential problem occurs. The (x, z) position at which the reflected beam intersects the roof of RICH2 does not differ much from the (x, z) position of another reflected beam coming from a spherical mirror segment of the same (or neighbouring) column where y is greater than 0. This means that if two neighbouring mirror segments near the top of the spherical mirror are selected for monitoring, then the APS cameras will have some overlap with respect to their nominal positions.

Calculation of Optimal Component Positions

To calculate the optimal position of the components, the focusing unit and APS camera are placed along the local Z plane of the mirror segment, perpendicular to the centre of the segment on the global XZ plane of RICH2 (figure 5.16). This reduces the number of axis variables of the alignment components relative to the mirror segment being monitored. Therefore, all of the components of the segment alignment monitors should be located along the local Z plane of the mirror segment monitored (figure 5.16).

This means that any calculations that are made to find the optimal positions of the alignment components should be made in a hybrid coordinate system, using the local XY plane of the mirror segment and then the global XZ plane of the RICH detector. These can then be converted into the global coordinate system of RICH2 to obtain the final placement values.

Taking the more complex example of a spherical mirror segment not at $y = 0$, the method for calculating the optimal positions of the alignment monitoring components follows a number of steps.

Firstly, a mirror segment must be selected for monitoring. As has been mentioned previously, the best mirror segments for monitoring are those that are near the beam pipe and thus more heavily used in the reflection of Cherenkov photons. In this example, a spherical mirror segment above $y = 0$ has been selected (see Figure 5.17). (Note that the floor of RICH2 is at $y = -3150\ mm$, the roof is at $y = 3150\ mm$ and $y = 0\ mm$ goes through the centre of the mirror).

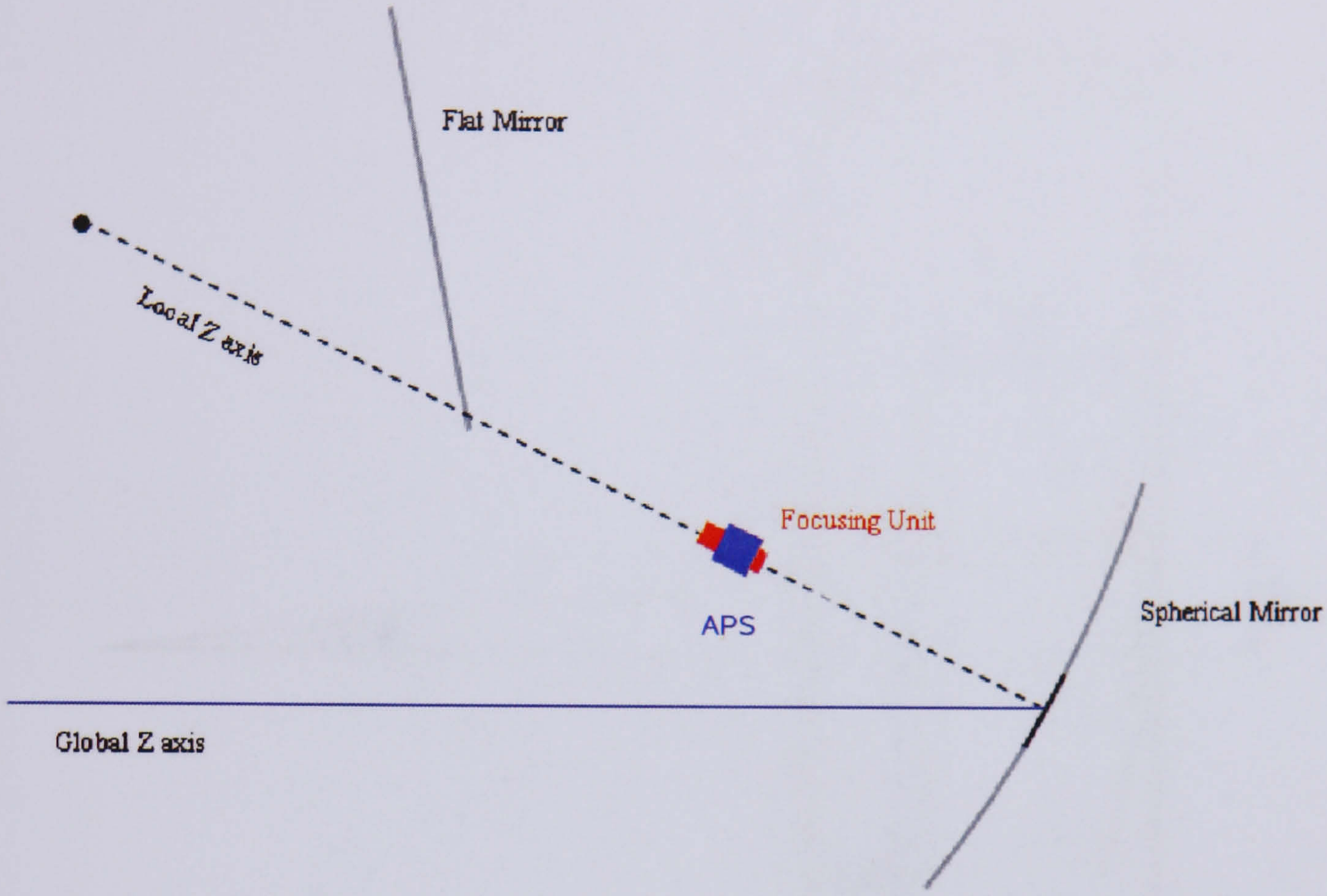

Figure 5.16: Component Location along the local Z plane of the mirror segment (top view).

The first step is to select a suitable distance (Hxz) along the local Z (on the global XZ) plane of the mirror segment at which to place the focusing unit. If this distance is too short, sensitivity will suffer, and if it is too large, the focusing unit may be potentially placed outside of the RICH detector (see Figure 5.17).

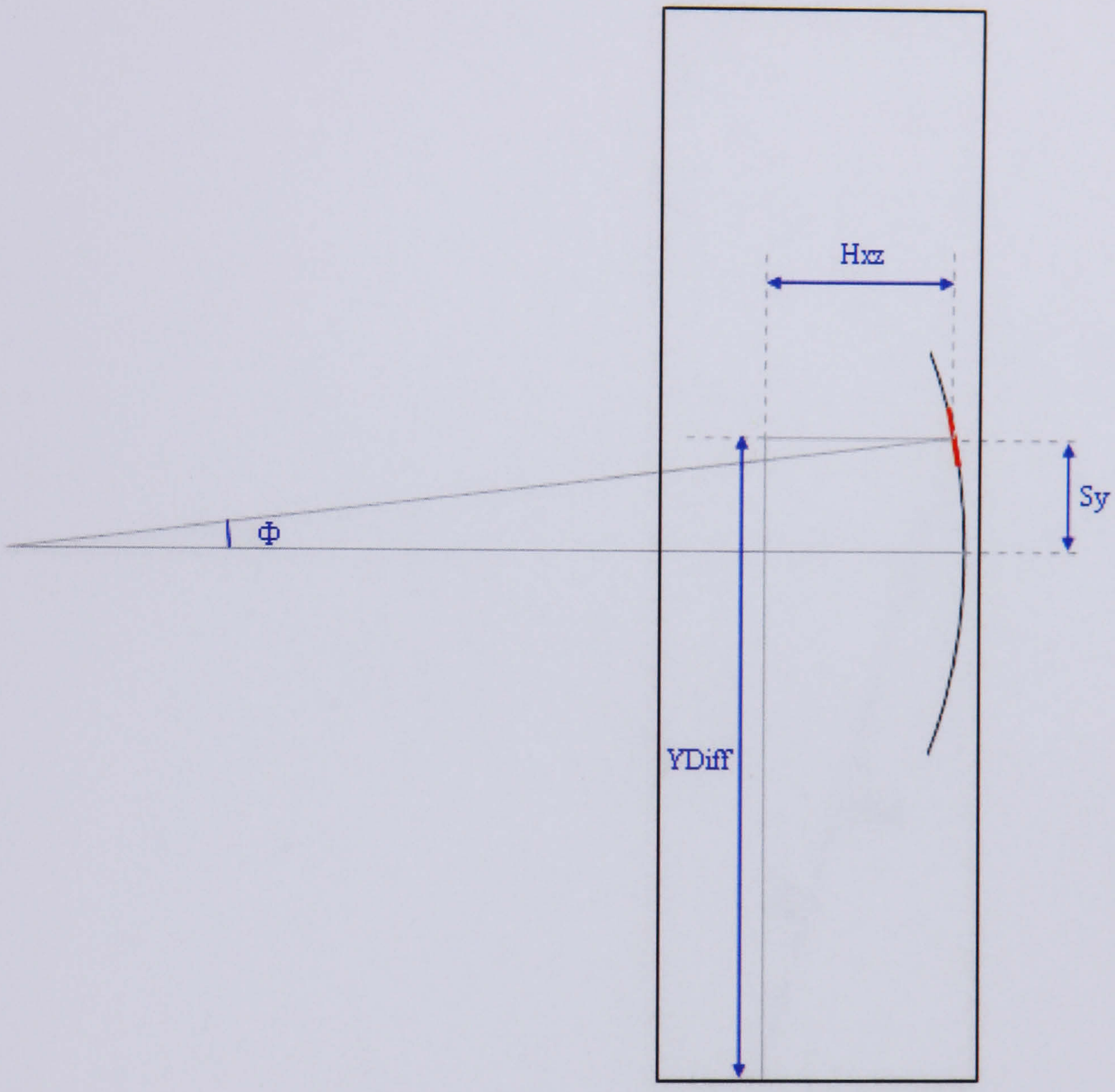

Figure 5.17: Step 1 of the Component Location Algorithm (side view).

Taking the local YZ plane of the mirror segment, the second step is to calculate the position and rotation of the focusing unit with respect to the mirror segment (see Figure 5.18). This point will be at the point Hxz from the mirror segment, and $y = -3150$.

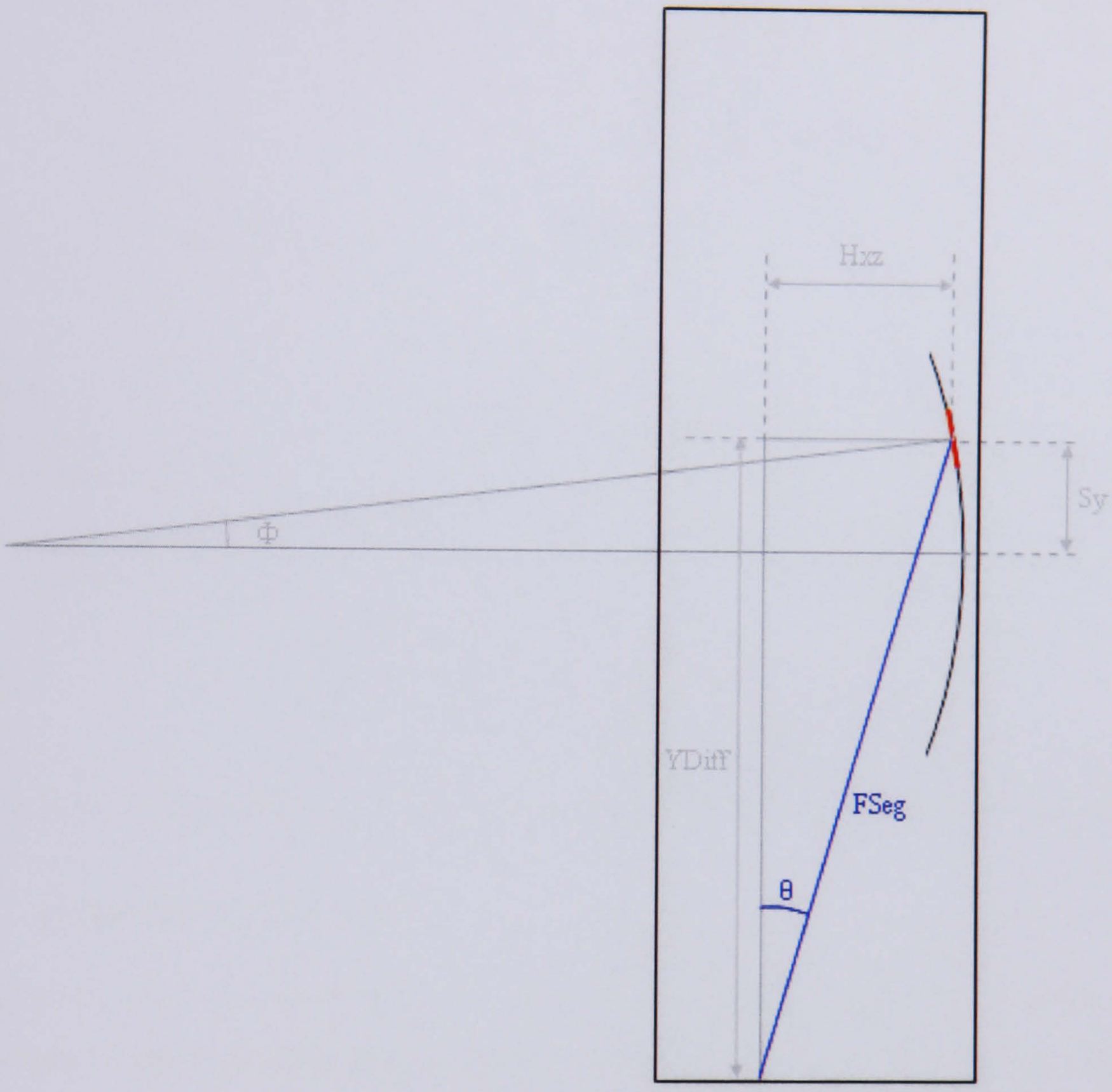

Figure 5.18: Step 2 of the Component Location Algorithm (side view).

Taking into account the X rotation of the mirror segment, the third step is to calculate the trajectory of the reflected beam, and thus the position and rotation of the APS camera along the local YZ plane of the mirror segment (Figure 5.19).

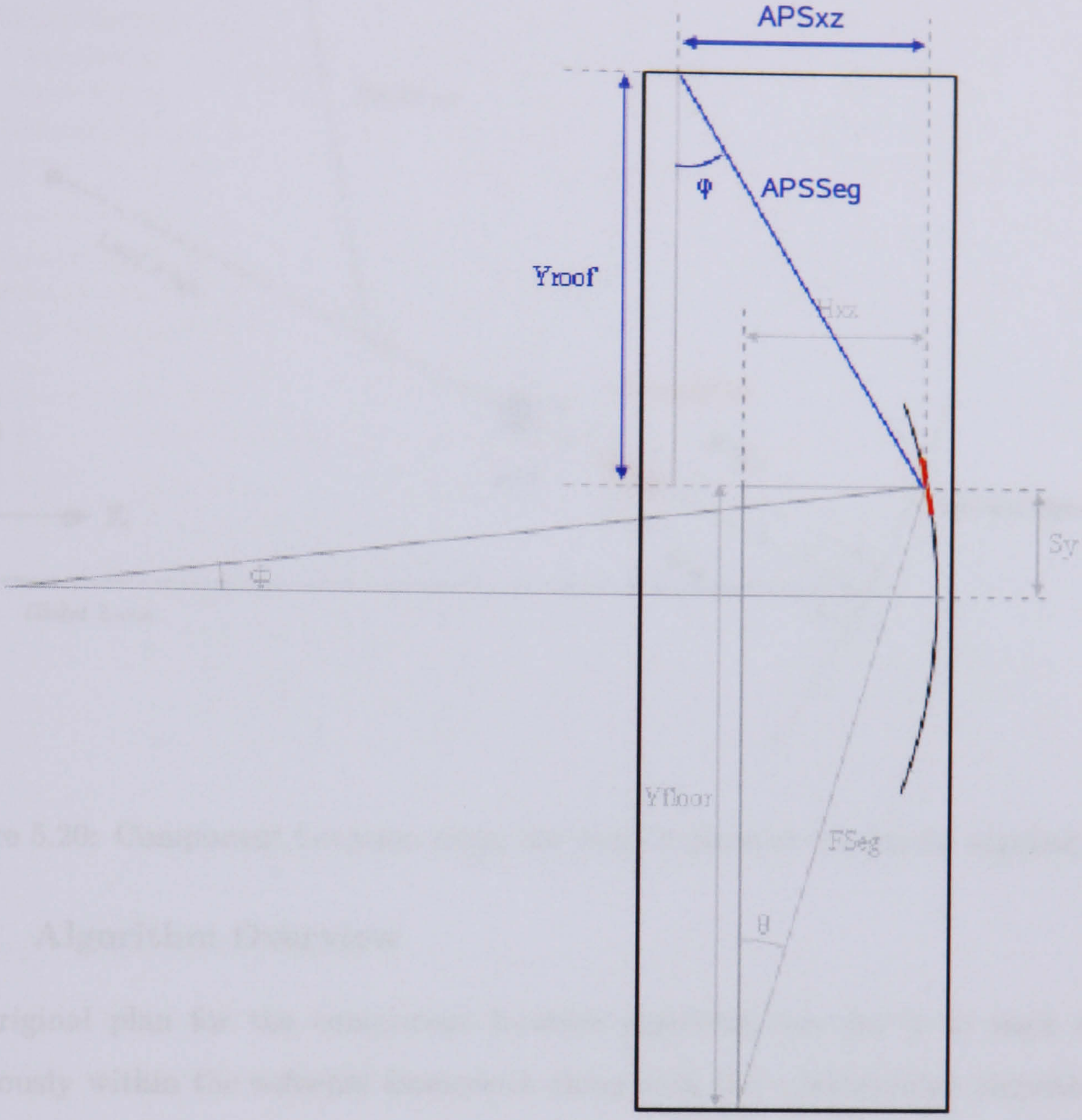

Figure 5.19: Step 3 of the Component Location Algorithm (side view).

The fourth and final step of the Component Location Algorithm is to calculate the positions and rotation of the focusing unit and APS camera in the global coordinate system XZ plane of RICH2. This final step requires the plotting of Hxz and APSxz along the global XZ trajectory of the centre of curvature and expressing the coordinates in terms of the global coordinate system (see Figure 5.20).

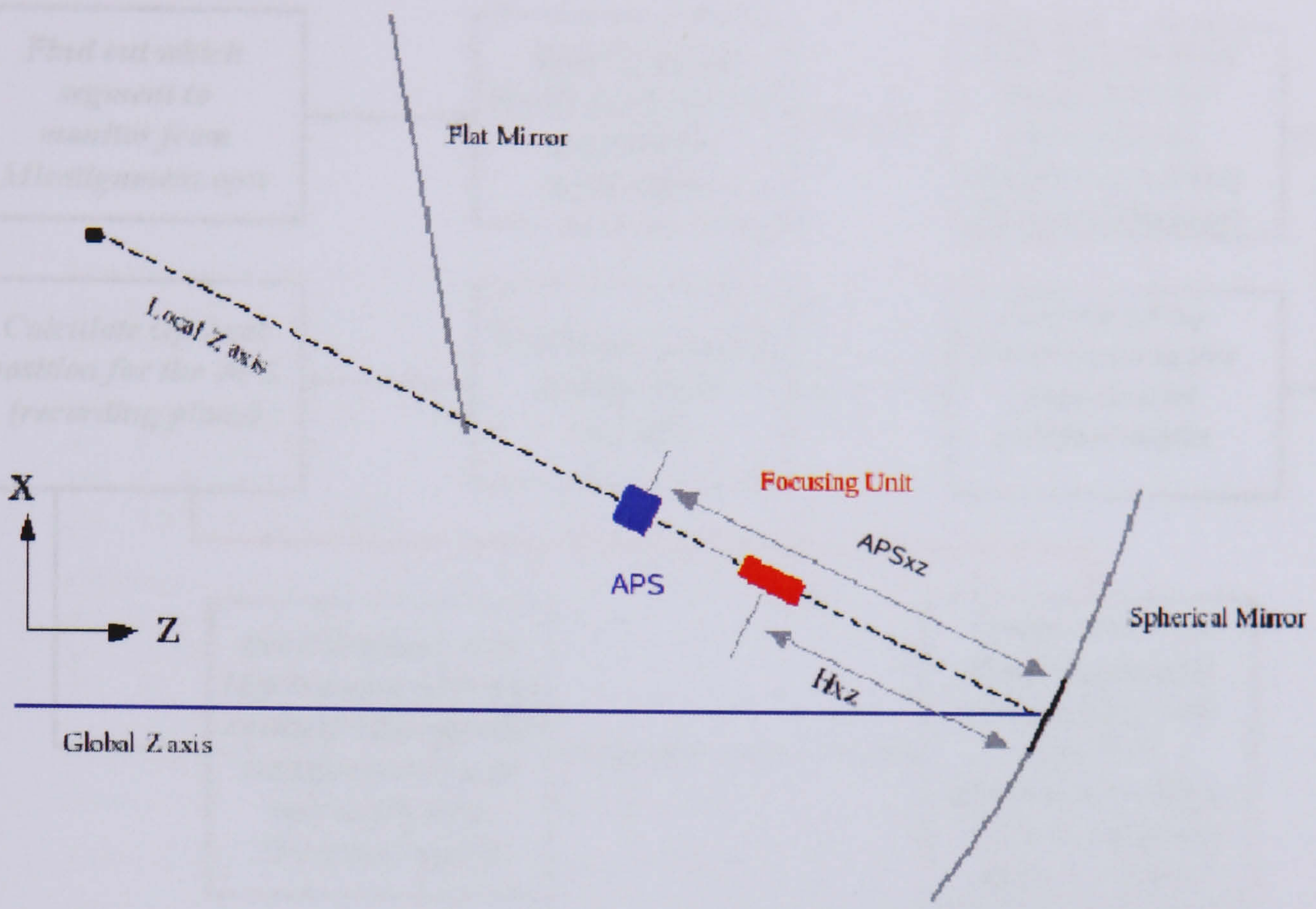

Figure 5.20: Component Location along the local Z plane of the mirror segment.

5.4.4 Algorithm Overview

The original plan for the component location algorithm was for it to work autonomously within the software framework along with the misalignment algorithm. In this way, the user could input the mirror segment number they wanted to monitor, and the algorithm would automatically place the photon gun and APS camera in their optimal positions. The architecture of such an algorithm is given in figure 5.21.

However, it is technically difficult to implement changes to the particle gun location after GAUSS has started. With this difficulty, further time constraint, and the fact that the main aim of the algorithm is to define the positions of the laser alignment system components, the best solution was to implement the component location algorithm as a stand-alone piece of software.

5.4.5 Results

In obtaining the final results from the component location algorithm, ideal values for the centre of curvature of the spherical mirror (8600 mm) and mirror positions were

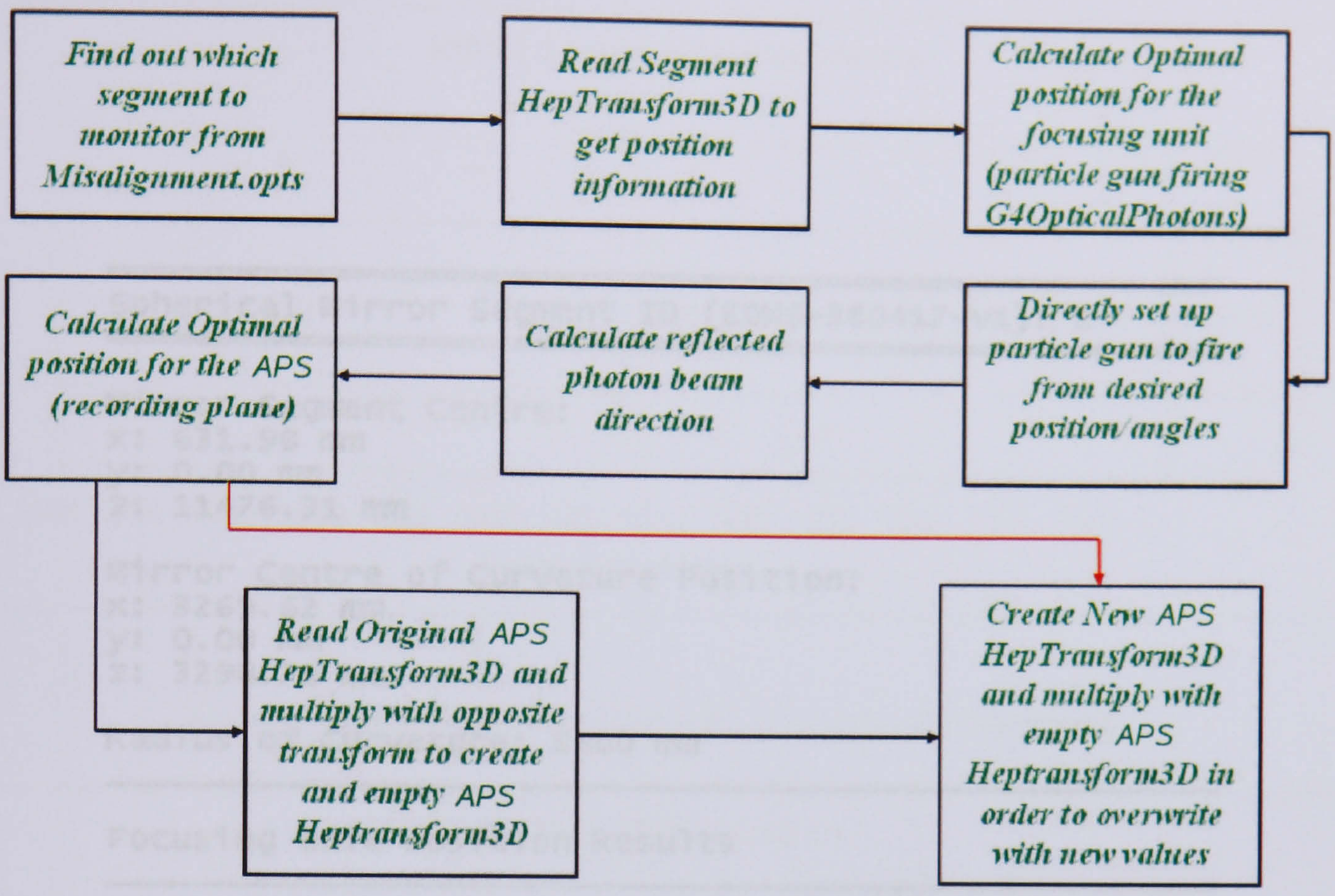

Figure 5.21: Misalignment Algorithm.

used [44]. These can be verified by making vector calculations.

Each result has three parts; information about the mirror segment monitored, calculation results for the position and rotation of the focusing unit and calculation results for the position and rotation of the APS camera. Figure 5.22 shows an example component location algorithm output for mirror 2 of the spherical mirrors as given in ref. [44].

The rotation results for the focusing unit are given as angles θ and ϕ in the polar coordinate system of the particle gun. Rotation results for the APS cameras are given in the Cartesian coordinate system of the RICH2 detector.

Once suitable positions (i.e. they are located within the bounds of RICH2 outside the acceptance) for all 16 of the focusing units and APS cameras have been obtained, the results can then be plotted to make sure that there are no potential position overlaps for the mounts for the components (see next chapter). Figures 5.23 and 5.24 show respectively the resulting positions for the focusing units and APS cameras.

On both sets of results, the four positions at the left of the figures are the focusing

```
Spherical Mirror Segment ID (EDMS-380417-V1): 2

Mirror Segment Centre:
x: 631.98 mm
y: 0.00 mm
z: 11476.31 mm

Mirror Centre of Curvature Position:
x: 3269.62 mm
y: 0.00 mm
z: 3290.78 mm

Radius of Curvature: 8600 mm

Focusing Unit Position Results

Global XZ Distance from mirror segment (Hxz): 1000 mm

Centre of aperture
x: 938.68 mm
y: 3008.00 mm
z: 10524.50 mm

Theta Rotation: 1.26582419 rads
Phi Rotation: 1.4691853 rads

CCD Position Results

Centre of Active Area
x: 935.83 mm
y: 2980.00 mm
z: 10533.36 mm

Y Rotation: 0.311726337 rads
X Rotation: -1.24984386 rads
```

Figure 5.22: Component Location Algorithm output.

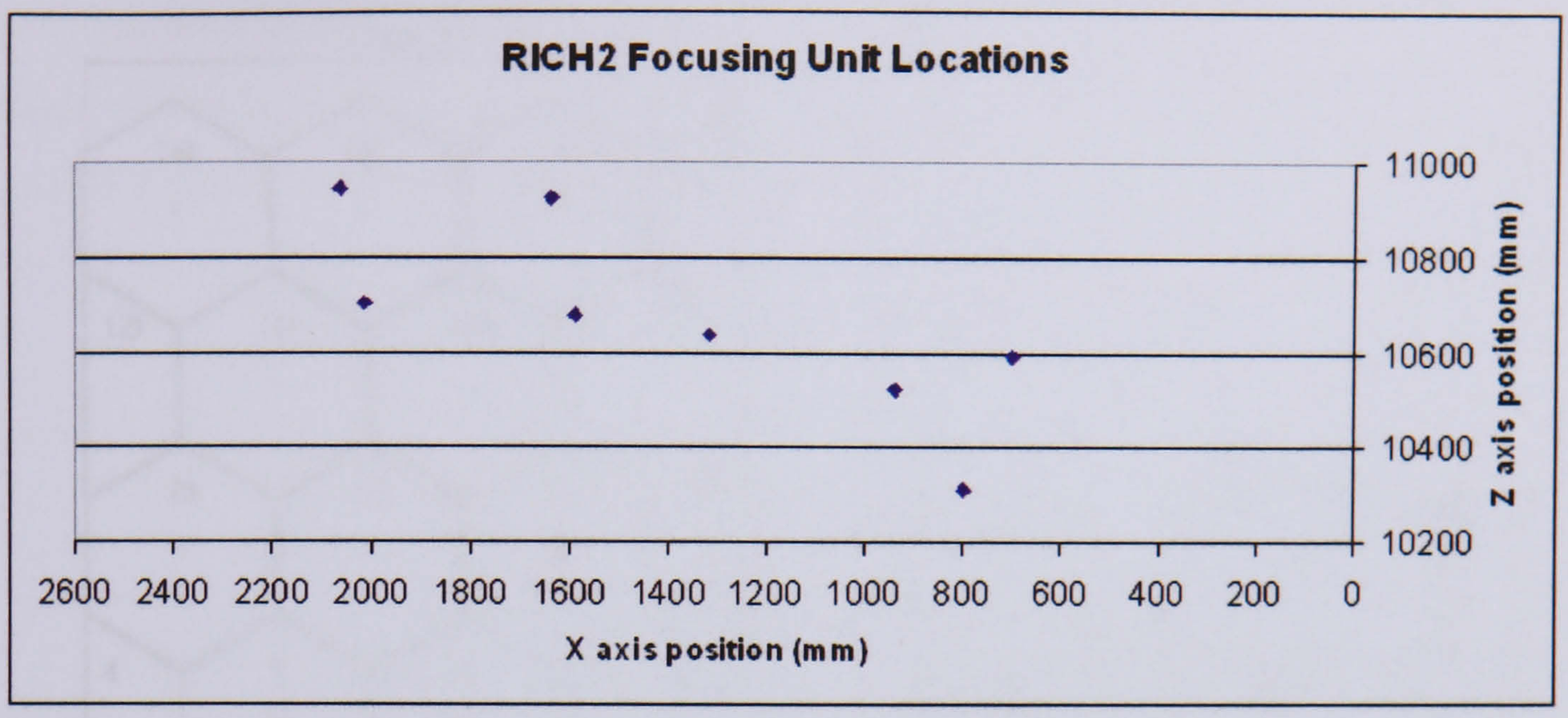

Figure 5.23: RICH2 focusing unit positions for positive x.

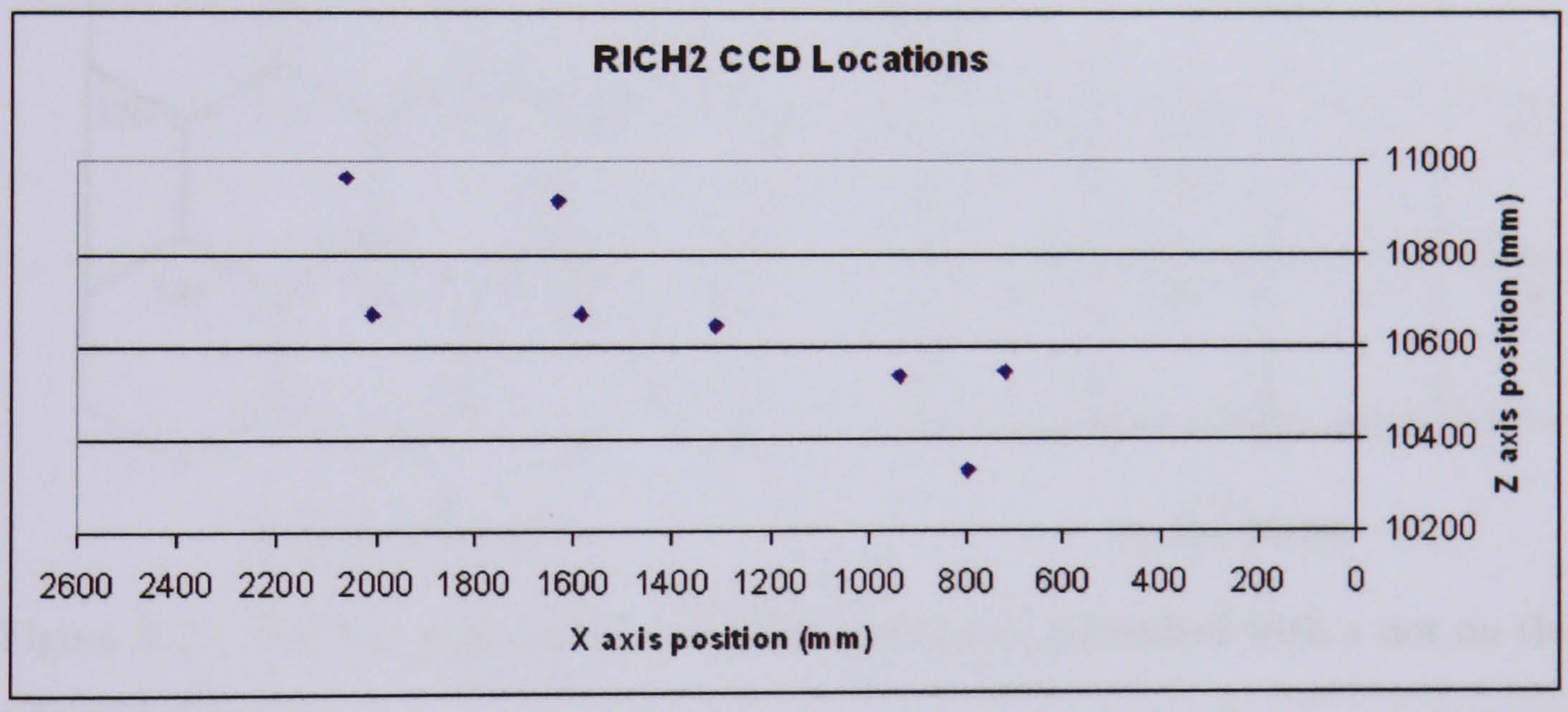

Figure 5.24: RICH 2 APS camera positions for positive x.

units and APS cameras monitoring the flat mirror segments, and the remaining four positions are the locations of the focusing units and APS cameras monitoring the spherical mirror segments. The mirror segments that will be monitored are shown in figure 5.25.

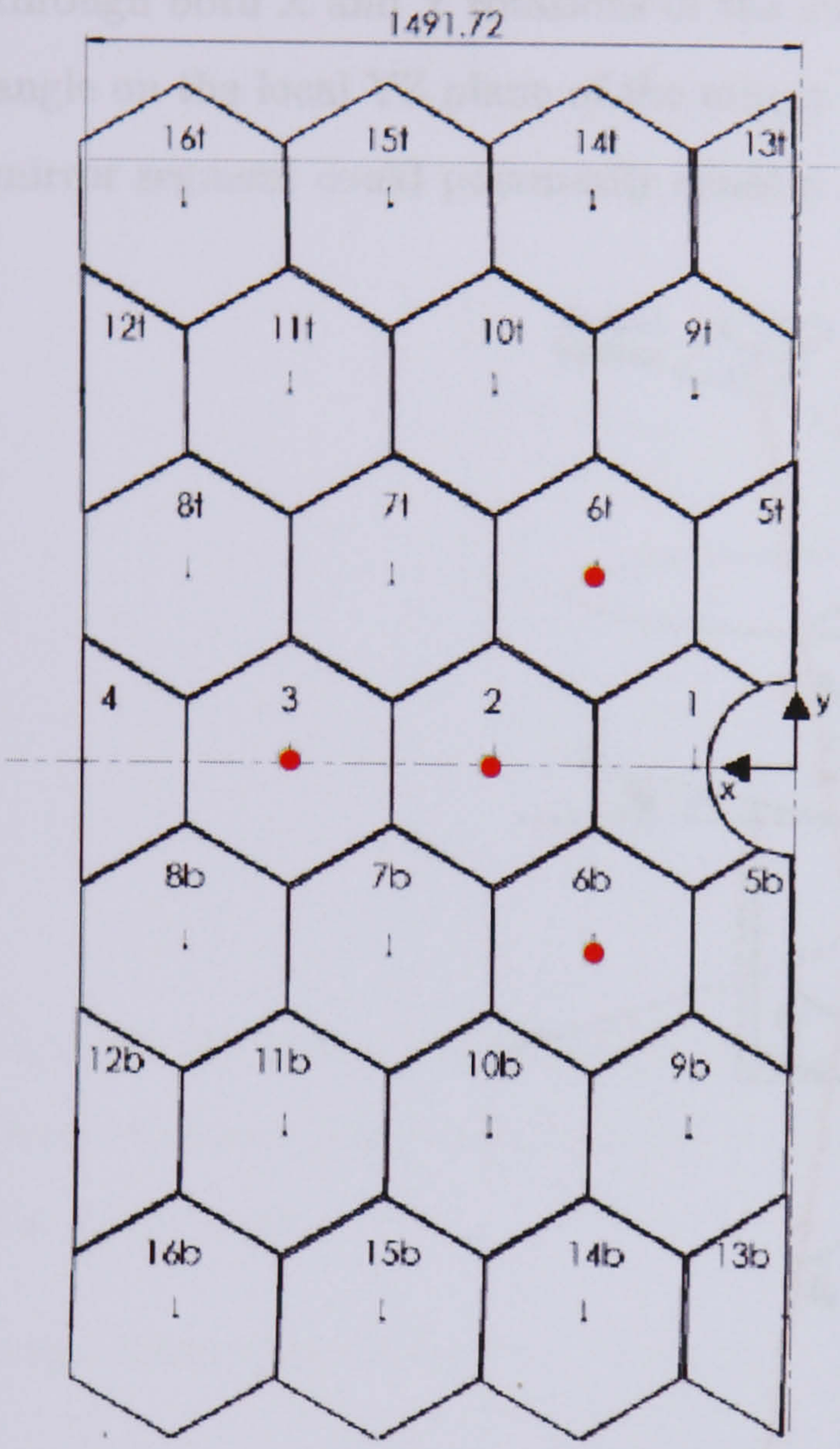

(a) Spherical Mirror

(b) Flat Mirror

Figure 5.25: The key segments that will be monitored (identified with a dot on the mirror segment).

5.5 Final Laser Alignment Performance

5.5.1 Misalignment Recovery Algorithm

The Misalignment Recovery Algorithm is a slight modification of a sample analysis algorithm written by Sajan Easo (RAL/CERN). Its function is to record the start point and end point of the photon beam. Through this, accurate studies can be made in the determination of the theoretical accuracy of the laser alignment monitoring system through use of the misalignment algorithm.

In the previous section, consideration was given to the path of the laser beam

through both X and Y rotations of the mirror segment. Because there is an incident angle on the local YZ plane of the mirror segment, a change in the Y rotation of the mirror segment could potentially cause a non-linear beam movement (figure 5.26).

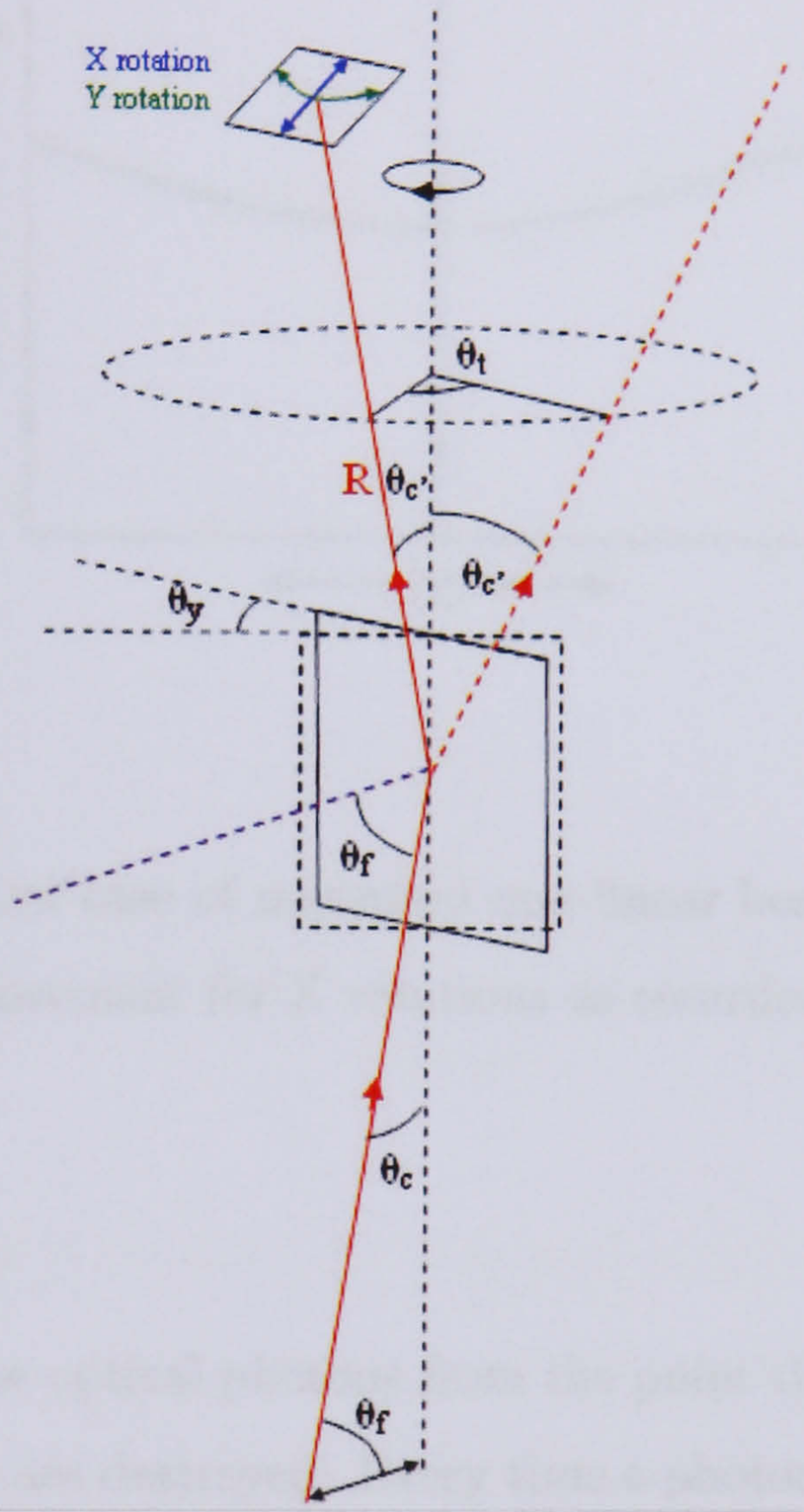

Figure 5.26: Non-linear beam movement for Y rotations vs. linear beam movement for X rotations.

This leads to a potential non-linear relationship on the active surface of the APS camera when measuring Y rotations (figure 5.27). It is therefore important to make sure that any significant measured non-linearity is correctly characterised.

Software Architecture

The analysis algorithm is written within the GaussRICH package [19] - an analysis tool for analysing specific aspects of events that pass through the RICH detectors.

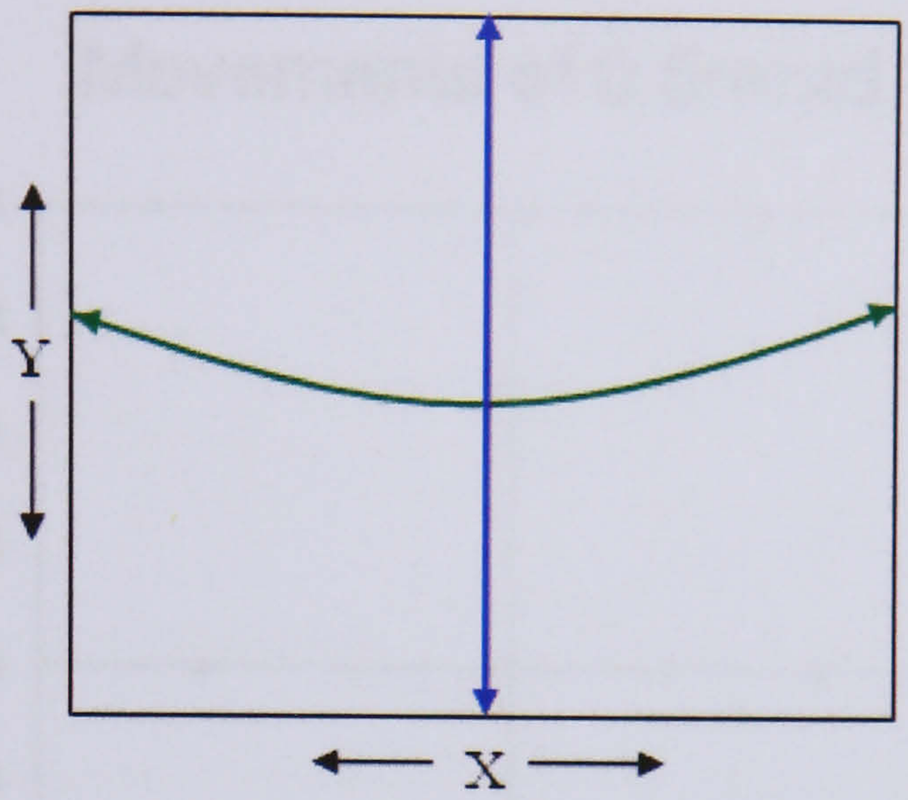

Figure 5.27: The potential case of measured non-linear beam movement for Y rotations vs. linear beam movement for X rotations as recorded on the active surface of the APS camera.

Algorithm Overview

This algorithm tracks the optical photons from the point they are created in RICH2 until the point that they are destroyed. Every time a photon interacts with an object and given a new trajectory, the algorithm records a pre-step point and a post-step point. The pre-step point is the point where the photon starts along a particular trajectory, and the post-step point is the point where the photon is prevented from continuing along that trajectory either through non-destructive interaction (at which point the photon is given a new pre-step point) or a destructive interaction (termination of the photon).

5.5.2 Results

The plotted results of the recovery algorithm, show that the non-linearity in Y rotation is negligible over the range of -0.5 *mrads* to 0.5 *mrads* (see figures 5.28, 5.29 and 5.30).

The results also show that an X rotation of 0.5 *mrads* equates to a *dy* displacement

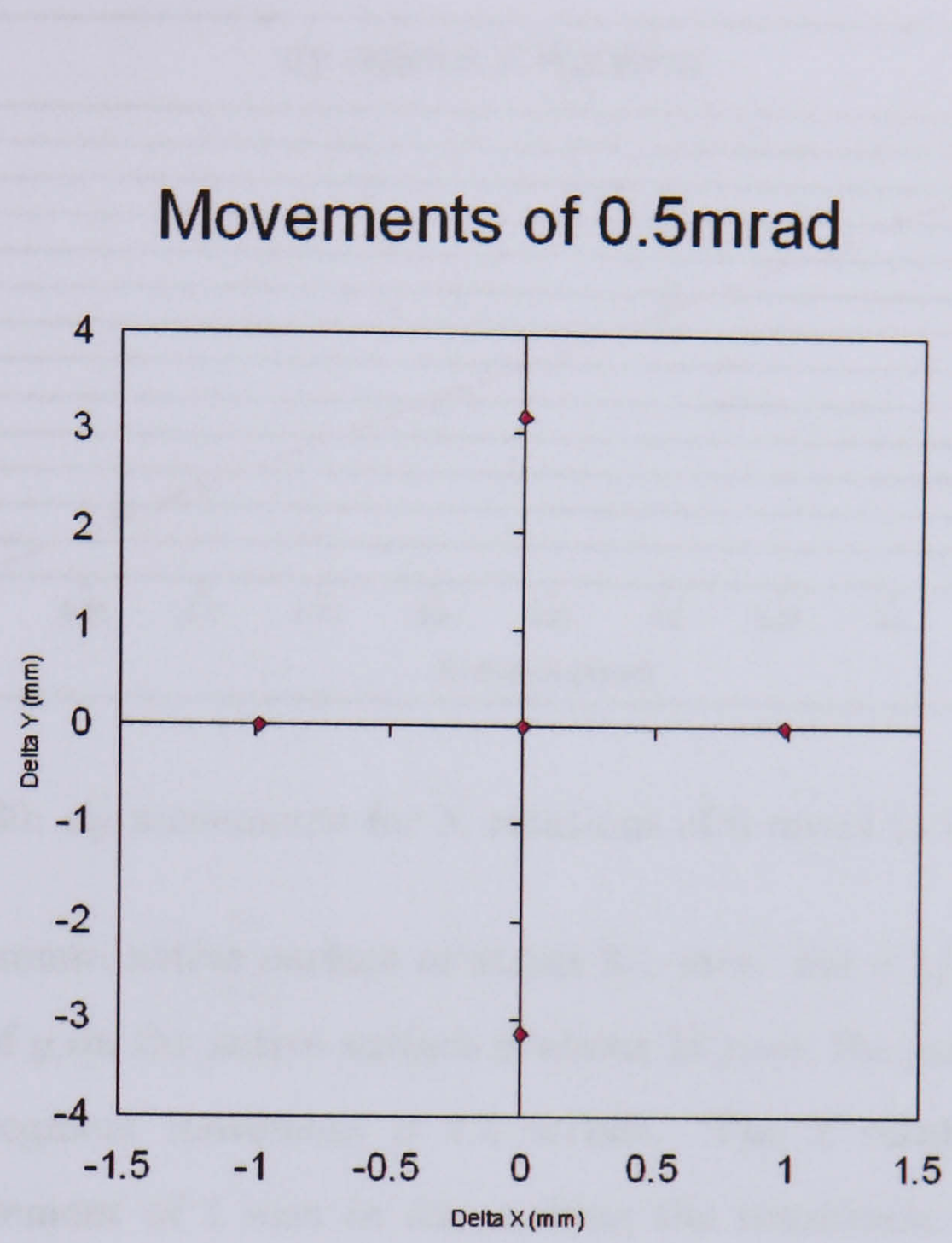

Figure 5.28: dx and dy movements for independent mirror segment rotations of 0.5 $mrad$ in X and Y.

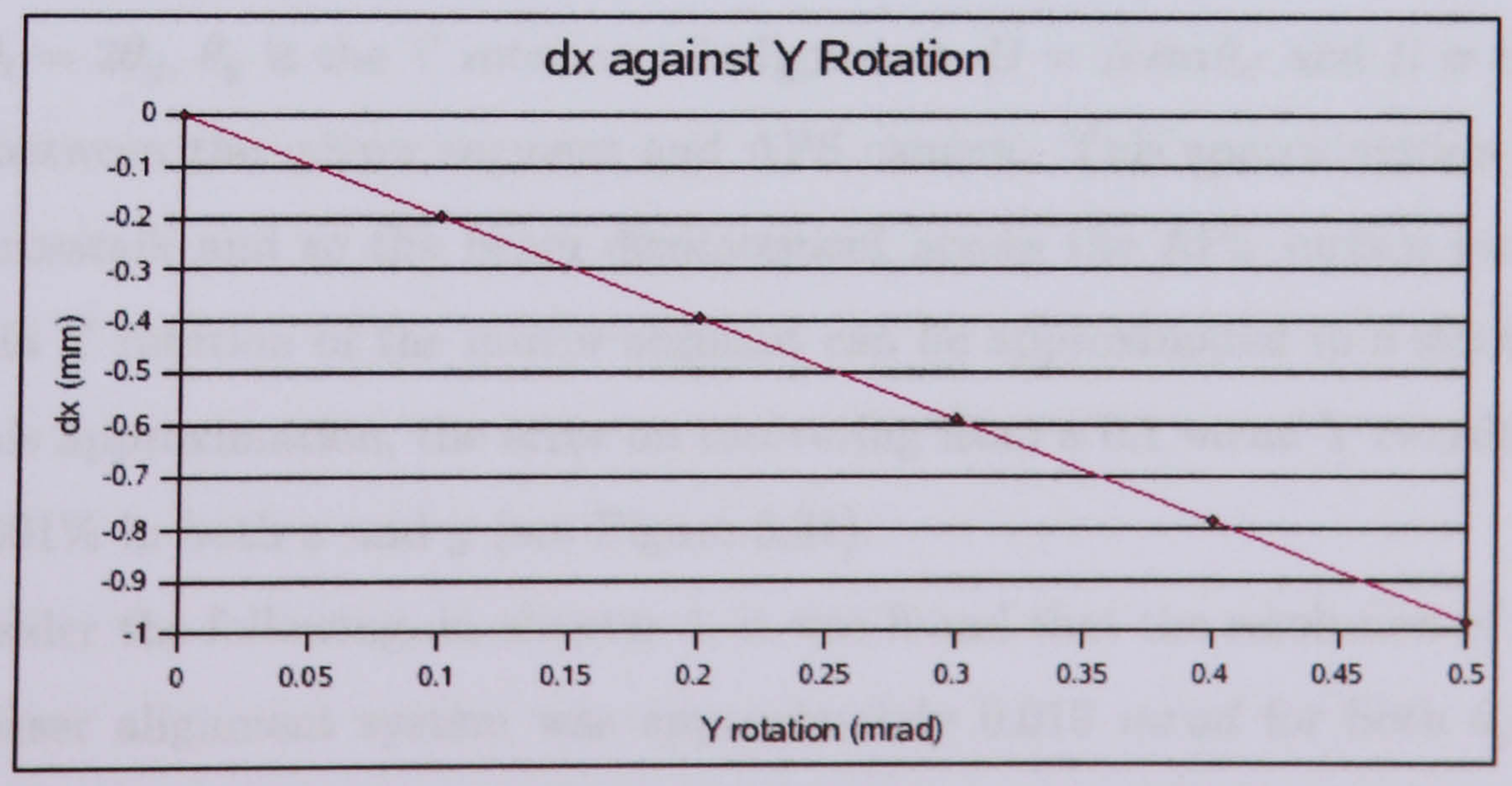

Figure 5.29: dx movements for Y rotations of 0 $mrad$ to 0.5 $mrad$.

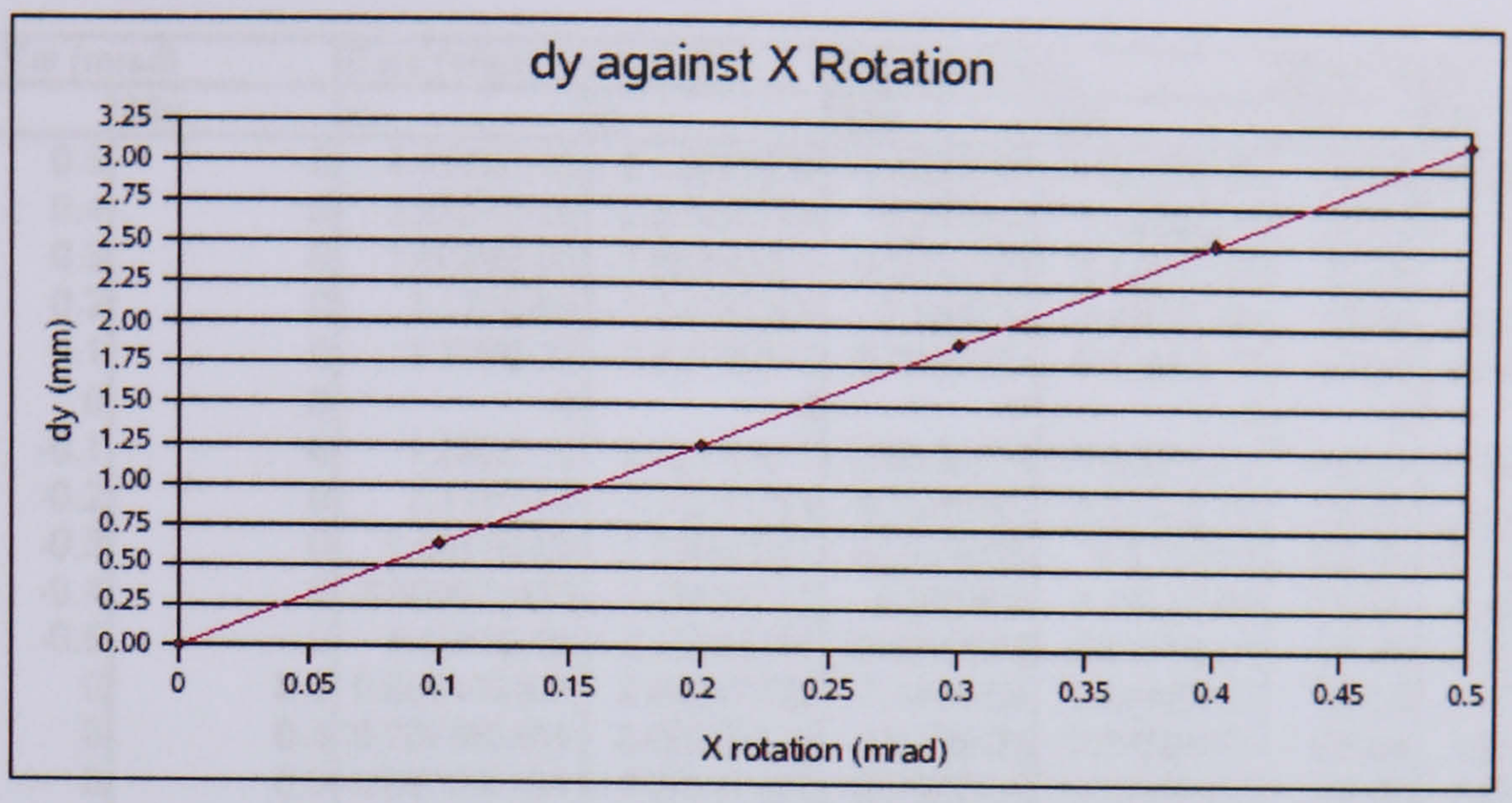

Figure 5.30: dy movements for X rotations of 0 $mrad$ to 0.5 $mrad$.

across the APS camera active surface of about 3.1 mm. For a $1/2''$ APS where the maximum range of y on the active surface is about 15 mm, the maximum detectable range of mirror segment movement is 2.5 $mrads$. The Y rotations of 0.5 mrads produce a displacement of 1 mm in dx, making the maximum range in dx to be 7.5 $mrad$.

As mentioned in chapter 4 dx movements for θ_y misalignments to a first approximation are given by:

$$dx = D \tan \theta_t \tag{5.4}$$

where $\theta_t = 2\theta_y$, θ_y is the Y rotation misalignment, $D = R \sin \theta_{c'}$ and R is the beam length between the mirror segment and APS camera. This approximation assumes no dy crosstalk and so the beam displacement across the APS surface for a given change in Y rotation of the mirror segment can be approximated to a straight line. With this approximation, the error on recovering from a 0.1 $mrad$ Y rotation is less than 0.001% in both x and y (see Figure 5.31).

Consider the following, in chapter 4, it was found that the resolution of the prototype laser alignment system was approximately 0.013 $mrad$ for both θ_y and θ_x rotations taking a pixel size of 6 μm and a fitting uncertainty of ± 6 pixels. Figure 5.31 shows that over a range of 0.5 $mrads$ the largest recovery error is of order $0.0001 mrad$. By adding these two errors in quadrature the total resolution remains

Mirror Rot (mrad)		Data (offset corrected)		Approximation		Error (mrad)	
Δθx	Δθy	x	y	Δθx	Δθy	Δθx	Δθy
0.5	0	4.4558E-05	-3.10583559	0.4999977	2.2631E-05	2E-06	-2.263E-05
0.4	0	2.8507E-05	-2.48466759	0.399998	1.4479E-05	2E-06	-1.448E-05
0.3	0	1.6029E-05	-1.86350059	0.2999985	8.1411E-06	2E-06	-8.141E-06
0.2	0	7.121E-06	-1.24233359	0.199999	3.6167E-06	1E-06	-3.617E-06
0.1	0	1.779E-06	-0.62116679	0.0999995	9.0355E-07	5E-07	-9.036E-07
0	0	0	0	0	0	0	0
-0.1	0	1.782E-06	0.62116671	-0.0999995	9.0507E-07	-5E-07	-9.051E-07
-0.2	0	7.119E-06	1.24233341	-0.1999989	3.6157E-06	-1E-06	-3.616E-06
-0.3	0	1.6011E-05	1.86350041	-0.2999985	8.132E-06	-2E-06	-8.132E-06
-0.4	0	0.000028452	2.48466741	-0.399998	1.4451E-05	-2E-06	-1.445E-05
-0.5	0	4.4441E-05	3.10583341	-0.4999973	2.2571E-05	-3E-06	-2.257E-05
0	0.5	0.984445104	0.00047482	-7.644E-05	0.49999751	8E-05	2.487E-06
0	0.4	0.787556104	0.00030514	-4.912E-05	0.39999802	5E-05	1.979E-06
0	0.3	0.590667104	0.00017281	-2.782E-05	0.29999853	3E-05	1.471E-06
0	0.2	0.393778104	7.785E-05	-1.253E-05	0.19999904	1E-05	9.63E-07
0	0.1	0.196889004	2.024E-05	-3.258E-06	0.09999949	3E-06	5.059E-07
0	0	0	0	0	0	0	0
0	-0.1	-0.196889	1.712E-05	-2.756E-06	-0.09999949	3E-06	-5.099E-07
0	-0.2	-0.3937781	7.16E-05	-1.153E-05	-0.19999903	1E-05	-9.67E-07
0	-0.3	-0.5906671	0.00016344	-2.631E-05	-0.29999853	3E-05	-1.475E-06
0	-0.4	-0.7875561	0.00029264	-4.711E-05	-0.39999802	5E-05	-1.983E-06
0	-0.5	-0.9844451	0.0004592	-7.393E-05	-0.49999751	7E-05	-2.491E-06

Figure 5.31: Table showing that approximation error is negligible, where $\Delta\theta_x$, $\Delta\theta_y$, x and y are measured in $mrad$.

to be 0.013 $mrad$ for both θ_y and θ_x rotations. Therefore, the recovery error is negligible.

5.6 Summary

The software development of the misalignment algorithm, covered in this chapter, has provided a method whereby mirror segments in the simulation can be individually and accurately misaligned. The development of the component location algorithm has led to the optimisation of the locations of the key geometry components of the laser mirror alignment monitoring system. The misalignment algorithm used in conjunction with the component location algorithm and the recovery algorithm, has been used to make a study of the characteristics of the laser mirror alignment system segment monitors. The result of this study has shown that non-linearity for segment movements over a detectable range are negligible, and that a APS chip of size $1/2''$ can detect movements of up to 2.5 $mrad$, so this is the minimum size APS that should be used for the system.

Chapter 6

RICH2 Final Alignment System Design

6.1 Alignment System Components

6.1.1 Fibres

The fibres of the laser alignment monitoring system must be radiation hard (for example, radiation hard fibres manufactured by NUFERN [4]). There are two options under consideration for delivering the light from the laser to each of the focusing units in RICH2.

The first option is to have a fibre bundle in the control room with the laser, and to attach it to sixteen 100 m jacketed radiation hard fibres that will then transport the light to gas-tight optical sockets on the side of RICH2. On the other side of the gas-tight sockets are further runs of radiation hard fibre that carry the light to the individual focusing units. This option has the advantage that a break in a length of optical fibre will not prevent light getting to the remaining focusing units. However, sixteen 100 m lengths of radiation hard fibre optic will complicate the system and will add to the cost and, therefore, other options must be considered.

The second option has three variations, but two of which are similar in that they both have a single 100 m length of protected radiation hard fibre to transport the light from the laser in the control room down to a fibre bundle at RICH2. The first

variation places the fibre bundle outside of the RICH detector, and uses sixteen gas tight sockets to transfer the light to the optic fibres inside RICH2 that are connected to the focusing units. The second variation places the fibre bundle inside the RICH detector, using only one gas tight socket to transfer the light from the 100 m long fibre to the fibre bundle. Though this variation lowers the likelihood of a gas leak in that there is only one gas tight socket, the fibre bundle must be covered in a non-reflective light-tight casing to prevent stray light from the fibres interfering with the HPD plane. The third variation is to use the laser to supply light to both sides of RICH2 via two 100 m lengths of fibre. Each fibre will connect to a bundle of 8 fibres that will then supply the light to the 8 focusing units on either side of the RICH detector. This latter variation of the two options is the solution that will be employed since it has a low gas leak risk, is easy to engineer and provides a separate optic fibre for each side of RICH2.

6.1.2 Optics

The optics to be used in the final system for each of the mirror segment alignment monitors, as mentioned in previous chapters, consists of a focusing unit, a beam splitter and a mirror.

It is imperative that these components are radiation hard. Materials that are not radiation hard such as optical quality BK7 glass turn cloudy when they are exposed to radiation. This lowering of transparency causes the light passing through them to scatter. Such a scenario in the RICH detectors could cause light to spray over the HPD planes and thus create a large amount of background stray light, lowering the efficiency of the ring detection algorithms. The mirrors and splitters are supplied by CVI [1] and have durable coatings, insensitive to laboratory solvents. The splitter is made out of fused silica, so should be radiation tolerant.

6.1.3 Camera Technology

The camera technology to be used in the final design must be able to withstand a fluorocarbon gas environment, therefore they may need to be encapsulated in a gas

tight transparent container. Furthermore, they must be able to withstand the radiation environment of the detector. Radiation hard CCD cameras are prohibitively expensive. CCD cameras that are not radiation hard experience speckling over time when exposed to such environments. The longer they are there, the speckling deteriorates until they are eventually unusable. The radiation levels outside the acceptance of the RICH2 detector should be relatively low. The radiation levels expected at Δy ± 3000 mm at the centre of RICH2 are 1 $kRad$ per year [68]. A radiation tolerant camera that can withstand such a radiation level for a period of time equivalent to the lifetime of the experiment (about 5 years) should be utilised. The camera of choice in the final design is the Lumenera LE-175 APS CMOS camera [2]. APS CMOS cameras are more radiation tolerant than standard CCD cameras and the LE-175 also has the advantage of ethernet, which means that data can be transmitted to the control room without using signal boosters. The camera is encapsulated in an aluminium casing and the sensor is protected by a glass cover.

6.2 Design of Component Mount Holders

The proposed component mounts for holding the optical components and securing them to the mount holders are off-the-shelf components. Therefore, it is necessary to design component mount holders to which the component mounts will attach to the top plates and base plates.

6.2.1 Floor Mount Holders

Figures 6.1 and 6.2 show the top view of the proposed design for the component mount holders.

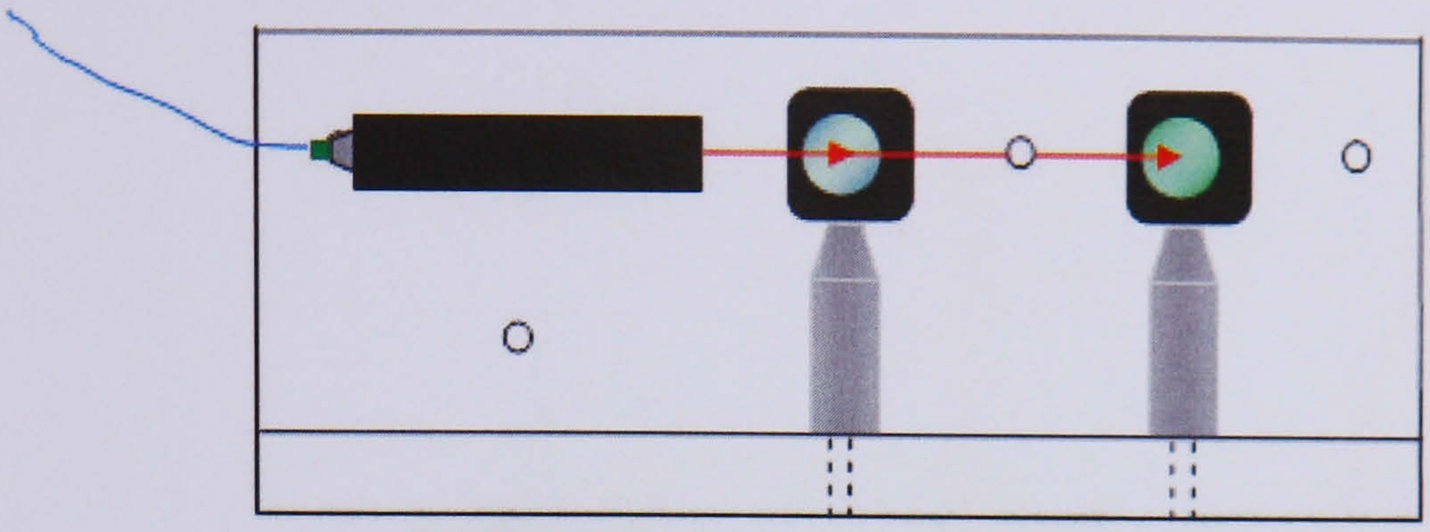

Figure 6.1: The plan view of the floor component mount holder for the focusing unit, beam splitter and mirror.

The design can be seen to be symmetric (figures 6.2 and 6.4) so that the mounts can be layed out in a symmetrical way between the left and right hand sides of RICH2.

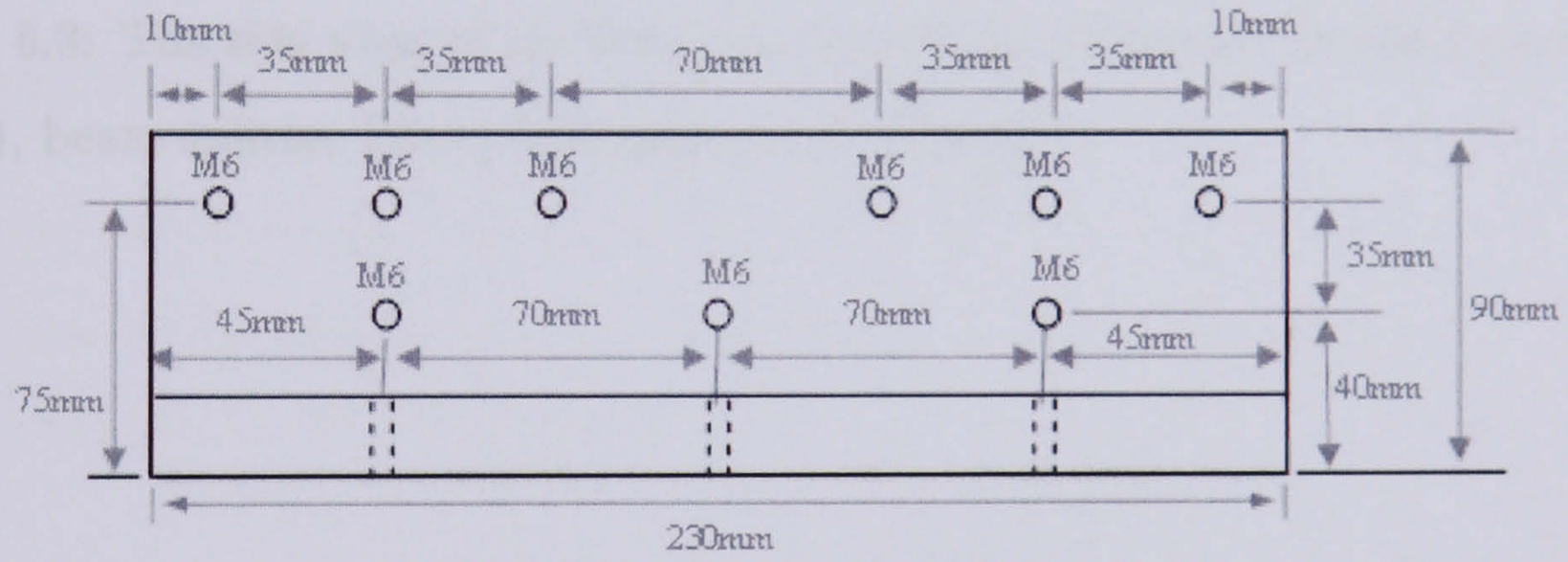

Figure 6.2: Plan view dimensions of the floor component mount holder for the focusing unit, beam splitter and mirror.

The previous chapters have referred to the focusing unit as one of the key geometry components, and much time has been spent in the consideration of its specific location. However, to be more precise, the important factor is the point that the signal beam is directed on a trajectory towards the mirror segment. Therefore the key geometry component in the final design is not the focusing unit but the laser mirror that directs the light to the mirror segment (figure 6.3).

The focusing unit, beam splitter and laser mirror can be seen to be completely aligned with each other, both on the vertical and horizontal global coordinate planes (figure 6.5).

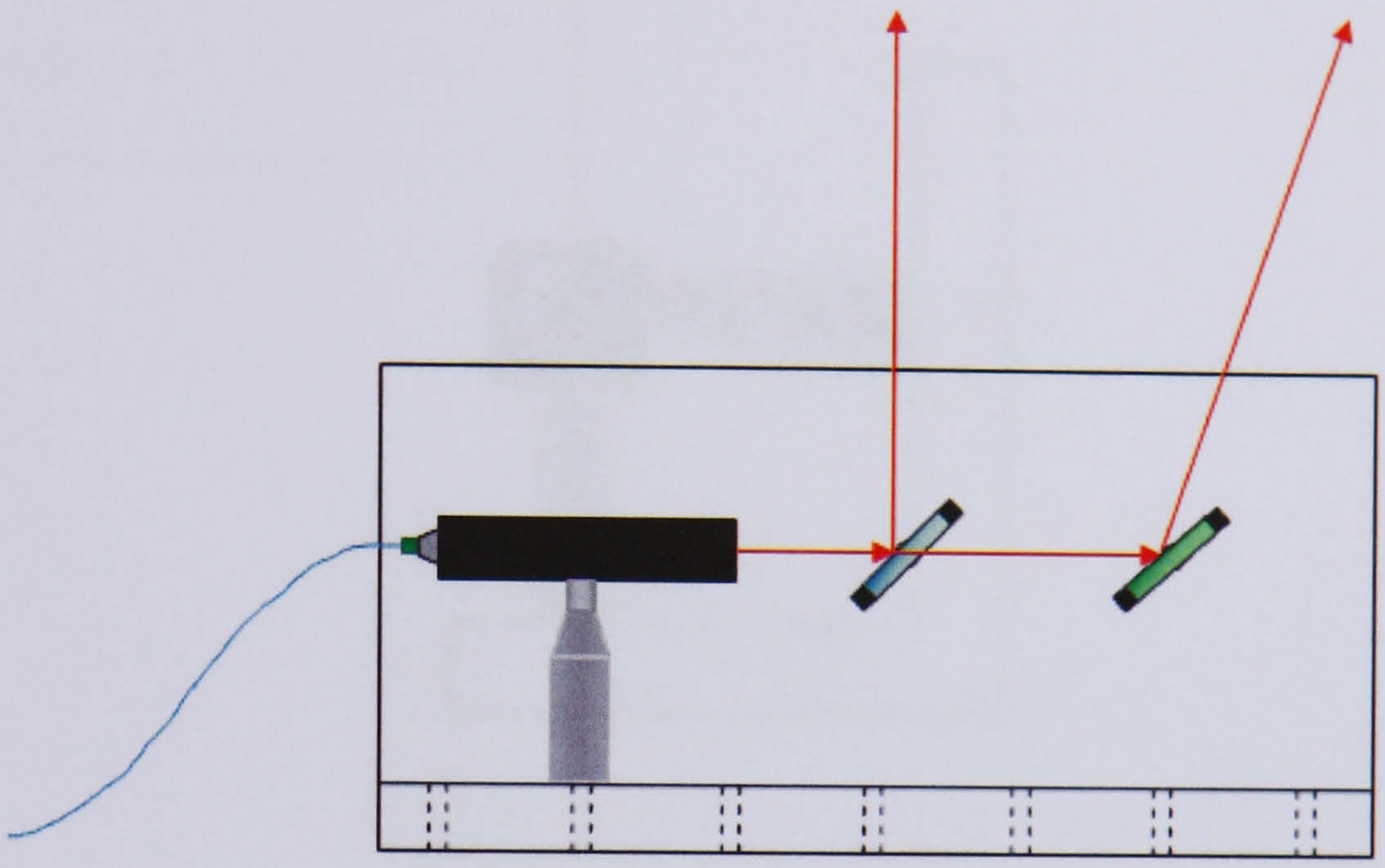

Figure 6.3: The side view of the floor component mount holder for the focusing unit (black), beam splitter (blue) and laser mirror (green).

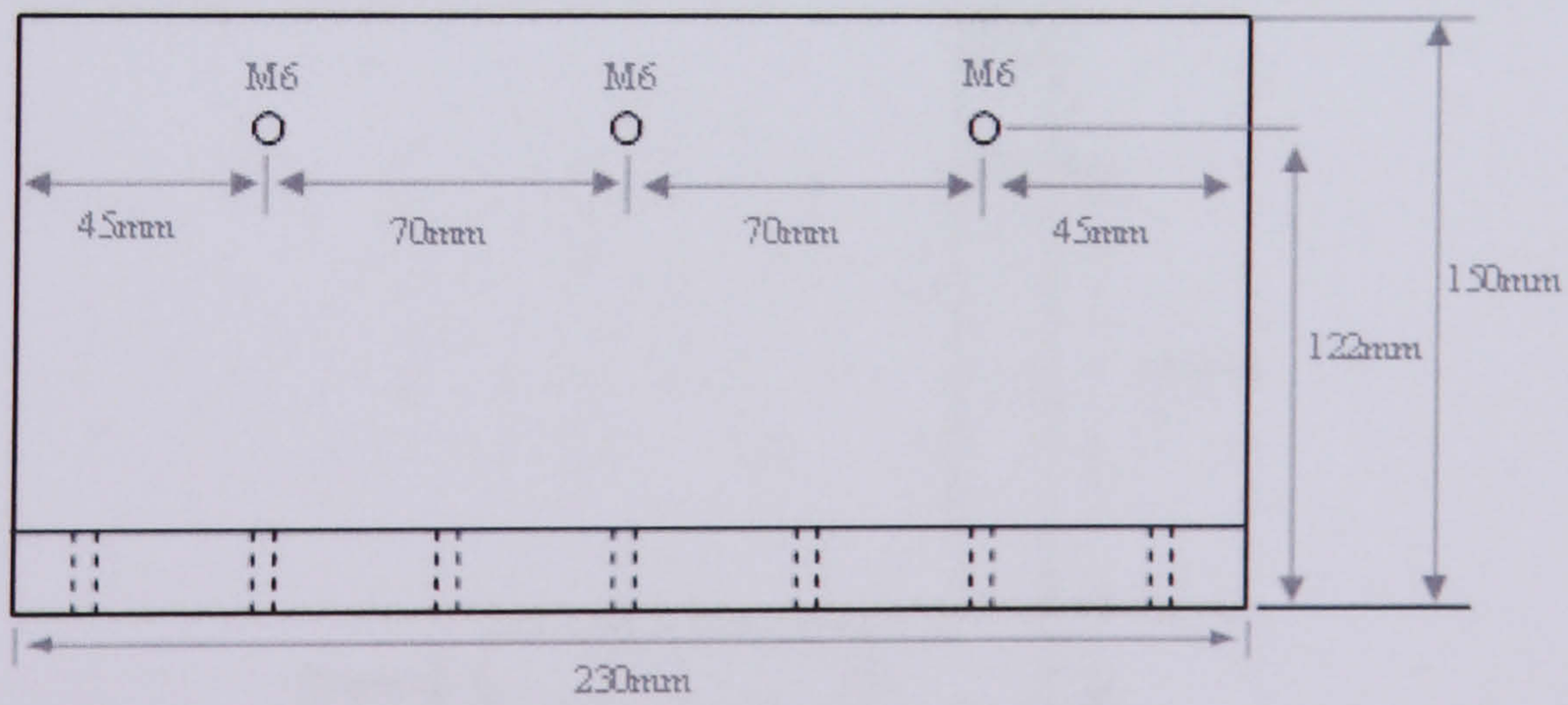

Figure 6.4: Side view dimensions of the floor component mount holder for the focusing unit, beam splitter and mirror.

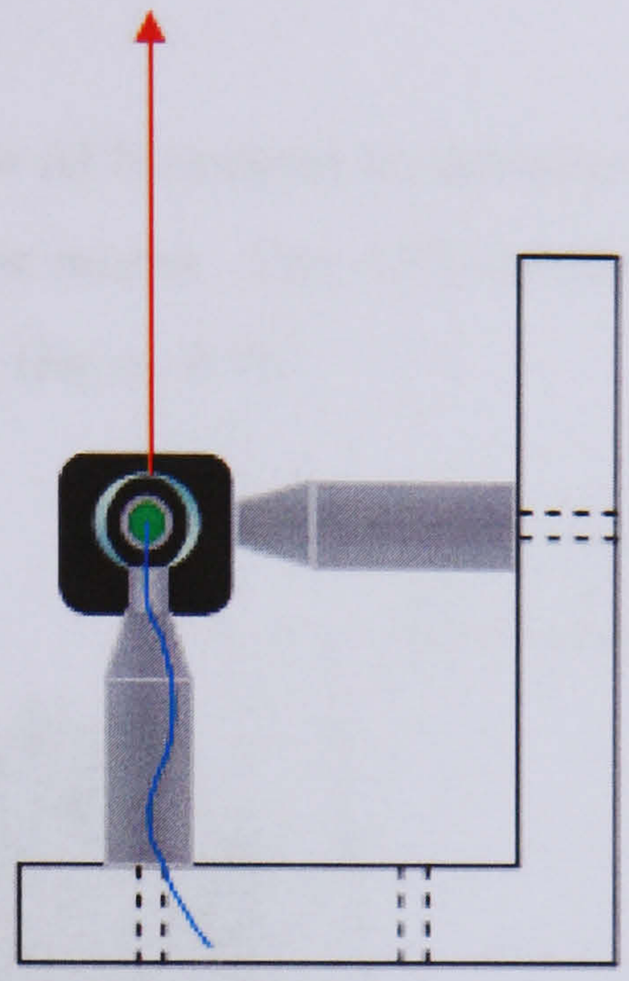

Figure 6.5: The end view of the floor component mount holder for the focusing unit, beam splitter and mirror.

Figure 6.6 shows the end view dimensions of the floor mount holder. The holder is attached by M6 screws down to the base plate that holds all of the mount holders for that side of the RICH2 detector.

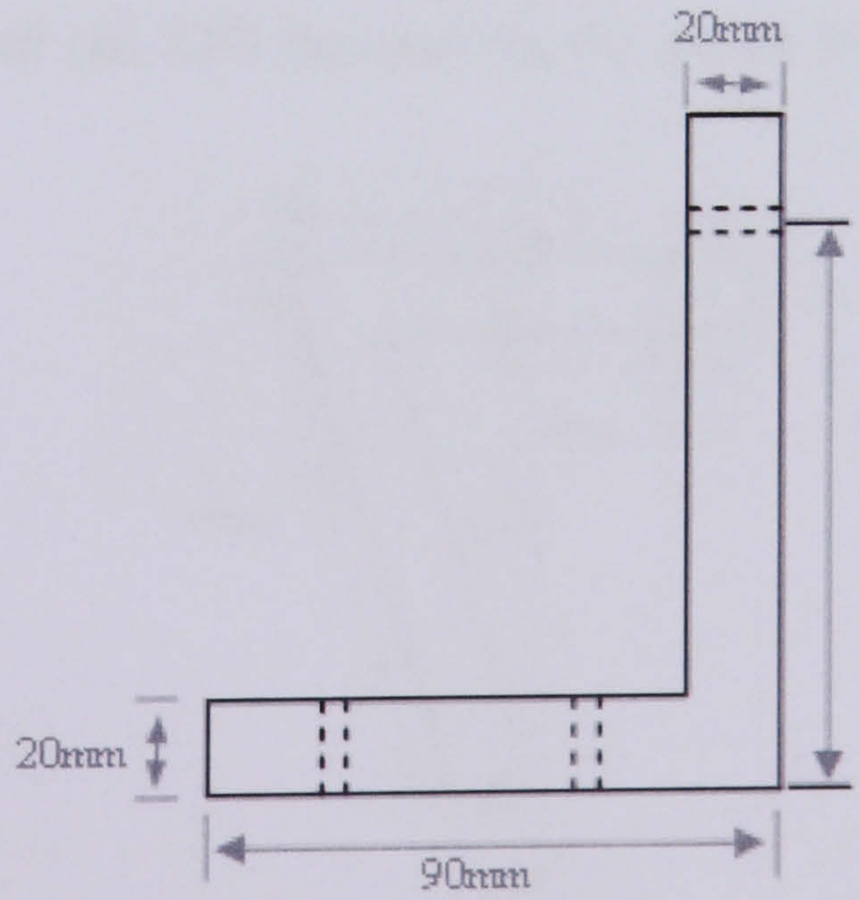

Figure 6.6: End view dimensions of the floor component mount holder for the focusing unit, beam splitter and mirror.

6.2.2 Roof Mounts

The roof mounts that hold the APS cameras do not require mount holders, since only one component is involved per mount. The APS camera is held at an angle roughly parallel to the incident beam (figure 6.7).

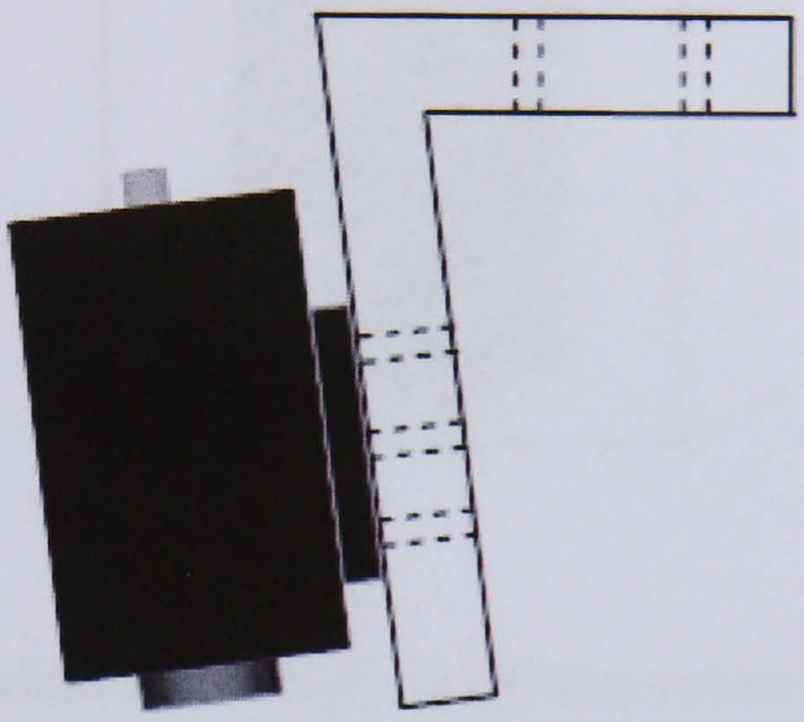

Figure 6.7: The side view of the roof component mount for the APS camera.

The dimensions (with the correct angle) of the mount are given in figure 6.8. The signal beams incident on the APS cameras are on average at an angle of 72^o. Therefore the angle of the APS cameras on the mount is fixed at 72^o.

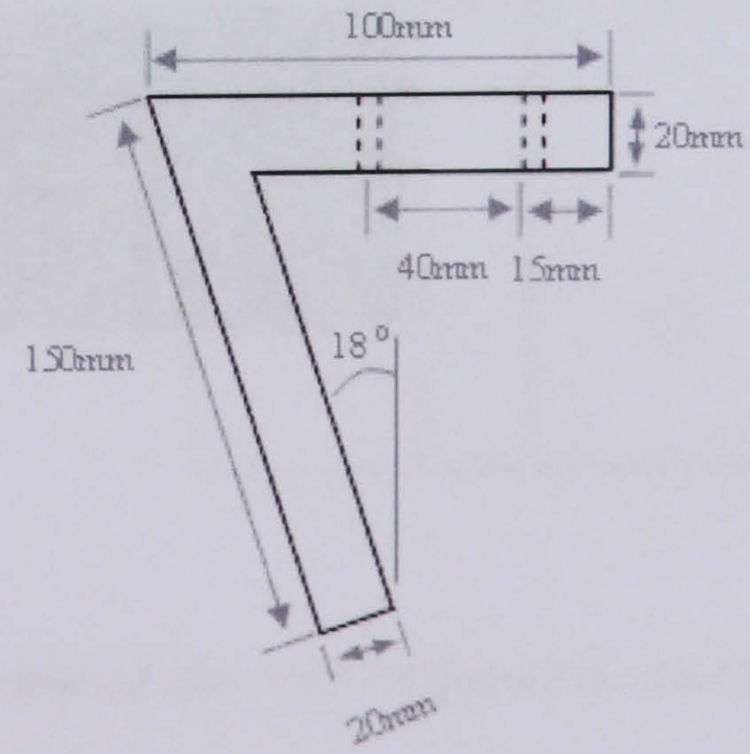

Figure 6.8: Side view dimensions of the roof component mount for the APS camera.

The positioning of the camera is central on the mount, and enough room is given

for the connection of the cables (figure 6.9).

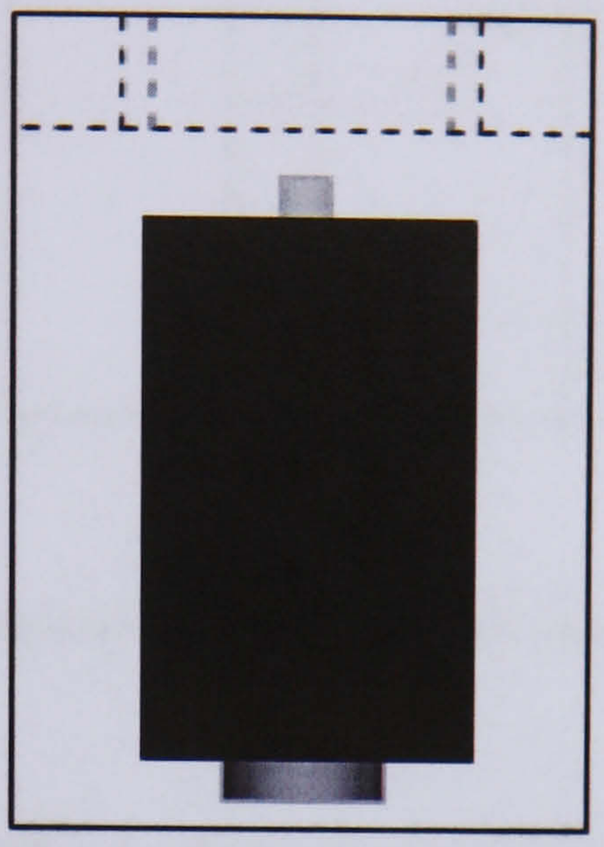

Figure 6.9: The end view of the roof component mount for the APS camera.

The APS camera roof mount is attached to the top plate by four M6 screws (figures 6.10 and 6.11). There are no means of adjustment on these mounts and therefore little room for movement over time. All the adjustment of a mirror segment alignment monitor is done using the floor mounts for that segment monitor.

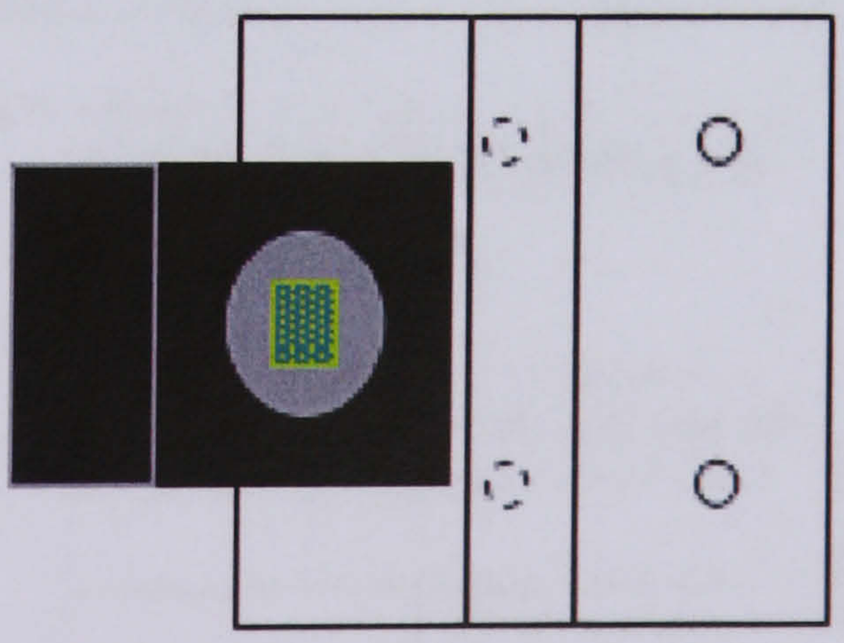

Figure 6.10: The plan view of the roof component mount for the APS camera.

The dimensions of the APS roof mount are given in figure 6.11. Both the roof mount and the floor mount holder were constructed out of aluminium and coated in a matt black paint.

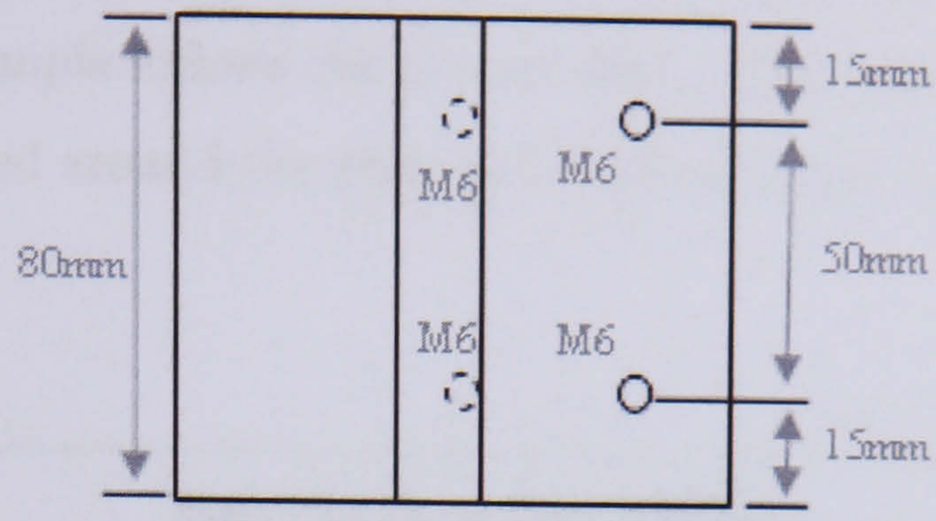

Figure 6.11: Plan view dimensions of the roof component mount for the APS camera.

6.3 Placement of Floor Mount Holders and Roof mounts

6.3.1 Floor Mount Holders

As has been previously explained, the key component on the floor mount holder is the laser mirror. This means that the laser mirror position is the pivot point for any rotation that the mount holder will be subject to. The mirrors that have been selected for monitoring are spherical mirrors $2, 3, 6b, 6t$ and flat mirrors $5b, 5t, 6b$ and $6t$ (see Figure 5.25). Figure 6.12 shows a diagram of the screw holes for the floor mount holder. The point of rotation where the laser mirror is, has been set at $(0, 0)$.

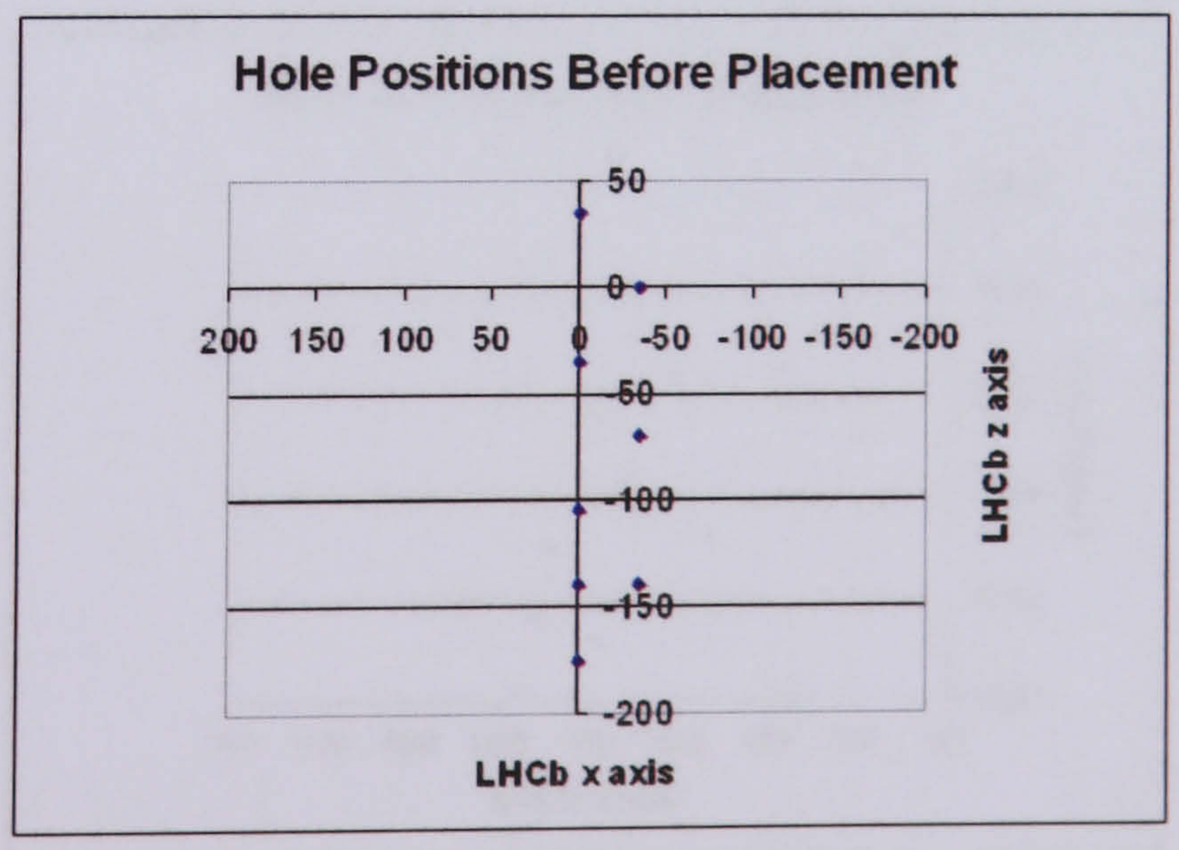

Figure 6.12: Hole positions in relation to the rotation point, before the rotation.

The next stage of the placement of the floor mount holder is to rotate it so that it is

directed towards the mirror segment it will monitor, after the required translation has been made. This example follows the process for placing spherical mirror segment 2. The rotation is centred around the pivot point which is the laser mirror (figure 6.13).

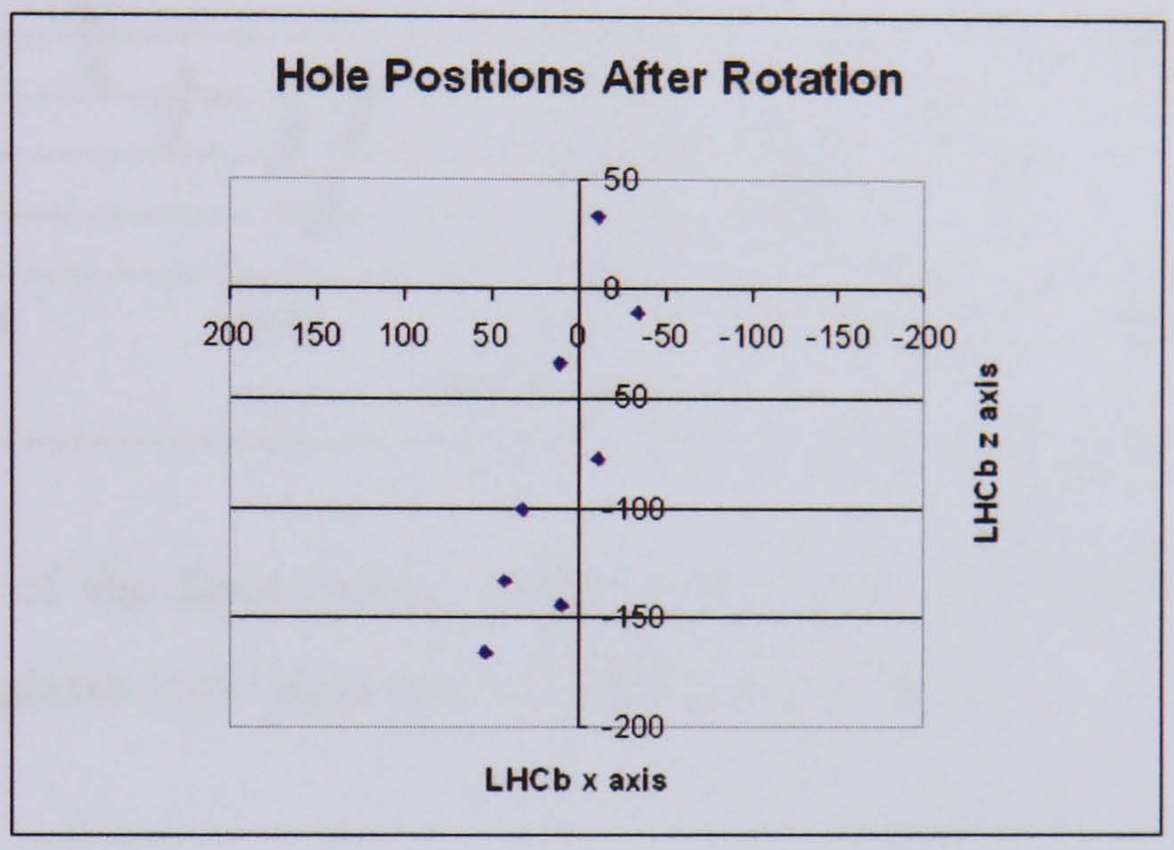

Figure 6.13: Hole positions in relation to the rotation point, after the rotation.

The final stage of the placement of the floor mount holder is to make a translation so that the pivot point is at the precise point that the Component Location Algorithm has given for that focusing unit (figure 6.14). Using this placement method for all

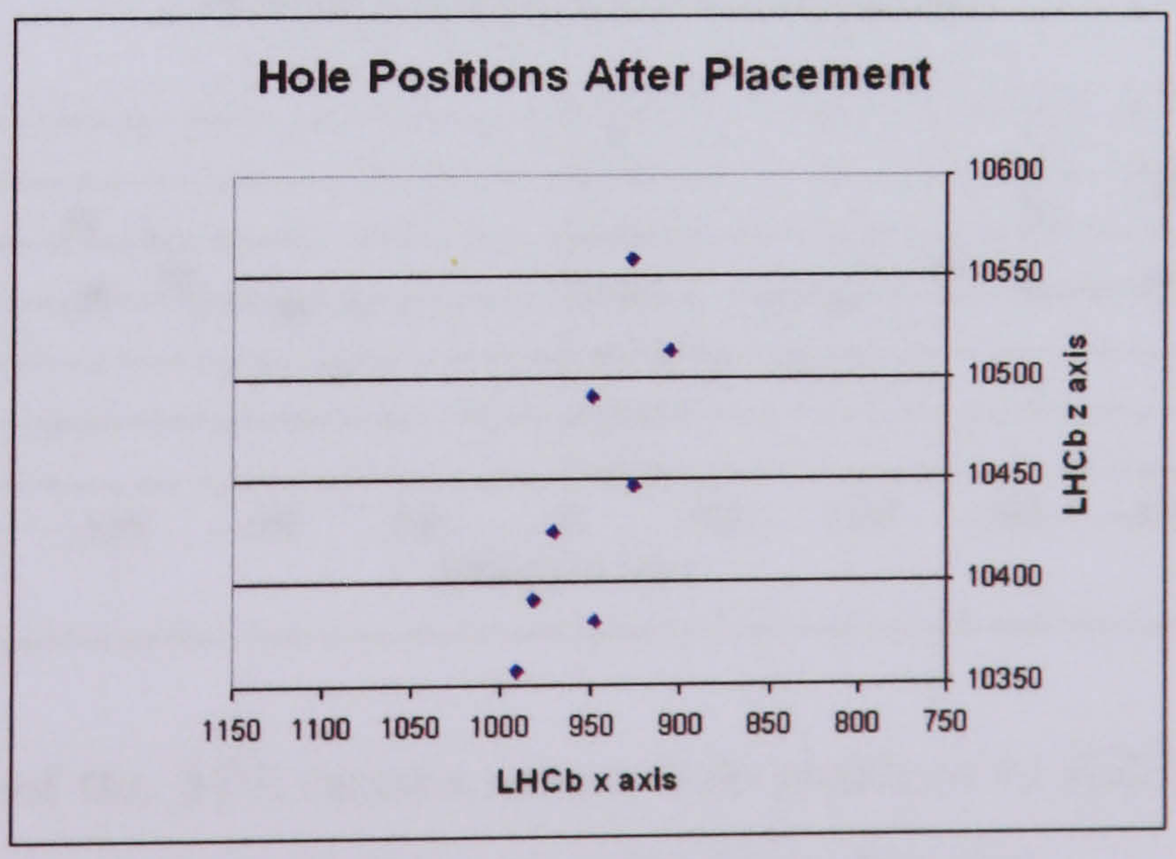

Figure 6.14: Hole positions after placement in the global coordinate system.

of the floor mount holders, in conjunction with the output values of the Component

Location algorithm, the product of all the hole positions for the floor plates can be shown (figure 6.15).

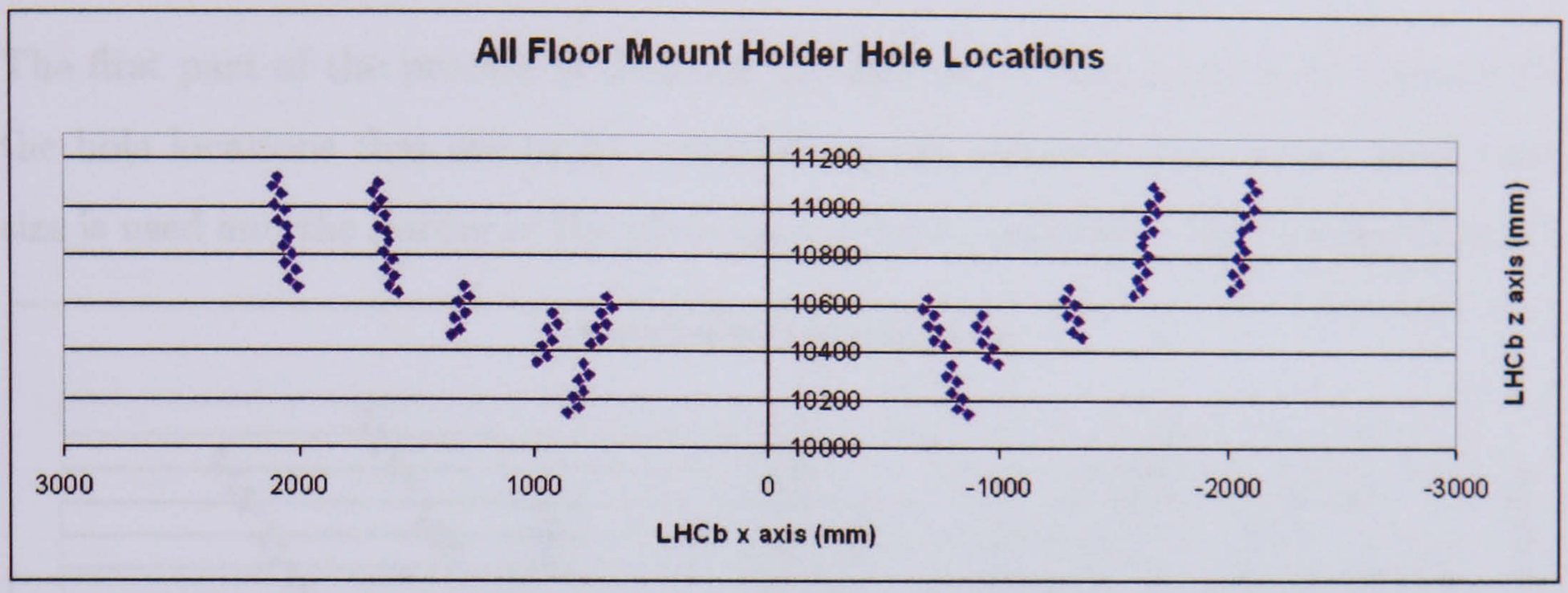

Figure 6.15: All of the floor mount holder hole positions in RICH2 that are to be located on floor plates (one plate per side of the detector).

6.3.2 Roof Mounts

The placement of the APS camera mounts follow the same process, but the pivot point is the XZ location of the active area of the APS. The placement results are give in figure 6.16.

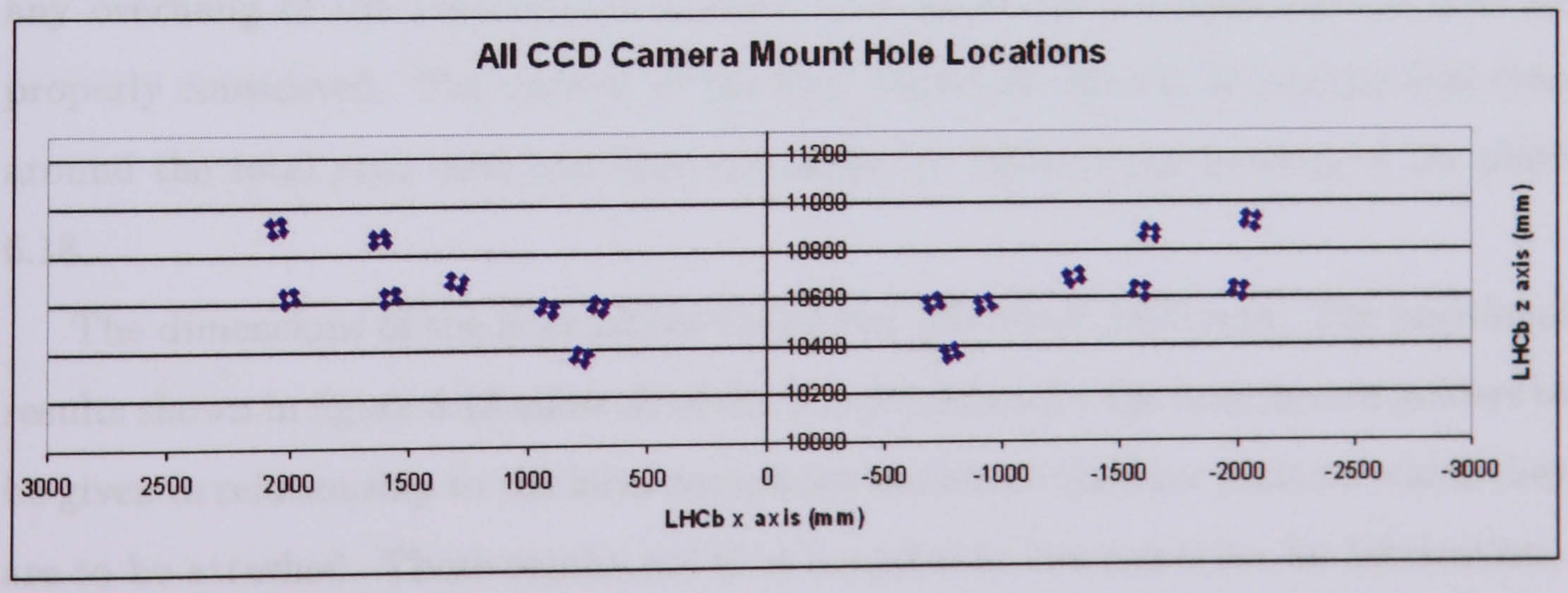

Figure 6.16: All of the APS camera mount hole positions in RICH2 that are to be located on the roof plates (one plate per side of the detector).

6.3.3 The Floor Plate and Roof Plate Sizes

Floor Plate

The first part of the process of deciding the size of the floor plate is to rotate all of the hole locations that are to be contained on the plate, so that only a small plate size is used and the border of the plate can be drawn parallel to the axis (figure 6.17).

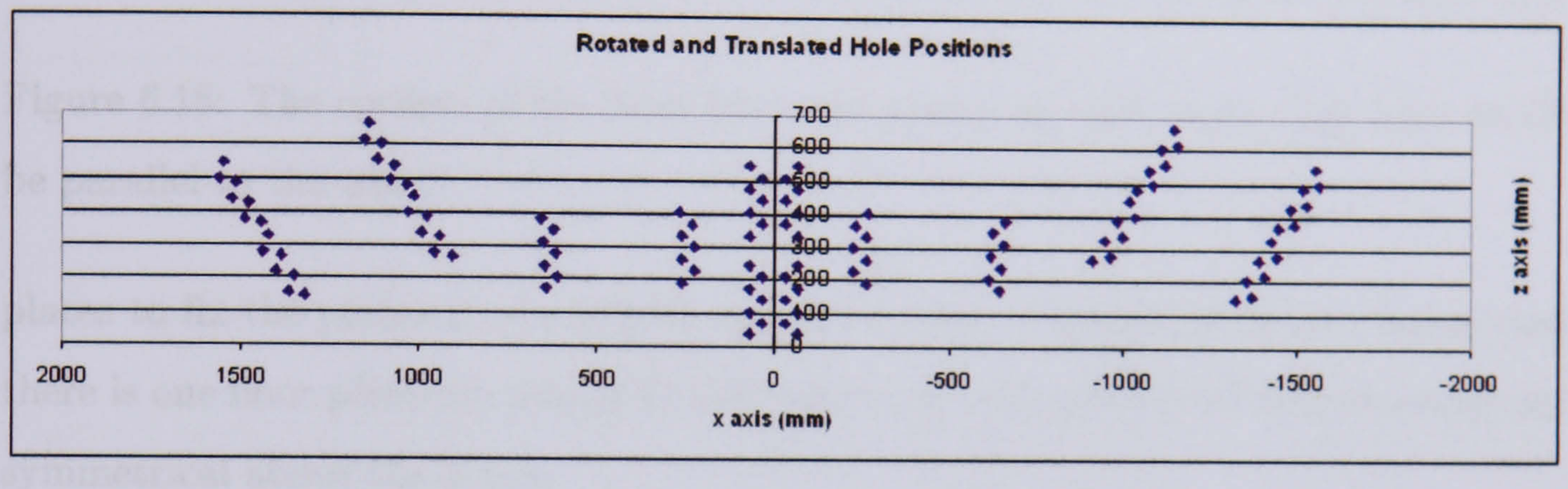

Figure 6.17: All of the holes are rotated round so that the holes for the monitoring component mounts of mirror segments $6b$ and $6t$ are parallel to the z axis.

The point of rotation is the bottom right M6 screw hole. The angle by which the holes have been rotated is equal to the Y rotation of spherical mirrors $6b$ and $6t$. A small translation is then made to move the holes away from the axis, this will prevent any overhang of the floor mount holders. The floor plate dimensions can now be properly considered. The corners of the floor plates are shown by placing four dots around the total area used and lines are drawn to indicate the borders of the plate 6.18.

The dimensions of the floor plates shown are 700 $mm\times$ 1650 mm. The positional results shown in figure 6.18 allow all of the hole locations for the floor mount holders to be given in relationship to the local coordinate system of the floor plate on which they are to be attached. These results are then supplied to the engineers for fabrication.

The final stage of the placement process is to rotate all of the holes and floor plates back by the angle equivalent to the angle of the spherical mirrors $6b$ and $6t$, and then make a translation to position the holes and corners to their correct location in RICH2 (figure 6.19). The global locations given will enable the engineers to correctly place the plate and all the components it holds within RICH2 and also to locate suitable

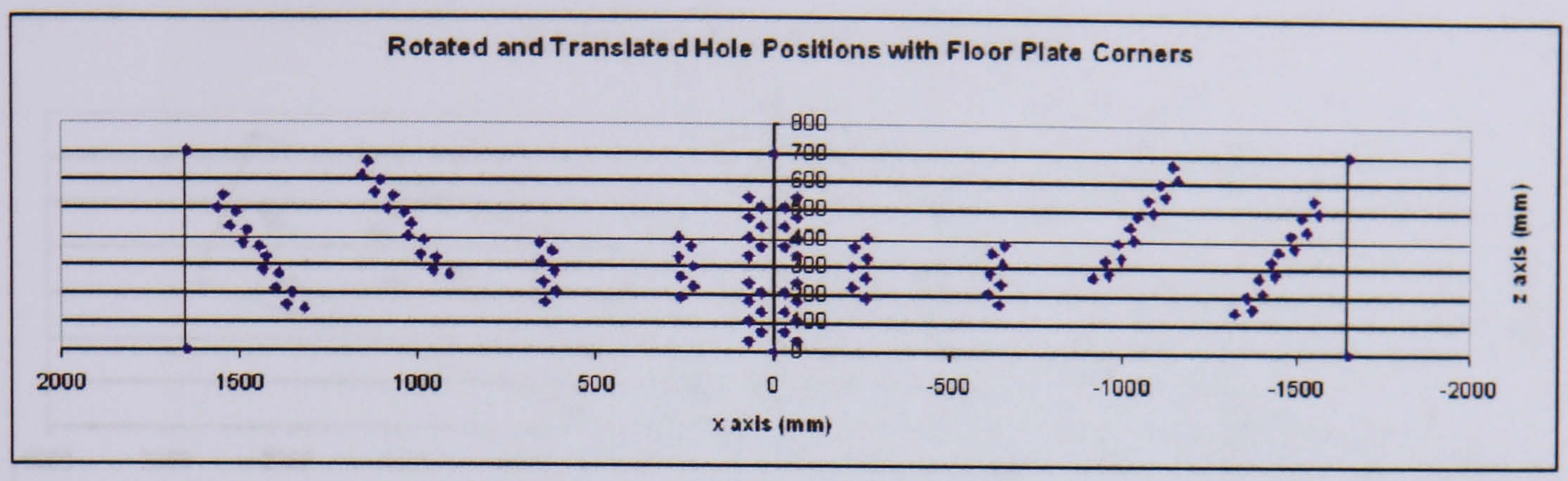

Figure 6.18: The corners of the floor plate are placed so that connecting lines would be parallel to the axis.

places to fix the plates to the RICH2 superstructure. Figure 6.19 clearly shows that there is one floor plate per side of RICH2 and that both plates and hole locations are symmetrical about the z axis.

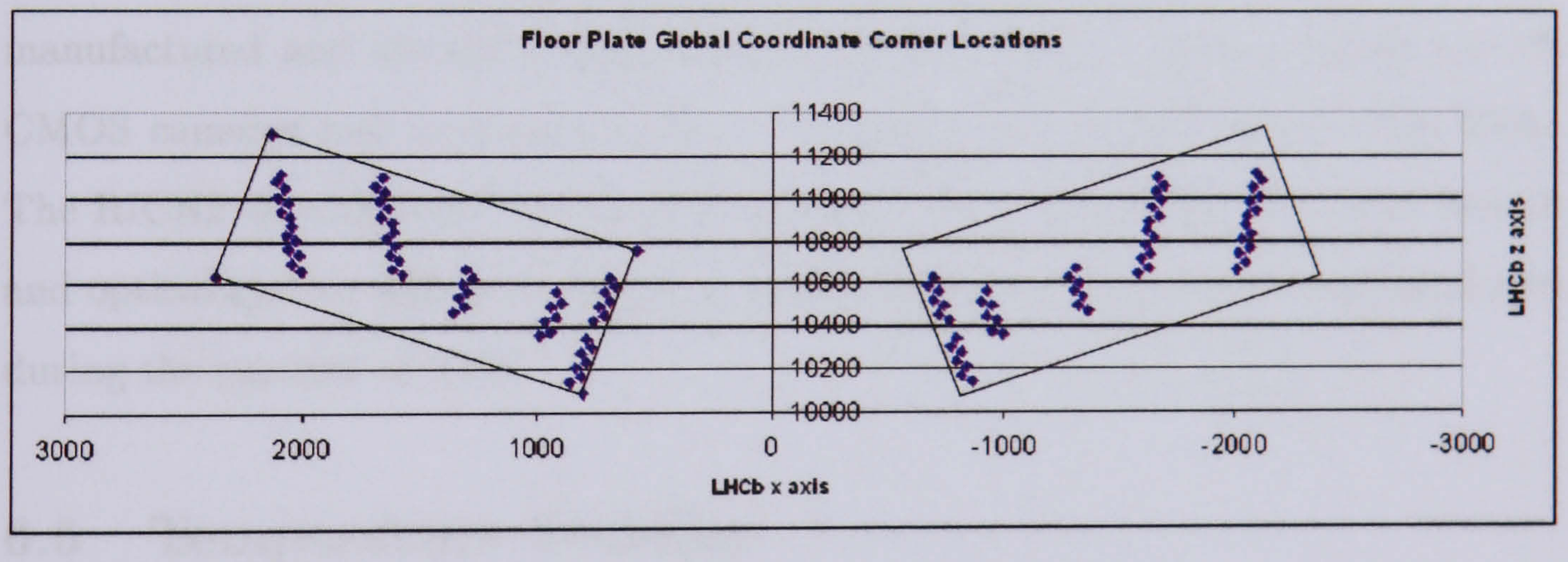

Figure 6.19: The final placement of the floor plate into position.

Roof Plate

The placement of the roof plate follows the same methodology as the placement of the floor plate. Figure 6.20 shows the results for the placement of the roof plate. Both the floor plates and roof plates are the same size to make placement and fabrication easier to engineer.

The final engineering drawings produced by M. Woodward have been included in Appendix A.

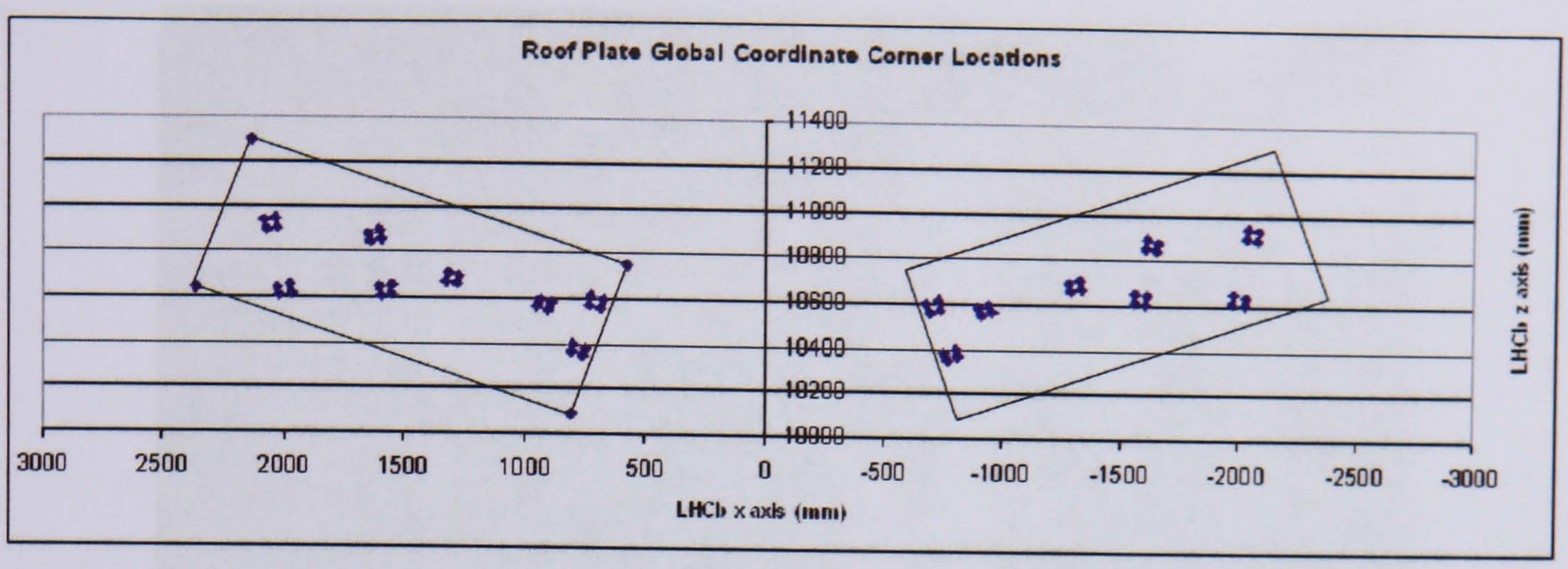

Figure 6.20: The final placement of the roof plate into position.

6.4 Installation Status

Figure 6.21 shows a picture of RICH2 when it was in its construction phase in September 2004. The floor and roof plates of the laser alignment system have now been manufactured and installed into RICH2 (February 2005). The Lumenera LE-175 CMOS cameras and roof mounts have also been installed and cabled (July 2005). The RICH2 detector was lowered into the pit in November 2005. The floor mounts and optical system will be installed in the RICH2 detector in the experimental area during the summer of 2006.

6.5 Temperature Stability

The long term stability of the segment monitors is critical to the proper functionality of the laser alignment monitoring system. For this reason, the mounting plates and component mount holders have been constructed out of Aluminium - the same material that the RICH2 super structure is constructed from. Aluminium has an expansion rate of 23 ppm per degree Kelvin. With respect to the floor component mount holders, the distance that is important to maintain is the separation of 70 mm between the beam splitter and mirror. A change in the separation between these two components has a direct impact on the separation of the signal and reference beams as they intersect the camera and introduce error into the measurement. Because the component mount holders and floor plates are made out of aluminium, they will

Figure 6.21: RICH2 in construction (September 2004).

expand at the same rate as the RICH2 super structure. The change in separation between the beam splitter and mirror is expected to be 1.61 $\mu m K^{-1}$. This means that a change in temperature of 3.7 K is needed to make a change in the measurement of one complete pixel for a flat segment measurement (where the flat segment is at $y = 0\ mm$). Such a change is insignificant since variations of 15 pixels or more are required to have a significant impact upon the alignment system measurements.

6.6 Summary

The placement of the roof mounts and floor mount holders in the final alignment system design has followed precisely the calculated locations of the component location algorithm. The floor mount holders and roof mounts are custom designed to meet the specific geometry requirements of the laser mirror alignment monitoring system. There are floor plates and roof plates on which to mount respectively the floor mount holders and APS camera roof mounts. These plates undertake a dual purpose; to reduce the number of screw holes to be made in the super structure of RICH2 and to provide stable platforms on which to mount the laser mirror alignment monitoring system components.

Chapter 7

Full Alignment Simulation

As discussed in section 4.1 of chapter 4, individual mirror segment tilts can be extracted using data from high energy tracks and their resultant Cherenkov rings. The total misalignment of the combined mirror tilts and the change in Cherenkov angle is related by the equation

$$\Delta\theta = acos(\phi_{ch}) + bsin(\phi_{ch}), \tag{7.1}$$

where a and b are projections of the Cherenkov mirror tilts in x and y respectively and $\Delta\theta$ is the change in Cherenkov angle at azimuthal angle ϕ_{ch}. This chapter will discuss the new results of the software compensation for misaligned mirror segments using seeds from 16 laser mirror alignment segment monitors.

7.1 Extraction of Mirror Tilts from Data

Because RICH2 is a two mirror system, the method for extracting the individual mirror tilts is a two stage process [61]. The first part of the process is to fill histograms for every spherical/flat mirror combination that a Cherenkov photon could use between the emission point and the photo-detector plane to extract parameters a and b. The second part of the process is to extract the individual mirror tilts by minimising the χ^2 equation of the form

$$\chi^2 = \sum_{i,j} \left[\frac{(a_{ij} - x_i^s - x_j^f)^2}{\sigma_{a_{ij}}^2} + \frac{(b_{ij} - y_i^s - y_j^f)^2}{\sigma_{b_{ij}}^2} \right] \tag{7.2}$$

where a and b are total tilts, x and y are the individual tilts for the i^{th} spherical (s) and j^{th} flat (f) mirrors, $\sigma = \frac{1}{\sqrt{N}}$ and N is the number of events in the histogram.

The contributions to the total error in x and y for each segment are dependent upon the geometry of the path that the Cherenkov photons takes for each mirror combination. Therefore equation 7.2 can be rewritten to include corrections to each of the tilts, that take into account a geometrical effect for each of the spherical/flat mirror combinations. We call these coefficients p and q, and they need to be extracted from the simulation. The modified χ^2 equation to be minimised is as follows:

$$\chi^2 = \sum_{i,j} \left[\frac{(a_{ij} - p^x_{ij} x^s_i - q^x_{ij} x^f_j)^2}{\sigma^2_{a_{ij}}} + \frac{(b_{ij} - p^y_{ij} y^s_i - q^y_{ij} y^f_j)^2}{\sigma^2_{b_{ij}}} \right]. \qquad (7.3)$$

7.2 Mirror Combination Contributions

In the process of extracting the individual tilts of the mirror segments, it is important to know the contributions of each segment in a spherical/flat mirror combination to the total tilt. Due to the longer path length that a Cherenkov photon must travel before finally arriving at the photo-detector plane, the spherical mirror will always have a larger contribution to the error than the flat mirror. However, the contributions between any two pairs of spherical and flat mirrors can be comparatively different due to slightly different Cherenkov photon path lengths for each spherical/flat mirror combination. Table 7.1 shows the coefficients due to contributions of various combinations of spherical and flat mirror segments. From this table it can be seen that each mirror segment is involved in more than one combination. The table only includes spherical and flat mirror segments 00-06, however, the full simulation uses the contributions from the whole range of spherical and flat mirror segments. The mirror numbering is shown in figure 7.1. The meaning of, for example, coefficients p^x_{ij} for the mirror combination 00/00 is that the tilt in the spherical mirror has to be multiplied by 1.9143 to obtain the observed coefficient amplitude a_{ij} of $cos(\phi_{ch})$, where ϕ_{ch} is the azimuthal angle. These coefficients were obtained empirically from a simulation of the mirror misalignments by A. Papanestis.

Comb. Sph(i)/Flat(j)	p_{ij}^x	q_{ij}^x	p_{ij}^y	q_{ij}^y
00/00	1.9143	1.03797	1.59502	0.491157
01/00	1.989	1.08956	1.75052	0.547331
01/01	1.93199	0.980127	1.64221	0.53446
01/02	1.85975	0.745694	1.54807	0.328945
02/01	2.07562	1.13113	1.75019	0.598982
02/02	1.94133	0.878648	1.60072	0.438049
02/03	1.92559	0.746576	1.58648	0.364013
03/02	2.16898	1.12185	1.75697	0.2499
03/03	1.89801	0.747529	1.63827	0.527034
04/00	1.84485	1.0385	1.56929	0.48035
04/01	1.83147	0.858623	1.49365	0.522952
04/04	1.9217	1.08201	1.71064	0.600334
04/05	1.87442	0.908197	1.66337	0.51978
05/01	1.94994	1.0286	1.65394	0.481793
05/02	1.81299	0.770431	1.48256	0.527971
05/05	1.99063	1.05409	1.721	0.538186
05/06	1.88963	0.817863	1.62971	0.495203
06/02	1.91661	0.955344	1.66915	0.855976
06/03	1.80354	0.655605	1.49658	0.455742

Table 7.1: A limited table of coefficients from mirror contributions for spherical and flat mirror segments 00 to 06, where i and j are specific spherical and flat mirror segments (see figure 7.1), p_{ij}^x and q_{ij}^x are the individual contributions of segments i and j in x and p_{ij}^y and q_{ij}^y are the individual contributions of segments i and j in y [62].

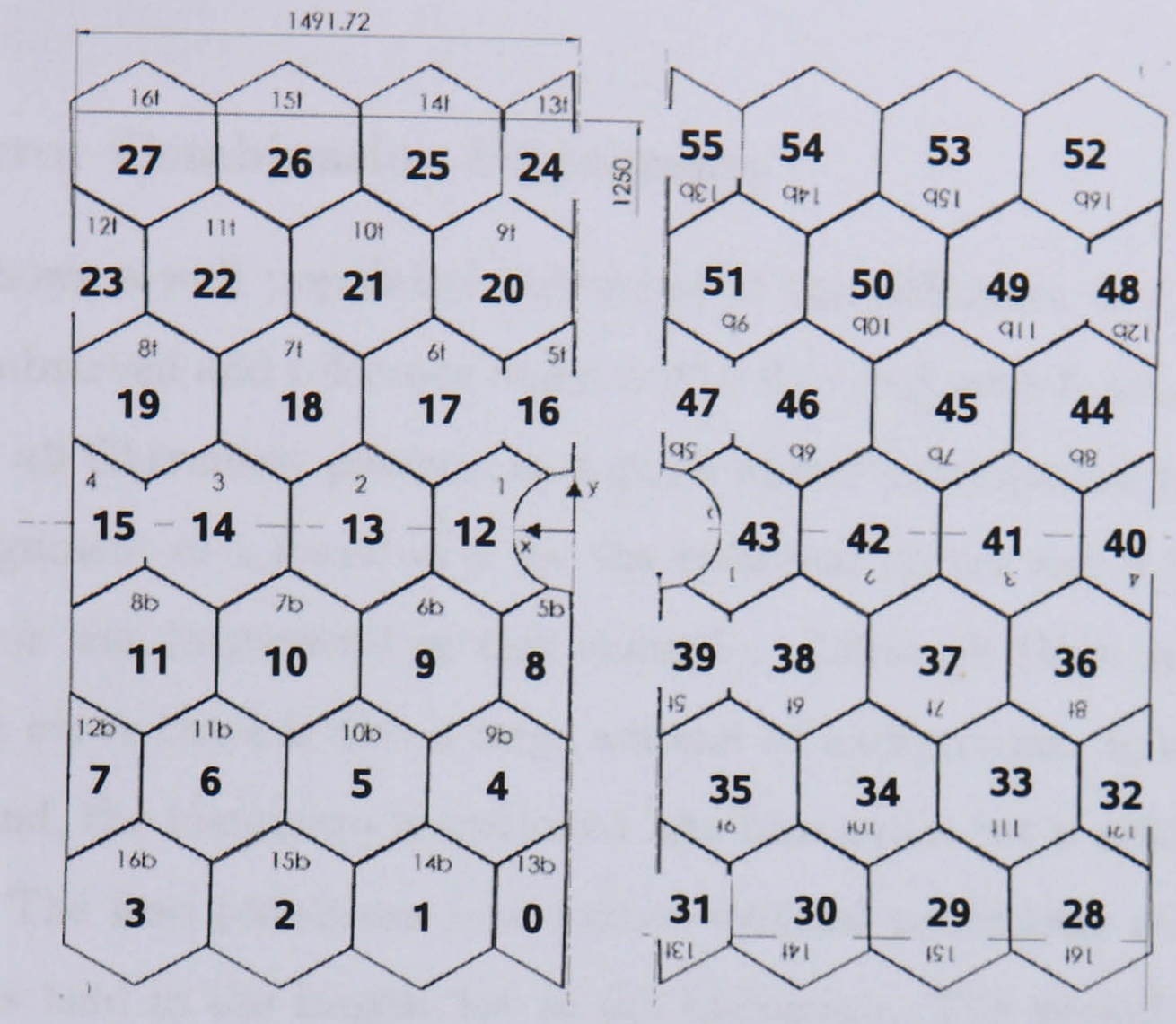

19	18	17	16
15	14	13	12
11	10	9	8
7	6	5	4
3	2	1	0

39	38	37	36
35	34	33	32
31	30	29	28
27	26	25	24
23	22	21	20

Figure 7.1: Mirror numbering in the full alignment simulation [62].

7.3 Simulation

The results of this chapter have been produced using 800,000 simulated $B_d \to \pi\pi$ events with mirror misalignments of between 0.7 *mrad* and 1 *mrad* introduced randomly. These events have been generated using the full GEANT4 [20] based GAUSS [55] Monte Carlo simulation for LHCb, then digitised using the RichReadout package [19] and reconstructed using BRUNEL [54]. Because the alignment from data requires near saturated Cherenkov rings, a cut is applied so that particles with a momentum of less than $30GeV$ are excluded. A. Papanestis (RAL) carried out this

simulation.

7.3.1 Mirror Combination Histograms

Figure 7.2 shows a well populated histogram of the difference in Cherenkov angle between the observed and reference angle ($\Delta\theta = \theta_{ch} - \theta_o$), as a function of azimuthal angle (ϕ) for all Cherenkov photons in a given mirror combination (spherical 1, flat 1). A misalignment of 1 $mrad$ in x for the spherical mirror and 0.7 $mrad$ in y for the flat mirror was introduced in this example. Although there is a well defined misalignment curve there is also a large amount of background. In order to remove the background, the histogram is sectioned into bins and a cut is made based on two parameters. The first parameter is a defined decimal percentage of the number of photon events held in the largest bin in the histogram. The second parameter is a defined decimal percentage of the number of photon events held in the largest bin of each column. If a bin fails to exceed either of these two threshold parameters it is excluded in the cut.

Figure 7.3 shows the results of the cut made on figure 7.3. All bins that have failed to exceed 61% of the number of photon events held in the largest bin of each column and 25% of the number of photon events held in the largest bin of the histogram have been excluded. The background has been effectively removed. Once the cut has been made, a fit to the data can be made (see figure 7.4).

It is evident that for mirror combinations where there are a high number of events in the histogram the fit is very good. However, some mirror combinations provide very few events (figure 7.5) and the resulting cut (figure 7.6) can be very poor leading to a fit that does not closely follow the data points (figure 7.7). Such mirror combinations are removed from the minimisation process so as not to deteriorate the overall accuracy of the software compensation for misaligned mirror segments.

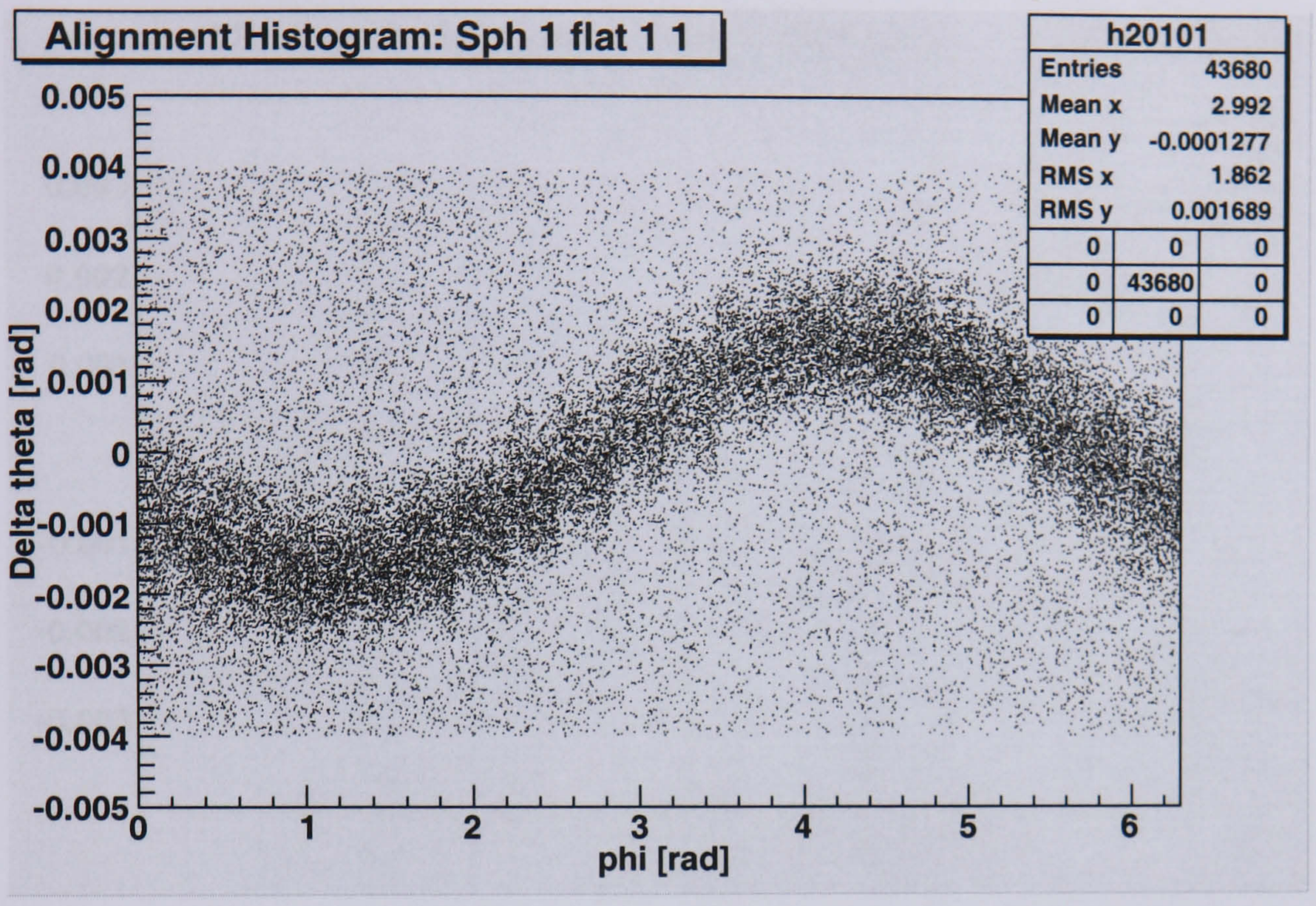

Figure 7.2: A histogram of alignment for spherical/ flat mirror combination 1/1.

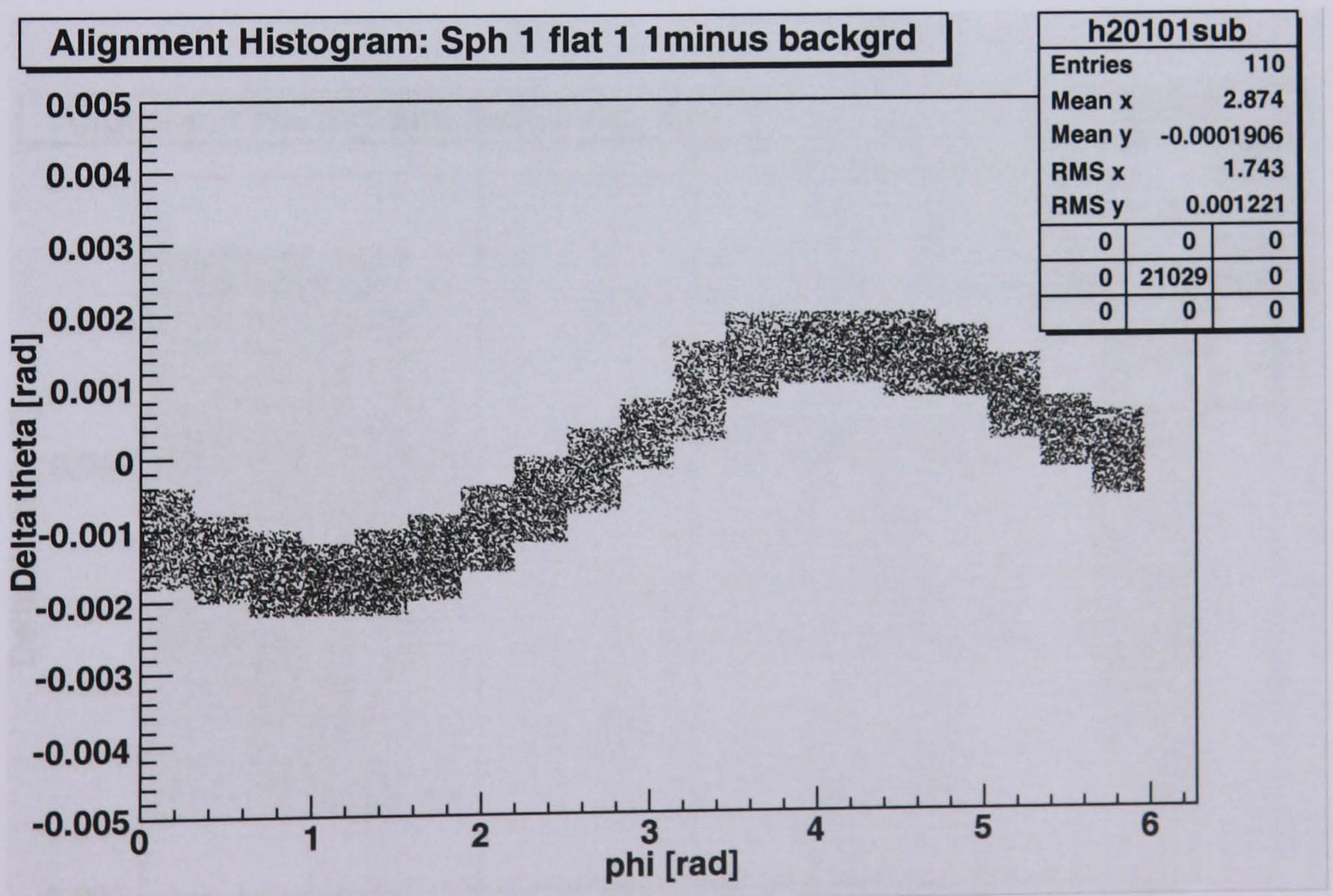

Figure 7.3: A histogram of alignment for spherical/ flat mirror combination 1/1 after the background rejection cut has been applied.

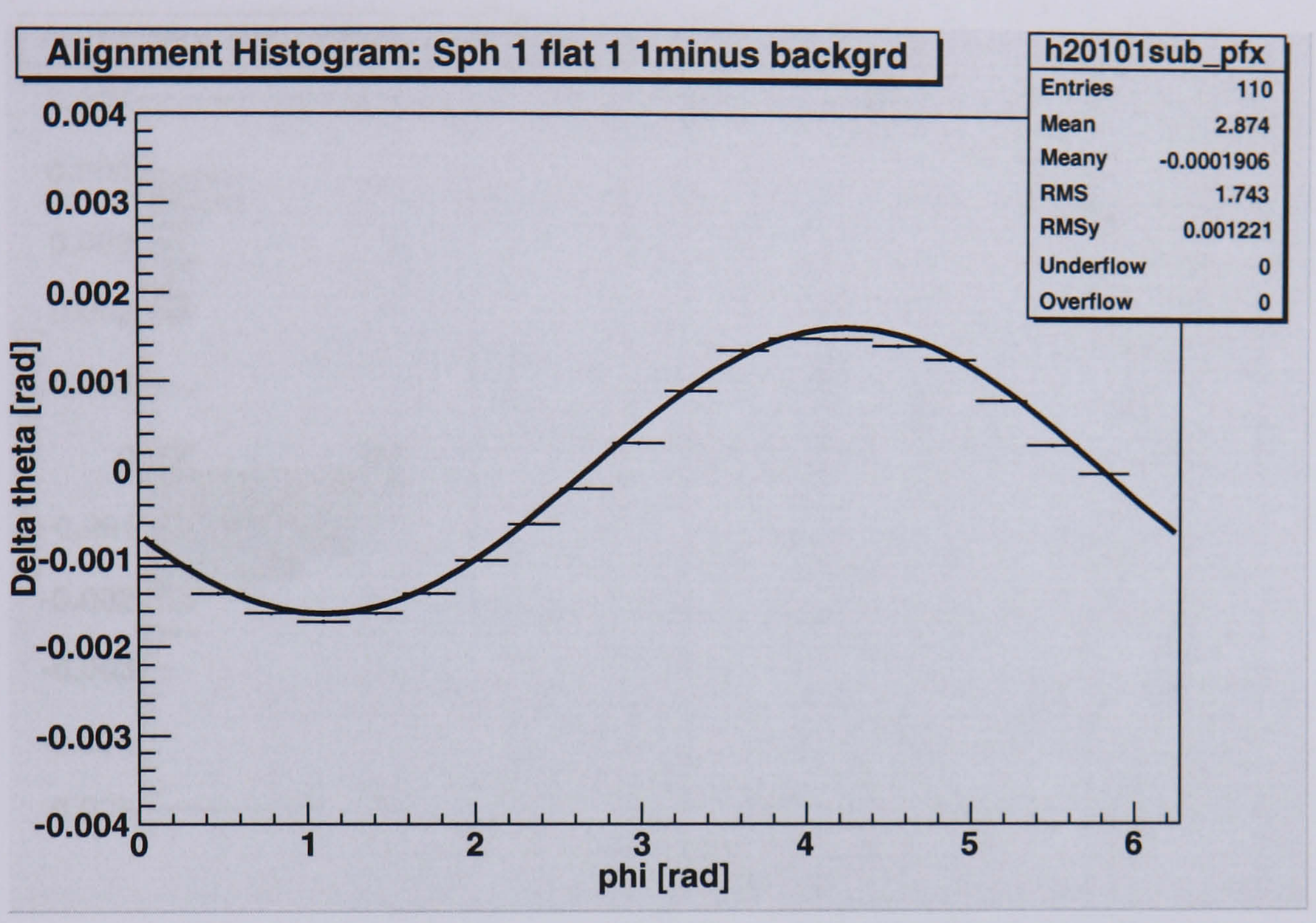

Figure 7.4: A fit to the histogram of alignment for spherical/flat mirror combination 1/1 after the background rejection cut.

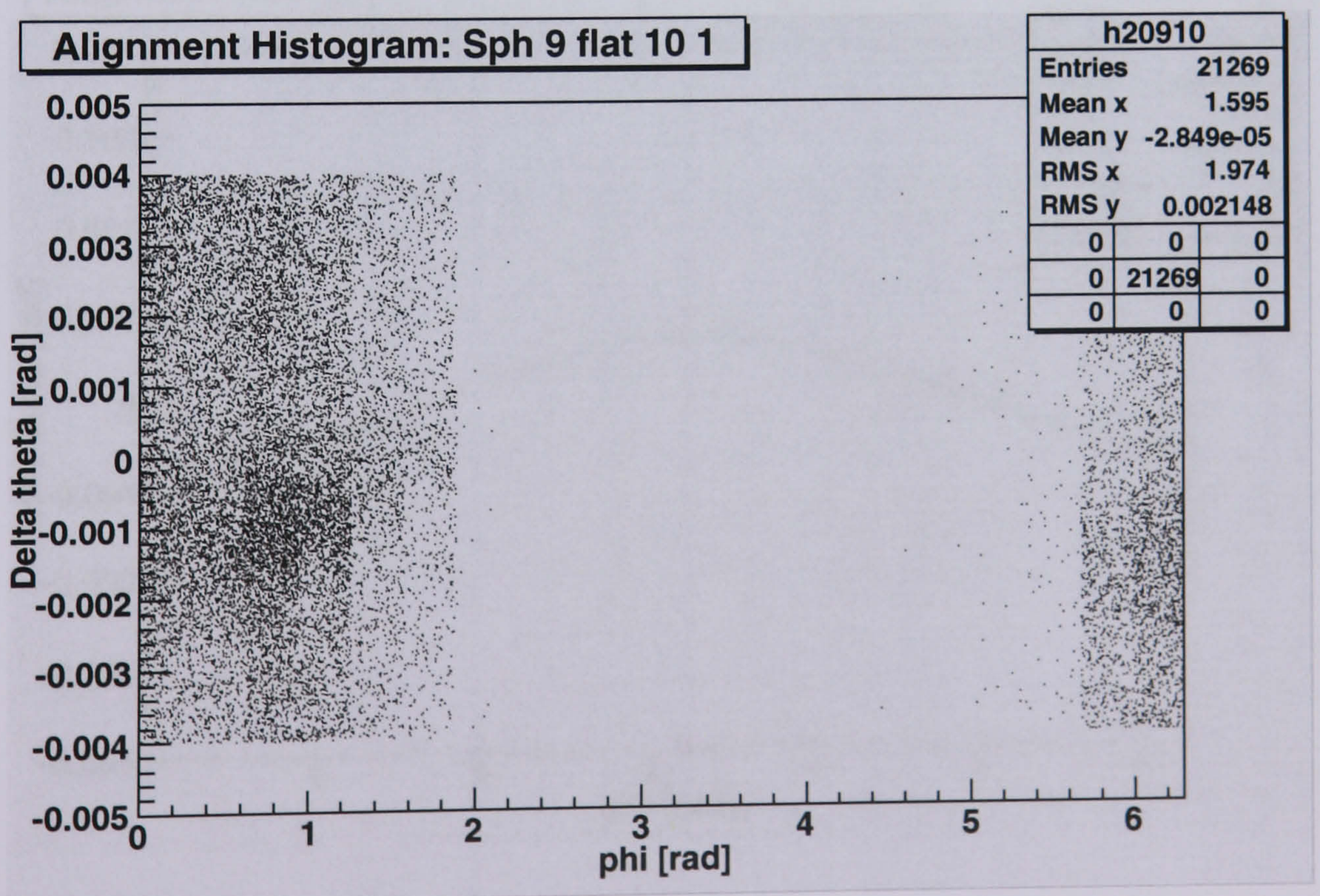

Figure 7.5: A histogram of alignment for spherical/flat mirror combination 9/10.

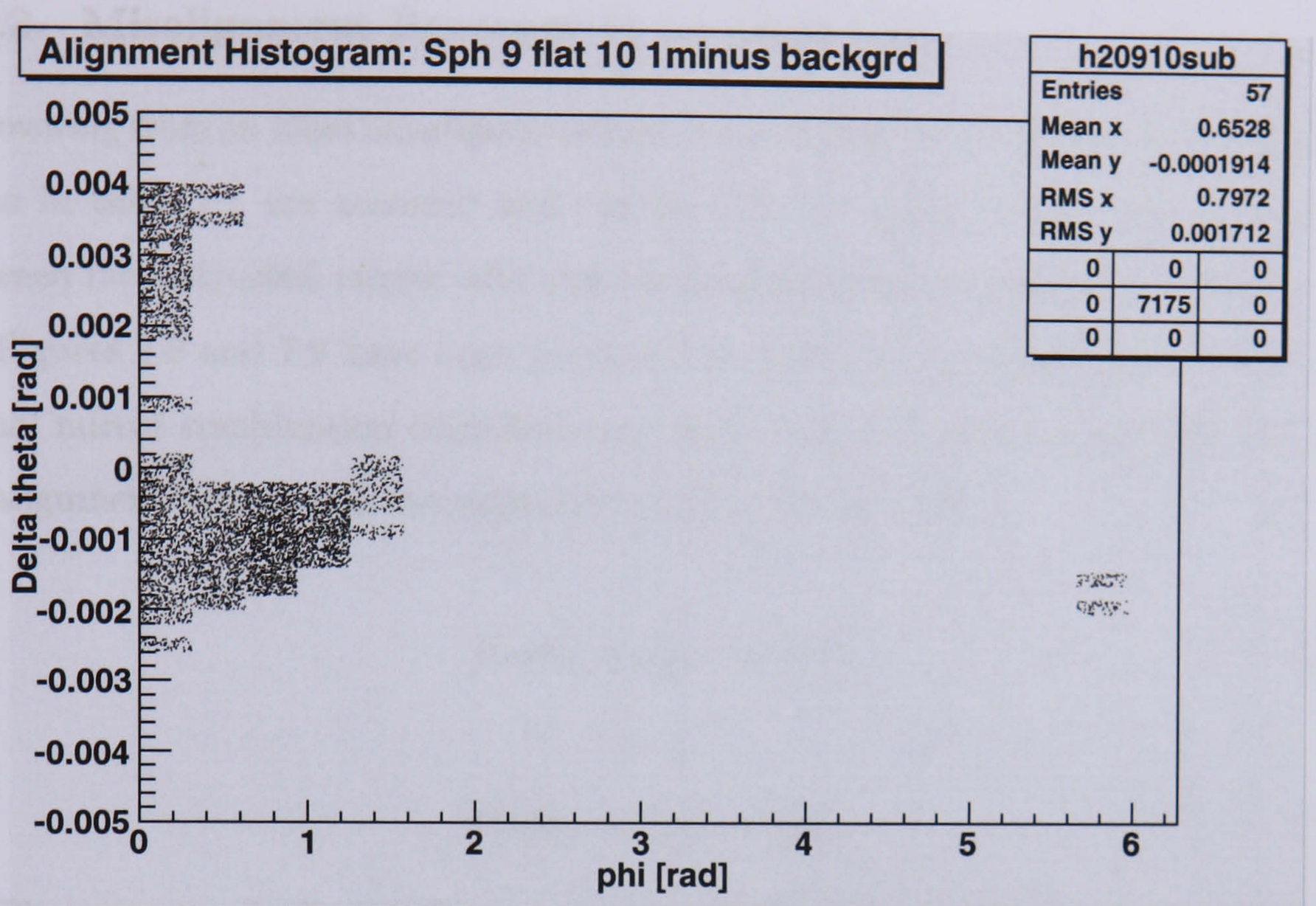

Figure 7.6: Histogram in Figure 7.5 after the background rejection cut has been made.

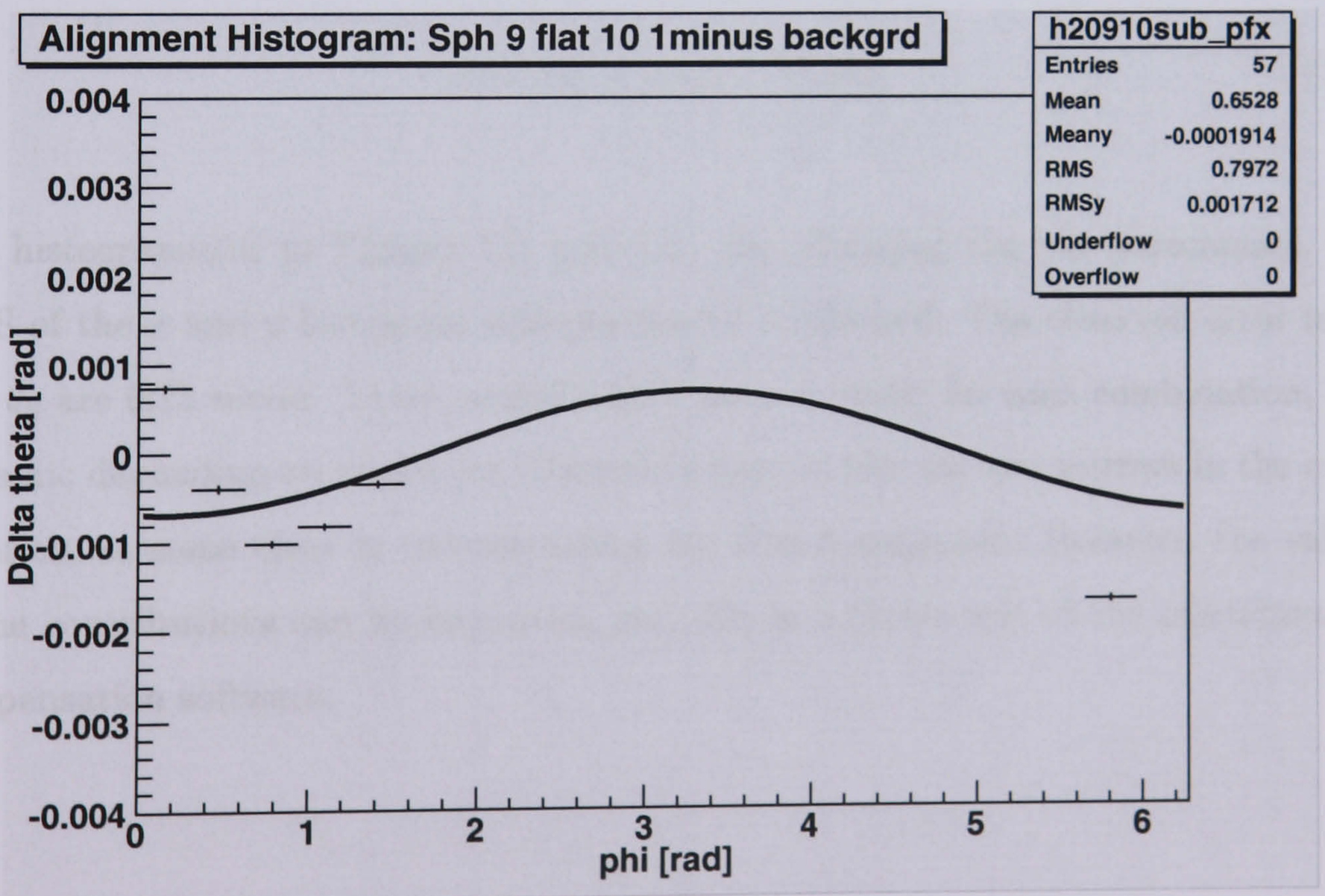

Figure 7.7: A fit to the histogram of alignment (Figure 7.6) after the background rejection cut.

7.3.2 Misalignment Recovery in an Ideal Case

Recovering from an ideal misalignment case is a good test to verify that the coefficients given in table 7.1 are accurate and can provide the appropriate correction factors between reconstructed mirror tilts and the misalignment introduced.

Figures 7.8 and 7.9 have been produced by taking the coefficients from the individual mirror combination contributions (Table 7.1) and multiplying them by their misalignment tilts to find the expected x and y tilts so that

$$Exp\theta_x = p^x_{ij}x^s_i + q^x_{ij}x^f_j \tag{7.4}$$

and

$$Exp\theta_y = p^y_{ij}y^s_i + q^y_{ij}y^f_j. \tag{7.5}$$

These expected tilts are then compared with the tilts that were introduced in the simulation:

$$Error\theta_x = Tilt_x - Exp\theta_x \tag{7.6}$$

$$Error\theta_y = Tilt_y - Exp\theta_y \tag{7.7}$$

and histogrammed in Figures 7.8 and 7.9. By changing the cut parameters, the RMS of the x and y histogram outputs can be minimised. The observed error in θ_x and θ_y are 0.15 $mrad$. These contributions are not static for each combination, but dynamic depending on where the Cherenkov photon hits the two mirrors in the combination, so some error in reconstructing the tilts is expected. However, the values of the contributions can be improved, and this is a future aim of the misalignment compensation software.

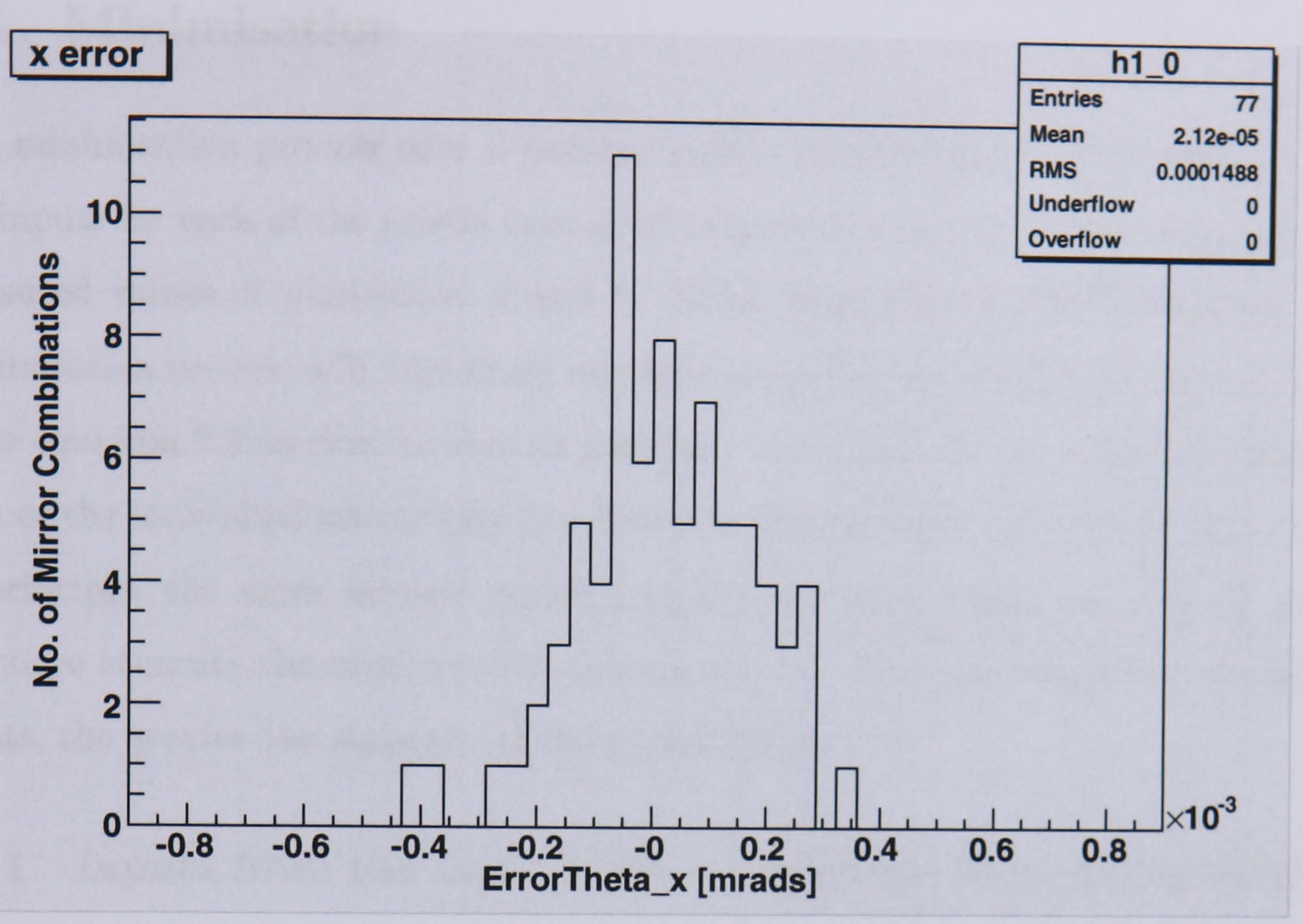

Figure 7.8: Errorθ_x, defined as the expected θ_x minus the tilt in θ_x, for all mirror combinations.

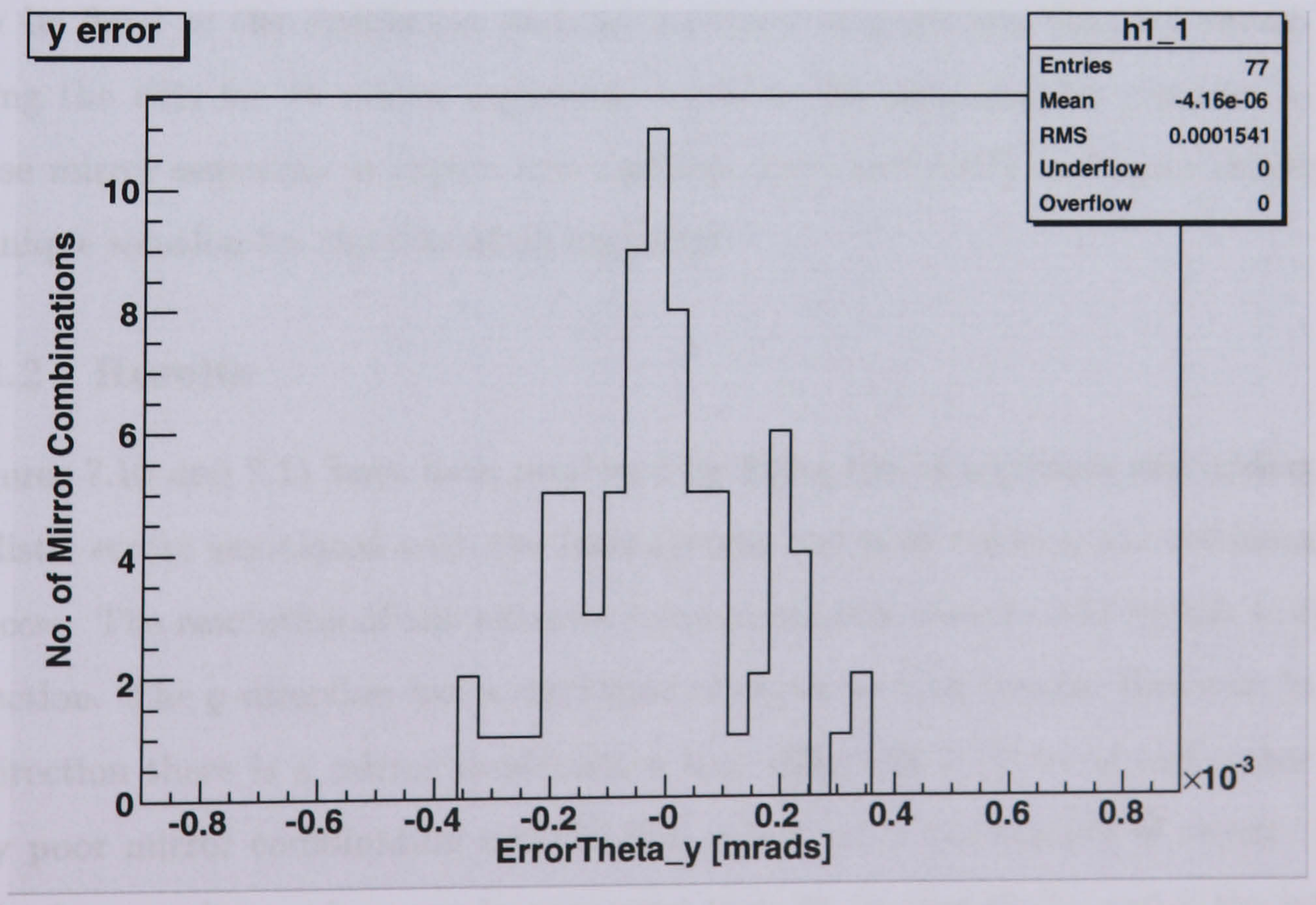

Figure 7.9: Errorθ_y, defined as the expected θ_y minus the tilt in θ_y, for all mirror combinations.

7.4 Minimisation

The minimisation process uses a package called MINUIT [22]. This package takes the inputs for each of the mirror combination contributions for x and y and also the measured values of parameters a and b. Using approximate mirror rotations, the minimisation process will take these inputs and resolve the individual mirror tilts to make equation 7.3 as close to zero as possible. The output of the minimisation gives each of the individual mirror tilts in relation to one (or more) mirrors of fixed value. In principle, the more mirrors whose positions are known and can thus be fixed, the more accurate the minimisation process will be. Also, the larger the number of events, the greater the accuracy of the minimisation.

7.4.1 Inputs from the Laser Mirror Alignment Monitoring System

As has been previously mentioned, the laser mirror alignment monitoring system will provide the positions of 16 mirror segments in RICH2. This means that the rotational values of the 16 segments that the laser alignment monitoring system will provide can be fixed in the simulation with an accuracy of much less than 0.1 *mrad*. By fixing the tilts for 16 mirror segments, it allows the minimisation program to use these mirror segments as inputs and converge more accurately and more rapidly on a unique solution for the tilts of all segments.

7.4.2 Results

Figures 7.10 and 7.11 have been produced by fixing the 16 segments and adding the realistic errors associated with the laser system and then running the minimisation process. The resolution of the software compensation is close to 0.12 *mrads* in the x direction. The y direction has a resolution of closer to 0.18 *mrads*. However, in the y direction there is a mirror combination that differs by 0.75 *mrad* and either has very poor mirror combination contribution values, or a low number of events. If it is the former, these values can be corrected through further study; and if the latter, the combination can be removed from the analysis. Corrections such as this to both x and y should greatly improve the resolution of the system.

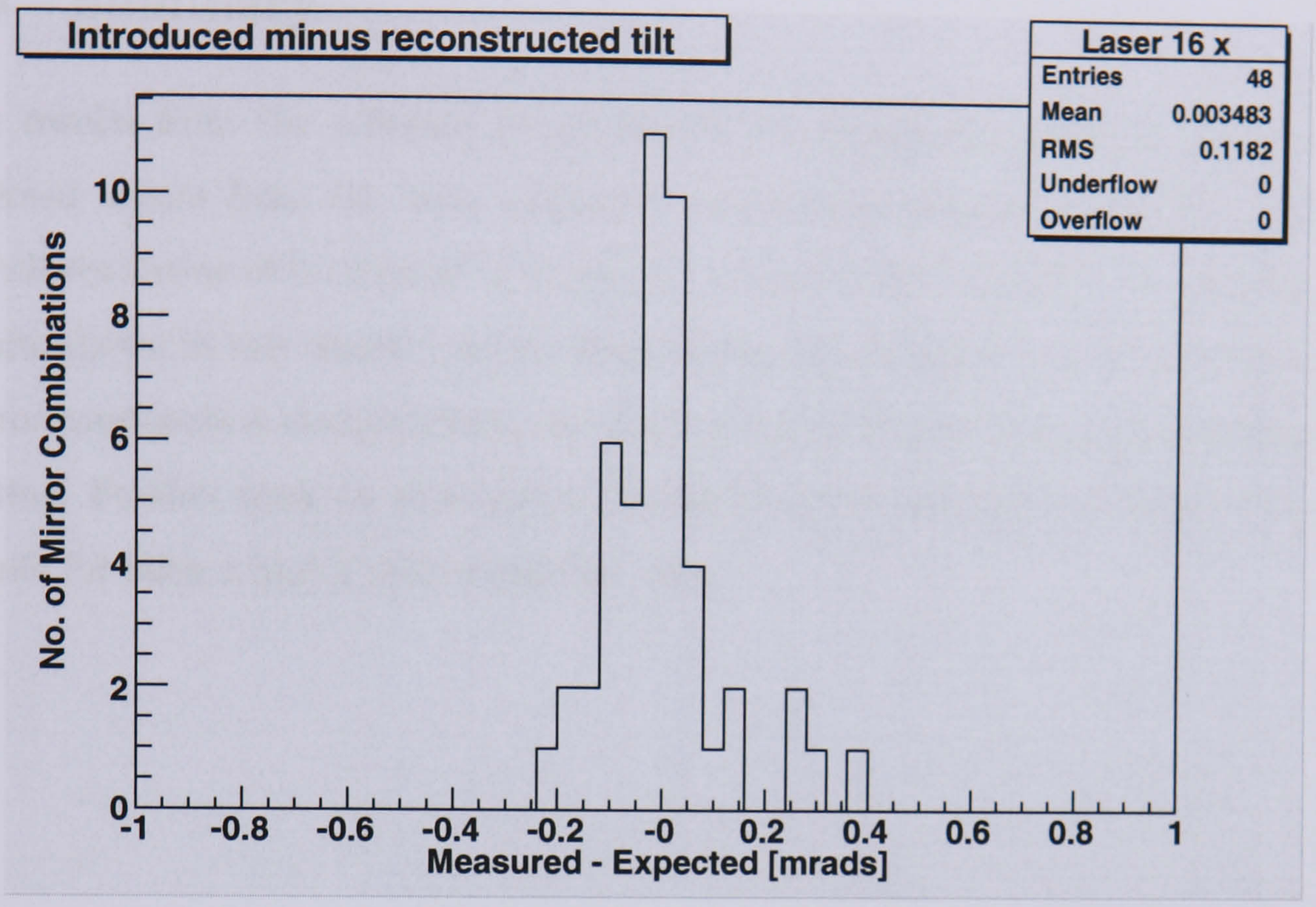

Figure 7.10: A plot of the number of mirror combinations against $\Delta\theta_x$ after the minimisation.

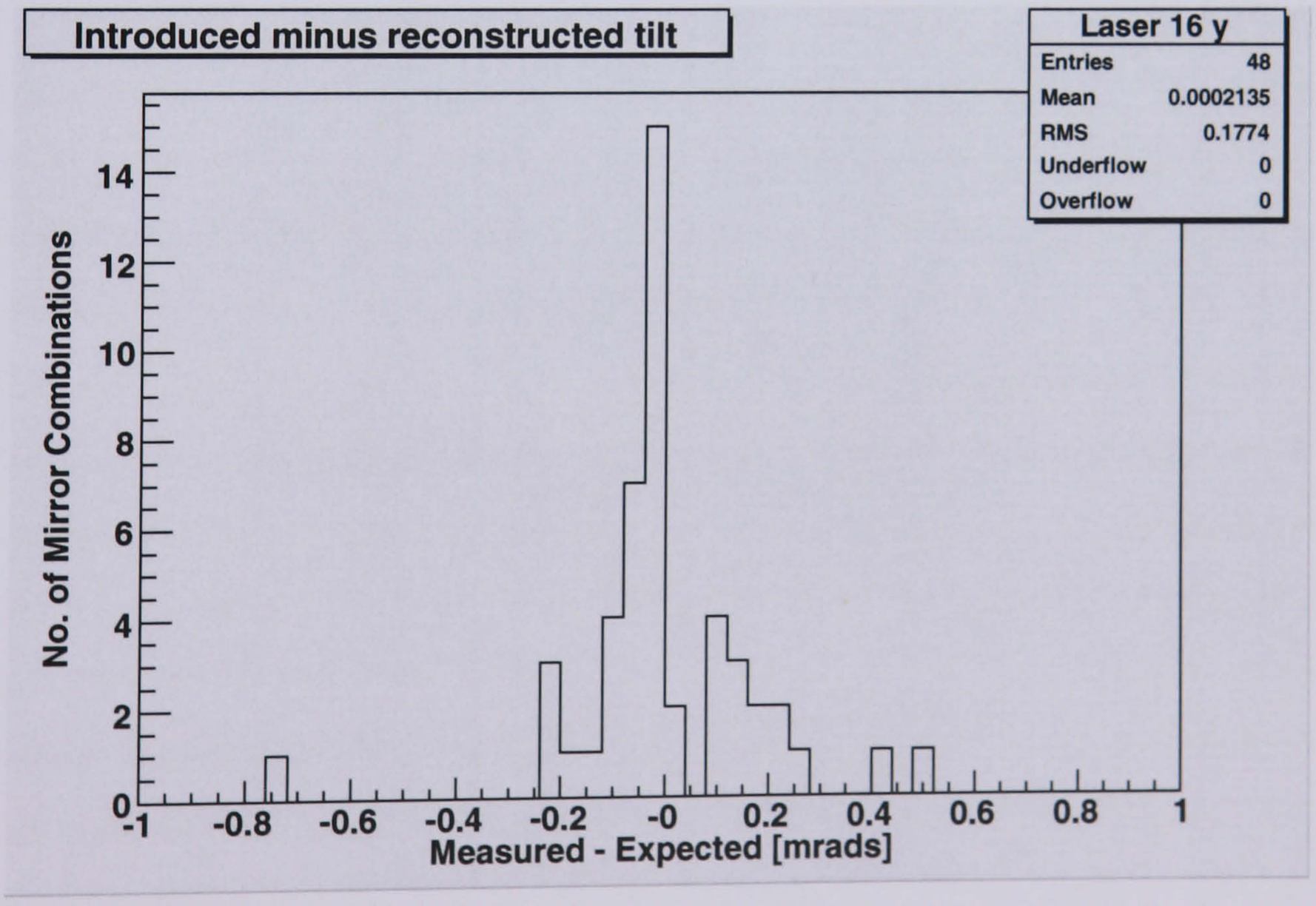

Figure 7.11: A plot of the number of mirror combinations against $\Delta\theta_y$ after the minimisation.

7.5 Summary

The results from the software compensation for misaligned mirror segments with 16 fixed inputs from the laser alignment monitoring system have shown that an overall resolution of 0.12 mrad in θ_x and 0.18 mrad in θ_y is possible. In principle the results shown in this chapter can be improved by producing a more accurate table of mirror combination contributions, and making multiple iterations of the minimisation routine. Further work on this system should bring the resolution to better than 0.1 *mrads* for both x and y mirror segment tilts.

Chapter 8

Conclusion

The Cherenkov angle for photons produced by saturated tracks in the CF_4 gas of the 2^{nd} RICH detector of LHCb is 31 *mrad*. The typical resolution for this angle is 0.7 *mrad*. The alignment of the RICH2 mirrors should not degrade this resolution, so a target of 0.1 *mrad* on mirror alignment resolution has been set. The RICH2 mirrors must remain thin to reduce the probability that the particles interact with them, so they therefore have to be segmented to retain rigidity. Each segment has the potential to move over time. Small movements in the mirror segments could produce large errors in the measurement of particle velocities and thus also in the identification of particles. Therefore, the positions of the mirror segments must be monitored over time to achieve optimal accuracy.

The method for monitoring these segments is to use a combination of software and a hardware based alignment monitoring system. The hardware system provides the precise positions of selected mirror segments as reference points. The software system will then use these reference points in conjunction with Cherenkov photon projections from saturated high energy tracks to resolve the positions of the remaining mirror segments. The hardware based alignment system must also provide any change in mirror segment position to 0.1 *mrad* or better. It must also be reliable and be able to survive a high radiation fluorocarbon environment for an extended period of time (the expected lifetime of the experiment is more than 5 years).

This thesis has described the design and characterisation of the hardware based laser mirror alignment monitoring system. We have developed a method for long term monitoring of the stability of the RICH2 mirror segments based on laser beams delivered by optic fibres, associated optical systems and readout based on an APS detector. The software developed for extracting the stability of the laser beam images from the APS detectors is based on techniques widely used in the image analysis industry. Through the use of simulation and prototype measurements, the ability of the system to recover mirror segment movements has been determined. It has been shown that:

1. Using an automated method for resolving the precise positions of the signal and alignment beams, that a fit can be made to show the difference between the two beams with an uncertainty of 11 pixels on the recording APS.

2. A linear approximation can be made to the relationship between a mirror segment Y rotation and the direction that the signal beam travels carrying an error of less than 1% over a change of 0.1 $mrad$.

3. The laser alignment monitoring system resolution has been measured to be 0.013 $mrad$ for both θ_y and θ_x rotations, with a long term stability of 0.014 $mrad$ in θ_y and 0.006 $mrad$ in θ_x.

4. The results from the software compensation for misaligned mirror segments with 16 fixed inputs from the laser alignment monitoring system procedure have shown that an overall resolution of 0.12 mrad in θ_x and 0.18 mrad in θ_y are possible.

This thesis has also described the attributes of the components to be used in the final system; the precise process of the placement of the components through the component location algorithm and also the design requirements for the engineers and precise position of the mounts and the plates on which they are held. These positions have been verified, and the plates have now been fabricated and installed into the RICH2 detector.

Final development of the system will be carried out by Paul Soler (Glasgow/RAL), Antonis Papanestis (RAL) and also Gabriel Vidal-Sitjes (Imperial College) who is working on using the laser mirror alignment monitoring system for the RICH1 detector.

Appendix A

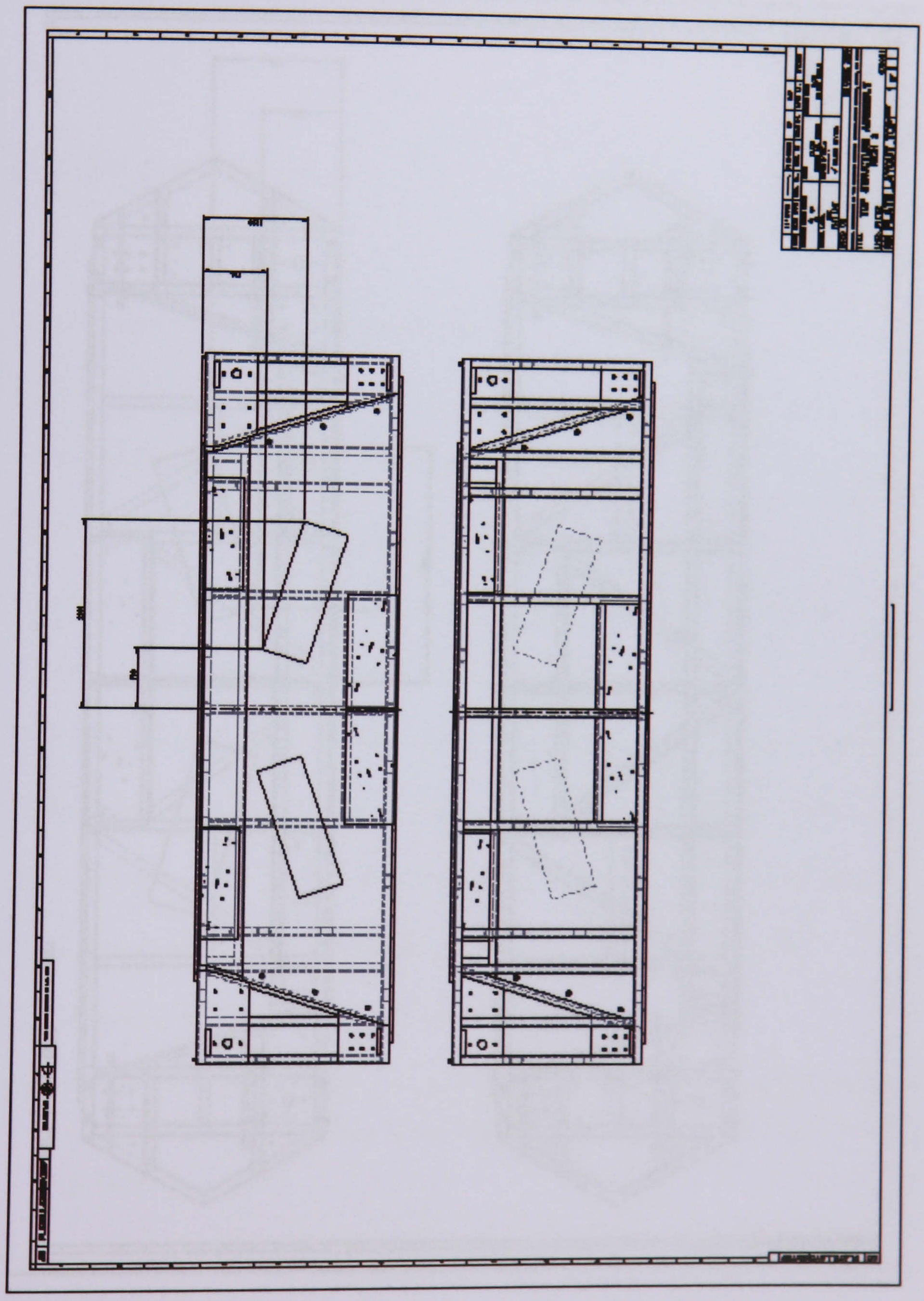

Figure 1: Engineering drawings for the top plate positions in RICH2

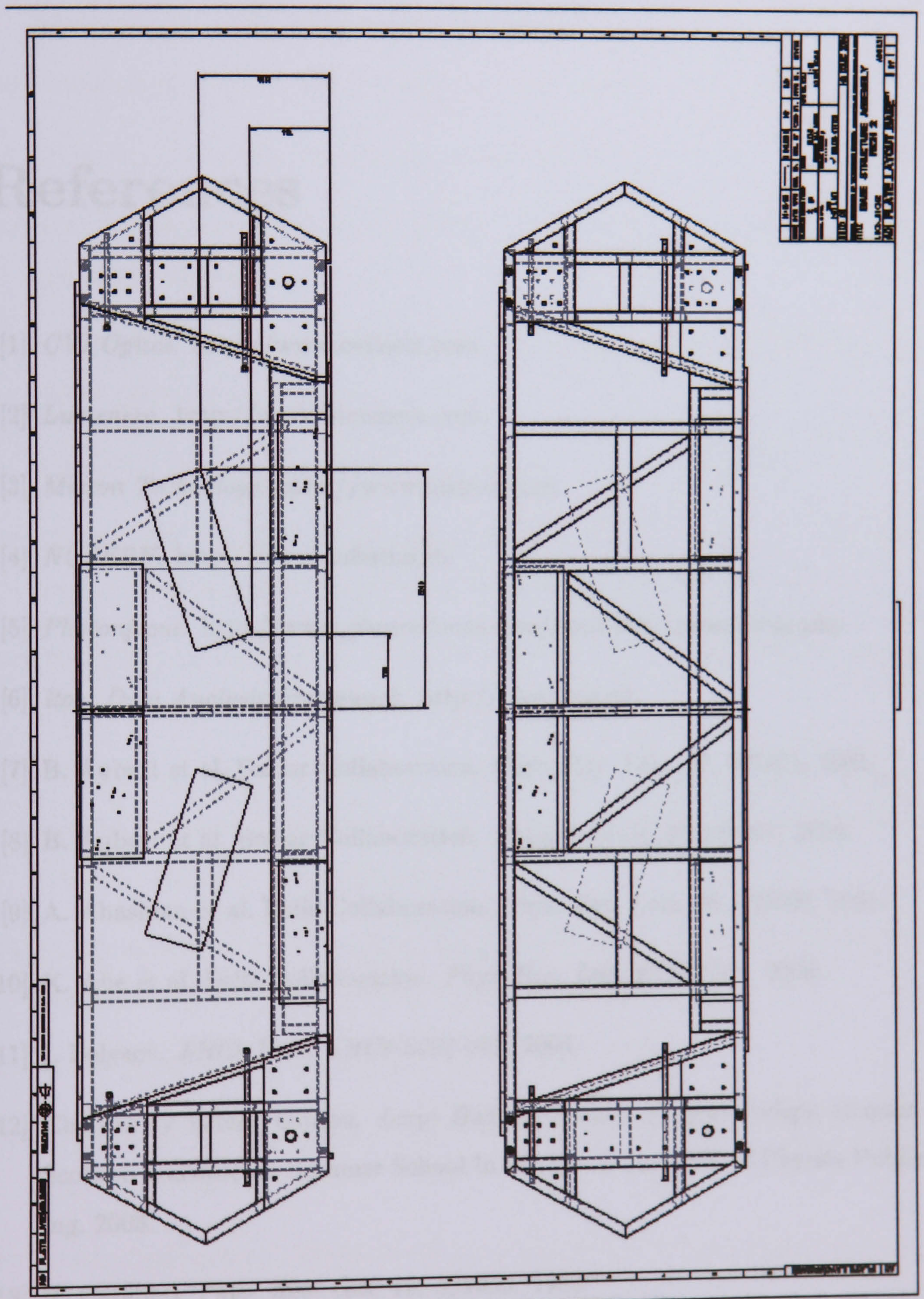

Figure 2: Engineering drawings for the base plate positions in RICH2

References

[1] *CVI Optics.* http://www.cvilaser.com.

[2] *Lumenera.* http://www.lumenera.com.

[3] *Micron Technology.* http://www.micron.com.

[4] *NUFERN.* http://www.nufern.com.

[5] *Photonfocus.* http://www.photonfocus.com/html/eng/cmos/linlog.php.

[6] *Root Data Analysis Framework.* http://root.cern.ch.

[7] B. Aubert et al. BaBar Collaboration. Phys. Rev. Lett. 87, 091801, 2001.

[8] B. Aubert et al. BaBar Collaboration. *Phys.Rev.Lett. 93 131801.* 2004.

[9] A. Abashian et al. Belle Collaboration. Phys. Rev. Lett. 86, 002509, 2001.

[10] K. Abe et al. Belle Collaboration. *Phys. Rev. Lett. 93 021601.* 2004.

[11] I. Belyaev. *LHCb Note, LHCb-2004-021.* 2004.

[12] Chapter by Valerie Gibson. *Large Hadron Collider Phenomenology*, chapter 8. Scottish Universities Summer School in Physics & Institute of Physics Publishing, 2003.

[13] N. Cabibbo. *Phys. Rev. Lett. 10, 531533.* 1963.

[14] Cahn and Goldhaber. *The Experimental Foundations of Particle Physics*, chapter 7. Cambridge, 1989.

[15] Anderson C.D. *Science (Washington, DC, United States) 1932, 76 CODEN: SCIEAS; ISSN: 0036-8075*, pages 238–239. 1932.

[16] Anderson C.D. *Phys. Rev. 43*, pages 491–494. 1933.

[17] Anderson C.D. *Phys. Rev. 51*, pages 884–886. 1937.

[18] GAUDI Framework CERN (2005). *http://proj-gaudi.web.cern.ch/proj-gaudi/welcome.html.*

[19] GaussRICH Package CERN (2005). *https://uimon.cern.ch/twiki/bin/view/-LHCb/RichSoftwarePackages.*

[20] GEANT4 Toolkit CERN (2005). *http://geant4.web.cern.ch/geant4/.*

[21] GiGa GEANT4-GAUDI Interface Package CERN (2005). *http://lhcb-comp.web.cern.ch/lhcb-comp/Frameworks/Geant4/default.htm.*

[22] Minuit Fitting Package CERN (2005). *http://seal.web.cern.ch/seal/snapshot/work-packages/mathlibs/minuit/home.html.*

[23] J Chadwick. *The Existence of a Neutron, Proceedings of the Royal Society of London. Series A, Containing Papers of a Mathematical and Physical Character, Volume 136, Issue 830*, pages 692–708. 1932.

[24] G.P.S. Occhialini C.M.G Lattes, H. Muirhead and C.F. Powell. *Processes involving charged mesons, Nature 159*, page 694. 1947.

[25] KTeV Collaboration. Phys. Rev. Lett. 83, 2227, 1999.

[26] LHCb Collaboration. *LHCb Calorimeters Technical Design Report CERN LHCC 2000-0036.* 2000.

[27] LHCb Collaboration. *LHCb RICH Technical Design Report 2000-037.* 2000.

[28] LHCb Collaboration. *LHCb Muon System Technical Design Report CERN LHCC 2001-010.* 2001.

[29] LHCb Collaboration. *LHCb Outer Tracker Technical Design Report CERN LHCC 2001-024.* 2001.

[30] LHCb Collaboration. *LHCb RICH2 Engineering Design Review Report 2002-009.* 2002.

[31] LHCb Collaboration. *LHCb Reoptimized Technical Design Report 2003-030.* 2003.

[32] LHCb Collaboration. *LHCb RICH1 Engineering Design Review Report 2004-xxx, EDMS 493831.* 2004.

[33] LHCb Collaboration. *LHCb Muon Technical Design Report, Addendum 2 CERN/LHCC 2005-012.* 2005.

[34] NA48 Collaboration. Physics Letters B, Volume 465, Number 1, 21 October 1999, pp. 335-348(14), 1999.

[35] R.O. Duda and P.E. Hart. *Pattern Classification and Scene Analysis.* Wiley, New York, 1973.

[36] CKMfitter Group (J. Charles et al.). *Eur. Phys. J. C41, 1-131, hep-ph/0406184.* 2005.

[37] X. T. Meng et al. *Gamma-ray radiation and annealing effects on colour CMOS image sensors.* Semicond. Sci. Technol. 18 No.1 (January) L1-L3, 2003.

[38] S. Eidelman et al. (Particle Data Group). *Phys. Lett. B 592, 1.* 2004.

[39] Y. Fukuda et al. SuperKamiokande Collaboration. *Phys. Rev. Lett. 81.* pages 1562–1587. 1998.

[40] E. Fermi and Zeits. f. E. Segre. *Physik 82,* page 729. 1933.

[41] R. P. Feynman and M. Gell-Mann. *Phys. Rev. 109, 193198.* 1958.

[42] C. Frei. *Optical Elements for Production Readiness Review* http://agenda.cern.ch/fullAgenda.php?ida=a03786#2003-04-28, 2003.

[43] C. Frei. *RICH2 - Mirror Supports.* http://agenda.cern.ch/fullAgenda.php?ida=a035954#2003-11-26, 2003.

[44] Christophe Frei. *Positions of the Mirror Segments in the RICH2 Detector, LHCb EDMS-380417-v1*, page 9. 2003.

[45] J. Agostinelli et al. GEANT4 Collaboration. *Nucl. Instr. and Meth. A 506*, pages 250–303. 2003.

[46] M. Gell-Mann. *Phys. Lett. 8:214.* 1964.

[47] G. R. Hopkinson and D. H. Lumb. *Noise Reduction Techniques for CCD Image Sensors.* J. Phys. E: Sci. Instrum., Vol. 15, 1982.

[48] P. V. C. Hough. *Method and Means for Recognizing Complex Patterns.* U.S. Patent 3069654, December 18, 1962.

[49] V. L. Fitch J. H. Christenson, J. W. Cronin and R. Turlay. *Phys. Rev. Lett. 13, 138140.* 1964.

[50] J. V. Jelley. *Cerenkov Radiation*, chapter 1, page 4. Pergamon Press, London, 1958.

[51] M. Kobayashi and T. Maskawa. *Prog. Theor. Phys. 49, 652.* 1973.

[52] P. Langacker. Czech. J. Phys. 55 B501-B514. Arxiv preprint hep-ph/0503068, 2005.

[53] S. Amato et al. LHCb Collaboration. *Magnet Technical Design Review Report CERN LHCC 2000-007.* 2000.

[54] Brunel Reconstruction Package LHCb Collaboration (2005). *http://lhcb-comp.web.cern.ch/lhcb-comp/Reconstruction/default.htm.*

[55] GAUSS Simulation Package (2005) LHCb Collaboration (2005). *http://lhcb-comp.web.cern.ch/lhcb-comp/Simulation/default.htm.*

[56] P. Loveridge. *RICH2 Superstructure FEA* http://agenda.cern.ch/fullAgenda.php?ida=a03473#2003-02-19. 2003.

[57] Dirac P. A. M. *The Quantum Theory of the Electron, Part II. Proc. Roy. Soc. London A118*, pages 351–361. 1928.

[58] Dirac P. A. M. *The Quantum Theory of the Electron. Proc. Roy. Soc. London A117*, pages 610–624. 1928.

[59] NobelPrize.org. http://nobelprize.org/physics/laureates/1922/index.html, 2000.

[60] Institute of Physics. IoP winter news letter, 2004.

[61] A. Papanestis. *LHCb note, LHCb-2001-141.* CERN, 2002.

[62] A. Papanestis. *Private Communication, 2nd September.* 2005.

[63] William K Pratt. *Digital Image Processing.* John Wiley & Sons, 1991.

[64] E. Rutherford. *The scattering of alpha and beta particles by matter and the structure of the atom.* Philosophical Magazine, ser 6, 21, 669-688, 1911.

[65] S. Kemeny S. Mendis and E. Fossum. *CMOS Active Pixel Image Sensor.* IEEE Transactions on Electronic. Vol. 41, No. 3, (March), 1994.

[66] A. Salam. *Elementary Particle Theory, edited by N. Svartholm (Almquist and Wiksell, Stockholm).* 1968.

[67] Fabio Sauli. Gem: A new concept for electron amplification in gas detectors. *Nucl.Instr.Meth.A 386*, pages 531–534, 1997.

[68] P. Soler. *Laser Alignment Mirror Monitoring Systems for the RICH, http://agenda.cern.ch/fullAgenda.php?ida=a054178#2005-06-30.* 2005.

[69] S. Weinberg. *Phys. Rev. Lett. 19, 1264.* 1967.

[70] W. Witzeling. *Status of the LHCb Experiment, http://lhcb-doc.web.cern.ch/lhcb-doc/presentations/conferencetalks/postscript/2004presentations/WernerWitzeling_proc.pdf.* 2004.

[71] L. Wolfenstein. *Phys. Rev. Lett. 51, 19451947.* 1983.

[72] H. Yukawa. *Proc. Phys. -Math. Soc. Japan, 17*, pages 55–56. 1935.

[73] G. Zweig. *CERN Preprint CERN-TH-412, NP-14146, Feb.* 1964.